

The Astrophysics of Strongly Interacting Systems

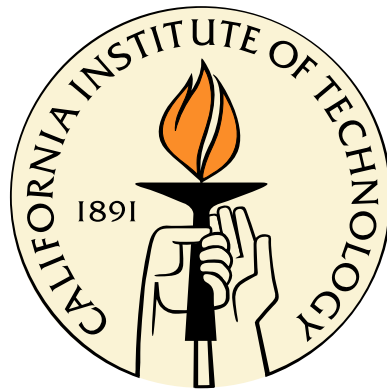
Thesis by

Tejaswi Venumadhav Nerella

In Partial Fulfillment of the Requirements

for the Degree of

Doctor of Philosophy



California Institute of Technology

Pasadena, California

2016

(Defended August 18, 2015)

© 2016

Tejaswi Venumadhav Nerella

All Rights Reserved

To my parents.

Acknowledgments

I have spent five wonderful and enriching years at Caltech, and I owe this to all my friends who have made my time here a lot of fun.

I consider myself extremely fortunate to have worked with my advisor, Chris Hirata, whom I consider a mentor and a friend. It is a great learning experience to watch Chris at the blackboard, and I am in awe at his ability to come up with a perfectly laid-out impromptu derivation of any physical effect. I am grateful for Chris's investment of time and effort in not just teaching me whatever was needed for a particular project, but rather in developing my breadth of knowledge.

I am grateful to Olivier Doré, Christian Ott, and Jamie Bock for agreeing to be on my thesis committee. I would also like to thank Olivier for all the conversations and support, and for being the closest I had to an on-campus advisor for the last two years of my Ph.D.

This thesis contains the first fruits of nearly twenty years of learning physics. This beautiful journey would never have started without my aunts' and grandparents' affection and care, and my teachers' support. I owe special thanks to my uncle, C.H.V.R. Gupta, for his enthusiasm and encouragement. I am also fortunate that Anisha chose to be my best friend and walk along with me on this path.

The most important acknowledgment is of the immense debt I owe my parents, whose belief and love has sustained me throughout.

Abstract

This thesis presents investigations in four areas of theoretical astrophysics: the production of sterile neutrino dark matter in the early Universe, the evolution of small-scale baryon perturbations during the epoch of cosmological recombination, the effect of primordial magnetic fields on the redshifted 21-cm emission from the pre-reionization era, and the nonlinear stability of tidally deformed neutron stars.

In the first part of the thesis, we study the asymmetry-driven resonant production of 7 keV-scale sterile neutrino dark matter in the primordial Universe at temperatures $T \gtrsim 100$ MeV. We report final DM phase space densities that are robust to uncertainties in the nature of the quark-hadron transition. We give transfer functions for cosmological density fluctuations that are useful for N-body simulations. We also provide a public code for the production calculation.

In the second part of the thesis, we study the instability of small-scale baryon pressure sound waves during cosmological recombination. We show that for relevant wavenumbers, inhomogeneous recombination is driven by the transport of ionizing continuum and Lyman- α photons. We find a maximum growth factor less than ≈ 1.2 in 10^7 random realizations of initial conditions. The low growth factors are due to the relatively short duration of the recombination epoch.

In the third part of the thesis, we propose a method of measuring weak magnetic fields, of order 10^{-19} G (or 10^{-21} G if scaled to the present day), with large coherence lengths in the intergalactic medium prior to and during the epoch of cosmic reionization. The method utilizes the Larmor precession of spin-polarized neutral hydrogen in the triplet state of the hyperfine transition. We perform detailed calculations of the microphysics behind this effect, and take into account all the processes that affect the hyperfine transition, including radiative decays, collisions, and optical pumping by Lyman- α photons.

In the final part of the thesis, we study the non-linear effects of tidal deformations of neutron stars (NS) in a compact binary. We compute the largest three- and four-mode couplings among the tidal mode and high-order p - and g -modes of similar radial wavenumber. We demonstrate the near-exact cancellation of their effects, and resolve the question of the stability of the tidally deformed NS to leading order. This result is significant for the extraction of binary parameters from gravitational wave observations.

Contents

Acknowledgments	iv
Abstract	v
List of Figures	x
List of Tables	xii
1 General introduction	1
1.1 Standard model of cosmology	2
1.1.1 Cosmological probes	3
1.2 Sterile neutrino dark matter	5
1.3 Baryon perturbations during recombination	7
1.4 Primordial magnetic fields and the 21-cm line	8
1.5 Tidal effects on neutron star oscillations	9
I Sterile neutrino dark matter	11
2 Preliminaries	12
2.1 Introduction	12
2.2 Overview of resonant sterile neutrino production	15
2.2.1 Assumptions	15
2.2.2 Boltzmann Formalism	17
2.2.3 Asymmetry and Thermal Potentials	18
3 Redistribution of lepton asymmetries	21
3.1 Definitions and parametrization	21
3.2 Susceptibilities of the strongly-interacting plasma	23

4	Neutrino opacity	29
4.1	Assumptions and definitions	29
4.2	Matrix elements	30
4.2.1	Reactions with two-particle final states	31
4.2.2	Rates for neutrinos to go to one-particle final states	36
4.3	Results	38
5	Sterile neutrino dark matter distribution	46
5.1	Sterile neutrino production	46
5.1.1	Time-temperature relation	46
5.1.2	Time-evolution of asymmetry	48
5.1.3	Resonant Production	48
5.2	Transfer functions for matter fluctuations	52
5.3	Discussion and conclusions	54
II Small-scale baryon perturbations during cosmological recombination		57
6	Preliminaries	58
6.1	Introduction	58
6.2	Motivation and simple estimate	60
6.3	Background parameters	63
7	Calculation of growth rates	67
7.1	Linear analysis of density and velocity fluctuations	67
7.2	Ionization fraction fluctuation: Saha equilibrium scaling	68
7.3	Radiative transfer in the continuum	71
7.4	Radiative transfer in Lyman- α	74
7.4.1	Solution of the Boltzmann equation	77
7.4.2	Perturbed recombination rate	86
7.5	Solution for the local growth rates	89
7.6	Distribution of growth factors	90
7.7	Discussion	92
7.A	Lyman- α transport: Diffusion-dominated regime	93
7.A.1	Length scale for diffusion	93
7.A.2	Recombination rate in diffusion-dominated regime	96
7.B	Limit of weak diffusion	97

7.B.1	Anisotropic part of hierarchy	97
7.B.2	The isotropic part	98
III	A new probe of magnetic fields in the pre-reionization epoch	100
8	Preliminaries	101
8.1	Introduction	101
8.2	Background	103
8.2.1	21-cm cosmology basics	103
8.2.2	Related methods: Hanle effect and ground-state alignment	105
8.3	Illustration and simple estimate of the effect	106
8.4	Notation and Basic Formalism	109
8.4.1	Atomic Density Matrix	112
8.4.2	Phase-space density matrix for radiation	115
9	Microphysics of the 21-cm line	118
9.1	Interaction Between Hydrogen Atoms and 21-cm Radiation	118
9.2	Other Processes Affecting the Atomic Density Matrix	121
9.2.1	Background magnetic field	122
9.2.2	Spin-exchange Collisions	122
9.2.3	Optical pumping by Lyman- α photons	125
10	From microphysics to observables	134
10.1	Radiative Transfer	134
10.1.1	Free-streaming term	134
10.1.2	Source term	136
10.2	Solution for the brightness temperature	139
10.3	Summary and Conclusions	144
10.A	Conventions for spherical tensors	145
10.B	Spherical Wave Basis for the Radiation's Phase-space Density Matrix	145
10.C	Three-point functions of the atoms and the radiation field	148
IV	The stability of tidally deformed neutron stars to three- and four-mode coupling	150
11	Preliminaries	151
11.1	Introduction	151

11.1.1	A toy model: Two dimensional oscillator	153
12	Formalism of mode couplings	156
12.1	Perturbations in tidally deformed stars	156
12.1.1	Lagrangian formulation of perturbations	156
12.1.2	Mode expansion of the Lagrangian	158
12.1.3	The static response to the tide	159
12.1.4	Stability of the deformed star	160
13	Four-mode coupling and the stability of the tidal deformation	163
13.1	Computing the four-mode coupling terms	163
13.1.1	The volume-preserving transform	164
13.1.2	Understanding the transform	167
13.1.3	Potential of star B	169
13.1.4	Matching stars A and B in the mode basis	171
13.1.5	Expressions for the Jacobian in the mode basis	172
13.1.6	Lagrangian perturbations of star A revisited	173
13.2	Estimating the remaining terms	175
13.2.1	The three-mode coupling	175
13.2.2	Size of the remaining terms	178
13.3	Discussion	181
13.A	Gravitational Potential Energy and the Cowling Approximation	185
13.B	Non-Axisymmetric Modes	185
13.C	Reversing the Flow of an Infinitesimal Coordinate Transform	187
13.D	Additional Details in Estimating the Perturbations to the Eigenfrequencies	188
13.E	Rotating tidal fields	191
13.E.1	Case of distinct modes, $e \neq d$	193
13.E.2	Case of the same mode, $e = d$	194
	Bibliography	197

List of Figures

1.1	Cosmological probes and their length scales, from Ref. [1]	5
2.1	Sterile neutrino dark matter parameter space. Figure provided by Kevork Abazajian.	16
2.2	Lowest order contributions to a propagating active neutrino's self energy	18
2.3	Matter potentials for massless neutrinos in the plasma's rest frame	20
3.1	Primordial plasma's susceptibilities: χ_2^Q , χ_2^B , χ_1^{QB} , and the redistribution of an input mu lepton asymmetry. Figure provided by Francis-Yan Cyr-Racine.	26
3.2	Asymmetry potential V^L per unit <i>unscaled</i> mu lepton asymmetry	28
4.1	Tree-level processes with two fermions in the initial and final states, which contribute to the opacity of a neutrino ν_X	41
4.2	Interactions of an incoming neutrino ν_X involving mesons, with only terms upto $O(p^2)$ in $3\chi\text{PT}$	42
4.3	Muon neutrino opacities through leptonic reactions at $T = 100$ MeV	42
4.4	Muon neutrino opacities through hadronic reactions at $T = 100$ MeV and 2 GeV	43
4.5	Total muon neutrino opacities	44
4.6	Total muon neutrino opacities for a range of energies and temperatures	45
5.1	Evolution of sterile neutrino phase space density	49
5.2	Sterile neutrino production mechanism: asymmetry and net sterile density evolution	50
5.3	Sterile neutrino production mechanism: final phase space densities	51
5.4	Matter transfer functions with sterile neutrino dark matter	53
6.1	Illustration of the instability of sound waves during recombination	61
6.2	Power spectrum of relative matter–radiation velocity at recombination	64
6.3	Relative matter–radiation velocity with redshift	66
7.1	Saha growth rate for small-scale matter fluctuations at recombination	70
7.2	Schematic diagram of radiation transport and small-scale fluctuations	71

7.3	Rates of radiative processes at recombination	78
7.4	Lyman- α spectral distortion at recombination	81
7.5	Basis solutions for the inhomogenous Boltzmann equation	84
7.6	Basis solution to Boltzmann equation with injected photons	87
7.7	Inhomogenous analog of the Peebles C factor	88
7.8	Growth rate for small-scale matter fluctuations at recombination, including radiative transport	89
7.9	Probability distribution of the growth factor of small-scale matter fluctuations	91
7.10	Photon diffusion in the Lyman- α line	95
8.1	Illustration of how an incident quadrupole spin-polarizes the triplet level of the hyperfine transition	107
8.2	Spin-polarized hydrogen atom in a density fluctuation, and its precession in a magnetic field	108
8.3	Power-spectrum of the 21cm brightness temperature fluctuations in the presence of a magnetic field	110
9.1	Hyperfine structure of the ground and first excited electronic levels of the hydrogen atom	126
11.1	Potential surfaces for a perturbed two-dimensional oscillator	155
13.1	Schematic of two perturbed stellar models	164
13.2	Depiction of the nonlinear tidal response as a sum of virtual displacements	168
13.3	Form of the perturbation and resulting corrections to the mode energies	187

List of Tables

4.1	Matrix elements for tree-level processes with two fermions in the initial and final states, which contribute to the opacity of a neutrino ν_X	32
4.2	Matrix elements for interactions of an incoming neutrino ν_X involving mesons, with only terms upto $O(p^2)$ in 3χ PT	35
4.3	Parameters for two-body fusions contributing to the neutrino opacity. Table provided by Christopher Hirata.	37
5.1	Parameters for particular sterile neutrino mixing angles	52
8.1	Glossary of symbols in 21cm physics	111
8.2	Notation for hyperfine states	114
10.1	Sizes of terms in the 21cm calculation	140
13.1	Key for the vector quantities involved in the two stellar models	165

Chapter 1

General introduction

This thesis presents a set of four investigations in theoretical astrophysics. The first three are cosmological in flavor, and set in the epochs of strong neutrino coupling, recombination and pre-reionization, respectively. When viewed in conjunction, they progressively describe the Universe from the first few milliseconds of its existence down to around 500 million years after the Big Bang. The fourth work is set in the arena of inspiraling neutron star binaries.

At first sight, each of these studies focuses on a different physical regime, and is self-contained and independent of the others. The cosmological work is set in environments with one or more thermal components with temperatures ranging from 10 GeV down to 10^{-2} eV, while the one dealing with neutron stars studies a non-thermal regime. Moreover, the relevant degrees of freedom are very different – they range from quantum fields in the primordial Universe, sound waves in baryons at recombination, and populations of hyperfine levels of neutral hydrogen in the pre-reionization era, to oscillatory modes of neutron stars. Despite this diversity, the work in this thesis shares a common theme: it seeks to study macroscopic consequences of *strongly* interacting degrees of freedom. In the first work, they are the hadronic fields near the quark-hadron transition, which interact via the (quite literally) strong force of the standard model of particle physics. The subsequent works study the *non-linear* behaviors of cosmological fluctuations at recombination, absorption and scattering of 21-cm radiation by neutral hydrogen atoms, and neutron star modes.

The first section of this introduction is devoted to the cosmology section of the thesis; it introduces the standard model of cosmology and a few important cosmological probes. Subsequent sections introduce the background for the work in each chapter, place it in the context of the standard model, and briefly summarize the original contributions in this thesis. The final section introduces neutron star inspirals and touches upon our results for their evolution.

1.1 Standard model of cosmology

This section is intended as an extremely brief survey. As such we make no attempt to be comprehensive, but focus on introducing just enough so that an interested reader can follow the later parts.

It is fair to say that we have converged on a coherent picture of the early Universe over the course of the past fifty years. This owes much to the revolution in observational cosmology that had its roots in the discovery of the Cosmic Microwave Background (CMB) in 1965 [2]. It started in earnest with the precise measurement of the CMB's blackbody spectrum in the early 1990s [3], and continued with the mapping of its temperature and polarization anisotropies [4–12], and the measurements of galaxy clustering [13–20], gravitational lensing of the CMB [21–24], and the Lyman- α forest in the spectrum of high-redshift quasars [25–29] in the 1990s and 2000s (the last three are measurements of the Large Scale Structure (LSS) in the Universe). Some of the other important cornerstones were measurements of the abundance of light elements in the Universe [30–37], and of the expansion history of universe using Type 1A supernovae [38–40].

The relatively simple model that emerges out of this mass of evidence is the standard model of cosmology, or the Λ cold dark matter model. It concisely describes an expanding homogenous, isotropic, and spatially flat background universe, which is initialized with a spectrum of scalar curvature fluctuations. In the present epoch, the energy density of the Universe consists of standard baryonic matter (about 5%), cold dark matter (about 27%), and dark energy (about 68%) [41–43]. There are also trace amounts of black body electromagnetic radiation (with a temperature of 2.73 K [44]), and three flavors of neutrinos (with a temperature of about 2 K) [45, 46]. The primordial curvature fluctuations are nearly, but not completely, scale invariant. Different parts of these fluctuations are out of causal contact at early times, when they do not evolve. The *cosmic horizon* represents the causally connected volume; it expands with time and eventually encompasses fluctuations of a particular length scale. After this epoch of horizon-entry, the fluctuations evolve due to the interactions of the standard model of particle physics.

The various components of the energy density have now been measured to a high degree of accuracy, and there are stringent bounds on any additional departures from the model's assumptions. Given this state of affairs, a casual observer might conclude that we have exhausted what we can understand about the large-scale composition and initial conditions of the universe. However, this point of view does not survive closer scrutiny, since the Λ CDM model involves a unsettling number of unknown components. At the very least, we are left with the following three outstanding questions: 1) What is dark matter composed of? 2) What is dark energy composed of? 3) What generates curvature fluctuations in the primordial universe?

We have made the most progress in answering the third question, at least on a superficial level.

The dominant paradigm for the initial conditions postulates an even earlier inflationary epoch that lasts about 10^{-32} seconds, and that is driven by the evolution of a scalar field (in the simplest case) [47–51]. Quantum mechanical perturbations of a scalar nature are generated during this period [52–57]. This scenario also includes a spectrum of *tensor* fluctuations in the metric, which are pushed outside the cosmic horizon during inflation [58, 59]. The tensor modes which re-enter the horizon during the epoch of recombination lead to small changes in the CMB’s temperature and polarization fluctuations [60–64], which include *curl modes* in the polarization that are not sourced by the scalar modes [65–67]. Keeping aside further questions about the nature of the field driving inflation, there is every hope that ongoing efforts to measure these curl modes can confirm this picture in the near future [68–71].

We do not have any nearly as compelling answers for the other two questions, i.e., the composition of dark matter and dark energy. In the case of dark matter, there have been a large number of proposed candidates, but there is no consensus on which is the most promising one. The case of dark energy is even more bleak; it would not be an exaggeration to say that we know as little about it as we did when it was first discovered. We will have nothing further to say about it in this thesis.

1.1.1 Cosmological probes

The remainder of this section is intended as a lightning review of the most important cosmological probes that we alluded to in the beginning of this section. As earlier, we do not cover every aspect, but rather briefly mention the parts that are relevant to our work.

The first probe we consider is Big Bang Nucleosynthesis (BBN), which studies how the light elements are synthesized via nuclear reactions in the early Universe [72–74]. The first nuclide heavier than protium (^1H) to be synthesized in substantial amounts is Deuterium (^2H) at temperatures $T \simeq 0.1$ MeV, which subsequently produces heavier nuclides such as Tritium (^3H), Helium (^3He and ^4He) and Lithium (^7Li) [75–77]. These nuclides are formed due to a chain of reactions that start with the simplest baryons, i.e., neutrons and protons. The rates of these reactions, and the resulting nuclides’ abundances, depend on the baryon-to-photon and neutron-to-proton ratios at the time. The former is an initial condition for the ΛCDM model, while the latter is set at the epoch of weak decoupling, when the temperature of the cosmic plasma is $T \simeq 1.5$ MeV [74, 78]. Thus, the abundances of light elements at low redshifts can constrain initial conditions in the primordial Universe [79, 80].

The next probes of interest are concerned with primordial fluctuations that enter the cosmic horizon at later times. These fluctuations’ length scales are typically measured in terms of their wavenumber k on a comoving grid that follows the cosmic expansion.

The first probe of the fluctuations is the cosmic microwave background, which is relic radiation from the Big Bang [81], that is released at the epoch of recombination when the Universe was around

380,000 years old, at a temperature $T \simeq 0.25$ eV [82–84]. Above this temperature, blackbody radiation interacted via Thomson scattering with a substantial fraction of free electrons; together with the heavier baryons, they formed a tightly-coupled plasma [85, 86]. The comoving sound horizon in the plasma at this epoch was $\simeq 150$ Mpc in size ($1 \text{ Mpc} = 3.08 \times 10^{24}$ cm). The plasma’s perturbations on these scales participated in so-called Baryon-Acoustic Oscillations (BAO) due to the substantial pressure support [87]. The perturbations in the plasma, along with ones in the gravitational potential, imprinted the characteristic pattern of peaks and troughs in the angular distribution of the CMB that we measure today [88–95].

During this epoch, the optical depth for Thomson scattering was large, but finite. Blackbody photons had a characteristic diffusion scale of $\lambda_D \simeq 10$ Mpc on the comoving grid at the epoch of recombination. The CMB anisotropies that we observe today are damped below this characteristic *Silk scale* [89, 91, 92, 96, 97]. This sets a fundamental limit to how much information we can recover from the CMB.

The next probe of interest is large scale structure, which arises due to the gravitational instability of matter overdensities in an expanding universe [98–101]. Perturbations in the dark matter distribution with wavenumber $k \lesssim 0.01 \text{ Mpc}^{-1}$ entered the cosmic horizon in the matter-dominated epoch, and grew with the scale factor a , while those below this scale experienced a period of logarithmic growth during the epoch of radiation domination [102–107]. This yields a *transfer function* for matter densities which has a cutoff scale, along with subtle structure due to baryonic effects, and late-time effects in the epoch of dark energy domination [108–113]. The inflationary spectrum of fluctuations, filtered by this transfer function, represents the spectrum of *linear* dark matter density fluctuations in the Universe. Measures of LSS, such as the galaxy distribution and the Lyman- α forest, are tracers of this underlying dark matter distribution.

Figure 1.1, taken from Ref. [1], shows the amplitude of the density fluctuations in the Universe as a function of length scale, and the various cosmological probes that provided the information. We observe that the CMB constrains the largest scales, below which it is restricted by Silk damping. Measures of the growth of LSS probe intermediate and smaller length scales.

The cosmological works presented in this thesis aim to study components of the standard model of cosmology that are not currently understood, improve the understanding of length scales not constrained by the common probes in Figure 1.1, and study the impact of new cosmological probes. We now proceed to briefly introduce in turn the chapters in this thesis, and place them in the content of the standard model of cosmology and the probes that we covered in this section. We provide more comprehensive introductions in the individual chapters.

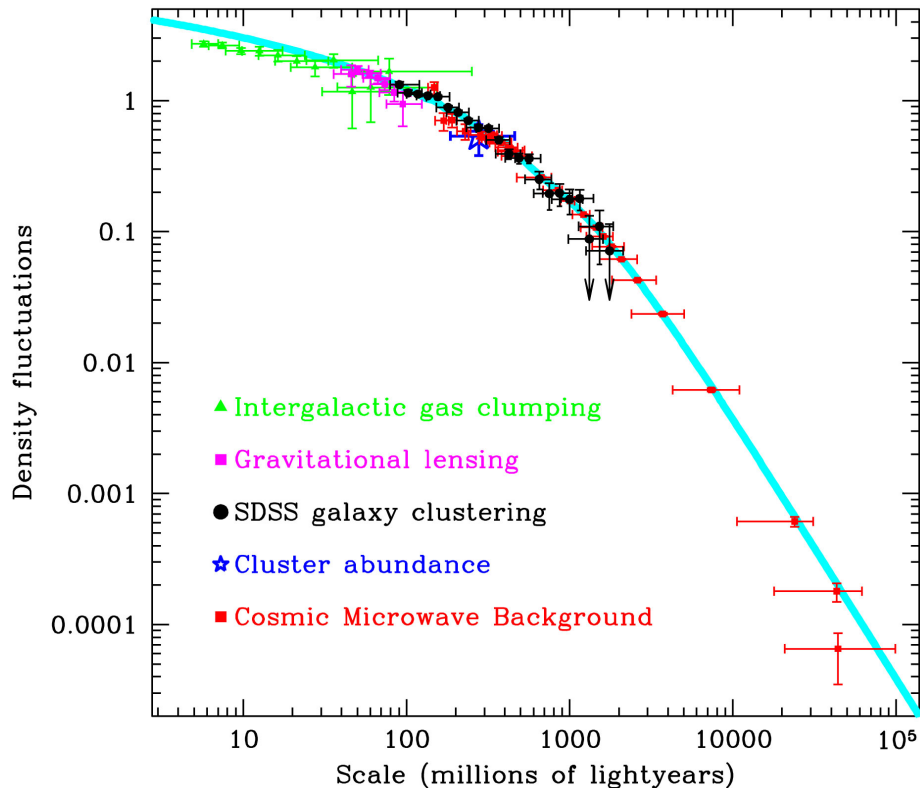


Figure 1.1: Cosmological probes and their length scales [1]: This figure shows the amplitude of the density fluctuations in the Universe vs length scale, along with the cosmological probes that provided the information. The blue line is the prediction of Λ CDM.¹

1.2 Sterile neutrino dark matter

Early on in Section 1.1, we introduced cold dark matter (CDM) as a component making up $\simeq 27\%$ of the energy budget of today's Universe. The CDM of the standard model of cosmology satisfies the following conditions:

- It is *cold*, i.e. it behaves like a gas of non-relativistic particles. During cosmological expansion, the CDM energy density scales with the scale factor a as $\rho_{\text{CDM}} \propto a^{-3}$.
- It is composed of *collisionless* particles, i.e. the constituent particles have a negligible cross-section for mutual interactions, if any.
- It is *dark*, i.e. it only interacts with standard model particles gravitationally.

From the particle physics side, one of the dominant paradigms for dark matter has been Weakly Interacting Massive Particles (WIMPs). In the most popular WIMP models, dark matter is composed of particles with masses of $m_{\text{DM}} \sim 100$ GeV. Their population is kept in equilibrium with

¹This figure is based on data that was available in 2006, and as such does not reflect state-of-the-art results. However, the basic physics and scales are unchanged.

the cosmic plasma at high temperatures due to electroweak interactions, but freezes out when the Hubble expansion rate falls below the interaction rate [46, 114, 115].

From the cosmology side, one set of modifications to the Λ CDM model are motivated by inconsistencies with structure on small scales. Density fluctuations on small scales are not described by linear theory in the current epoch; on such scales, the linear fluctuations of LSS described in Section 1.1.1 are processed by nonlinear growth [116–121]. A few of the major inconsistencies on small scales are departures from the Λ CDM predictions for the density profiles of collapsed objects or *haloes* [122–126], and the shape and normalization of their number distribution at mass ranges of $M_{\text{H}} \sim 10^9\text{--}10 M_{\odot}$ ($1M_{\odot} = 2 \times 10^{33}$ g) [127–130]. These discrepancies have stimulated a lively debate: suggested causes include the effects of baryonic feedback [124, 131, 132], and interactions in the dark matter sector, that violate the second assumption presented above [122, 133, 134].

Part I of the thesis studies a dark matter candidate that violates the first (compared to CDM) and third of the assumptions presented above. It explores the possibility that an additional, sterile neutrino flavor makes up the population of dark matter [135, 136]. Sterile neutrinos with masses in the keV range evade CMB bounds by acting as DM at temperatures $T \simeq 0.25$ eV, and are compatible with BBN due to their negligible energy density compared to the Fermi-Dirac value at $T \simeq 1$ MeV. Such sterile neutrinos could be produced via oscillations of standard-model neutrinos at temperatures $T \gtrsim 100$ MeV [137–139]. Sterile and active neutrino mixing, which is needed for the former’s production, also leads to their decay [140, 141]. For typical values of the sterile neutrino mass this predicts an X-ray flux from the DM distribution in the low redshift Universe [137, 142]. Motivated by reported X-ray signals that could be due to sterile neutrino decay, we consider 7 keV-scale masses [143–145].

We impose the following conditions: (a) the flux of the X-ray signal is consistent with the observed one, and (b) the amount of dark matter is consistent with the Planck value. These conditions require active–sterile mixing angles satisfying $\sin^2 2\theta \simeq 4 \times 10^{-11}$ and a entropy-scaled lepton asymmetry $\mathcal{L}/s_{\text{SM}} \simeq 8 \times 10^{-5}$ in the primordial plasma at temperatures $T \gtrsim 10$ GeV. The last condition also ensures that the sterile neutrino dark matter is resonantly produced at certain momenta [136–139], and is cold enough to be compatible with cosmological structure on length scales $k \simeq 1 h \text{ Mpc}^{-1}$ (h is defined by the Hubble rate today, according to $H_0 = 100h \text{ km s}^{-1}\text{Mpc}^{-1}$) as measured by the Lyman- α forest (the green points in Figure 1.1) [146–154].

In this work we computed the following properties of the primordial plasma through the quark-hadron transition at $T_{\text{QCD}} \simeq 170$ MeV: (a) the redistribution of an input lepton asymmetry, and (b) neutrino opacities due to weak interactions. We used these results in a detailed study of sterile neutrino production, and in the process obtained: (a) final dark matter phase space densities, and (b) modified transfer functions for cosmological density fluctuations with cutoffs at $k \simeq 10 h \text{ Mpc}^{-1}$ due to sterile neutrino streaming [107, 155–157]. These transfer functions significantly depart from

earlier ones for warm DM that were used in N-body simulations [158, 159], and will help compare the predictions of the sterile neutrino model with cosmological structure formation on small scales.

1.3 Baryon perturbations during recombination

The CMB anisotropies of Section 1.1.1 peak on degree angular scales today. They reflect acoustic oscillations of photon perturbations with wavenumbers $k \sim 10^{-2} \text{ Mpc}^{-1}$ during the recombination epoch. Due to the large optical depth to Thomson scattering at the time, baryon perturbations on these length scales are in phase with those in the photons [91]. In the tail of the recombination epoch, electrons and photons begin to *decouple* and develop relative velocities on large scales [92, 160]. In Part II of this thesis, we study fluctuations in the baryon fluid (baryon pressure sound waves) on small scales, i.e. with wavenumbers $k \gtrsim 10^3 \text{ Mpc}^{-1}$, in this epoch.

The standard lore for the evolution of baryon fluctuations is a competition between gravity and their pressure support. In this framework, the *Jeans scale* marks the transition between fluctuations that are stable due to pressure support, and those that collapse due to gravity [98]. After baryons and photons kinetically decouple, the pressure support is provided by non-relativistic hydrogen atoms, and the resulting comoving Jeans length is $k_J \simeq 10^2 \text{ Mpc}^{-1}$ [85]. Thus the fluctuations we consider are stable in this framework (also see Ref. [161]). However, previous work indicated that they could grow due to an alternate mechanism; this appealed to an instability of sound waves in a recombining plasma with large-scale relative velocities between photons and baryons, which are naturally present during decoupling [162]. Chapter 6 lays out this instability’s mechanism.

The original analyses of this effect modeled recombination in an inhomogenous universe as a perturbation to the parameters of the homogenous solution [162–164]. In our work, we perform a detailed study of recombination in a perturbed plasma, and analyze its effect on the instability of fluctuations in the baryons on small scales.

Recombination in the *homogenous* primordial plasma is complicated by the high ionization cross section for neutral hydrogen, owing to which continuum photons ($h\nu > 13.6 \text{ eV}$) are reabsorbed promptly after they are produced. Thus recombination dominantly occurs to the excited states of hydrogen, which ultimately de-excite to the ground $1s$ state through either the $2p$ channel (by emitting Lyman- α photons) or the $2s$ channel (by a two photon decay) [83, 84, 165–167]. Thus, an accurate evolution of the ionization fraction requires the populations of a large number of excited states of the hydrogen atom [168–170].

Recombination in a inhomogenous plasma is much more complicated, since it depends on the *transport* of both ionizing continuum and Lyman- α photons between the crests and troughs of the density perturbations. In Chapter 7, we solve the radiative transfer of photons in both these frequency ranges using a simplified three-level atom model. This work is a natural step in extending

the solution of recombination in the the early Universe in the homogenous case, and in the case with large-scale perturbations ($k \simeq 0.1 \text{ Mpc}^{-1}$), to one with inhomogeneities on small scales ($k \gtrsim 10^3 \text{ Mpc}^{-1}$).

Finally, we use these results to study the growth of small scale baryon perturbations. Our results indicate that the instability persists at intermediate scales, but that its growth is suppressed due to the relatively short duration of the recombination epoch during which the electrons and photons are coupled.

It is important to understand the evolution of small scale modes, since they are not well constrained by neither the CMB fluctuations (Silk damped on comoving scales below $\simeq 10 \text{ Mpc}$), nor LSS. Due to the large number of these modes, any growth and dissipation in the epoch of recombination could have implications for the spectral shape of the CMB [171–173].

1.4 Primordial magnetic fields and the 21–cm line

In the third work presented in this thesis, we use the fluctuations of large scale structure at redshifts $z \gtrsim 10$ to study primordial magnetic fields in the Universe. In order to do so, we use the redshifted 21–cm emission of neutral hydrogen. We now briefly introduce this probe.

The bulk of the photons that make up the CMB today last scattered off free electrons in the cosmic plasma during the epoch of recombination at redshifts $z \simeq 1100$. The subsequent period is the so-called *dark ages*; the hydrogen in the Universe largely is in the atomic form, with trace amounts of ionized protons and electrons that are thermally coupled to the CMB until redshifts $z \simeq 200$ [82–84]. The dark ages ended with the birth of the first stars and galaxies, and the reionization of the intergalactic medium due to the radiation emitted from these sources [174–177].

We currently have no direct observational probes of the dark ages; indirect evidence suggests that cosmic reionization might have happened during redshifts $6 \lesssim z_{\text{rec}} \lesssim 10$ [43, 178–180]. A large number of radio experiments aim to study the Epoch of Reionization (EOR) by measuring the redshifted 21–cm line of neutral hydrogen, which is abundant in the dark ages [174, 181–187]. It will be particularly hard to detect due to local foregrounds, but it promises to be the ultimate probe of the inflationary fluctuations (that are shown in Figure 1.1). This is due to the particularly simple connection between the observable (i.e. the line’s brightness temperature) and the underlying fluctuations, the three-dimensional nature of the data due to the redshift dimension, and the large coverage in wavenumber space [181, 182]. Given the exciting developments that are anticipated in this area, it is germane to consider new scientific avenues that can be explored given the data from future experiments. The mechanism in Part III of this thesis is one such example; understanding it requires consideration of the microphysics of the 21–cm line.

The 21–cm line corresponds to the transition between the hyperfine sublevels of the hydrogen

ground state, which originate in the coupling between the spins of the proton and the electron. The main channel for the transition between these levels is a magnetic dipole, and hence the excited states are extremely long lived. We show in Chapter 8 that atoms in the triplet state are spin-polarized due to the density fluctuations of LSS. These long-lived spins undergo Larmor precession in the presence of a magnetic field.

We show how the precession modulates fluctuations in the brightness temperature of the 21-cm line against the CMB. Consideration of the relative geometry of the spins, the direction of the magnetic field, and the observer’s line of sight shows that the modulations encode both the amplitude and direction of a large-scale magnetic field that the atoms are immersed in. Moreover, the long lifetime of the triplet state makes the technique naturally sensitive to extremely weak field strengths, of order 10^{-19} G (or 10^{-21} G if scaled to the present day). We calculate the size of the effect by taking into account all the processes that affect the hyperfine transition, including radiative decays, collisions, and optical pumping by Lyman- α photons.

The traditional diagnostics of a magnetic field in the interstellar or intergalactic medium (IGM) include the Faraday rotation of polarized sources [188, 189], and effects on the growth of LSS [190] and the CMB’s temperature anisotropies and spectral shape [191, 192]. These methods have placed upper bounds of 10^{-9} G on the field strength in the IGM. More recently, non-observations of TeV sources by the Fermi mission have been interpreted as implying the existence of magnetic fields stronger than 10^{-15} G coherent on the Mpc scale in local LSS voids [193–195]. There is substantial debate about the validity of the assumptions, and the size of the bounds [196–201]. The method we propose is futuristic, but much more sensitive than existing techniques to constrain large scale magnetic fields. Given the rapid pace of progress in 21-cm cosmology, it has the potential to probe mechanisms for magnetogenesis on large scales.

1.5 Tidal effects on neutron star oscillations

The final chapter of thesis is set in a very different scenario from the first three. It studies the effect of tidal interactions on the oscillatory modes of neutron stars that are part of binary systems.

The evolution of binary systems under their mutual gravitational influence is one of the enduring themes of celestial mechanics. There are two main sets of corrections to the classical picture of stable Keplerian orbits. Within Newtonian mechanics, there is a rich phenomenology of tidal effects when one or both of the bodies is spatially extended [202]. In the strong field regime, we also have corrections due to general relativity, which cause orbits to decay via the emission of gravitational waves [203–205]. The latter effect is pronounced in the case of binaries hosting compact objects; in particular, neutron star (NS) binaries are thought to be bright sources of both gravitational and electromagnetic radiation during their inspiral and eventual merger [206–209].

Over the past sixty years or so, there has been a large-scale quest for the direct detection of the gravitational radiation from such binary inspirals [210–212]. Based on current estimates of the rates of these events in the local Universe, we can be cautiously optimistic that the upcoming generation of gravitational wave detectors will accomplish this feat [213]. Beyond the discovery era, observed gravitational waveforms should enable precise measurements of the binary’s parameters [214–216].

Precise measurements of the waveforms can also potentially inform us about the first family of corrections, i.e. tidal effects: thus we have the promise of indirectly measuring the neutron star’s equation of state (its response to compression). Such effects rely on the precise measurement of the waveform’s phase [217–220] or cutoff frequency [221–223]. Hence it is important to accurately model the orbital evolution to extract accurate templates.

Typical neutron stars have masses near the solar mass, but packed within a radius $R_* \simeq 10$ km [224]. Considering nearly equal-mass binaries with separation a , the tidal potential due to the companion scales with the dimensionless tidal strength $\epsilon = (R_*/a)^3$ [202, 225]. As the orbit shrinks due to gravitational wave emission, the neutron stars eventually approach close enough for one or both of them to be tidally disrupted. The exact separation at which this happens depends on the NS equation of state, but is generically at around three to four radii. Thus the evolution of the binary is usually modeled with a long inspiral phase (where the weak tidal effects due to the small strength ϵ can be treated within perturbation theory) and a comparatively short disruption and merger phase [226, 227].

The work in Part IV of this thesis was motivated by the work in Ref. [228], which studied the non-linear effects of the tidal deformation in NS–NS inspirals. The latter indicated that, though the NSs were stably deformed within linear theory, the non-linear effects of the tidal deformation led to an instability. Depending on the saturation, such behavior could lead to a large correction to the inspiral’s orbital phase, and possibly fatally compromise the simple link between the binary’s parameters and the gravitational waveform. This result relied on a large *three-mode coupling* between the NSs tidal deformation and high order pressure and gravity waves.

In our work, we show that additional *four-mode couplings* enter into the analysis at the same order as the three-mode terms previously considered, within the framework of perturbation theory. We introduced a novel method to calculate these four-mode couplings, and showed how their stabilizing effect nearly exactly cancelled the destabilizing effect of the three-mode couplings.

Within the context of NS inspirals, the work in this thesis shows that tidal interactions do not impact the phase evolution of gravitational waves, and consequently do not compromise the program to extract the binary’s parameters from the waveforms. In a larger context, these results will be useful in studies of non-linear effects of tidal deformations in other, longer lived systems, such as binaries hosting white dwarfs.

Part I

Sterile neutrino dark matter

Chapter 2

Preliminaries¹

2.1 Introduction

Deep in the radiation dominated epoch of the Universe, the three neutrinos present in the standard model (SM) of particle physics [229] make up a significant population of relativistic species within the primeval cosmic plasma. We have strong evidence of their existence at these early epochs from probes of the primordial Universe such as the Cosmic Microwave Background (CMB) (probing temperature $T \sim 0.25$ eV) [42], and the synthesis of light elements during the epoch of Big Bang Nucleosynthesis (BBN) which depends on the neutron-to-proton ratio set at $T_{\text{dec}} \sim 1.5$ MeV [80], the temperature of weak neutrino decoupling. Above this temperature, SM neutrinos interact with species that carry weak charge, through which they remain coupled to the primordial plasma [230].

There is a long history of speculation about additional neutrino species (see Ref. [231] for a recent review). Owing to the precise measurement of the invisible decay width of the SM Z boson [229], any extra neutrino species must be “sterile” (i.e. electroweak singlets) [232]. Furthermore, precise measurements of the CMB [42, 233] and of the primeval abundance of light elements [37, 234] strongly constrain the presence of extra relativistic species in the early Universe. These constraints indicate that (i) unlike SM neutrinos, light sterile neutrinos never fully thermalize with the rest of the cosmic plasma [235–239], or (ii) that sterile neutrinos are massive enough to form the inferred population of dark matter (DM) in the Universe (see e.g. Ref. [240]). Sterile neutrinos with masses in the keV range act as DM in the CMB era, but are relativistic in the BBN era, when they do not significantly impact the expansion rate due to their negligible energy density (compared to the Fermi-Dirac value).

Early works in this direction studied right-handed sterile neutrinos with masses $m_s \approx 0.1 - 100$ keV, produced by the oscillation of left-handed SM neutrinos [135, 137, 241–243]. The mixing angle

¹The material in Chapters 2–5 was adapted from the preprint *Sterile neutrino dark matter: A tale of weak interactions in the strong coupling epoch*, Venumadhav, T., Cyr-Racine, F.-Y., Abazajian, K. N., & Hirata, C. M. 2015, arXiv:1507.06655, currently under consideration for publication in Physical Review D. Reproduced here with permission, copyright (2015) by the American Physical Society.

between the SM and sterile neutrinos is fixed by the present day DM abundance. In the original Dodelson-Widrow scenario [135], sterile neutrinos are produced with a momentum distribution reflecting that of the active neutrino species, and thus constitute “warm” DM [158, 244–246]. However, small-scale structure formation [247–254] and X-ray observations [142, 255–258] appear in significant conflict with the fiducial Dodelson-Widrow scenario, hence prompting the search for alternative sterile neutrino production mechanisms [136–138, 259–274].

In this work, we examine in detail the resonant production of sterile neutrinos in the presence of a small primordial lepton asymmetry. Originally proposed by Shi and Fuller [136], this production mechanism makes use of a small lepton asymmetry to modify the plasma’s interaction with SM neutrinos in such a manner as to resonantly produce sterile neutrinos at particular momenta [137–139]. This generically results in a ‘colder’ DM distribution, which improves consistency with models of cosmological structure formation [146–154], while requiring a modest primordial lepton asymmetry, which is relatively poorly constrained [275–279].

Sterile and active neutrino mixing, which is needed for the former’s production, also leads to their decay [140, 141]. For typical values of the sterile neutrino mass this predicts an X-ray flux from the DM distribution in the low redshift Universe [137, 142]. This has been the subject of much recent interest, due to hints of an excess flux at ~ 3.5 keV in stacked X-ray spectra of several galaxy clusters [143] and in observations of M31, the Milky Way, and Perseus [144, 145]. There is currently an active debate on the existence, significance, and interpretation of this excess [280–287]. In the present work, we use this tentative signal as a motivation to study in detail the physics of sterile neutrino production in the early Universe, but the machinery we develop is more generally applicable to the broader parameter space of the Shi-Fuller mechanism.

We present here an updated calculation of resonantly-produced sterile neutrinos and relax several simplifications that had been adopted previously in the literature. Furthermore, we leverage recent advances in our understanding of the quark-hadron transition in order to include a more realistic treatment of the strongly-interacting sector. Our motivation is twofold: a) improve the treatment of lepton asymmetry, which is a crucial beyond-SM ingredient in the mechanism, and b) provide realistic sterile neutrino phase space densities (PSDs) and transfer functions for matter fluctuations, which are starting points for studying cosmological implications on small scales. Our improvements to the sterile neutrino production calculation can broadly be classified in three categories.

Firstly, we study how the cosmic plasma reprocesses a primordial lepton asymmetry. For models that can explain the above X-ray excess, the majority of sterile neutrinos are produced at temperatures above 100 MeV [139]. At these temperatures, there is a significant population of either quarks or mesons, depending on whether the temperature is above or below the quark-hadron transition. Since these hadronic species are coupled to neutrinos and charged leptons through weak processes, the establishment of chemical equilibrium among the different constituents of the cosmic plasma

will automatically transfer a primordial lepton asymmetry to the hadronic sector. An illustrative example is the reaction

$$\nu_\mu + \mu^+ \rightleftharpoons \pi^+, \quad (2.1)$$

which can redistribute an initial neutrino asymmetry into charged lepton and hadronic asymmetries. At lower temperatures, the asymmetry is redistributed to a lesser degree between the leptonic flavors. As we discuss in the body of the work, this redistribution modifies the dynamics of the resonant sterile neutrino production, resulting in a modified final PSD.

Secondly, we incorporate several new elements to the calculations of the neutrino opacity (i.e. the imaginary part of the self-energy) at temperatures $10 \text{ MeV} \leq T \leq 10 \text{ GeV}$. Accurate neutrino opacities are needed since they basically control the production rate of sterile neutrinos through cosmic epochs. Early works on neutrino interactions in the early Universe [137, 230, 288] assumed that neutrinos largely scattered off relativistic particles and thus scaled their cross-sections with the center-of-mass (CM) energy. In addition, these calculations also neglected the effects of particle statistics. Under these two simplifying assumptions, the opacity $\Gamma(E_{\nu_\alpha})$ for an input neutrino of energy E_{ν_α} is of the form

$$\Gamma(E_{\nu_\alpha}) = \lambda(T) G_F^2 T^4 E_{\nu_\alpha}, \quad (2.2)$$

where G_F is the Fermi coupling constant, and $\lambda(T)$ is a constant that depends on the number and type of available relativistic species in the cosmic plasma. References [243, 289] subsequently developed a framework to include particle masses, loop corrections, and particle statistics in the neutrino opacity calculation. In the present work, we add previously-neglected contributions to the opacity such as two- and three-body fusion reactions, and also use chiral perturbation theory to compute the hadronic contribution to the opacity below the quark-hadron transition. We find both quantitative and qualitative modifications to the form of Eq. (2.2). Wherever we present matrix elements, we use the ‘-+++’ metric signature.

Thirdly, we fold the asymmetry redistribution and opacity calculations into the sterile neutrino production computation, and provide updated PSDs for the range of parameters relevant to the X-ray excess. As part of this process, we carefully review and correct the numerical implementation of the sterile neutrino production used in Ref. [152]. Our sterile neutrino production code is publicly available at <https://github.com/ntveem/sterile-dm>. We finally use the updated sterile neutrino PSDs in a standard cosmological Boltzmann code [290] and provide new dark matter transfer functions.

We organize the presentation such that the beginning chapters deal with SM physics, while the later ones apply their results to the production of sterile neutrino dark matter. In the rest of this chapter, we introduce the production mechanism. We then proceed to study the weak interactions of active neutrinos in Chapters 3 and 4; we study the redistribution of asymmetries in the former, and

active neutrino opacities in the latter. Finally, we study the resulting sterile neutrino DM distribution in Chapter 5. We follow sterile neutrino production in Section 5.1, and evaluate transfer functions for matter fluctuations in Section 5.2. We finish with a discussion of our assumptions and uncertainties in Section 5.3, and collect technical details into the appendices.

2.2 Overview of resonant sterile neutrino production

In this section, we briefly review the resonant production of sterile neutrinos in the early Universe. We first present the specific scenario that we consider in this work, and then discuss the Boltzmann formalism used to compute the out-of-equilibrium production of sterile neutrinos. We finally discuss how the presence of the thermal bath and lepton asymmetry change the neutrino self-energy and govern the sterile neutrino production. We refer the reader to Refs. [136, 137, 139] for more details.

2.2.1 Assumptions

In our current study, we focus on the following scenario.

1. We consider an extra sterile neutrino species, ν_s , that is massive compared to the SM neutrinos $\nu_{e/\mu/\tau}$, which we take to be effectively massless. The propagation (light/heavy) and interaction (active/sterile) eigenstates are related by a unitary transformation, the most general version of which is a 4×4 matrix. We assume that the sterile neutrino mixes with only one of the SM ones, which we take to be the muon neutrino, i.e.,

$$\begin{pmatrix} \Psi_{\nu_\mu} \\ \Psi_{\nu_s} \end{pmatrix} = \begin{pmatrix} \cos \theta & \sin \theta \\ -\sin \theta & \cos \theta \end{pmatrix} \begin{pmatrix} \Psi_0 \\ \Psi_{m_s} \end{pmatrix}. \quad (2.3)$$

The fields on the left- and right-hand sides are interaction and mass (m_s) eigenstates, respectively, and θ is the active-sterile mixing angle. The choice of a muon neutrino is arbitrary, and reflects the choice of previous work [137, 152].

2. We assign a non-zero lepton asymmetry to the primordial plasma. In the general case, each SM flavor has its own asymmetry, but we assume a non-zero value only for the mu flavor (i.e. the one that mixes with the sterile neutrino):

$$\Delta \hat{n}_{\nu_\alpha} + \Delta \hat{n}_{\alpha^-} \equiv \hat{\mathcal{L}}_\alpha = \delta_{\alpha\mu} \hat{\mathcal{L}}_\mu, \quad (2.4)$$

where the dimensionless asymmetry $\Delta \hat{n}_A$ in species A is the temperature-scaled difference between the particle and anti-particle densities, $\Delta \hat{n}_A \equiv (n_A - n_{\bar{A}})/T^3$, and $\delta_{\alpha\mu}$ is the Kronecker delta. In general, entropy-scaled asymmetries are preferable, since they are conserved through

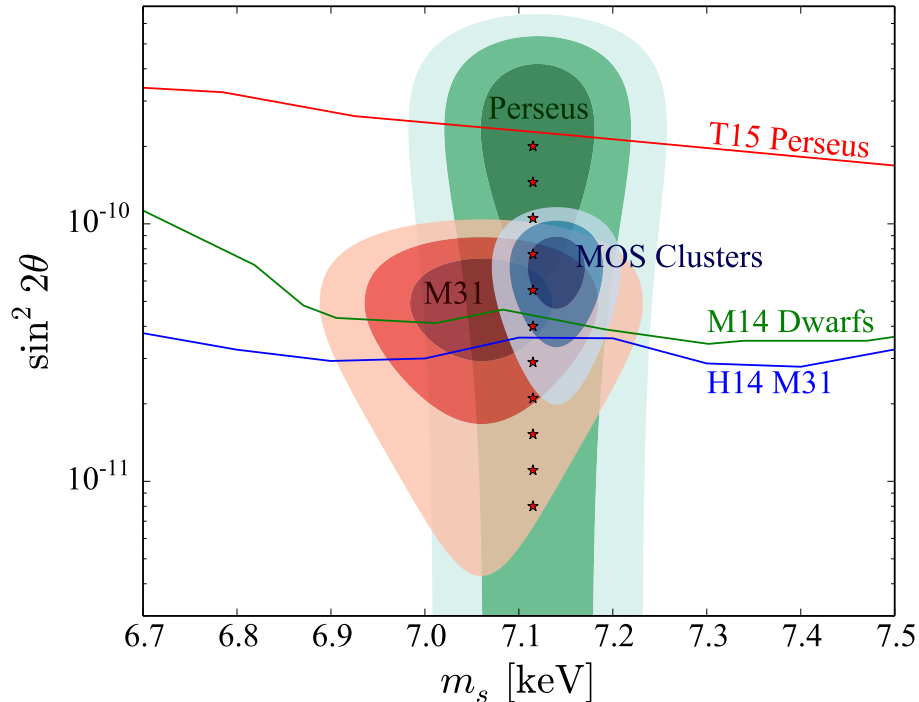


Figure 2.1: Sterile neutrino DM parameter space: shaded regions are consistent with the X-ray signal at 1, 2, and 3 σ . The best determined parameters are from the MOS stacked clusters of Ref. [143]. Statistically consistent signals are found in their core-removed Perseus spectrum, and M31 [144]. The lines show constraints at the 90% level from *Chandra* observations of M31 (H14) [291], stacked dwarf galaxies (M14) [292], and *Suzaku* observations of Perseus (T15) [293]. Stars mark the models that we study in the body of the work. Figure provided by Kevork Abazajian.

epochs of annihilation. However, the definition used in Eq. (2.4) simplifies comparison with lattice QCD calculations in Chapter 3. We fix by hand the mu lepton asymmetry at high temperatures to produce the canonical DM density, $\Omega_{\text{DM}} h^2 = 0.1188$ in the current epoch [42].

In the rest of this work, we use a hat to indicate temperature scaled quantities. We choose to study the parameter space of interest for resonantly produced sterile neutrino DM consistent with the recent X-ray signal. Figure 2.1 shows a section of the m_s and $\sin^2 2\theta$ plane with contours for the unidentified lines of Refs. [143, 144], along with constraints from *Chandra* observations of M31 [291], stacked dwarf galaxies [292], and *Suzaku* observations of Perseus [293]. The stars show a range of mixing angles at a specific value of m_s , and mark models that we study in Chapter 5.

For all these models, the bulk of the sterile neutrinos are produced at temperatures well below the masses of the weak gauge bosons (~ 80 GeV), but above weak decoupling at $T \sim 1.5$ MeV [139]. Active-active neutrino oscillations in the primordial plasma are suppressed at these temperatures [294], and hence it is consistent to assign individual asymmetries in Eq. (2.4) and neglect electron and tau neutrino mixing in Eq. (2.3).

2.2.2 Boltzmann Formalism

In its full generality, out-of-equilibrium sterile neutrino production (via oscillations) is best described by the evolution of the two-state density matrix of the neutrinos in the active–sterile (interaction) basis [295–298].

For the parameter range in Figure 2.1, most sterile neutrinos are produced above temperatures $T \gtrsim 100$ MeV. At these temperatures, the two state system is collisionally dominated, i.e., the interaction contribution dominates the vacuum oscillations. In this regime, the evolution of the density matrix separates out and yields a quasi-classical Boltzmann transport equation for the diagonal terms, which are the PSDs of the active and sterile components [299–301]. The Boltzmann equation for the sterile neutrino PSD is

$$\begin{aligned} \frac{\partial}{\partial t} f_{\nu_s}(p, t) - H p \frac{\partial}{\partial p} f_{\nu_s}(p, t) = & \\ & \sum_{\nu_x+a+\dots\rightarrow i+\dots} \int \frac{d^3 p_a}{(2\pi)^3 2E_a} \cdots \frac{d^3 p_i}{(2\pi)^3 2E_i} \cdots (2\pi)^4 \delta^4(p + p_a + \cdots - p_i - \cdots) \\ & \times \frac{1}{2} \left[\langle P_m(\nu_\mu \rightarrow \nu_s; p, t) \rangle (1 - f_{\nu_s}) \sum |\mathcal{M}|_{i+\dots\rightarrow a+\nu_\mu+\dots}^2 f_i \cdots (1 \mp f_a) (1 - f_{\nu_\mu}) \cdots \right. \\ & \left. - \langle P_m(\nu_s \rightarrow \nu_\mu; p, t) \rangle f_{\nu_s} (1 - f_{\nu_\mu}) \sum |\mathcal{M}|_{\nu_\mu+a+\dots\rightarrow i+\dots}^2 f_a \cdots (1 \mp f_i) \cdots \right]. \quad (2.5) \end{aligned}$$

We can write an analogous equation for the antineutrinos. Here, the $f(p)$ are PSDs for particles with three-momentum p and energy E , and H is the Hubble expansion rate. The right-hand side sums over all reactions that consume or produce a muon neutrino. The symbol $\sum |\mathcal{M}|^2$ denotes the squared and spin-summed matrix element for the reaction, and the multiplicative factors of $(1 \mp f)$ implement Pauli blocking/Bose enhancement, respectively. The factor of $1/2$ accounts for the fact that only one (i.e. the muon neutrino) state in the two-state system interacts [295–297]. The P_m are active–sterile oscillation probabilities in matter, which depend on the vacuum mixing angle θ , and are modified by interactions with the medium. The latter are parametrized by the neutrino self energy [288], and the ‘quantum damping’ rate for active neutrinos. In terms of these quantities, the oscillation probabilities are [300, 301]

$$\begin{aligned} \langle P_m(\nu_\mu \leftrightarrow \nu_s; p, t) \rangle = (1/2) \Delta^2(p) \sin^2 2\theta \left\{ \Delta^2(p) \sin^2 2\theta + D^2(p) \right. \\ \left. + [\Delta(p) \cos 2\theta - V^L - V^{\text{th}}(p)]^2 \right\}^{-1}. \quad (2.6) \end{aligned}$$

We have introduced the symbol $\Delta(p)$ for the vacuum oscillation rate, $\Delta(p) \equiv \delta m_{\nu_\mu, \nu_s}^2 / 2p$, and split the neutrino self energy into the lepton asymmetry potential V^L , and the thermal potential V^{th} (the asymmetry contribution enters with the opposite sign in the version of Eq. (2.6) for antineutrinos). The quantity $D(p)$ is the quantum damping rate, and equals half the net interaction rate of active

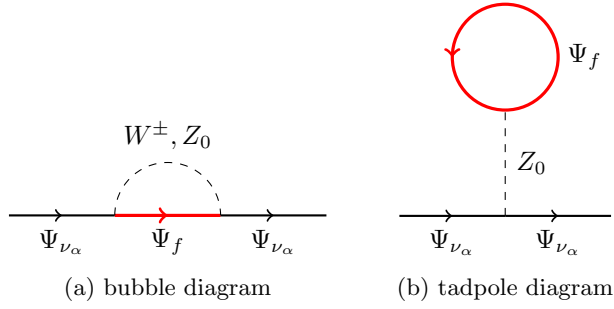


Figure 2.2: Lowest order contributions to a propagating active neutrino's self energy. In panel (a), f is any species with weak charge, and in panel (b), $f = \nu_\alpha, \alpha^-$. Red lines are thermal propagators.

neutrinos [the factor of half enters for the same reason as it does in Eq. (2.5)]. The net interaction rate for a muon neutrino is

$$\Gamma_{\nu_\mu}(p) = \sum_{\nu_s + a + \dots \rightarrow i + \dots} \int \frac{d^3 p_a}{(2\pi)^3 2E_a} \dots \frac{d^3 p_i}{(2\pi)^3 2E_i} \dots (2\pi)^4 \delta^4(p + p_a + \dots - p_i - \dots) \times \sum |\mathcal{M}|_{\nu_\mu + a + \dots \rightarrow i + \dots}^2 f_a \dots (1 \mp f_i) \dots \quad (2.7)$$

We simplify the phase-space integrals in Eq. (2.5) by using detailed balance to equate the forward and backward reaction rates. The resulting Boltzmann equation for quantum-damped and collisionally-driven sterile neutrino production is [137]

$$\frac{\partial}{\partial t} f_{\nu_s}(p, t) - H p \frac{\partial}{\partial p} f_{\nu_s}(p, t) \approx \frac{\Gamma_{\nu_\mu}(p)}{2} \langle P_m(\nu_\mu \leftrightarrow \nu_s; p, t) \rangle [f_{\nu_\mu}(p, t) - f_{\nu_s}(p, t)], \quad (2.8)$$

with a related equation for antineutrinos. There are subtleties with the effects of quantum-damping in the case of resonance [302], but tests with the full density matrix formalism find that the quasi-classical treatment is appropriate [139].

2.2.3 Asymmetry and Thermal Potentials

We now expand on the origins of the asymmetry and thermal potentials appearing in Eq. (2.6). These potentials encapsulate the self energy of propagating active neutrinos due to interactions with the plasma. Under the conditions we are interested in, there are three contributions to the neutrino self energy: a) an imaginary part proportional to the net neutrino opacity, b) a real part due to finite weak gauge boson masses (V^{th}), and c) a real part proportional to asymmetries in weakly interacting particles (V^{L}). We follow the treatment in Ref. [288], and recast it in terms of the quantities that we compute later. Figure 2.2 shows lowest-order contributions to active neutrinos' self energy. Thick red lines are thermal propagators of weakly charged species in the background plasma. There are two

corrections — bubbles and tadpoles, shown in Figure 2.2a and 2.2b, respectively. The background fermion is a lepton of the same flavor in the former, and any weakly charged species in the latter.

A massless active neutrino's ‘dressed’ propagator is

$$G_{\nu_\alpha}^{-1}(p_{\nu_\alpha}) = \not{p}_{\nu_\alpha} - b_{\nu_\alpha}(p_{\nu_\alpha})\not{\psi}(1 - \gamma_5)/2, \quad (2.9a)$$

$$b_{\nu_\alpha}(p_{\nu_\alpha}) = b_{\nu_\alpha}^{(0)} + b_{\nu_\alpha}^{(1)}\omega_{\nu_\alpha}, \quad \omega_{\nu_\alpha} = -p_{\nu_\alpha} \cdot u. \quad (2.9b)$$

Here, p_{ν_α} and u are the neutrino and plasma's four-momenta, ψ is shorthand for $\gamma^\mu v_\mu$, and b_{ν_α} is the left handed neutrino's self energy. Equation (2.9b) divides this self energy into two contributions that affect the particle and anti-particle poles of Eq. (2.9a) differently. Figure 2.3 illustrates their association with asymmetry and thermal potentials:

$$V_{\nu_\alpha}^L = b_{\nu_\alpha}^{(0)}, \quad (2.10)$$

$$V_{\nu_\alpha}^{\text{th}}(E_{\nu_\alpha}) = b_{\nu_\alpha}^{(1)}E_{\nu_\alpha}. \quad (2.11)$$

Ref. [288] computes these terms by summing over all species in Figure 2.2. Both kinds of diagrams contribute to the asymmetry potential, while only bubble diagrams contribute to the thermal potential. We write the answer in terms of the leptons' asymmetries, and the densities of the strong fluid's conserved quantities:

$$V_{\nu_\alpha}^L = \sqrt{2}G_F \left[\sum_{\beta \in \{e, \mu, \tau\}} (\delta_{\alpha\beta} - \frac{1}{2} + 2 \sin^2 \theta_W) \Delta n_{\beta^-} + \sum_{\beta \in \{e, \mu, \tau\}} (1 + \delta_{\alpha\beta}) \Delta n_{\nu_\beta} - \frac{1}{2} \Delta n_B + (1 - 2 \sin^2 \theta_W) \Delta n_Q \right], \quad (2.12a)$$

$$V_{\nu_\alpha}^{\text{th}}(E_{\nu_\alpha}) = -\frac{8\sqrt{2}G_F}{3} \left[\frac{\rho_{\nu_\alpha}}{M_Z^2} + \frac{\rho_\alpha}{M_W^2} \right] E_{\nu_\alpha}. \quad (2.12b)$$

In the above equations, θ_W is the weak mixing angle, and $M_{Z/W}$ are the masses of the weak gauge bosons. The symbol $\delta_{\alpha\beta}$ is a Kronecker delta, the quantities ρ_α and ρ_{ν_α} are net energy densities of charged and neutral leptons, respectively, and Δn_B and Δn_Q are densities of the baryon number B, and electric charge Q, respectively. The standard model baryon number asymmetry is small compared to the lepton asymmetry of interest [80], and hence can be set to zero for the purposes of this calculation.

According to the assumptions in the first part of this section, the plasma starts out with a net lepton asymmetry in the mu flavor. As we showed in Section 2.1, this asymmetry is redistributed between muons and muon neutrinos. Moreover, leptons of other flavors acquire asymmetries that respect Eq. (2.4), and the strong fluid acquires a net electric charge density Δn_Q to maintain overall neutrality. Equation (2.12a) shows how the asymmetry potential depends on the redistributed

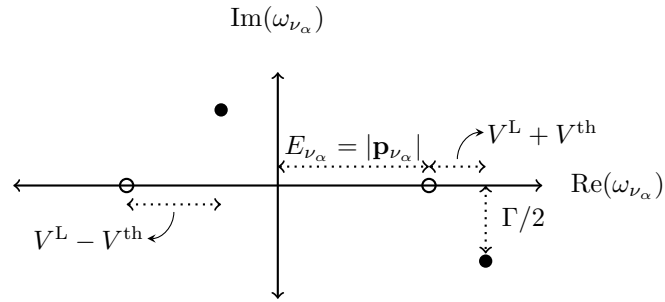


Figure 2.3: Matter potentials for massless neutrinos in the plasma's rest frame: filled and un-filled circles are poles at finite and zero temperature, respectively. See Chapter 4 for the imaginary shift.

asymmetries.

In the ensuing chapters, we study aspects of the weak interactions of active neutrinos that affect the sterile neutrino production.

Chapter 3

Redistribution of lepton asymmetries

Weak processes couple leptonic and hadronic degrees of freedom in the primordial plasma. In this section, we study this coupling's effect on lepton asymmetries¹. We first recast the required quantities in terms of a few relevant susceptibilities in Section 3.1, which we compute over a range of temperatures in Section 3.2.

3.1 Definitions and parametrization

Let us consider the primordial plasma at temperatures above the quark-hadron transition temperature, T_{QCD} . The following reactions couple leptons of different flavors, and the quark and lepton sectors:

$$\nu_\alpha + \beta^- \rightleftharpoons \nu_\beta + \alpha^-, \quad (3.1a)$$

$$\nu_\alpha + \alpha^+ \rightleftharpoons a + \bar{b}, \quad (3.1b)$$

where a and b are quarks with charges of $+2/3$ and $-1/3$, respectively. Free quarks no longer exist at temperatures below T_{QCD} , and the reactions in Eq. (3.1b) transition to ones involving mesons, like Eq. (2.1).

In principle, we could study the effect of all these reactions on input asymmetries, but it is a daunting task; one that is further complicated by the quark-hadron transition. The following consideration of the relevant timescales suggests a solution. In the radiation dominated era, the Hubble rate is $H \approx 2 \times 10^5 \text{ s}^{-1} g_*^{1/2} (T/\text{GeV})^2$. At temperatures above the quark-hadron transition, the rates of reactions in (3.1) are $\Gamma(T) \simeq G_{\text{F}}^2 T^5 \approx 2 \times 10^{14} \text{ s}^{-1} (T/\text{GeV})^5$, while the relevant rates

¹During this preparation of this manuscript, we became aware of Ref. [303], which points out the relevance of this effect to sterile neutrino production, and estimates it under the simplifying Stefan-Boltzmann approximation for free quarks, along with a modified number of colors as a phenomenological correction for the effects of confinement.

below the transition are those of pion decays. The most important channel for the latter is the muonic decay, $\pi^+ \rightarrow \mu^+ + \nu_\mu$, which is faster than the Hubble rate ($\Gamma_{\pi^+ \rightarrow \mu^+ + \nu_\mu} = 3.8 \times 10^7 \text{ s}^{-1}$). Thus, a significant number of the reactions in Eq. (3.1) are faster than the Hubble rate².

This has two primary consequences. Firstly, high reaction rates enforce *kinetic* equilibrium, i.e. all active species' PSDs approach the Fermi-Dirac or Bose-Einstein forms. Secondly, forward and backward reactions are in *chemical* equilibrium, one effect of which is to equate the chemical potentials for both sides (the Saha equation). However, it has another implication: the plasma's complicated internal dynamics can be abstracted into a few parameters or susceptibilities that completely specify its response to small external 'forces', or in this case, input asymmetries. All that remains is to compute the susceptibilities relevant to our problem.

We now define a few useful quantities and notation. Given any conserved quantity F , the symbol μ_F denotes its chemical potential. The asymmetry $\Delta \hat{n}_A$, in a particle A , is a function of its chemical potential $\hat{\mu}_A \equiv \mu_A/T$. The quantities $\Delta \hat{n}_A$ and $\hat{\mu}_A$ are small, and in the linearized limit, related by

$$\Delta \hat{n}_A = \hat{\chi}_A \hat{\mu}_A, \quad (3.2)$$

where $\hat{\chi}_A \equiv \chi_A/T^2$ is the number-density susceptibility. The lepton asymmetries in the three flavors are

$$\begin{aligned} \hat{\mathcal{L}}_\alpha &= \Delta \hat{n}_{\alpha^-} + \Delta \hat{n}_{\nu_\alpha} \\ &= \hat{\chi}_{\alpha^-} \hat{\mu}_{\alpha^-} + \hat{\chi}_{\nu_\alpha} \hat{\mu}_{\nu_\alpha}, \quad \alpha \in \{e, \mu, \tau\}. \end{aligned} \quad (3.3)$$

The strong fluid is described by the densities of its conserved quantities: the charge and baryon-number densities $\Delta \hat{n}_Q$ and $\Delta \hat{n}_B$, respectively³. The chemical equilibrium of the reactions in Eq. (3.1) implies

$$\hat{\mu}_{\nu_\alpha} - \hat{\mu}_{\alpha^-} - \hat{\mu}_Q = 0, \quad \alpha \in \{e, \mu, \tau\}. \quad (3.4)$$

Here $\hat{\mu}_Q$ is the chemical potential for adding a unit of electric charge. The conserved quantities' densities are related to their chemical potentials by their susceptibilities:

$$\begin{pmatrix} \Delta \hat{n}_Q \\ \Delta \hat{n}_B \end{pmatrix} = \begin{pmatrix} \hat{\chi}_2^Q & \hat{\chi}_{11}^{\text{QB}} \\ \hat{\chi}_{11}^{\text{BQ}} & \hat{\chi}_2^B \end{pmatrix} \begin{pmatrix} \hat{\mu}_Q \\ \hat{\mu}_B \end{pmatrix}. \quad (3.5)$$

²The electronic channel for the pion decay, $\pi^+ \rightarrow e^+ + \nu_e$ is helicity-suppressed ($\Gamma_{\pi^+ \rightarrow e^+ + \nu_e} = 4.7 \times 10^3 \text{ s}^{-1}$) and of the order of the Hubble rate at temperatures $T \simeq 50 \text{ MeV}$, hence one might worry that leptons with electronic flavor depart from equilibrium. This is resolved by the observation that they are coupled to muonic species by other non-helicity suppressed, and consequently faster, reactions such as $e^+ + \nu_e \leftrightarrow \mu^+ + \nu_\mu$ and $\mu^+ \leftrightarrow e^+ + \nu_e + \bar{\nu}_\mu$.

³We do not follow the strangeness, S , since it is not conserved in weak reactions. Above the transitions, it disappears at the Cabbibo-suppressed rate $\Gamma_S \simeq |V_{us}|^2 G_F^2 T^5 \approx 10^{13} \text{ s}^{-1} (T/\text{GeV})^5$, while below the transition the relevant rate is the Kaon inverse lifetime, $\Gamma_{K^\pm} = 8.1 \times 10^7 \text{ s}^{-1}$.

Equation (3.5), along with net charge and baryon number conservation, yields the constraint equations

$$\Delta\hat{n}_B = \hat{\chi}_{11}^{\text{BQ}}\hat{\mu}_Q + \hat{\chi}_2^{\text{B}}\hat{\mu}_B \approx 0, \quad (3.6)$$

$$\begin{aligned} 0 &= \hat{\chi}_2^{\text{Q}}\hat{\mu}_Q + \hat{\chi}_{11}^{\text{QB}}\hat{\mu}_B - \sum_{\alpha \in \{e, \mu, \tau\}} \Delta\hat{n}_{\alpha^-} \\ &= \hat{\chi}_2^{\text{Q}}\hat{\mu}_Q + \hat{\chi}_{11}^{\text{QB}}\hat{\mu}_B - \sum_{\alpha \in \{e, \mu, \tau\}} \hat{\chi}_{\alpha^-} \hat{\mu}_{\alpha^-}. \end{aligned} \quad (3.7)$$

Equations (3.3), (3.4), (3.6), and (3.7) are eight linear equations for eight unknowns. The resulting asymmetries (obtained via their chemical potentials) are the ‘redistributed’ input lepton asymmetries \mathcal{L}_α .

We symbolically represent the solutions as

$$\hat{\mu}_A = \sum_{\alpha \in \{e, \mu, \tau\}} \frac{\partial \hat{\mu}_A}{\partial \hat{\mathcal{L}}_\alpha} \hat{\mathcal{L}}_\alpha, \quad (3.8)$$

where the coefficients ($\partial \hat{\mu}_A / \partial \hat{\mathcal{L}}_\alpha$) depend on the susceptibilities of both the leptons and the strong fluid. We also express the redistributed asymmetries as

$$\Delta\hat{n}_A = \sum_{\alpha \in \{e, \mu, \tau\}} \frac{\partial \Delta\hat{n}_A}{\partial \hat{\mathcal{L}}_\alpha} \hat{\mathcal{L}}_\alpha = \sum_{\alpha \in \{e, \mu, \tau\}} \hat{\chi}_A \frac{\partial \hat{\mu}_A}{\partial \hat{\mathcal{L}}_\alpha} \hat{\mathcal{L}}_\alpha. \quad (3.9)$$

At the temperatures of interest, the lepton susceptibilities are essentially given by the free particle, or Stefan-Boltzmann, formula:

$$\hat{\chi}_A(\hat{m}_A) = -\frac{g_A}{\pi^2} \int_0^\infty d\hat{p} \hat{p}^2 \hat{n}'_{\text{F}} \left(\sqrt{\hat{p}^2 + \hat{m}_A^2} \right). \quad (3.10)$$

In this equation, g_A and $\hat{m}_A \equiv m_A/T$ are the spin degeneracy and mass, respectively, and $\hat{n}'_{\text{F}}(x) = (d/dx)\{1/[\exp(x) + 1]\}$ is the derivative of the Fermi-Dirac distribution.

3.2 Susceptibilities of the strongly-interacting plasma¹

The sterile neutrino production calculation requires knowledge of the strongly-interacting plasma’s susceptibilities over a broad range of temperatures, both above and below the quark-hadron transition. We evaluate them using a number of techniques: perturbative quantum chromodynamics (QCD) at high temperatures, matching to lattice QCD results near the quark-hadron transition,

¹I have removed the part of this section that explicitly computed the susceptibilities of the strong fluid at low and high temperatures, and have replaced it with a description of the method. The computation is Francis-Yan Cyr-Racine’s work, and can be found in the preprint [304].

and a hadron resonance gas (HRG) approximation at low temperatures. We now briefly describe our methodology.

We first rewrite the definition of the dimensionless susceptibilities in Eq. (3.5) as

$$\hat{\chi}_2^X = \left. \frac{\partial \Delta \hat{n}_X}{\partial \hat{\mu}_X} \right|_{\hat{\mu}_X=0} \quad \text{and} \quad \hat{\chi}_{11}^{XY} = \left. \frac{\partial \Delta \hat{n}_Y}{\partial \hat{\mu}_X} \right|_{\hat{\mu}_X, \hat{\mu}_Y=0}, \quad (3.11)$$

where $X, Y \in \{B, Q\}$, $\hat{\mu}_X \equiv \mu_X/T$ is the chemical potential of the conserved charge X . The key step is to recast the asymmetries, $\Delta \hat{n}_Y$, in terms of the QCD pressure, which is a thermodynamic quantity, i.e.,

$$\Delta \hat{n}_Y = \frac{\partial \hat{p}_{\text{QCD}}}{\partial \hat{\mu}_Y}. \quad (3.12)$$

The pressure \hat{p}_{QCD} is given by the logarithm of the QCD partition function Z_{QCD} .

$$\hat{p}_{\text{QCD}} \equiv \frac{p_{\text{QCD}}}{T^4} = \frac{1}{VT^3} \ln Z_{\text{QCD}}(V, T, \mu_Q, \mu_B), \quad (3.13)$$

where V is the volume. Thus, the susceptibilities are the following derivatives of the QCD pressure:

$$\hat{\chi}_2^X = \left. \frac{\partial^2 \hat{p}_{\text{QCD}}}{\partial \hat{\mu}_X^2} \right|_{\hat{\mu}_X=0} \quad \text{and} \quad \hat{\chi}_{11}^{XY} = \left. \frac{\partial^2 \hat{p}_{\text{QCD}}}{\partial \hat{\mu}_X \partial \hat{\mu}_Y} \right|_{\hat{\mu}_X, \hat{\mu}_Y=0}. \quad (3.14)$$

At low and high temperatures, i.e. $T \ll T_{\text{QCD}}$ and $T \gg T_{\text{QCD}}$, the QCD degrees of freedom in the plasma are conventionally described by an ideal gas of particles. At low temperatures, these particles are all the known hadronic resonances. We compute the partition function using the hadron resonance gas (HRG) model [305, 306].

At high temperatures, the QCD coupling constant is small; hence to the lowest order of approximation, the degrees of freedom are an ideal gas of quarks (alternatively known as the Stefan-Boltzmann approximation [307]). As we approach the quark-hadron transition, the coupling constant rises. We incorporate the coupling constant into the QCD pressure calculation using a standard perturbative approach, based on the formalism in Ref. [308].

Perturbative techniques become inadequate at intermediate temperatures, i.e., at $T \simeq T_{\text{QCD}}$. We rely on lattice calculations that report susceptibilities through the quark-hadron transition (see e.g. [309, 310]). These calculations rely on the thermodynamic relation between the susceptibilities and moments of the fluctuations of conserved quantities.

$$\langle \Delta \hat{n}_X \Delta \hat{n}_Y \rangle \Big|_{\hat{\mu}_X = \hat{\mu}_Y = 0} = \frac{\partial \Delta \hat{n}_X}{\partial \hat{\mu}_Y} \Big|_{\hat{\mu}_X = \hat{\mu}_Y = 0}. \quad (3.15)$$

This is most easily obtained from the thermodynamic definition in Eq. (3.12). The moments on the

left-hand side are easily accessible in lattice QCD simulations [311]. Our strategy to compute the susceptibility tensor over the whole required range of temperatures is as follows: we first separately calculate it both above and below the quark-hadron transition using either perturbative or HRG techniques, and then smoothly join the results with those from lattice QCD computations in the regions of overlap.

Specifically, we use the results from the Wuppertal-Budapest (WB) lattice QCD collaboration [309] and the HotQCD collaboration [310]. Even though the groups use different staggered fermion actions on the lattice, their results are broadly consistent with one another. They report the susceptibilities $\hat{\chi}_2^{\text{Q}}$, $\hat{\chi}_2^{\text{B}}$, and $\hat{\chi}_{11}^{\text{QB}}$, together with their estimated errors, in (2+1)-flavor QCD extrapolated to the continuum limit ⁴.

We combine results from the three regimes into a single smooth susceptibility tensor, valid over the range of temperatures relevant to the production of sterile neutrinos with masses of order $\mathcal{O}(10 \text{ keV})$. Figures 3.1a, 3.1b, and 3.1c display the susceptibilities $\hat{\chi}_2^{\text{Q}}$, $\hat{\chi}_2^{\text{B}}$, and $\hat{\chi}_{11}^{\text{QB}}$ for temperatures satisfying $10 \text{ MeV} < T < 10 \text{ GeV}$. The thick solid black lines are our smooth fits to the three regimes, while the dashed red and cyan dotted lines are the HRG and perturbative results, respectively. We also show the results from the WB lattice QCD collaboration in the neighborhood of the quark-hadron transition. For comparison, we also show the susceptibilities computed in the Stefan-Boltzmann limit, i.e., assuming free quarks throughout and using Eq. (3.10).

The lattice QCD results are in good agreement with the perturbative calculations described above for the temperature range $250 \text{ MeV} \lesssim T \lesssim 300 \text{ MeV}$, above which they underpredict the primeval plasma's susceptibility owing to the charm quark's influence [312]. Therefore, we do not consider the lattice QCD calculations at temperatures above $T \gtrsim 300 \text{ MeV}$ to avoid biasing our results, and instead use the perturbative *QCD* approach.

We observe that the HRG calculation agrees well with the lattice QCD result for $T \lesssim 150 \text{ MeV}$, but systematically overpredicts the susceptibilities at higher temperatures. The perturbative approach is consistent with the available lattice QCD data at $T \gtrsim 225 \text{ MeV}$, but again systematically overpredicts the susceptibilities at lower temperatures. Generally, the Stefan-Boltzmann approximation overestimates the susceptibilities by a factor of order unity, except near the quark-hadron transition. Interestingly, we observe an accidental cancellation in the off-diagonal susceptibility, $\hat{\chi}_{11}^{\text{QB}}$, in the (2+1)-flavor model which does not appear in the $N_f = 5$ theory. This arises because the sum of the electric charges of the up, down, and strange quarks exactly vanishes. Hence, we expect $\hat{\chi}_{11}^{\text{QB}} \rightarrow 0$ for temperatures above the strange quark mass in the (2+1)-flavor model. In the $N_f = 5$ model, however, the charm quark becomes rapidly important at $T \gtrsim 300 \text{ MeV}$, leading to a sharp turnover in $\hat{\chi}_{11}^{\text{QB}}$ near this temperature.

⁴The WB collaboration does not directly report $\hat{\chi}_{11}^{\text{QB}}$, but we infer it from their results via a change-of-basis operation.

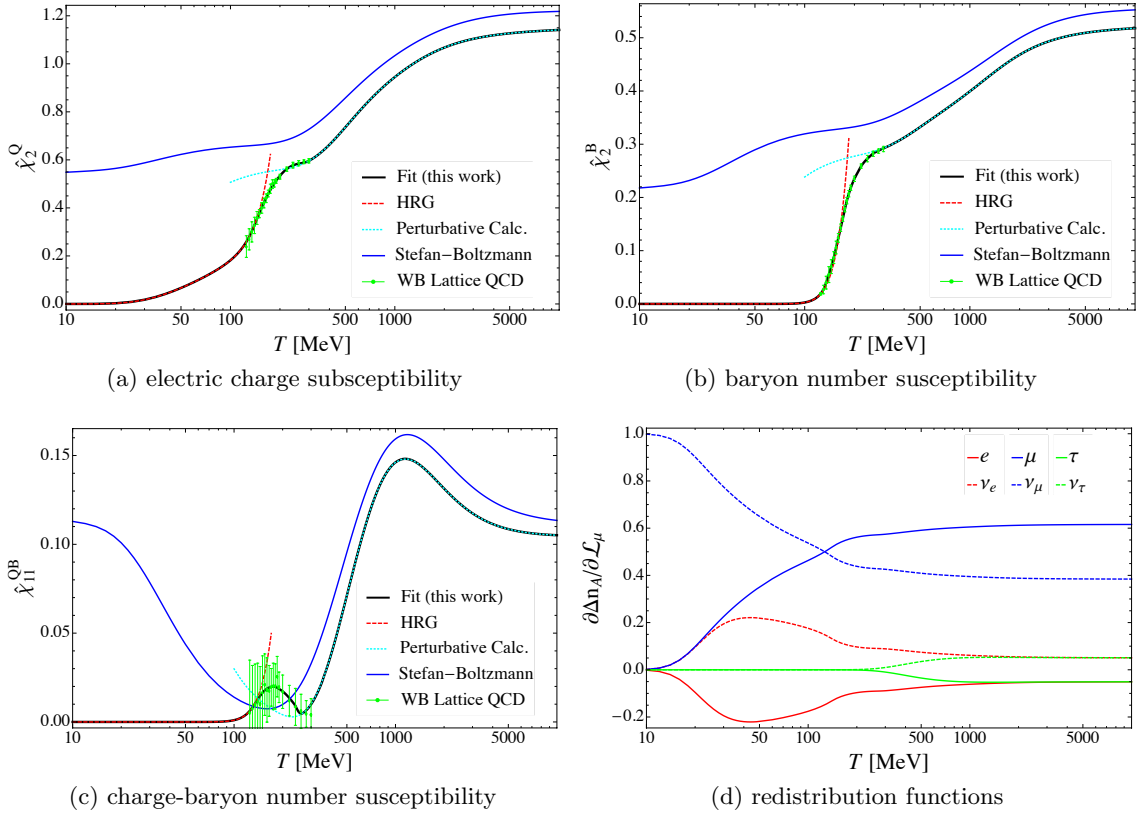


Figure 3.1: Panels (a)-(c): Components of the quadratic susceptibility tensor for the primordial plasma’s electric charge and baryon number. In all panels, the thick solid black line shows our smooth fit used in the computation of sterile neutrino production. At low temperatures, we illustrate the HRG results with dashed red lines, while the high-temperature perturbative results are shown with dotted cyan lines. We also show the results from the WB lattice QCD collaboration[309] with green errorbars. For comparison, we also display the Stefan-Boltzmann approximation to the susceptibilities assuming free quarks at all temperatures. Panel (d): Effective populations of all leptonic degrees of freedom after the redistribution of an infinitesimal mu leptonic asymmetry at all temperatures. Figure provided by Francis-Yan Cyr-Racine.

Given a set of infinitesimal lepton asymmetries, we solve for the chemical potentials using the above susceptibilities in Eqs. (3.3), (3.4), (3.6), and (3.7). We obtain the redistributed asymmetries in all the constituent species by using these chemical potentials, along with the appropriate susceptibilities in Eq. (3.9). Figure 3.1d plots the redistributed asymmetries for an infinitesimal input mu leptonic asymmetry. We note the following features:

1. At temperatures $T > 2$ GeV, the redistribution is efficient and $\simeq 60\%$ of the mu leptonic asymmetry ends up in the muons. All the charged leptons are effectively massless at this epoch, and hence the populations of the electron and tau flavors are identical.
2. The rise in the mu and tau lepton populations above temperatures of $\simeq 25$ MeV and 300 MeV reflects, in part, the rise in their particle number susceptibilities as the temperature becomes comparable to their masses [see Eq. (3.10)]. However, the largest contribution to the former is

from the disappearance of the hadronic degrees of freedom below the quark-hadron transition, and the associated drop in the strongly interacting fluid’s susceptibilities.

3. The ‘kink’ in all the redistributed asymmetries close to temperatures $T \simeq 170$ MeV is a signature of the sharp change in the strongly interacting fluid’s susceptibilities at the quark-hadron transition [see Figs. 3.1a, 3.1b and 3.1c].
4. At lower temperatures, $T \lesssim 30$ MeV, the redistribution is inefficient and most of the asymmetry ends up in the muon neutrinos. Moreover, the electron neutrino and the muon have identical (small) populations. This is characteristic of inelastic neutrino scattering, $\nu_\mu + e^- \rightarrow \nu_e + \mu^-$, which is the most important channel at these temperatures (the hadronic susceptibilities are negligible at this epoch).

These redistributed asymmetries impact sterile neutrino production via the asymmetry potential, $V_{\nu_\mu}^L$. Equation (2.12a) expresses this potential in terms of the asymmetries in the populations of the individual charged and neutral leptons, along with those in the charge and baryon number of the strongly interacting fluid. As earlier, for an infinitesimal input mu leptonic asymmetry, the individual asymmetries are formally represented by the functions in Eq. (3.9); the solutions for the charged and neutral leptons are as plotted in Figure 3.1d. We obtain the electric charge density of the strongly interacting fluid, Δn_Q , using net electric charge neutrality, i.e. Eqs. (3.5) and (3.7). Tables of susceptibilities, along with the functions in Eq. (3.9) at a number of temperatures from 10 GeV down to 10 MeV can be found at <https://github.com/ntveem/sterile-dm/tree/master/data/tables>.

Figure 3.2 shows the potential per unit *physical* μ lepton asymmetry using these solutions; this quantity is constant and equals $2\sqrt{2} = 2.83$ in the absence of redistribution. As shown in the figure, asymmetry redistribution corrects the potential at the ten-percent level above temperatures $T \gtrsim 100$ MeV, which is where the bulk of the sterile neutrinos are produced. This contribution changes the resonant momenta, and the resultant sterile neutrino dark matter’s phase-space densities; we explore this further in Section 5.1.

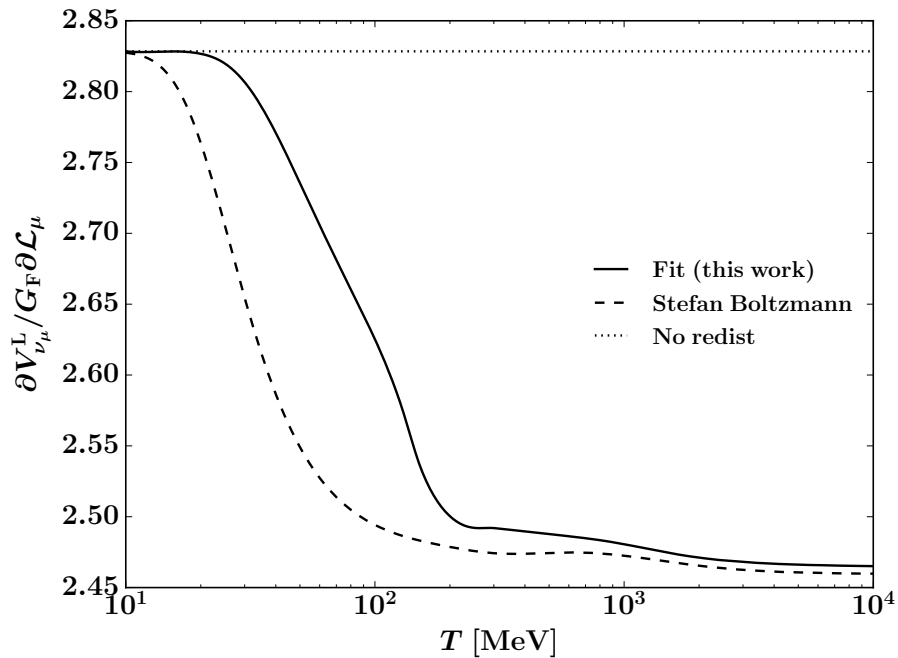


Figure 3.2: Asymmetry potential V^L per unit *unscaled* mu lepton asymmetry. Solid line shows the effect of redistribution using a combination of perturbative QCD, lattice calculations and the HRG approximation. Dashed line shows the result using Stefan-Boltzmann approximation for free quarks. The value is constant ($= 2\sqrt{2} = 2.83$) in the absence of redistribution [see Eq. (2.12a)]. The redistribution is a $\simeq 10\%$ correction at the most relevant temperatures for sterile neutrino production ($T \gtrsim 100$ MeV).

Chapter 4

Neutrino opacity

In this Chapter, we outline our calculation of muon neutrino opacities in the early universe. Initial work in this area focused on reactions involving leptons, in the context of neutrino decoupling, active–active neutrino oscillations and supernova calculations [230, 313, 314]. In particular, Ref. [313] lists a number of relevant matrix elements. Our calculations apply to earlier epochs, with a larger number of reactions due to the population of hadronic species above the quark-hadron transition.

Early work on sterile neutrino production used simple prescriptions for the resultant increase in reaction rates [137, 139]. Recent work in Refs. [243, 289] provides a theoretical framework to include particle masses and statistics in the neutrino opacity calculation, and formalism for loop corrections. We include a number of additional contributions to the neutrino opacities that are significant at the temperatures relevant to sterile neutrino production.

4.1 Assumptions and definitions

We adopt the following simplifying assumptions:

1. We neglect small asymmetries in the participating species' populations (as for the thermal potential). This is justified since the scattering rates are non-zero even in a CP symmetric plasma. Moreover, we assume thermal and kinetic equilibrium, due to which the populations of all active species are Fermi-Dirac/Bose-Einstein distributions.
2. We integrate out the massive gauge bosons, Z and W^\pm and approximate the weak interaction by a four-fermion contact term. Consequently, the reactions separate into leptonic and hadronic processes, depending on the species involved. Moreover, we neglect the thermal populations of Z^0 and W^\pm . These steps are valid at low temperatures and momentum transfers, i.e., $T, s/t/u \ll M_{W^\pm/Z^0} \approx 80$ GeV. We operate in the temperature and energy ranges

$$10 \text{ MeV} < T < 10 \text{ GeV}, \tag{4.1}$$

$$10^{-4} < E_{\nu_\mu}/T < 20. \quad (4.2)$$

The approximation fails at the higher energies at the upper end of the temperature range. However, as we see in Section 5.1, the bulk of the sterile neutrinos are produced at lower temperatures.

3. We assume incoming and outgoing particles to be non-interacting within two limits: below and above the quark-hadron transition (see §3.3 of Ref. [46]). Below the transition, we include hadronic channels with pseudoscalar and vector mesons¹, and neglect the small population of baryons. Above the transition, we include reactions with free quarks, i.e. we neglect the strong coupling constant. This approximation fails at temperatures $T \simeq T_{\text{QCD}}$ [308]. We show opacities interpolated through the transition using a few prescriptions, whose consequences for sterile neutrino production we explore in Section 5.1.

The collision integral for a massless muon neutrino is

$$C[f_{\nu_\mu}(E_{\nu_\mu})] = -\Gamma(E_{\nu_\mu})f_{\nu_\mu}(E_{\nu_\mu}) + \Gamma(E_{\nu_\mu})e^{-E_{\nu_\mu}/T}(1 - f_{\nu_\mu}(E_{\nu_\mu})), \quad (4.3)$$

where Γ and f_{ν_μ} are the interaction rate (opacity) and PSD, respectively. (This expression satisfies detailed balance; see assumption # 1.) The interaction rate is given by a sum over all reactions that consume the muon neutrino [see Eq. (2.7)].

It is useful to define the scaled interaction rate

$$\tilde{\Gamma}(E_{\nu_\mu}) = \frac{\Gamma(E_{\nu_\mu})}{G_{\text{F}}^2 T^4 E_{\nu_\mu}}. \quad (4.4)$$

In the limit where all the particles involved are relativistic, weak cross-sections are proportional to the squared energy in the CM reference frame. If we ignore particle statistics, reaction rates follow the scaling of Eq. (2.2), and hence the scaled rate is proportional to the number of relativistic degrees of freedom involved [288]. We present the scaled rates in the rest of this section in order to contrast our results with this intuition.

In the rest of this Chapter, we enumerate reactions contributing to the opacity, and present matrix elements and final rates under the above approximations.

4.2 Matrix elements

In this Section, we lay out matrix elements for reactions that contribute to the neutrino opacity, under the assumptions laid out in Section 4.1. We classify reactions by the number of particles in

¹We also include quark production in s-channel reactions at high CM energies. See Section 4.2.1 for details.

their initial and final states. We now present their matrix elements in an organized manner.

4.2.1 Reactions with two-particle final states

We compute reaction rates for momenta and temperatures where we can integrate the weak gauge bosons out and approximate the weak interaction by a four-particle vertex. For tree-level processes under this approximation, if one of the ingoing particles is a neutrino, one of the other particles is either a neutrino or a charged lepton of the same flavor. We classify two-particle to two-particle reactions as leptonic or hadronic based on the nature of the remaining two particles.

We first study reactions that involve only fermions, which include ones involving solely leptons and those involving quarks. Following this, we study mesonic channels, which are active below the quark-hadron transition.

4.2.1.1 Four-fermion reactions with two particle final states

It is a lengthy, albeit straightforward, task to enumerate all leptonic reactions that contribute to the neutrino opacity. Ref. [313] lists a complete set of reactions at temperatures of a few MeV. Our calculations extend to higher temperatures, and hence we also include reactions involving tau leptons. It is harder to study hadronic reactions in a consistent manner through the quark-hadron transition temperature, T_{QCD} .

We adopt assumption # 3 of Section 4.1 for the hadronic rates: we neglect the strong coupling constant and its running at temperatures $T > T_{\text{QCD}}$, and hence calculate opacities with free quarks. The matrix elements in this section assume standard-model quark currents that couple to the weak gauge bosons, Z^0 and W^\pm (see for example Ref. [315]). We study the low temperature limit in subsequent sections.

Figure 4.1 shows the different classes of processes at tree-level which involve an incoming neutrino, ν_X , and two particles in the outgoing state. Regardless of whether leptonic or quark currents are involved, the squared and spin-summed matrix elements of all such reactions are proportional to one of three forms:

$$\begin{aligned} \mathcal{I}(Q_f, T_f^3, m_f) = 128G_{\text{F}}^2 & \left[Q_f^2 \sin^4 \theta_W (p_1 \cdot p_4)(p_2 \cdot p_3) + (Q_f \sin^2 \theta_W - T_f^3)^2 (p_1 \cdot p_2)(p_3 \cdot p_4) \right. \\ & \left. + m_f^2 (Q_f \sin^2 \theta_W - T_f^3) Q_f \sin^2 \theta_W (p_1 \cdot p_3) \right]. \end{aligned} \quad (4.5)$$

$$\begin{aligned} \bar{\mathcal{I}}(Q_f, T_f^3, m_f) = 128G_{\text{F}}^2 & \left[Q_f^2 \sin^4 \theta_W (p_1 \cdot p_2)(p_3 \cdot p_4) + (Q_f \sin^2 \theta_W - T_f^3)^2 (p_1 \cdot p_4)(p_2 \cdot p_3) \right. \\ & \left. + m_f^2 (Q_f \sin^2 \theta_W - T_f^3) Q_f \sin^2 \theta_W (p_1 \cdot p_3) \right]. \end{aligned} \quad (4.6)$$

$$\begin{aligned} \mathcal{J}(Q_f, T_f^3, m_f) = 128G_{\text{F}}^2 & \left[Q_f^2 \sin^4 \theta_W (p_1 \cdot p_3)(p_2 \cdot p_4) + (Q_f \sin^2 \theta_W - T_f^3)^2 (p_1 \cdot p_4)(p_2 \cdot p_3) \right. \\ & \left. - m_f^2 (Q_f \sin^2 \theta_W - T_f^3) Q_f \sin^2 \theta_W (p_1 \cdot p_2) \right]. \end{aligned} \quad (4.7)$$

Reaction	Label	$Sg_c \sum M ^2(Q_f, T_f^3, m_f)$
$\nu_X + \nu_X \rightarrow \nu_X + \nu_X$	4.1c	$(1/4)\mathcal{I}(0, 1, 0)$
$\nu_X + \bar{\nu}_X \rightarrow \nu_X + \bar{\nu}_X$	4.1d	$\bar{\mathcal{I}}(0, 1, 0)$
$\nu_X + X^- \rightarrow \nu_X + X^-$	4.1e	$\mathcal{I}(-1, 1/2, m_X)$
$\nu_X + X^+ \rightarrow \nu_X + X^+$	4.1f	$\bar{\mathcal{I}}(-1, 1/2, m_X)$
$\nu_X + Y^- \rightarrow \nu_X + Y^-$	4.1a	$\mathcal{I}(-1, -1/2, m_Y)$
$\nu_X + Y^+ \rightarrow \nu_X + Y^+$	4.1b	$\bar{\mathcal{I}}(-1, -1/2, m_Y)$
$\nu_X + \nu_Y \rightarrow \nu_X + \nu_Y$	4.1a	$\mathcal{I}(0, 1/2, 0)$
$\nu_X + \bar{\nu}_Y \rightarrow \nu_X + \bar{\nu}_Y$	4.1b	$\bar{\mathcal{I}}(0, 1/2, 0)$
$\nu_X + u/c/t \rightarrow \nu_X + u/c/t$	4.1a	$3\mathcal{I}(2/3, 1/2, m_{u/c/t})$
$\nu_X + \bar{u}/\bar{c}/\bar{t} \rightarrow \nu_X + \bar{u}/\bar{c}/\bar{t}$	4.1b	$3\bar{\mathcal{I}}(2/3, 1/2, m_{u/c/t})$
$\nu_X + d/s/b \rightarrow \nu_X + d/s/b$	4.1a	$3\mathcal{I}(-1/3, -1/2, m_{d/s/b})$
$\nu_X + \bar{d}/\bar{s}/\bar{b} \rightarrow \nu_X + \bar{d}/\bar{s}/\bar{b}$	4.1b	$3\bar{\mathcal{I}}(-1/3, -1/2, m_{d/s/b})$
$\nu_X + X^+ \rightarrow \nu_Y + Y^+$	4.1g	$\mathcal{J}(0, 1, 0)$
$\nu_X + X^+ \rightarrow \beta + \bar{\alpha}$		
$\beta \in \{u, c, t\}$		
$\alpha \in \{d, s, b\}$	4.1h	$3 V_{\beta\alpha} ^2\mathcal{J}(0, 1, 0)$
$\nu_X + Y^- \rightarrow X^- + \nu_Y$	4.1i	$\mathcal{I}(0, 1, 0)$
$\nu_X + \bar{\nu}_Y \rightarrow X^- + Y^+$	4.1j	$\bar{\mathcal{I}}(0, 1, 0)$
$\nu_X + \alpha \rightarrow X^- + \beta$		
$\alpha \in \{d, s, b\}$		
$\beta \in \{u, c, t\}$	4.1k	$3 V_{\beta\alpha} ^2\mathcal{I}(0, 1, 0)$
$\nu_X + \bar{\alpha} \rightarrow X^- + \bar{\beta}$		
$\alpha \in \{u, c, t\}$		
$\beta \in \{d, s, b\}$	4.1k	$3 V_{\alpha\beta} ^2\bar{\mathcal{I}}(0, 1, 0)$
$\nu_X + \bar{\nu}_X \rightarrow X^- + X^+$	4.1n	$\mathcal{J}(-1, 1/2, m_X)$
$\nu_X + \bar{\nu}_X \rightarrow \nu_Y + \bar{\nu}_Y$	4.1m	$\mathcal{J}(0, 1/2, 0)$
$\nu_X + \bar{\nu}_X \rightarrow Y^- + Y^+$	4.1m	$\mathcal{J}(-1, -1/2, m_Y)$
$\nu_X + \bar{\nu}_X \rightarrow u/c/t + \bar{u}/\bar{c}/\bar{t}$	4.1m	$3\mathcal{J}(2/3, 1/2, m_{u/c/t})$
$\nu_X + \bar{\nu}_X \rightarrow d/s/b + \bar{d}/\bar{s}/\bar{b}$	4.1m	$3\mathcal{J}(-1/3, -1/2, m_{d/s/b})$

Table 4.1: Matrix elements of reactions involving a neutrino ν_X . Listed above are the moduli squared multiplied with the appropriate symmetry factors and color degeneracy factors to be included in collision integrals, for the diagrams shown in Figure 4.1. They are given in terms of the definitions of \mathcal{I} , $\bar{\mathcal{I}}$ and \mathcal{J} in Eqs. (4.5), (4.6), and (4.7).

Table 4.1 enumerates all reactions involving leptons and quarks, along with their counterpart in Figure 4.1), and the moduli squared to be used in collision integrals.

4.2.1.2 Reactions involving mesons with two particle final states

The physical rates for hadronic reactions diverge from our calculated ones close to the transition, since the strong coupling constant is non-zero. Treating this self-consistently is beyond the scope of this work. When we use the computed rates in production calculations in Chapter 5, we present results for a few unphysical interpolations through the transition.

At even lower temperatures, $T < T_{\text{QCD}}$, we cannot use the free quark approximation. The most important hadronic degrees of freedom are the pseudoscalar meson octet, which are pseudo-Goldstone bosons associated with the spontaneous breaking of the axial part of an approximate

$SU(3)_L \times SU(3)_R$ flavor symmetry [315]. We use three quark chiral perturbation theory (3 χ PT) to write down the currents that couple to Z^0 and W^\pm , and through them evaluate the mesonic contribution to the neutrino opacity.

Consider a 3×3 unitary matrix, $U(x)$, which represents low-lying hadronic excitations at temperatures $T < T_{\text{QCD}}$. We express $U(x)$ in terms of the pion fields $\pi^a(x)$ as follows:

$$U(x) = \exp \left[2i \frac{\pi^a(x) T^a}{f_\pi} \right], \quad a \in [1, 8], \quad (4.8)$$

$$\frac{2\pi^a(x) T^a}{f_\pi} = \frac{1}{f_\pi} \begin{pmatrix} \pi^0 + \frac{1}{\sqrt{3}}\eta & \sqrt{2}\pi^+ & \sqrt{2}K^+ \\ \sqrt{2}\pi^- & -\pi^0 + \frac{1}{\sqrt{3}}\eta & \sqrt{2}K^0 \\ \sqrt{2}K^- & \sqrt{2}K^0 & -\frac{2}{\sqrt{3}}\eta \end{pmatrix}, \quad (4.9)$$

where f_π is an energy-scale associated with the breaking of the $SU(3)_A$ symmetry, and T^a are generators of $SU(3)$. The most massive member of this octet, the η meson, has a mass of $m_\eta = 547.8$ MeV [229]. We only use this prescription at $T \leq 150$ MeV, so these low lying excitations are sufficient to describe all relevant *incoming* hadronic degrees of freedom.

In the framework of 3 χ PT, the dynamics of the pion fields are described by an effective Lagrangian for $U(x)$ coupled to matrix valued $SU(3)_L$ and $SU(3)_R$ gauge fields l_μ and r_μ , respectively. The first approximation to the Lagrangian is the lowest term in a derivative expansion:

$$\mathcal{L} = -\frac{1}{4} f_\pi^2 \text{Tr} [D^\mu U^\dagger D_\mu U], \quad \text{with} \quad D_\mu U = \partial_\mu U - i l_\mu U + i U r_\mu. \quad (4.10)$$

The gauge fields l_μ and r_μ are Hermitian matrices, which we decompose as

$$(l/r)_\mu = (l/r)_\mu^a T^a + (\mathcal{V}_\mu \mp \mathcal{A}_\mu) I, \quad a \in [1, 8]. \quad (4.11)$$

The fields \mathcal{V}_μ and \mathcal{A}_μ are vector and axial-vector parts of l_μ and r_μ . We identify the electroweak gauge bosons of the standard model, Z_μ^0 , W_μ^\pm and A_μ [or equivalently, the underlying $SU(2) \times U(1)$ gauge fields A_μ^a and B_μ], with elements of $(l^a/r^a/\mathcal{V}/\mathcal{A})_\mu$ by equating their action on the pion fields $\pi^a(x)$ or the excitation $U(x)$ via the right-hand side of Eq. (4.10). The results of this procedure are

$$g_2 A_\mu^1 = l_\mu^1, \quad (4.12a)$$

$$g_2 A_\mu^2 = l_\mu^2, \quad (4.12b)$$

$$g_2 A_\mu^3 = l_\mu^3 + \frac{1}{\sqrt{3}} l_\mu^8 - \frac{1}{12} \mathcal{V}_\mu + \frac{1}{12} \mathcal{A}_\mu, \quad (4.12c)$$

$$e A_\mu = l_\mu^3 + r_\mu^3 + \frac{1}{\sqrt{3}} l_\mu^8 + \frac{1}{\sqrt{3}} r_\mu^8. \quad (4.12d)$$

Here g_2 is the $SU(2)$ coupling constant, and $e = g_2 \sin \theta_W$. The overlap of A_μ^3 with the anomalous

\mathcal{A}_μ is an artifact of the omission of the charm quark from our analysis. If the charm quark were included (as it has to be to make the SM non-anomalous) then there is no coupling to an anomalous current. As long as there are no charm quarks (always true at the temperatures where 3χ PT is applied) this current looks like that associated with the anomalous $U(1)_A$.

We read off the currents that couple to the gauge fields using the definition $J_{l/r/\mathcal{V}/\mathcal{A}}^{(a)\mu} = \partial\mathcal{L}/\partial(l^a/r^a/\mathcal{V}/\mathcal{A})_\mu$, and the Lagrangian of Eq. (4.10). We transform the resultings to obtain the currents that couple to the SM electroweak gauge fields, Z_μ^0, W_μ^\pm and A_μ :

$$J^{+\mu} = \frac{1}{\sqrt{2}} \left[V_{ud}^* \left(f_\pi \partial^\mu \pi^+ + i\pi^0 \overleftrightarrow{\partial}^\mu \pi^+ - \frac{i}{\sqrt{2}} \overline{K^0} \overleftrightarrow{\partial}^\mu K^+ \right) + V_{us}^* \left(-\frac{i}{\sqrt{2}} \overline{K^0} \overleftrightarrow{\partial}^\mu \pi^+ + \frac{i}{2} \pi^0 \overleftrightarrow{\partial}^\mu K^+ + \frac{\sqrt{3}i}{2} \eta \overleftrightarrow{\partial}^\mu K^+ \right) \right], \quad (4.13a)$$

$$J^{-\mu} = \frac{1}{\sqrt{2}} \left[V_{ud} \left(f_\pi \partial^\mu \pi^- - i\pi^0 \overleftrightarrow{\partial}^\mu \pi^- + \frac{i}{\sqrt{2}} \overline{K^0} \overleftrightarrow{\partial}^\mu K^- \right) + V_{us} \left(\frac{i}{\sqrt{2}} \overline{K^0} \overleftrightarrow{\partial}^\mu \pi^- - \frac{i}{2} \pi^0 \overleftrightarrow{\partial}^\mu K^- - \frac{\sqrt{3}i}{2} \eta \overleftrightarrow{\partial}^\mu K^- \right) \right], \quad (4.13b)$$

$$J_z^\mu = J_3^\mu - \sin^2 \theta_W J_{\text{EM}}^\mu, \quad (4.13c)$$

$$J_3^\mu = \frac{1}{2} \left[f_\pi \left(\partial^\mu \pi^0 + \frac{1}{\sqrt{3}} \partial^\mu \eta \right) + i\pi^+ \overleftrightarrow{\partial}^\mu \pi^- + iK^+ \overleftrightarrow{\partial}^\mu K^- \right], \quad (4.13d)$$

$$J_{\text{EM}}^\mu = i\pi^+ \overleftrightarrow{\partial}^\mu \pi^- + iK^+ \overleftrightarrow{\partial}^\mu K^-. \quad (4.13e)$$

These currents agree with the leading order parts of the functionals computed in Ref. [316].

A final complication is that 3χ PT, and the currents derived from it, are valid only when the momentum in the intermediate weak gauge bosons is low compared to the energy scale $4\pi f_\pi \sim 1$ GeV [315]). The physical currents that couple to the SM electroweak gauge fields are continuous functions of this momentum; they approach the SM free quark currents for large momentum values. This manifests as the production of quarks in the large CM energy limit in s-channel reactions, and as ‘deep-inelastic scattering’ off the mesons’ quark content in the large momentum-transfer limit in t-channel reactions. These limits are important to consider at the higher energies for which we calculate neutrino opacities using 3χ PT (the total energy range is shown in Figures 4.5a and 4.6).

We do not self-consistently compute these corrections to the currents, as it is beyond the scope of this work. Instead, we modify the s-channel reaction rates in a phenomenological manner: we apply a cutoff in the CM energy at 1 GeV with a width of 50 MeV, below which we use the 3χ PT currents, and above which we use the SM free quark currents. We do not incorporate any corrections to t-channel reactions; this would involve some knowledge of the parton distribution functions for the mesons involved.

Figure 4.2 shows the relevant scattering processes involving mesons, keeping only terms upto $O(p^2)$ in 3χ PT. For the diagrams involving a Z boson, it is kinematically possible to have it couple to a neutral meson too, but such processes are suppressed in 3χ PT.

Reaction	Label	$\sum M ^2$
$\nu_X + \pi^+ \rightarrow \nu_X + \pi^+$	4.2a	$2(\frac{1}{2} - \sin^2 \theta_W)^2 \mathcal{A}$
$\nu_X + K^+ \rightarrow \nu_X + K^+$	4.2a	$2(\frac{1}{2} - \sin^2 \theta_W)^2 \mathcal{A}$
$\nu_X + \pi^- \rightarrow \nu_X + \pi^-$	4.2b	$2(\frac{1}{2} - \sin^2 \theta_W)^2 \mathcal{A}$
$\nu_X + K^- \rightarrow \nu_X + K^-$	4.2b	$2(\frac{1}{2} - \sin^2 \theta_W)^2 \mathcal{A}$
$\nu_X + X^+ \rightarrow \pi^+ + \pi^0$	4.2c	$ V_{ud} ^2 \mathcal{B}$
$\nu_X + X^+ \rightarrow K^+ + \overline{K^0}$	4.2c	$\frac{1}{2} V_{ud} ^2 \mathcal{B}$
$\nu_X + X^+ \rightarrow \pi^+ + K^0$	4.2c	$\frac{1}{2} V_{us} ^2 \mathcal{B}$
$\nu_X + X^+ \rightarrow K^+ + \pi^0$	4.2c	$\frac{1}{4} V_{us} ^2 \mathcal{B}$
$\nu_X + X^+ \rightarrow K^+ + \eta$	4.2c	$\frac{3}{4} V_{us} ^2 \mathcal{B}$
$\nu_X + \pi^- \rightarrow X^- + \pi^0$	4.2d	$ V_{ud} ^2 \mathcal{A}$
$\nu_X + K^- \rightarrow X^- + \overline{K^0}$	4.2d	$\frac{1}{2} V_{ud} ^2 \mathcal{A}$
$\nu_X + \pi^- \rightarrow X^- + K^0$	4.2d	$\frac{1}{2} V_{us} ^2 \mathcal{A}$
$\nu_X + K^- \rightarrow X^- + \pi^0$	4.2d	$\frac{1}{4} V_{us} ^2 \mathcal{A}$
$\nu_X + K^- \rightarrow X^- + \eta$	4.2d	$\frac{3}{4} V_{us} ^2 \mathcal{A}$
$\nu_X + \pi^0 \rightarrow X^- + \pi^+$	4.2e	$ V_{ud} ^2 \mathcal{A}$
$\nu_X + \overline{K^0} \rightarrow X^- + K^+$	4.2e	$\frac{1}{2} V_{ud} ^2 \mathcal{A}$
$\nu_X + \overline{K^0} \rightarrow X^- + \pi^+$	4.2e	$\frac{1}{2} V_{us} ^2 \mathcal{A}$
$\nu_X + \pi^0 \rightarrow X^- + K^+$	4.2e	$\frac{1}{4} V_{us} ^2 \mathcal{A}$
$\nu_X + \eta \rightarrow X^- + K^+$	4.2e	$\frac{3}{4} V_{us} ^2 \mathcal{A}$
$\nu_X + \bar{\nu}_X \rightarrow \pi^+ + \pi^-$	4.2f	$2(1/2 - \sin^2 \theta_W)^2 \mathcal{B}$
$\nu_X + \bar{\nu}_X \rightarrow K^+ + K^-$	4.2f	$2(1/2 - \sin^2 \theta_W)^2 \mathcal{B}$

Table 4.2: Matrix elements for interactions of an incoming neutrino ν_X involving mesons, with only terms upto $O(p^2)$ in 3χ PT. Listed above are the moduli squared to be included in collision integrals, for the diagrams shown in Figure 4.2. They are given in terms of the definitions of \mathcal{A}, \mathcal{B} in Eqs. (4.14), (4.15).

The squared and spin-summed matrix elements of all mesonic reactions are proportional to one of two forms:

$$\begin{aligned} \mathcal{A} &= G_F^2 \text{Tr} \left[\not{p}_3 (\not{p}_4 + \not{p}_2) (1 - \gamma_5) \not{p}_1 (\not{p}_4 + \not{p}_2) (1 - \gamma_5) \right] \\ &= 8G_F^2 \left[2\{p_3 \cdot (p_4 + p_2)\} \{p_1 \cdot (p_4 + p_2)\} - \{p_3 \cdot p_1\} \{p_4 + p_2\}^2 \right], \end{aligned} \quad (4.14)$$

$$\begin{aligned} \mathcal{B} &= G_F^2 \text{Tr} \left[\not{p}_2 (\not{p}_4 - \not{p}_3) (1 - \gamma_5) \not{p}_1 (\not{p}_4 - \not{p}_3) (1 - \gamma_5) \right] \\ &= 8G_F^2 \left[2\{p_2 \cdot (p_4 - p_3)\} \{p_1 \cdot (p_4 - p_3)\} - \{p_2 \cdot p_1\} \{p_4 - p_3\}^2 \right]. \end{aligned} \quad (4.15)$$

Table 4.2 lists the moduli squared of various reactions, along with the corresponding sub-figure in Fig. 4.2, in terms of these functions.

We observe that the squared and spin-summed matrix elements, be it for tree-level processes involving leptons and free quarks (computed using the SM currents), or for those involving pseudoscalar mesons (computed using terms upto $O(p^2)$ in 3χ PT), are at-most quadratic functions of the Mandelstam variables. This greatly facilitates a semi-automated computation of the two-particle to two-particle reactions' contribution to the neutrino opacity. which we very briefly describe next.

4.2.1.3 Rates for two-particle to two-particle reactions

Consider a general two-particle to two-particle reaction, $\nu_\alpha + A \rightarrow B + C$, that consumes a massless input neutrino, ν_α . The particles A, B , and C can all be fermions (leptons or quarks), or contain a pair of bosons (pseudoscalar mesons). We expand Eq. (2.7) to write down the following expression for the scattering rate as a collision integral:

$$\Gamma(E_{\nu_\alpha}) = \frac{1}{2E_{\nu_\alpha}} \int d^3\tilde{\mathbf{p}}_A d^3\tilde{\mathbf{p}}_B d^3\tilde{\mathbf{p}}_C (2\pi)^4 \delta(p_{\nu_\alpha} + p_A - p_B - p_C) \\ \times S \sum |\mathcal{M}|^2 f_A(E_A) (1 \mp f_B(E_B)) (1 \mp f_C(E_C)), \quad (4.16)$$

where the symbol $d^3\tilde{\mathbf{p}}$ is shorthand for the Lorentz invariant phase space volume element $d^3\mathbf{p}/[(2\pi)^3 2E(\mathbf{p})]$, the symbol $\sum |\mathcal{M}|^2$ is the absolute value of the matrix element squared and summed over all spin states, S is a symmetry factor for identical particles in the initial and/or final states, and the $f(E)$ s are appropriate Bose-Einstein/Fermi-Dirac phase space distributions depending on the statistics of the particles, with plus and minus signs for bosons and fermions, respectively.

We follow the treatment in Ref. [313] to reduce the nine-dimensional phase space integral of Eq. (4.16) to a numerically manageable three-dimensional integral over the variables $|\mathbf{p}_A|, |\mathbf{p}_B|$ and $\mu_B = \hat{\mathbf{p}}_B \cdot \hat{\mathbf{p}}_{\nu_\alpha}$. This procedure involves using the delta function to perform the integral over \mathbf{p}_C , and using the form of the matrix elements for tree-level processes to analytically perform the integral over $\mu_A = \hat{\mathbf{p}}_A \cdot \hat{\mathbf{p}}_{\nu_\alpha}$. We refer the reader to Ref. [313] for more details. The form of the matrix elements also lends itself to easy parameterization in terms of a small number of classes; along with the procedure described above, this enables a simple numerical implementation of the calculation of these reactions' contributions to the neutrino scattering rate.

4.2.2 Rates for neutrinos to go to one-particle final states

We must also consider the contribution to the neutrino interaction rate, $\Gamma(E_{\nu_\alpha})$, from interactions with two-particle final states (“fusion” or inverse decay). A four-fermion interaction such as the weak interaction (at $E \ll m_W, m_Z$) can produce such a final state in two ways. One, applicable at $T < T_{\text{QCD}}$, is two-body fusion to produce a meson, e.g. $\nu_\mu + \mu^+ \rightarrow \pi^+$. The other is the ‘three-body fusion’, e.g. $\nu_\mu + \bar{\nu}_e + e^- \rightarrow \mu^-$. By construction, these fusion processes are the inverse of a decay process. We describe our treatment of these processes in the rest of this section.

4.2.2.1 Two-body fusion processes¹

¹I have removed the part of this section that explicitly computes the rates of two body fusions, and only retained the results for completeness' sake. The computation is Christopher Hirata's work, and can be found in the preprint [304].

Table 4.3: The parameters for reactions that go into Eq. (4.18). Reactions relevant for the neutrino opacity are shown; antineutrinos are similar. Particle masses are obtained from the Particle Data Group. Decay partial widths are obtained from the sources indicated. All reactions in which a neutrino can produce a hadronic resonance below 1 GeV are included.

Reaction	m_A MeV	g_A	v	$\Gamma_{\text{reverse}}^{\text{vac}}$ MeV	Rate method
Reactions involving the pseudoscalar meson octet					
$\nu_e + e^+ \rightarrow \pi^+$	139.57	1	0.999987	3.110×10^{-18}	PDG
$\nu_\mu + \mu^+ \rightarrow \pi^+$	139.57	1	0.4269	2.528×10^{-14}	PDG
$\nu_e + e^+ \rightarrow K^+$	493.68	1	0.999989	8.41×10^{-19}	PDG
$\nu_\mu + \mu^+ \rightarrow K^+$	493.68	1	0.95419	3.38×10^{-14}	PDG
Reactions involving vector mesons with nonzero isospin					
$\nu_X + \bar{\nu}_X \rightarrow \rho^0$	775.26	3	1	9.78×10^{-12}	Average of τ decay and $e^+e^- \rightarrow \rho^0$; assumed isospin $SU(2)^1$
$\nu_e + e^+ \rightarrow \rho^+$	775.26	3	0.9999996	7.00×10^{-11}	τ decay
$\nu_\mu + \mu^+ \rightarrow \rho^+$	775.26	3	0.98143	6.80×10^{-11}	τ decay
$\nu_e + e^+ \rightarrow K^*(892)^+$	891.66	3	0.9999997	5.45×10^{-12}	τ decay
$\nu_\mu + \mu^+ \rightarrow K^*(892)^+$	891.66	3	0.98596	5.33×10^{-12}	τ decay
Reactions involving vector mesons with zero isospin					
$\nu_X + \bar{\nu}_X \rightarrow \omega(782)$	782.65	3	1	7×10^{-13}	$e^+e^- \rightarrow \omega(782)$; assumed quark content $(\bar{u}u + \bar{d}d)/\sqrt{2}$

A two-body fusion process must involve a meson in either the initial or the final state, and – if it is to absorb a neutrino – must then be semi-leptonic. The neutral current processes of this form (e.g. a neutral meson is created by the fusion of $\nu_\alpha \bar{\nu}_\alpha \rightarrow \pi^0$) are helicity-forbidden and have zero amplitude at tree-level. The charged current processes can have either the meson in the initial state and the charged lepton in the final state (e.g. $K^- \nu_\tau \rightarrow \tau^-$) or the meson in the final state (e.g. $\nu_\mu \mu^+ \rightarrow \pi^+$). The “charged lepton in the final state” case is possible only if the charged lepton is more massive than the meson, i.e. if that lepton is a τ ; at $T < T_{\text{QCD}}$ this not energetically feasible for typical values of the incoming particles’ momenta, since $m_\tau \gg T_{\text{QCD}}$. Therefore, we focus on the problem of a charged meson in the final state. The reaction is

$$\nu_\alpha + \alpha^+ \rightarrow A^+, \quad (4.17)$$

where $\alpha = e$ or μ and $A = \pi$ or K . We are interested in the thermal absorption rate Γ_{fusion} for the neutrinos as a function of temperature T and neutrino energy E_ν .

Consideration of the kinematics of the fusion process gives us the following rate:

$$\Gamma_{\text{fusion}}(E_{\nu_\alpha}) = \frac{g_A m_A \Gamma_{A^+ \rightarrow \nu_\alpha \alpha^+}^{\text{vac}} T}{v(1 + e^{-E_{\nu_\alpha}/T}) E_{\nu_\alpha}^2} \ln \frac{1 + e^{E_{\nu_\alpha}/T} e^{-(v^2 m_A^2 + 4E_{\nu_\alpha}^2)/(4v E_{\nu_\alpha} T)}}{1 - e^{-(v^2 m_A^2 + 4E_{\nu_\alpha}^2)/(4v E_{\nu_\alpha} T)}}, \quad (4.18)$$

where g_A is the degeneracy factor ($g_A = 1$ for pions and kaons), $v = 1 - m_\alpha^2/m_A^2$. Note that the numerical calculation of the logarithm must be treated carefully since for $E_{A,\text{min}} - E_{\nu_\alpha} \gg T$ we are taking the logarithm of a number that is very close to 1. For calculational purposes, we replace the logarithm in Eq. (4.18) by a truncation of its Taylor expansion at the fifth order wherever the argument deviates from unity by less than $\epsilon = 10^{-3}$.

The rate parameters for the key two-body fusion reactions are shown in Table 4.3.

4.2.2.2 Three-body fusion processes

The final set of reactions that contribute to the neutrino opacity are three-body fusions. As earlier, these reactions can be either leptonic or hadronic in nature. We adopt the prescription outlined in Section 4.2.1 for the hadronic reactions. Given the hadronic and leptonic currents coupling to the SM electroweak gauge bosons, we can enumerate all three-body reactions that contribute to the neutrino opacity by omitting in turn the products in the reactions of Tables 4.1 and 4.2, adding their charge conjugates to the reactants, subject to the constraint that the products rest mass is strictly greater than the sum of the reactants. An example is tau lepton production via $\nu_\mu + \mu^+ + \nu_\tau \rightarrow \tau^+$.

The matrix element for any three-body fusion reaction is related to one for a two-particle to two-particle reaction by crossing symmetry. Thus, we do not need to compute any new matrix elements for this section. However, we need to modify the treatment of the kinematics from the previous case. Consider a general three-body fusion reaction, $\nu_\alpha + A + B \rightarrow C$. The scattering rate for an input neutrino energy E_{ν_α} is given by the collision integral:

$$\Gamma(E_{\nu_\alpha}) = \frac{1}{2E_{\nu_\alpha}} \int d^3\tilde{\mathbf{p}}_A d^3\tilde{\mathbf{p}}_B d^3\tilde{\mathbf{p}}_C (2\pi)^4 \delta(p_{\nu_\alpha} + p_A + p_B - p_C) \times S \sum |\mathcal{M}|^2 f_A(E_A) f_B(E_B) (1 \mp f_C(E_C)). \quad (4.19)$$

All the symbols are defined identically to Eq. (4.16). The procedure to reduce the dimensionality of this integral is exactly analogous to that in Section 4.2.1.3 and Ref. [313], with one important difference. The variables finally left to numerically integrate over are, as earlier, $|\mathbf{p}_A|$, $|\mathbf{p}_B|$, and $\mu_B = \hat{\mathbf{p}}_{\nu_\alpha} \cdot \hat{\mathbf{p}}_B$. If we consider the integration domain for the two-particle to two-particle case, for a given value of $|\mathbf{p}_A|$, energy constraints allow a maximum value of $|\mathbf{p}_B|$. For a three-body fusion, $|\mathbf{p}_B|$ has no upper bound, which greatly expands the allowed phase-space. With this caveat, the rest of the procedure proceeds as it did for the other case.

4.3 Results

Figure 4.3 shows the leptonic contribution to the muon neutrino opacity at a temperature $T = 100$ MeV, using the matrix elements for reactions in Table 4.1, and related three-body fusions. For convenience, we only show reactions in the top five at any particular momentum bin. In the numerical implementation, we evaluate the dimensionless quantity $\Gamma(E_{\nu_\mu})/G_F^2 T^5$ (proportional to the *unscaled* rates) to an accuracy of 10^{-6} after simplifying the collision integrals in Eq. (4.16) and (4.19).

The quark-hadron transition considerably complicates the hadronic reactions. We appeal to assumption # 3 of Section 2.2.1 and evaluate their rates in two limits: at low and high temperatures, i.e. $T < T_{\text{QCD}}$ and $T > T_{\text{QCD}}$ respectively. Tables 4.1 and 4.2 list the hadronic two-particle to two-particle reactions contributing to the muon neutrino opacity. At high temperatures, we use all

reactions involving free quarks, while at temperatures $T \lesssim T_{\text{QCD}}$, we assume that all incoming hadronic degrees of freedom belong to the pseudoscalar meson nonet (the heaviest member of which is the eta meson, with a mass of $m_\eta = 547.8$ MeV). As in the leptonic case, we also include three-body fusions involving pseudoscalar mesons or quarks. Examples are K^0 and charm quark production via $\nu_\mu + \mu^+ + \pi^- \rightarrow K^0$ and $\nu_\mu + \mu^+ + s \rightarrow c$, respectively.

A complication is that at low temperatures, free quark and parton currents contribute to the initial and final states for large momentum transfer in the t- and s-channel respectively (see Section 4.2.1). For s-channel reactions, we thus treat individual meson resonances for center of mass energies < 1 GeV, and use the free quark model for inclusive cross sections at > 1 GeV. Also important are ‘two-body fusions’, i.e. reactions with two particles in the initial state and one in the final state, with the latter being a pseudoscalar or vector meson. Table 4.3 in Section 4.2.2 lists all such reactions included in our opacities.

Figure 4.4 shows the hadronic contribution to the muon neutrino opacity at low and high temperatures, using the matrix elements for two-particle to two-particle reactions, the associated three-body and two-body fusions. As earlier, we only show reactions in the top five at any momentum bin; the numerical implementation of the first two classes is unchanged.

Figure 4.5a shows the *total* opacities with muon neutrino energy at temperatures of 100 MeV and 2 GeV. We note a few salient features of these rates.

Firstly, we note that the leptonic and hadronic two-particle to two-particle reaction rates approach the scaling of Eq. (2.2) at large energies; the downturn at lower energies is due to Pauli blocking.

Secondly, both sets of rates exhibit a rise at low energies, which reflects non-zero limiting values of the *unscaled* rates. This is due to the behavior of cross sections for inelastic collisions involving massive particles, such as the three body collision $\nu_\mu + e^- + \bar{\nu}_e \rightarrow \mu^-$ or the scattering process $\nu_\mu + \mu^+ \rightarrow \nu_e + e^+$. We illustrate this by calculating the cross-section for the latter, while neglecting the positron’s rest mass and Pauli blocking for simplicity. The squared and spin-summed/averaged matrix element for this process is

$$\langle |\mathcal{M}|^2 \rangle = 128G_{\text{F}}^2 (p_{\nu_\mu} \cdot p_{e^+}) (p_{\mu^+} \cdot p_{\nu_e}). \quad (4.20)$$

In the limit of zero neutrino energy

$$(p_{\mu^+} \cdot p_{\nu_e}) = -m_\mu^2/2 + \mathcal{O}(E_{\nu_\mu}), \quad (4.21)$$

which implies that modulus squared is

$$\langle |\mathcal{M}|^2 \rangle = -64G_{\text{F}}^2 m_\mu^2 (p_{\nu_\mu} \cdot p_{e^+}) + \mathcal{O}(E_{\nu_\mu}). \quad (4.22)$$

Hence the cross section for the μ -neutrino, integrated over outgoing particles' directions, is

$$\sigma_{\nu_\mu} = \frac{G_F^2 m_\mu^2}{\pi} + \mathcal{O}(E_{\nu_\mu}). \quad (4.23)$$

Such non-zero limiting values are responsible for the rise in the *scaled* rates for soft neutrinos in Figs. 4.3 and 4.4

Thirdly, the hadronic opacities at low temperatures, i.e. $T < T_{\text{QCD}}$, exhibit a series of peaks. These are signatures of two-body fusions, which are broad resonances in the propagators of the weak gauge bosons. These include the production of pseudoscalar mesons (e.g. pion production via $\nu_\mu + \mu^+ \rightarrow \pi^+$) and vector mesons (e.g. ρ^0 production via $\nu_\mu + \bar{\nu}_\mu \rightarrow \rho^0$). In the total opacities of Figure 4.5a, the former is visible as a peak at intermediate momenta, while the latter are smeared out at large momenta.

Finally, we observe from Figure 4.5a that the total opacities at high energies exhibit a jump as the temperature passes through T_{QCD} . This is due to the increase in the number of hadronic degrees of freedom, as evidenced by the sizes of the jumps in hadronic- and leptonic contributions (the latter due to the tau lepton turning on).

This is shown clearly in Figure 4.5b, which shows the scaled muon neutrino opacities at high energies for a range of temperatures. Note that these rates assume that the hadronic species above and below the transition are free quarks and mesons, respectively (assumption # 3 in our list above). For comparison, the figure shows the number of relativistic degrees of freedom, g_* , both under this assumption and from Ref. [308], which implements the running of the strong coupling constant. We note the significant deviation close to the quark-hadron transition ($T_{\text{QCD}} = 210$ MeV in the lattice calculations underlying Ref. [308]).

Motivated by this, we explore two methods of interpolating opacities through the quark-hadron transition. In each of them, we choose a cutoff temperature, T_c , above which we use the free quark results, and use a cubic spline interpolation in between. We emphasize that this is not physically motivated; the actual rates and their matrix elements need to incorporate the strong coupling constant and its running. The figure shows interpolations with $T_c = 250$ MeV and 1000 MeV, which we expect to bracket the range of rates.

With this caveat, Figs. 4.6a and 4.6b show interpolated μ neutrino opacities for a range of energies and temperatures, with $T_c = 250$ MeV and 1000 MeV, respectively. In the rest of this work, we use these scattering rates and the potentials defined in Section 2.2 to study sterile neutrino production via oscillation in the early universe. We use both interpolations through the quark-hadron transition in order to illustrate the results' sensitivity to the scattering rates.

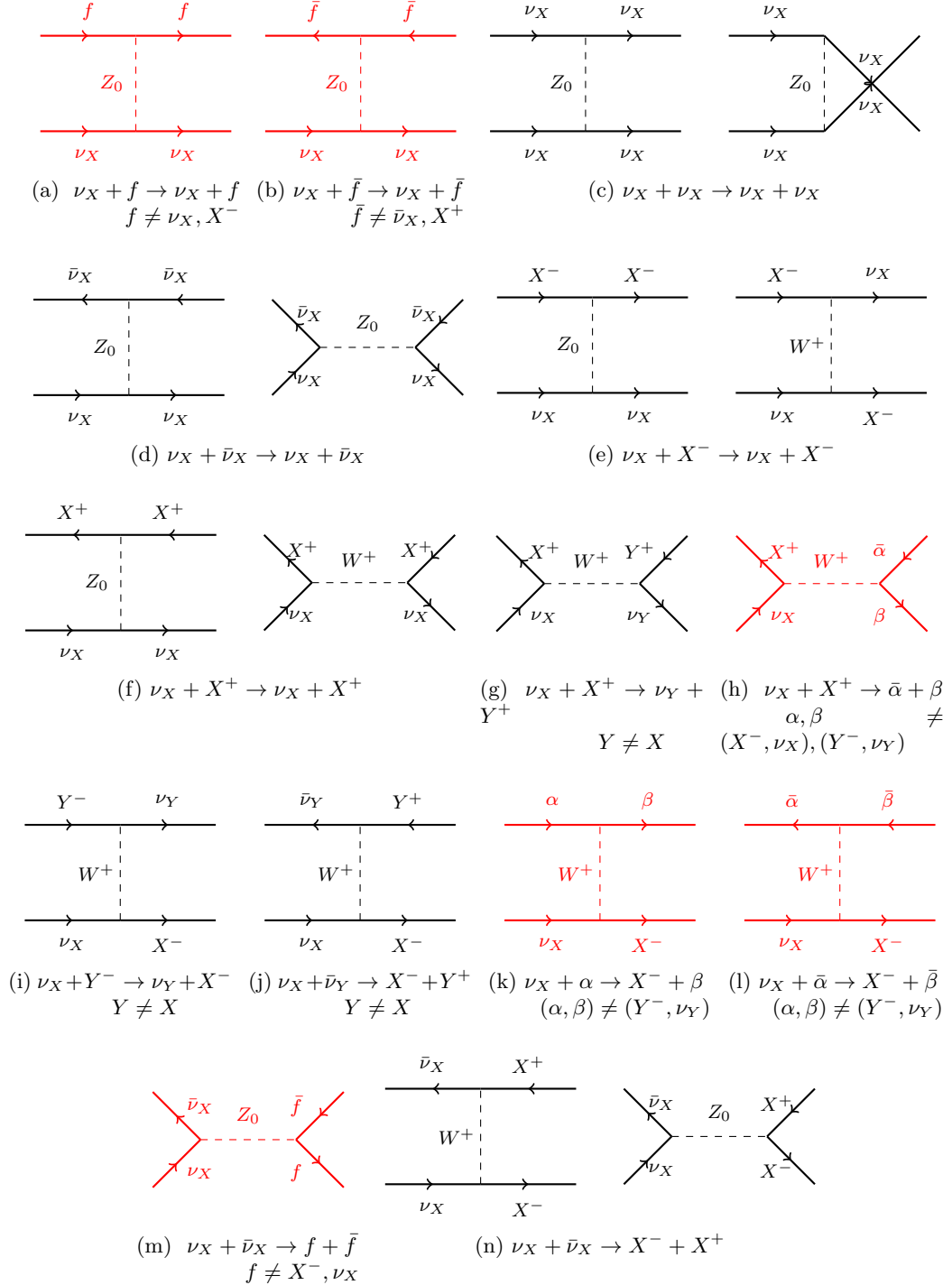


Figure 4.1: Tree-level processes with two fermions in the initial and final states, which contribute to the opacity of a neutrino ν_X . Diagrams for processes that can involve hadronic degrees of freedom are colored red to distinguish them.

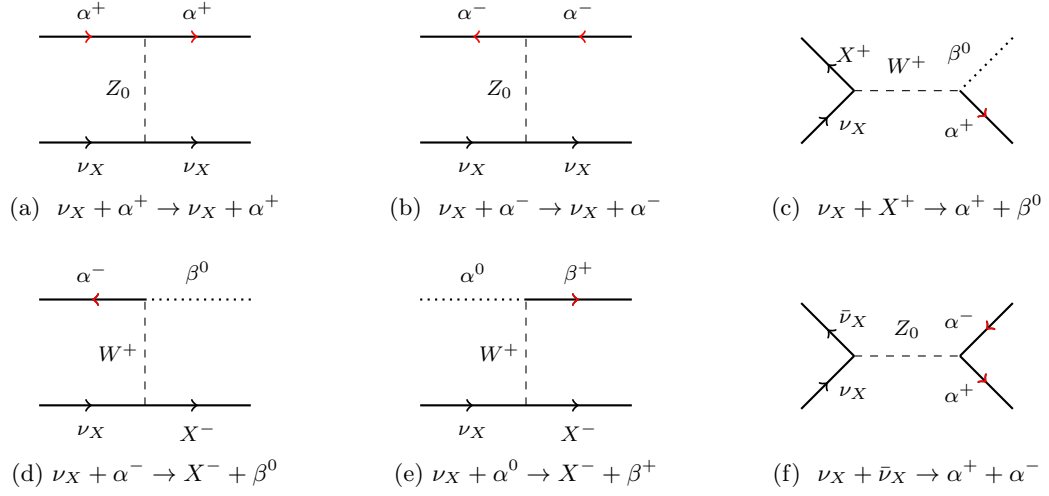


Figure 4.2: Interactions of an incoming neutrino ν_X involving mesons, with only terms upto $O(p^2)$ in 3χ PT. The charge of the meson is shown with a red arrow.

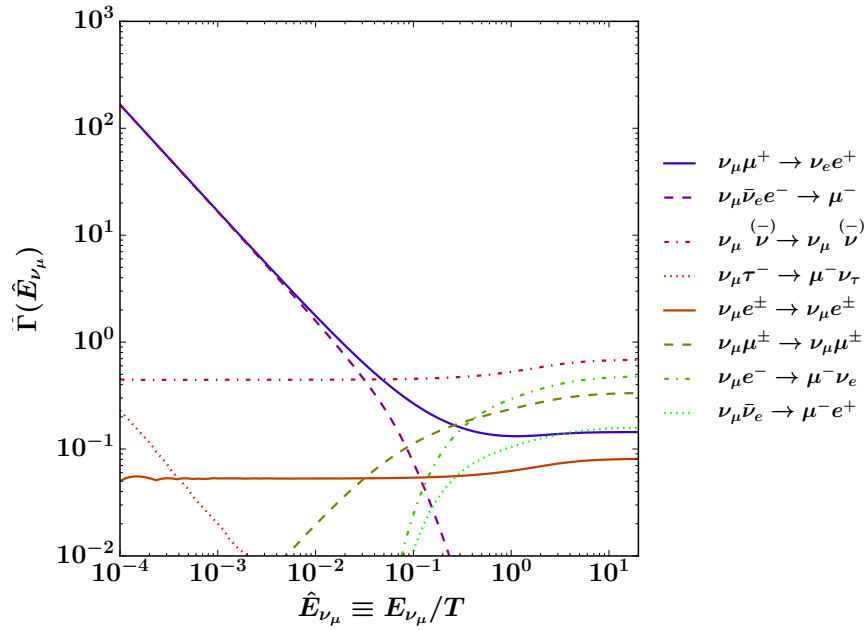


Figure 4.3: Scaled muon neutrino opacities through leptonic reactions, vs energy at $T = 100$ MeV. Only reactions in the top five at any particular momentum bin are shown. The symbol $\bar{\nu}^{(-)}$ stands for $\nu/\bar{\nu}$.

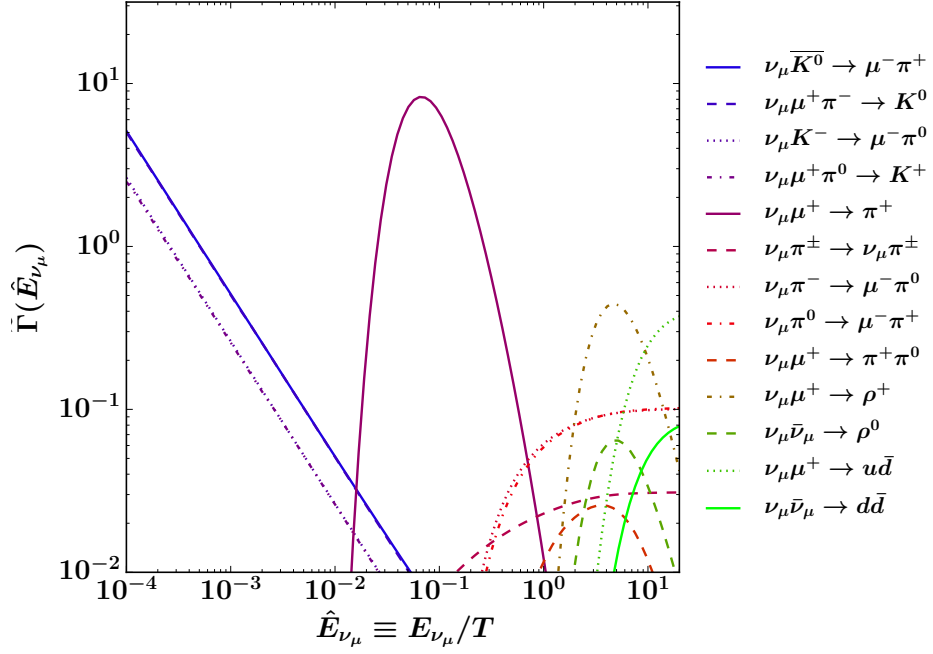
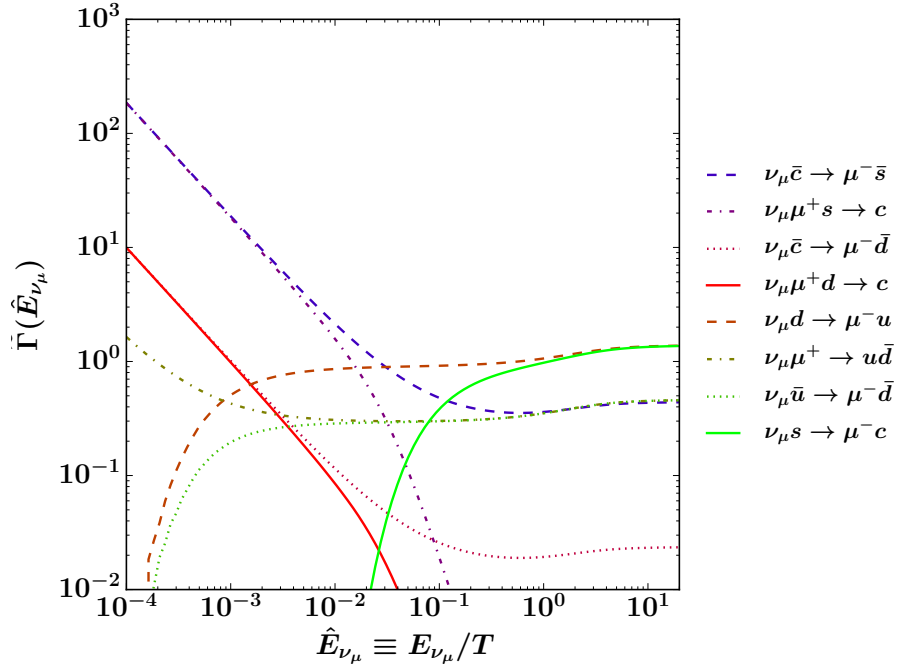
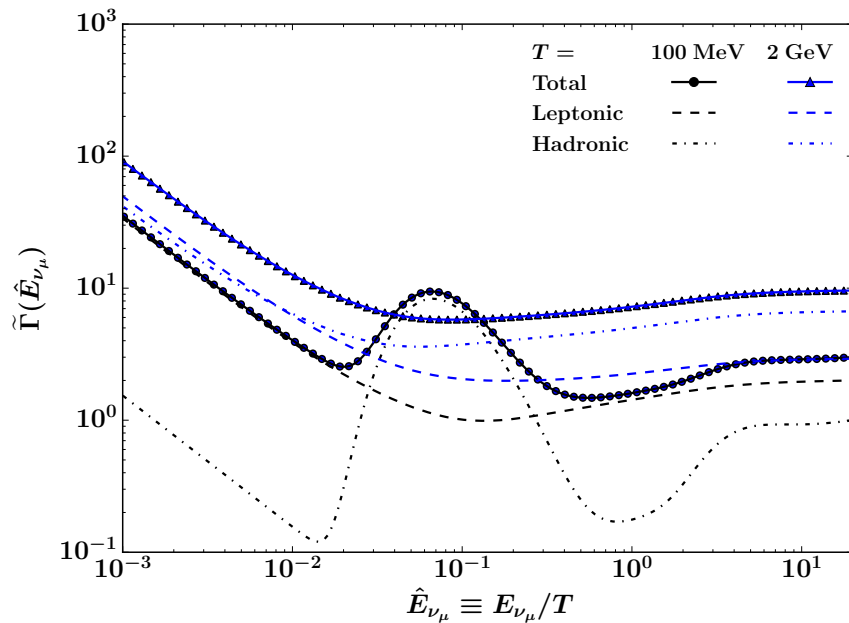
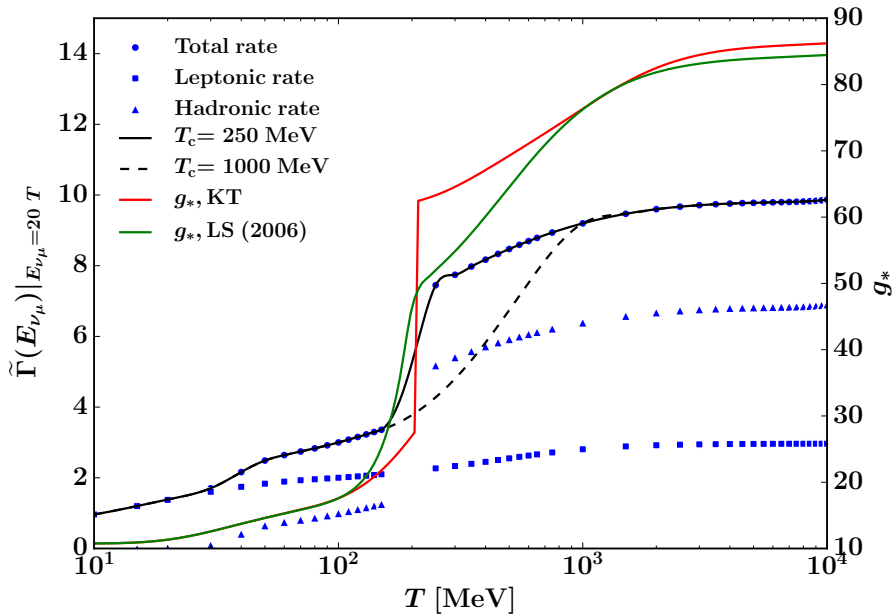
(a) $T = 100$ MeV(b) $T = 2$ GeV

Figure 4.4: Scaled muon neutrino opacities through hadronic reactions, vs energy: panels (a) and (b) show rates at $T = 100$ MeV and 2 GeV, respectively. Only reactions in the top five at any particular momentum bin are shown.



(a) rates vs energy



(b) rates vs temperature

Figure 4.5: Scaled muon neutrino opacities: panel (a) shows total, leptonic, and hadronic opacities vs energy at $T = 100$ MeV and 2 GeV. Panel (b) shows opacities at high energies ($E_{\nu_\mu} = 20T$) vs temperature: black lines are two interpolations through T_{QCD} . They are cubic splines labeled by their cutoff temperature, T_c , as defined in the text. Colored lines are numbers of relativistic degrees of freedom: g_* , KT under assumption # 3, i.e., that of Kolb and Turner [46] with $T_{\text{QCD}} = 210$ MeV, chosen to match Ref. [308], whose results are g_* , LS(2006).

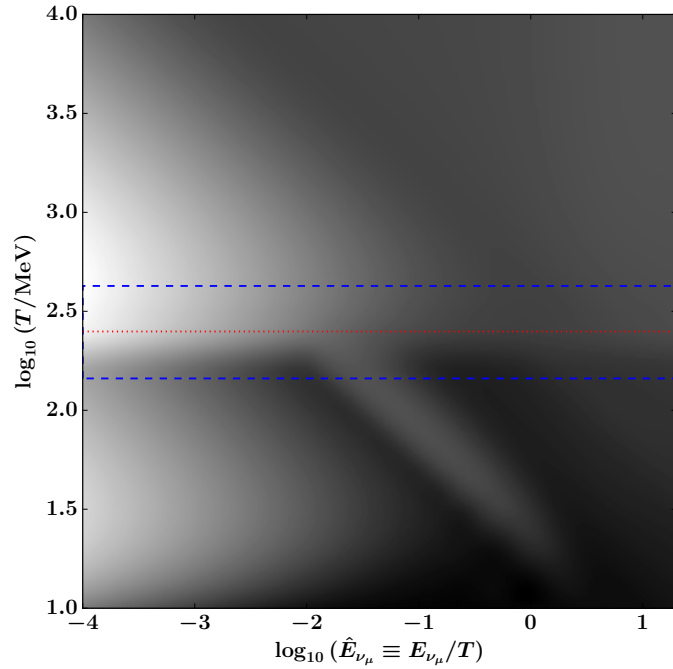
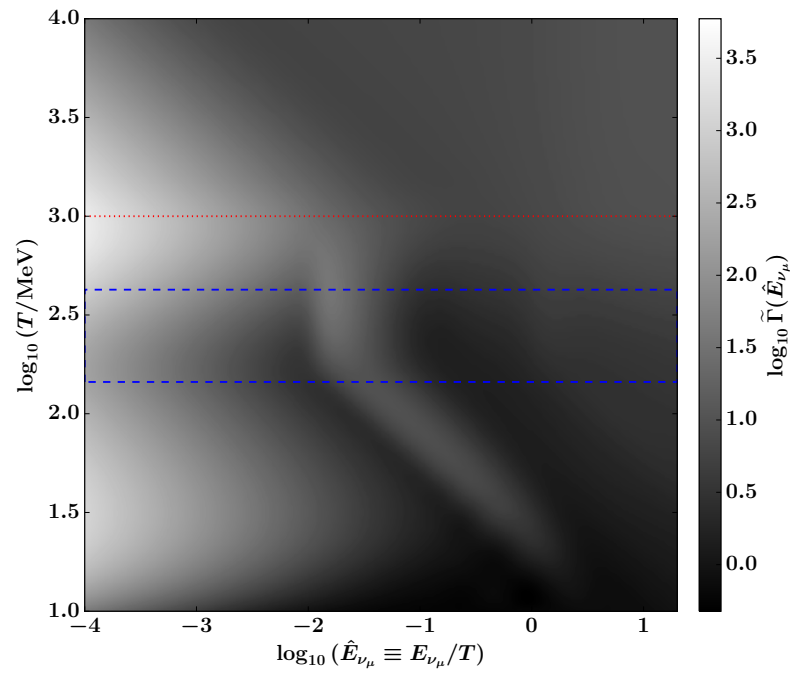
(a) $T_c = 250$ MeV(b) $T_c = 1000$ MeV

Figure 4.6: Scaled muon neutrino opacities for a range of energies and temperatures. Panels (a) and (b) show two interpolations for opacity vs energy and temperature. They are bicubic splines, and the red lines label the cutoff temperatures, T_c , as defined in the text. Blue dashed lines mark ranges where the values of g_* in Ref. [46] and [308] differ by more than 10%, and are a rough guide to where these rates can be trusted.

Chapter 5

Sterile neutrino dark matter distribution

5.1 Sterile neutrino production

In this section, we incorporate the standard model calculations of Chapters 3 and 4 into the sterile neutrino production mechanism, whose broad outline we provided in Section 2.2.

We evolve the sterile neutrino and anti-neutrino PSDs, $f_{\nu_s}(p)$ and $f_{\bar{\nu}_s}(p)$, using the Boltzmann equation of Eq. (2.8). We use the primordial plasma's temperature T as a clock, and numerically integrate a thousand logarithmically spaced Lagrangian momentum bins from a temperature of 10 GeV down to 10 MeV. For the models illustrated by stars in Figure 2.1, the vast majority of the production happens between these temperatures. We use the muon neutrino opacities derived in Chapter 4 and provide results using the two interpolation schemes presented in Figure 4.6, which bracket the range of uncertainties due to the quark-hadron transition. We use Eq. (2.12b) for the thermal potential $V_{\nu_\mu}^{\text{th}}$, and the results presented in Figure 3.2 for the asymmetry potential $V_{\nu_\mu}^{\text{L}}$ incorporating the redistribution of Chapter 3.

In order to close the system of equations, we also need the evolution of the plasma temperature T and mu leptonic asymmetry $\hat{\mathcal{L}}_\mu$ with coordinate time t . Before discussing the details of the sterile neutrino production, we briefly review these two relations.

5.1.1 Time-temperature relation

In this subsection, we derive the time-temperature relationship prior to the epoch of weak decoupling. The Hubble rate, H , is

$$\frac{d}{dt} \ln a = H = \sqrt{\frac{8\pi}{3m_{\text{P}}^2}(\rho_{\text{SM}} + \rho_{\nu_s})}, \quad (5.1)$$

where a is the scale factor, $m_{\text{P}} = 1.2 \times 10^{19}$ GeV is the Planck mass, and ρ_{SM} and ρ_{ν_s} are energy densities in standard model particles and sterile neutrinos, respectively. The latter is given by an

integral over the PSDs, $\rho_{\nu_s} = (1/2\pi^2) \int p^2 dp \sqrt{p^2 + m_s^2} [f_{\nu_s}(p) + f_{\bar{\nu}_s}(p)]$. During Hubble expansion from a to $a + \delta a$ a) the sterile neutrino PSDs evolve to $f_{\nu_s/\bar{\nu}_s}(p) + \delta f_{\nu_s/\bar{\nu}_s}(p)$ due to a combination of mixing with muon neutrinos, and their momentum redshifting as $pa \equiv \text{constant}$, and b) due to large neutrino opacities, all active species maintain equilibrium PSDs with a common temperature whose evolution is affected by the production of sterile neutrinos.

The continuity equation for the *total* stress-energy tensor is

$$3 \frac{d}{dT} \ln a = - \frac{d}{dT} (\rho_{\text{SM}} + \rho_{\nu_s}) (\rho_{\text{SM}} + P_{\text{SM}} + \rho_{\nu_s} + P_{\nu_s})^{-1}, \quad (5.2)$$

where P_{SM/ν_s} are SM and sterile neutrino pressures, respectively. The sterile energy density evolves according to

$$\frac{d\rho_{\nu_s}}{dT} = \frac{\partial \rho_{\nu_s}}{\partial \ln a} \frac{d \ln a}{dT} + \frac{\partial \rho_{\nu_s}}{\partial t} \frac{dt}{dT}. \quad (5.3)$$

The two terms on the right-hand side are the free-streaming and oscillation contributions, respectively.

$$\frac{\partial \rho_{\nu_s}}{\partial \ln a} = -3(\rho_{\nu_s} + P_{\nu_s}), \quad (5.4)$$

$$\frac{\partial \rho_{\nu_s}}{\partial t} = \int \frac{dp}{2\pi^2} p^2 \sqrt{p^2 + m_s^2} \frac{\partial}{\partial t} [f_{\nu_s}(p) + f_{\bar{\nu}_s}(p)]. \quad (5.5)$$

We substitute Eqs. (5.3) and (5.4) into Eq. (5.2) and solve for the relation between the scale factor and temperature

$$3 \frac{d \ln a}{dT} = - \left(\frac{d\rho_{\text{SM}}}{dT} + \frac{\partial \rho_{\nu_s}}{\partial t} \frac{dt}{dT} \right) (\rho_{\text{SM}} + P_{\text{SM}})^{-1}. \quad (5.6)$$

Substituting Eq. (5.1), we obtain the time-temperature relation¹

$$\frac{dT}{dt} = - \frac{3H[\rho_{\text{SM}} + P_{\text{SM}}] + (\partial \rho_{\nu_s} / \partial t)}{d\rho_{\text{SM}}/dT}. \quad (5.7)$$

Defining the number of SM relativistic degrees of freedom for the energy and entropy densities via

$$\rho_{\text{SM}} = \frac{\pi^2}{30} g_* T^4, \quad (5.8)$$

$$s_{\text{SM}} = \frac{\rho_{\text{SM}} + P_{\text{SM}}}{T} = \frac{2\pi^2}{45} g_{*,s} T^3, \quad (5.9)$$

¹We note that we correct here an error introduced in Ref. [137].

we have the final form of the time-temperature relation

$$\frac{dT}{dt} = -\frac{4Hg_{*,s}T^4 + (30/\pi^2)(\partial\rho_{\nu_s}/\partial t)}{d[g_*T^4]/dT}. \quad (5.10)$$

We use numbers of relativistic degrees of freedom g_* and $g_{*,s}$ from Ref. [308] in our numerical implementation.

5.1.2 Time-evolution of asymmetry

The temperature-scaled muon asymmetry, $\hat{\mathcal{L}}_\mu$, evolves both from the depletion of relativistic degrees of freedom due to annihilations and from the production of sterile neutrinos. There are subtleties in dealing with the latter in the case of resonant production [317], but for the semi-classical approach outlined in Section 2.2.2, we can write down the contribution in terms of the evolution of sterile neutrino PSD. Keeping in mind the definition of the lepton asymmetry in Eq. (2.4), the asymmetry evolution due to both contributions together is

$$\begin{aligned} \frac{d\hat{\mathcal{L}}_\mu}{dt} &= \frac{d}{dt} \int \frac{d\hat{p} \hat{p}^2}{2\pi^2} [f_{\nu_\mu}(p) - f_{\bar{\nu}_\mu}(p) + 2f_{\mu^-}(p) - 2f_{\mu^+}(p)] \\ &= -3 \left[H + \frac{d \ln T}{dt} \right] \hat{\mathcal{L}}_\mu - \int \frac{d\hat{p} \hat{p}^2}{2\pi^2} \frac{\partial}{\partial t} [f_{\nu_s}(p) - f_{\bar{\nu}_s}(p)], \end{aligned} \quad (5.11)$$

where the symbol \hat{p} is the temperature-scaled momentum, $\hat{p} \equiv p/T$. The first term in the square bracket in the last line above can be evaluated with the help of Eqs. (5.1) and (5.10), while the second term can be evaluated using Eq. (2.8). Our large number of momentum bins (1000) allows us to use spline integration at every time step in order to perform the momentum integrals in Eqs. (5.11) and (5.5). We set up our Lagrangian momentum bins such that $5 \times 10^{-3} \leq p/T \leq 20$ at temperature $T = 10$ GeV. We have checked that this range is more than sufficient to accurately capture the most relevant range of the sterile neutrino PSDs.

5.1.3 Resonant Production

As described in Section 2.2, the presence of a lepton asymmetry leads to a resonant production of sterile neutrinos with specific momenta. Through Eq. (2.8), the resonant momenta at a particular temperature satisfy

$$\Delta(p) \cos 2\theta - V^L - V^{\text{th}}(p) = 0. \quad (5.12)$$

Substituting the definition of $\Delta(p)$ and the potentials from Eq. (2.12), we obtain

$$\frac{m_s^2}{2p} - \frac{dV^L}{d\mathcal{L}_\mu} \mathcal{L}_\mu - \frac{dV^{\text{th}}(p)}{dp} p = 0. \quad (5.13)$$

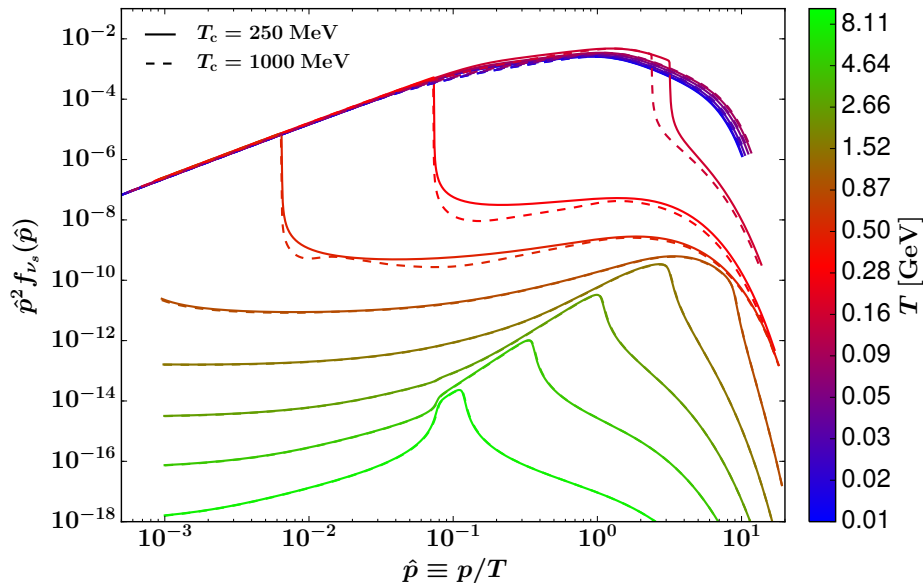
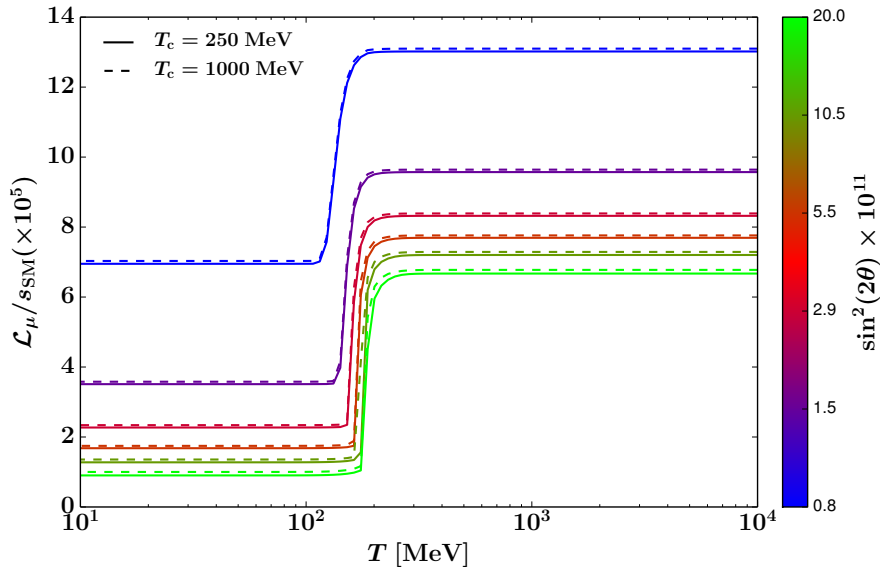


Figure 5.1: We illustrate the temperature-evolution of the sterile neutrino’s PSD for the central model of Figure 2.1 with $(m_s, \sin^2 2\theta) = (7.1 \text{ keV}, 4 \times 10^{-11})$. Solid and dashed lines distinguish results with neutrino opacities from Figure 4.6a and 4.6b, respectively.

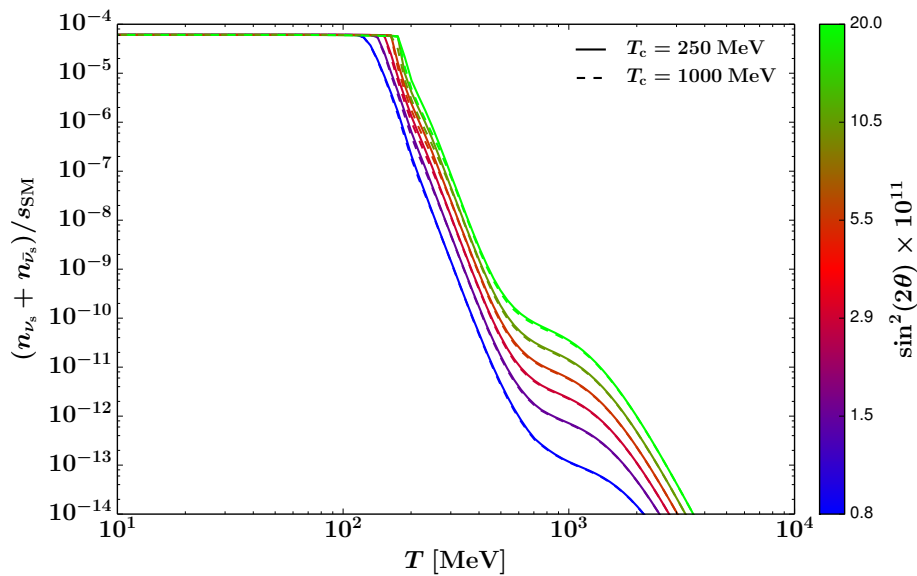
There are two roots, i.e. two momenta resonant at any temperature [137]. Consideration of the terms’ approximate temperature scaling shows that each scaled root ($\hat{p} \equiv p/T$) sweeps to larger values at lower temperatures (ignoring changes in the numbers of relativistic degrees of freedom). This is reflected in Figure 5.1, which shows the sterile neutrino PSD’s evolution with temperature for the central model in Figure 2.1 with $m_s = 7.1 \text{ keV}$ and $\sin^2 2\theta = 4 \times 10^{-11}$. We observe that most of the neutrinos are produced at the lower resonance and at temperatures close to T_{QCD} . This is illustrated by Figs. 5.2a and 5.2b, which show the evolution of the entropy-scaled² μ lepton asymmetry and the net sterile neutrino and antineutrino density for the range of models marked by stars in Figure 2.1. The latter is also sensitive to thermal (nonresonant) production, which operates at all temperatures, but is subdominant for the mixing angles of interest.

Figures 5.3a and 5.3b show the sterile neutrino and antineutrino PSDs at $T = 10 \text{ MeV}$ for these models. We note that the sterile antineutrinos are produced off-resonance for the positive lepton asymmetries we consider here, and their abundance is thus significantly suppressed compared to that of the sterile neutrinos. Solid and dashed lines in Figure 5.3 show results for the two interpolations of the μ neutrino opacities through T_{QCD} presented in Figure 4.6, which differ in the temperature range $150 \text{ MeV} < T < 1 \text{ GeV}$. For small values of the mixing angle, we observe that there is little difference between the PSDs computed using our two different interpolation schemes for the neutrino opacity. For these models, most of the production happens at temperatures below the quark-hadron

²We show this scaling rather than the one with temperature, since it is conserved through epochs of annihilation.



(a) mu lepton asymmetry



(b) net sterile density

Figure 5.2: Sterile neutrino production mechanism: panels (a) and (b) show the evolution of the entropy scaled mu lepton asymmetry and the net sterile number density with temperature. For each model with a given mass and mixing angle, the mu lepton asymmetry at high temperatures is tuned by hand to produce the right relic abundance. Colors differentiate models in Figure 2.1, and solid and dashed lines distinguish results with neutrino opacities from Figure 4.6a and 4.6b, respectively.

transition where our two opacity approximation schemes are essentially the same, hence leading to similar PSDs. As the mixing angle is increased, the production is pushed toward higher temperatures (see Figure 5.2b) where the difference between our two interpolation schemes is greater, leading to a larger uncertainties in the final PSDs.

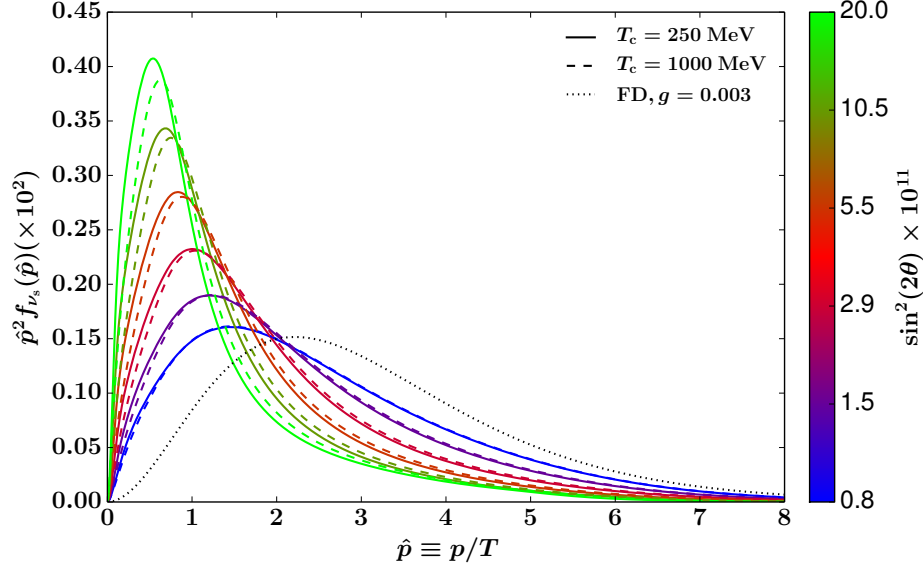
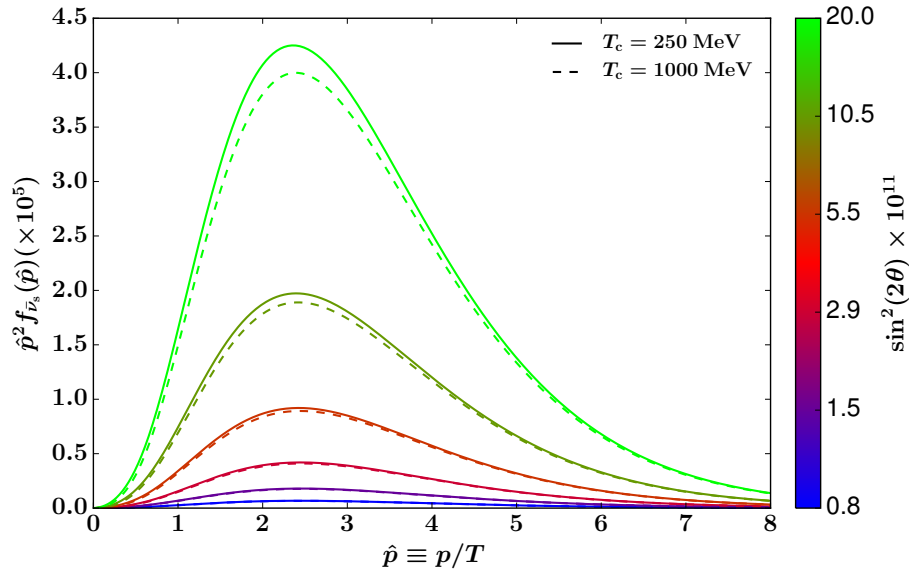
(a) sterile neutrino PSDs at $T = 10$ MeV(b) sterile antineutrino PSDs at $T = 10$ MeV

Figure 5.3: Sterile neutrino production mechanism: panels (a) and (b) show sterile neutrino and antineutrino PSDs, respectively, at $T = 10$ MeV. Colors differentiate models in Figure 2.1, and solid and dashed lines distinguish results with neutrino opacities from Figure 4.6a and 4.6b, respectively. Note the different numerical factors multiplying the y-axis of panels (b) and (d). The dotted line in panel (b) is a massless Fermi-Dirac distribution with degeneracy $g = 0.003$.

Table 5.1 lists parameters describing the production and final sterile neutrino DM PSDs for the models marked in Figure 2.1. Also provided are the ranges for different interpolated μ neutrino opacities through the quark-hadron transition as in Figure 4.6. Note that the sterile PSDs in Figs. 5.3a and 5.3b are non-thermal; we show the mean momentum $\langle p/T \rangle$ relative to the active

Table 5.1: Parameters for the models marked in Figure 2.1, with $m_s = 7.1$ keV and $\Omega_{\text{DM}}h^2 = 0.119$ [42]. The ranges displayed in the three last columns account for the uncertainties in the neutrino opacities near the quark-hadron transition.

$\sin^2 2\theta$	$(\mathcal{L}_\mu/s_{\text{SM}})_i$	$(\mathcal{L}_\mu/s_{\text{SM}})_f$	$\langle p/T \rangle^3$
$\times 10^{-11}$	at $T = 10$ GeV	at $T = 10$ MeV	
	$\times 10^{-5}$	$\times 10^{-5}$	
0.800	13.0 – 13.1	6.95 – 7.03	2.60 – 2.61
1.104	10.80 – 10.88	4.74 – 4.81	2.45 – 2.47
1.523	9.57 – 9.64	3.51 – 3.58	2.28 – 2.32
2.101	8.81 – 8.88	2.76 – 2.83	2.12 – 2.16
2.899	8.32 – 8.39	2.27 – 2.34	1.95 – 2.01
4.000	7.96 – 8.03	1.93 – 2.00	1.80 – 1.87
5.519	7.69 – 7.76	1.68 – 1.74	1.66 – 1.74
7.615	7.45 – 7.53	1.47 – 1.54	1.53 – 1.62
10.506	7.20 – 7.29	1.28 – 1.36	1.43 – 1.52
14.496	6.95 – 7.05	1.09 – 1.18	1.35 – 1.44
20.000	6.7 – 6.8	0.9 – 1.0	1.29 – 1.38

neutrino temperature scale.

A key element to take away from Table 5.1 and Figs. 5.3a and 5.3b is that the ‘warmer’ models with larger values of $\langle p/T \rangle$ are less sensitive to the uncertainty in the quark-hadron transition. This is important since these warmer models can be most easily constrained by small-scale structure formation. Therefore, uncertainties in the strong plasma near T_{QCD} are unlikely to affect the robustness of these constraints.

5.2 Transfer functions for matter fluctuations

In this section, we study the effect of sterile neutrinos on the growth of density fluctuations in the early universe. We focus on the lepton asymmetry-driven mechanism outlined in Section 2.2, and on modes of the matter distribution with co-moving wavenumbers $k \in [1, 100] h \text{Mpc}^{-1}$. These scales are probed by the Lyman- α forest in quasar spectra (see [318] and references therein), and populations of dwarf galaxies in the Local Group (see [319, 320] and references therein). All these scales enter the horizon after the redshift $z_{\text{H}} \simeq 4 \times 10^7$, when the temperature of the photon-baryon plasma is $T \simeq 10$ keV. The sterile neutrino models shown in Figure 2.1 cease to be produced below temperatures $T \sim 100$ MeV; hence we can assume they are essentially collisionless in this section.

The main effect of such a collisionless component on matter fluctuations is suppression due to free-streaming in the epochs where it is relativistic [155, 156]. Previous works extensively studied this in the context of warm and/or neutrino DM models (see Refs. [107, 157] and references therein), and identified the characteristic scales at which the suppression set in as a function of the neutrinos’

³The sterile DM distributions are non-thermal; we compute $\langle p/T \rangle$ using the active neutrino temperature. Below the epoch of e^\pm annihilation, the latter is related to the CMB temperature by the factor $(4/11)^{1/3} = 0.714$. We note that for a Fermi-Dirac distribution $\langle p/T \rangle \simeq 3.15$.

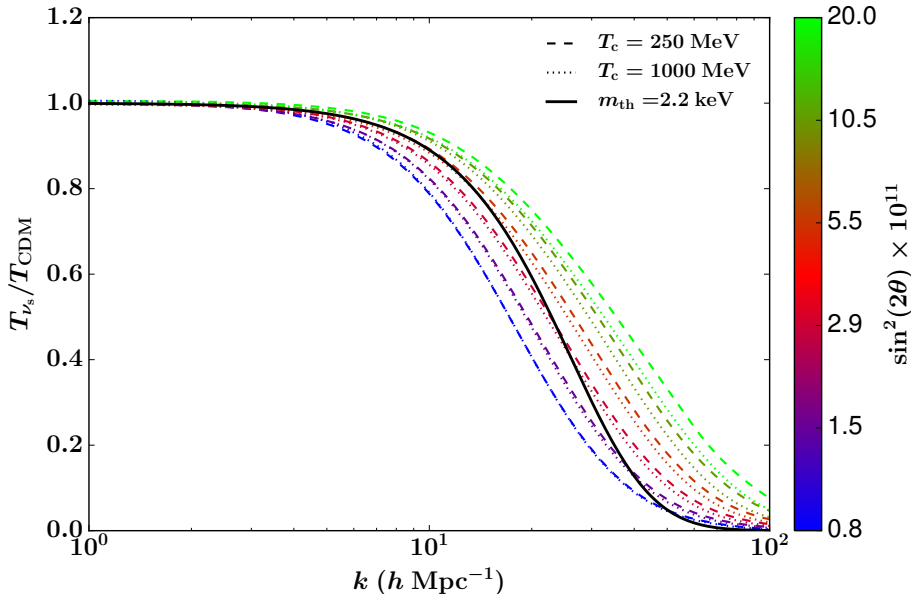


Figure 5.4: Suppression of the transfer functions of overall density fluctuations relative to the Λ CDM ones for sterile neutrino models in Figure 2.1, as a function of wavenumber. Dashed and dotted lines show results for the interpolated μ neutrino scattering rates of Figs. 4.6a and 4.6b, respectively. The solid black line is the numerical fit for a thermal warm DM transfer function as given in Ref. [159].

mass and mean momentum [137].

In order to obtain the suppression’s detailed form, we need to incorporate the PSDs of the sterile neutrinos and antineutrinos into the Boltzmann equation for the DM component. This entails solving a perturbed form of Eq. (2.8), with additional terms due to inhomogeneities, but without the source (production) terms. The scales of interest are non-linear in the current epoch, but we only provide the linear transfer functions at $z = 0$, which can be used as initial conditions for cosmological N-body simulations.

We use the publicly available CLASS solver [290] to integrate the perturbed linear Boltzmann equation⁴. We initiate the solver with the Planck background parameters [80], except with the CDM component replaced by collisionless components with PSDs as shown in Figs. 5.3a and 5.3b. Since we are interested in the detailed shape of the transfer function, we turn off the default fluid approximation for non-cold relics [322].

Figure 5.4 shows the resulting suppression as a function of the comoving wavenumber. We illustrate the suppression in the fluctuations’ transfer functions relative to their values in Λ CDM. Also shown is the commonly-used fit to a thermal warm DM transfer function given in Refs. [158, 159] with an ‘equivalent thermal mass’ of $m_{\text{th}} = 2.2$ keV; fits for models marked with stars in Figure 2.1 have a range of 1.6 to 3.2 keV.

⁴Our choice was motivated by the availability of well-documented modules to deal with non-cold relics. We have checked our results against those obtained from a modified version of the publicly available CAMB solver [321].

However, the strong difference in shape with the thermal WDM transfer function warrants use of the exact sterile neutrino dark matter transfer functions. The thermal warm DM PSDs relevant to the fit are rescaled versions of the Fermi-Dirac distribution; as can be seen from Figure 5.3a, the resonantly-produced DM's PSD has an excess at low momenta that cannot be reproduced by such a rescaling. Hence, our DM transfer functions do not exhibit the fits' steep $\sim k^{-10}$ dependence at large wavenumbers and the resultant severe suppression of power on small scales. This indicates that the models considered in the present work are more likely to be in agreement with small-scale structure formation constraints, as recently pointed out in Refs. [146–151, 154].

5.3 Discussion and conclusions

Sterile neutrinos are a well-motivated extension of the standard model of particle physics, and offer a promising candidate for the inferred DM population of the Universe. In this work, we performed a detailed study of the resonant production of sterile neutrinos with masses and mixing angles relevant to the recent X-ray excess. In doing so, we explored the rich phenomenology associated with the active neutrinos' weak interaction with the primordial plasma. These interactions efficiently redistribute primordial lepton asymmetries among all the available degrees of freedom, and impact the temperature and momentum dependence of neutrino opacities. We incorporated these effects into the sterile production calculation, corrected and extended the existing numerical implementation, and obtained revised DM phase space densities. We finally computed transfer functions for fluctuations in the matter density, which can be used as starting points for N -body simulations of cosmological structure formation.

For the parameters relevant to the X-ray excess, resonant sterile neutrino production coincidentally occurs in the vicinity of the quark-hadron transition (see Figure 5.2b). Strongly interacting degrees of freedom affect the production in two ways: a) they influence both asymmetry redistribution and neutrino opacities through their interaction with the weak gauge bosons (Z and W^\pm), and b) the transition from free quarks to hadrons at T_{QCD} influences the time-temperature relation [Eq. (5.10)]. We now consider the robustness of each of these elements to the remaining uncertainties in the quark-hadron transition.

The asymmetry redistribution among the strongly-interacting degrees of freedom depends on the susceptibility of the quark-hadron plasma to baryon number and electric charge fluctuations. At high temperatures, we use tree-level perturbative QCD to compute the susceptibilities. There are uncertainties concerning the exact values of the quark masses, loop corrections, and the exact implementation of the $\overline{\text{MS}}$ renormalization scheme. We expect these to have little effect on the final sterile neutrino PSDs since the bulk of the production occurs at lower temperatures, where the lattice QCD- and HRG-derived susceptibilities are most relevant. Thus, uncertainties in the asymmetry

redistribution are likely dominated by systematic errors in the lattice calculations [309], measurement errors in the hadronic resonances' masses, and inaccuracies inherent in the HRG approach near the quark-hadron transition. Our confidence in the fit we use in this work is bolstered by the fact that a) an independent lattice QCD calculation [310] finds very similar susceptibilities to those we used, and b) the HRG approach – without any free parameters – is in very good agreement with the lattice calculation for $T \lesssim 150$ MeV. It is therefore unlikely that uncertainties in the susceptibilities will lead to dramatic changes in the sterile neutrino PSDs.

The validity of our neutrino opacities is much less clear: we have attempted to calculate them in as much detail as possible, but the hadronic parts still retain significant uncertainties due to the quark-hadron transition. We expect that opacities at high and low temperatures are well described by the rates of reactions involving free-quarks, and the lightest pseudoscalar and vector mesons, which are shown in Chapter 4. For temperatures near T_{QCD} , we have considered two interpolation schemes (shown in Figure 4.6) that we expect might bracket the range of possibilities. We have computed the sterile neutrino PSDs for both cases and shown that they are fairly robust to the choice used, especially for models with larger values of the average momentum $\langle p/T \rangle$. We leave the calculation of self-consistent opacities through the transition to future work. Yet another approximation we have made is that of equilibrium distributions for all active species, which has been studied in a different context in Ref. [323]. We expect this to be valid at the temperatures relevant to the models we study.

To compute the Hubble expansion rate and time-temperature relation, we have used the plasma's equations of state provided in Ref. [308], which are obtained by matching to the lattice QCD results of [324]. As the former's authors point out, this result is still uncertain at temperatures close to the quark-hadron transition. It would be interesting to update their result with the latest lattice QCD computations, which suggest a lower transition temperature [325]. We expect the uncertainties associated with the plasma's equation of state to be at most similar in magnitude to those coming from the neutrino opacity [243].

Another simplification we adopted is the semi-classical Boltzmann equation, which greatly facilitates our study of the oscillation-driven production. As mentioned in Section 2.2.2, the most general analysis considers the evolution of a two-state density matrix, rather than phase-space densities. The validity of the semi-classical approach rests on the assumption that collisions dominate the off-diagonal element of the Hamiltonian that is responsible for vacuum oscillations [299–301]. For typical momenta at the temperatures of interest, the ratio of these terms is $\Delta(T) \sin^2 2\theta / D(T) \simeq 0.6 \times (T/100 \text{ MeV})^{-6} (m_s/7\text{keV})^2 (\sin^2 2\theta/10^{-11})^{1/2}$. The production of sterile neutrinos happens at temperatures above, but close to where these terms become comparable (note the ratio's steep temperature dependence). Thus, we expect that the results in this work are relatively unaffected by this approximation, but further work in this direction can settle this question.

Finally, we examine the assumptions underlying the model itself, which were enumerated in Section 2.2.1. If there is indeed an extra neutrino that is an electroweak singlet, it is not restricted to mix with only one flavor. However, the general case where the sterile neutrino mixes with all flavors introduces extra mixing angles, which cannot be constrained as easily from observations. The same can be said about the assumption of a lepton asymmetry in a single flavor. We briefly remark on the possibility of the sterile neutrinos mixing with electron or tau flavors instead. The redistribution of Chapter 3 is almost identical for the cases with electronic and muonic lepton asymmetries, but is different in the tauonic case. This is due to the significantly larger mass of the corresponding charged lepton ($m_\tau = 1.77$ GeV [229]), which is annihilated away at higher temperatures. Thus most of an input tau asymmetry ends up in the tau neutrino below $T \lesssim 400$ MeV, and the quark hadron transition does not impact the redistribution. The electron and tau neutrino opacities are different from the muonic case, and so is the balance between the thermal and asymmetry potentials, which affects the resonant momenta and ultimately the final dark matter PSDs – we leave for future work the possibility of sterile neutrinos mixing with those flavors.

Also worth considering is active–active neutrino mixing, which does not conserve asymmetries in the individual flavors. This was studied in Ref. [294], which showed that such asymmetries are frozen in at the temperatures of interest. An interesting possibility is to revisit this study and use the redistributed asymmetries of Chapter 3 to calculate the active neutrino self energies at this epoch.

In conclusion, we find remarkable that sterile neutrino models that are in agreement with the X-ray excess have transfer function shapes that can significantly impact structure formation on sub-galactic scales. Fixing the leptonic asymmetry to produce the right DM relic density, the resonantly-produced sterile neutrino transfer function goes from ‘warm’ to ‘cold’ as the mixing angle is increased from small to large values. This indicates that upcoming X-ray observations [326, 327] and ongoing efforts to study small-scale structure can together cover all of the allowed mixing angle parameter space, and consequently confirm or disfavor the model.

Part II

Small-scale baryon perturbations during cosmological recombination

Chapter 6

Preliminaries¹

6.1 Introduction

The early universe is largely composed of atomic matter, or baryons, radiation and cold dark matter. The main resources available to study this era are the Cosmic Microwave Background (CMB) and Large Scale Structure (LSS). Primary anisotropies of the CMB are a result of the imprint of primordial fluctuations on radiation at early times [328, 329], while secondary anisotropies probe the matter distribution at late times [330]. LSS surveys are a complementary probe of the clustering of matter at late times [331].

The distribution and dynamics of baryons during early epochs of the Universe is poorly constrained by this data. The angular distribution of power in the CMB constrains them on large scales, through their coupling with the radiation and its effect on the Baryon Acoustic Oscillations. The CMB is well-described by a spectrum of adiabatic fluctuations at these scales – these are motions of both the baryon and radiation fluids. Tight bounds exist on the primordial fluctuations of solely the baryon fluid at these scales – the so-called isocurvature modes [328].

This investigation deals with the complementary limit of fluctuations in the baryon field on very small scales. In the CMB, this information is lost due to diffusion damping of the anisotropies. The spectral distortion associated with diffusion damping has been suggested as a probe of modes on these small scales [173]. The proposed PRISM mission aims to study CMB spectral distortions [332].

In the rest of this work, we use the term “matter” to refer to baryons, for reasons of readability; we are not concerned with the dynamics of cold dark matter. We concentrate on small-scale fluctuations of the matter field, and their evolution through the epoch of recombination. In particular, we undertake a detailed study of an instability which can amplify sub-Jeans length fluctuations at recombination suggested by Shaviv [162]. The mechanism of interest is potentially applicable to wave numbers in the range $10^2 \lesssim k \lesssim 3 \times 10^5 \text{ Mpc}^{-1}$ comoving. This is at much smaller scales

¹The material in Chapters 6–7 was adapted from the paper *Stability of small-scale baryon perturbations during cosmological recombination*, Venumadhav, T., & Hirata, C. 2015, Phys. Rev. D, 91, 123009, and reproduced here with permission, copyright (2014) by the American Physical Society.

than the standing acoustic waves responsible for peaks in the CMB power spectrum and baryon acoustic oscillations in the matter power spectrum (e.g. [87, 333]), which are damped below the Silk scale [334] $k_{\text{Silk}} \sim 0.1 \text{ Mpc}^{-1}$. We expect the pre-recombination amplitudes of modes at $k \gg k_{\text{Silk}}$ to be extremely small, but if an instability is present then a “seed” amplitude could be generated by nonlinear generation of small-scale isocurvature modes [335], or even thermal fluctuations if the growth rate is fast enough.

Shaviv’s instability acts on sound waves propagating in a partially ionized gas, in the presence of a background flux of radiation. The scenario is illustrated in Figure 6.1. The key observation is that the fraction of ionized atoms is different in overdense and underdense regions; the ionization fraction, x_e , is lower in overdense regions where recombination proceeds faster due to the increased flux of free electrons seen by the ionized atoms.

Sound waves are propagating longitudinal waves in the matter fluid – if we orient ourselves along the wave-vector, \mathbf{k} , the local velocity at a compression is in the forward direction, while the opposite is true for rarefactions. Thus, the earlier observation leads to a negative correlation between the ionization fraction and the local velocity in the region of propagation.

In the presence of a background flux of radiation in the matter’s bulk rest-frame, the radiative force acting on a mass element is related to the radiation flux, or alternatively its velocity \mathbf{v}_γ , by the opacity, which is proportional in turn to the ionization fraction, x_e . Over a time-period of the sound wave, the resulting force per unit mass \mathbf{a} performs an amount of work Δw given by

$$\Delta w = \oint \mathbf{a} \cdot d\mathbf{r} \sim \frac{u_\gamma \sigma}{m_H c} \mathbf{v}_\gamma \cdot \oint x_e d\mathbf{r}, \quad (6.1)$$

where in the second equation, the multiplicative factor involving the energy density of the radiation (u_γ), its interaction cross section with matter (σ), the particle mass (the hydrogen mass m_H) and the speed of light c relates the force per unit mass to the ionization fraction. The net work done over a time period is nonzero due to the difference in ionization fractions during the forward and backward motion. From consideration of Figure 6.1, the work integral of Eq. (6.1) is positive if the flux, \mathbf{v}_γ , is directed opposite to the wavevector, \mathbf{k} .

The first estimate of the growth rates due to this mechanism, due to Shaviv [162], used the assumption of local thermal equilibrium (LTE) to derive the variations in the ionization fraction. Recombination in the real universe proceeds out of LTE, and most of the hydrogen first recombines to excited states before reaching the ground state [83, 84, 165–167, 169, 170, 336]. Subsequent work [163, 164] used the three level approximation to model non-LTE recombination, and incorporated the diffusion of microwave background photons, following which the expected growth rates were revised downward.

The standard treatment of recombination assumes that the ionization state is set by the local

radiation field. This is valid in the homogenous case, since the transport of photons out of the region of interest is perfectly balanced by the influx from other regions. This is no longer true in the inhomogenous case, and these two components (the influx and outflux) do not balance each other. In particular, *direct* recombinations to the ground state, which did not affect the homogenous ionization fraction, x_e , are important in determining its fluctuation, δx_e .

In this work, we incorporate the transport of both continuum and Lyman- α ($\text{Ly}\alpha$) photons. We find simple analytical expressions for this “non-local” contribution to the evolution of the ionization fraction, and provide revised estimates for the growth rates of the small-scale sound-waves.

We organize the presentation as follows: the rest of this chapter is devoted to introducing the instability and some background. In Section 6.2, we expand upon the simple estimate given above for the work done on the fluctuations, and estimate the associated growth rates. In Section 6.3, we list the relevant background variables, and the various factors which determine their size during the epochs of interest. Chapter 7 is devoted to the detailed study of the atomic physics, and the growth of the instability. We start with the standard Newtonian equations for the density and velocity in Section 7.1, following which we estimate growth rates using a simple scaling relation for the ionization fraction fluctuation in Section 7.2. We then move beyond this simple treatment, and study in detail the radiative transport of photons between different parts of the fluctuations – Sections 7.3 and 7.4 deal with the transport of continuum and Lyman- α photons, respectively. Finally, we bring all the pieces together and estimate the growth rates of the small-scale fluctuations in Section 7.5, and find their distribution in a stochastic background of large-scale relative velocities in Section 7.6. We finish with a short discussion of our results and their implications in Section 7.7, and collect some technical details in the appendix.

6.2 Motivation and simple estimate

This section closely follows the analysis of [162].

We use the two fluid approximation, where matter and radiation fluids are coupled by Thomson scattering of photons off free electrons. The characteristic response time, $\tau_{e\gamma}$, is inversely related to the matter’s opacity per unit mass, κ . For a given relative velocity between the two fluids, $\mathbf{v}_e - \mathbf{v}_\gamma = \mathbf{v}_{e\gamma}$, the force per unit mass is expressed in terms of the response time as

$$\mathbf{a} = \frac{d\langle \mathbf{v}_{e\gamma} \rangle}{dt} = \frac{\kappa}{c} \mathbf{F}_\gamma = -\frac{\langle \mathbf{v}_{e\gamma} \rangle}{\tau_{e\gamma}}, \quad (6.2)$$

where \mathbf{F}_γ is the photon flux seen in the matter’s rest frame. This force, and the related response time, are most easily obtained by considering the Doppler shifted background radiation field in the

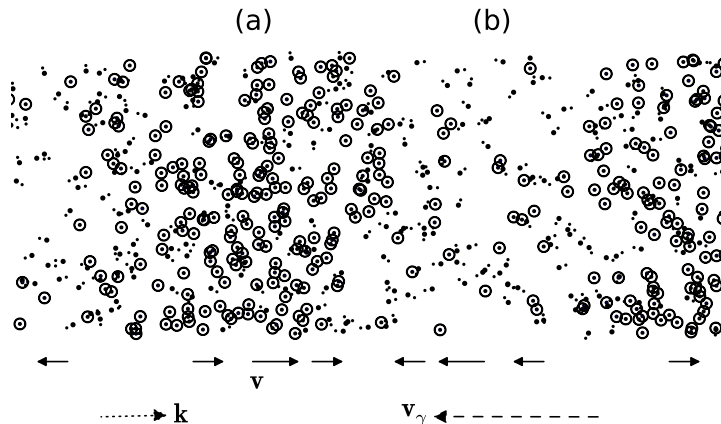


Figure 6.1: Illustration of the instability of sound waves during recombination. The symbol \odot represents a neutral atom, while large and small dots represent positive ions and free electrons, respectively. The sound wave propagates to the right. Regions of compression and rarefaction, marked with (a) and (b), have lower and higher free electron fractions respectively. Solid arrows show the local velocity at various points along the wave in the bulk-rest frame of the matter. If the background flux of radiation, \mathbf{v}_γ , is directed to the left, the work done on the wave by the radiative force at (b) is larger than that extracted from it at (a).

matter's rest frame. The result is [337]

$$\frac{1}{\tau_{e\gamma}} = \frac{4}{3} \frac{\sigma_T}{m_H c} a_{\text{rad}} T_r^4 x_e, \quad (6.3)$$

where x_e is the hydrogen ionization fraction, σ_T is the Thomson scattering cross-section and a_{rad} is the radiation energy density constant. The matter temperature, T_m closely follows the radiation temperature, T_r , at these times. With this understanding, we omit the subscript on the temperature in subsequent equations.

Primordial adiabatic fluctuations entering the horizon lead to large-scale motions of the matter and radiation fluids. Their physical size, λ_H is ≈ 250 kpc at recombination. Due to the small but finite response time, $\tau_{e\gamma}$, during this epoch, the matter velocity does not perfectly follow the local radiation velocity; this leads to a spectrum of relative velocities that can be estimated from the background cosmology [161].

We consider motions of the matter fluid alone, as contrasted with the large-scale adiabatic modes involving both matter and radiation. In particular, we concentrate the evolution of very small wavelength modes through the epoch of recombination out to late redshifts of $z = 800$. We consider

modes that are isothermal in nature, i.e., have a uniform matter temperature. As noted in the discussion (Section 7.7), this condition restricts our analysis to modes with wavenumbers k smaller than $\approx 3.5 \times 10^5 \text{ Mpc}^{-1}$. The large scale adiabatic modes are effectively fixed on the timescales relevant to these small-scale modes, and provide a background radiation flux due to their associated relative velocity. The radiative force due to this flux is given by Eq. (6.2).

The ionization fraction and opacity vary with the local density during recombination. Thus small-scale fluctuations of the matter density are associated with a modulation of the local force, denoted by $\delta \mathbf{a}$. The in-phase component of $\delta \mathbf{a}$ feeds power from the large-scale relative motions into small-scales.

The rest of this section estimates the size of this effect in a simplified scenario with direct recombination to the ground state of neutral hydrogen. With this assumption, the ionization fraction is given by the Saha equilibrium value, which we denote by x_e^S . This is set by the balance between the recombination of free electrons to the ground $1s$ state, and photoionization by microwave background photons:

$$\frac{(x_e^S)^2}{1 - x_e^S} = \frac{(2\pi m_e k_B T)^{3/2}}{h^3 n_H} e^{-(E_I/k_B T)}, \quad (6.4)$$

where E_I is the ionization energy of a hydrogen atom in the ground $1s$ state, and n_H is the hydrogen number density. We take the logarithm of both sides of Eq. (6.4), and perturb it to estimate the power-law exponent relating the perturbed free electron fraction and hydrogen density as follows:

$$\alpha_S = \frac{\delta \log x_e^S}{\delta \log n_H} = -\frac{(1 - x_e^S)}{(2 - x_e^S)}, \quad (6.5)$$

where we have used the assumption that the small-scale fluctuations do not perturb the temperature, T . The Saha electron fraction is approximately $x_e^S \approx 4 \times 10^{-3}$ at recombination, so the exponent $\alpha_S \approx -0.5$.

Consider a region with a background relative velocity between matter and radiation, $\mathbf{v}_{e,0} - \mathbf{v}_{\gamma,0} = \mathbf{v}_0$. The associated force per unit mass, \mathbf{a}_0 , is related to the relative velocity \mathbf{v}_0 by the response time $\tau_{e\gamma}$, according to Eq. (6.2). The local matter density, velocity, and force per unit mass are perturbed due to the small-scale fluctuation. For a sound wave, these perturbations are of the form

$$\frac{\delta \rho_m}{\rho_m} = \delta_m e^{i(\mathbf{k} \cdot \mathbf{r} - \omega t)}, \quad (6.6a)$$

$$\mathbf{v}_m = v_{s,I} \delta_m \hat{\mathbf{k}} e^{i(\mathbf{k} \cdot \mathbf{r} - \omega t)}, \quad (6.6b)$$

$$\delta \mathbf{a} = \frac{\delta \kappa}{\kappa} \mathbf{a}_0 = \frac{\delta x_e^S}{x_e^S} \mathbf{a}_0 \approx -|\alpha_S| \delta_m \mathbf{a}_0 e^{i(\mathbf{k} \cdot \mathbf{r} - \omega t)}. \quad (6.6c)$$

In the above relations, $v_{s,I}$ denotes the isothermal sound speed. It is determined by the matter temperature according to $v_{s,I} = [k_B T (1 + x_e^S) / m_H]^{1/2}$. Averaged over the phase of the wave, the

power input into the fluctuation by the extra force, $\delta\mathbf{a}$ of Eq. (6.6c), is

$$\langle p \rangle = \frac{1}{2} \text{Re}(\mathbf{v}_m \cdot \delta\mathbf{a}^*) = -\frac{1}{2} |\alpha_S| \delta_m^2 v_{s,I} \mathbf{a}_0 \cdot \hat{\mathbf{k}} \quad (6.7)$$

$$= \frac{1}{2} |\alpha_S| \delta_m^2 v_{s,I} \frac{\mathbf{v}_0 \cdot \hat{\mathbf{k}}}{\tau_{e\gamma}}. \quad (6.8)$$

The first line uses Eq. (6.6b) and (6.6c) for the velocity and force, respectively, while the second uses Eq. (6.2) for the background force and the definition of the response time $\tau_{e\gamma}$ in Eq. (6.3). The energy per unit mass in the fluctuation is $\langle \epsilon \rangle = (1/2)v_{m,\text{max}}^2 = (1/2)\delta_m^2 v_{s,I}^2$. Hence the growth rate for the amplitude, \mathcal{G} , can be estimated from the input power of Eq. (6.8) as

$$\mathcal{G} = \frac{\langle p \rangle}{2\langle \epsilon \rangle} = \frac{|\alpha_S|}{2\tau_{e\gamma}} \frac{\mathbf{v}_0 \cdot \hat{\mathbf{k}}}{v_{s,I}}. \quad (6.9)$$

The growth of the instability is maximal during the epoch with large relative velocities and moderate response times. Relative velocities of the order of the isothermal sound speed are needed to produce an appreciable growth rate. The last part of Section 6.3 deals with the distribution of large scale relative velocities in detail. In particular, Figure 6.3 shows the mean relative speed, and the isothermal sound speed, as a function of redshift, z . We see that large relative velocities are much more probable in the post-recombination era; however, this effect is mitigated by the growing response time. Ultimately, the instability is limited by the relatively narrow duration of cosmic recombination.

6.3 Background parameters

This section describes the relevant properties of the background on which the small fluctuations of interest live.

We assume a standard spatially flat Λ cold dark matter cosmology with the Planck cosmological parameters [42]. The derived quantities of interest to us are the hydrogen number density and ionization fraction, and the relative velocities between matter and radiation on large scales due to adiabatic fluctuations of primordial origin.

The simplest of these to obtain is the hydrogen number density, n_H , which is given by

$$n_H(z) = 248.7 \text{ cm}^{-3} \left(\frac{1+z}{1100} \right)^3 \frac{\Omega_b h^2}{0.022} \frac{1 - Y_{\text{He}}}{0.752}, \quad (6.10)$$

where $\Omega_b h^2$ is the Baryon fraction and Y_{He} is the Helium mass fraction.

It is considerably harder to estimate the hydrogen ionization fraction, x_e , as a function of redshift. It is especially challenging to follow it through the epoch of recombination, when the universe

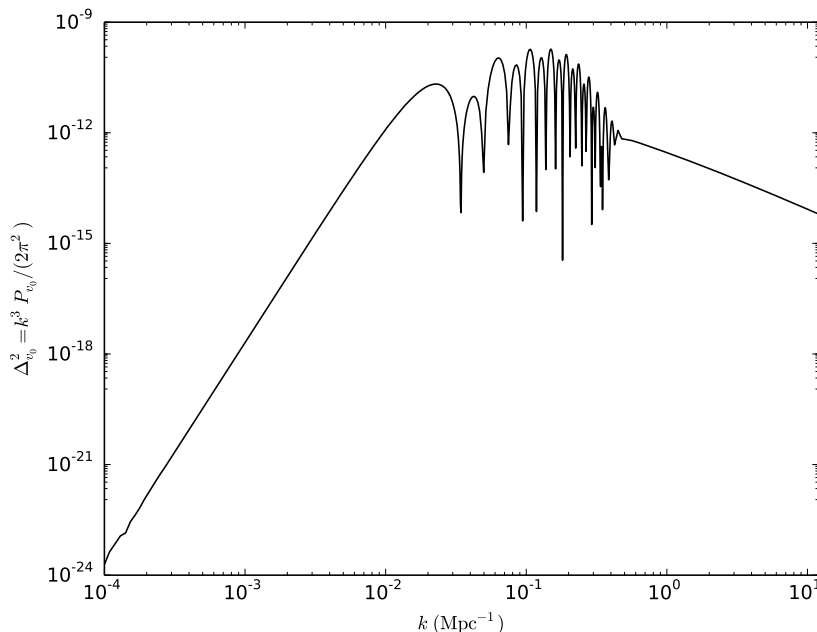


Figure 6.2: Power spectrum of relative velocities between matter and radiation at the redshift of recombination, $z_0 = 1100$. This assumes that these velocities arise from primordial adiabatic fluctuations. (This figure uses units in which velocity \mathbf{v}_0 is dimensionless.)

transitions from a plasma of free electrons and hydrogen nuclei to a largely neutral phase with traces of free electrons that are strongly coupled to the cosmic microwave background (CMB) radiation.

This difficulty arises from the fact that direct transitions to the ground $1s$ state of hydrogen contribute very little to recombination, since they produce ionizing photons themselves. Instead, recombination mainly proceeds through excited states of neutral hydrogen. In order to derive the evolution of the ionization fraction to sub-percent level accuracy, we should follow the populations of a large number of excited states of the hydrogen atom [169, 170].

We eschew this sophisticated analysis for a conceptually simpler, and less accurate, model of recombination originally proposed in Refs. [83, 84]. This is adequate for the purposes of this investigation, since we follow *fluctuations* in the ionization fraction. The errors introduced in the fluctuations by using the approximate model should be at the few-percent level.

This model approximates the hydrogen atom as a three level system; it assumes that the excited states of the true hydrogen atom are in thermal equilibrium with each other, and cascade down to the $n = 2$ level through fast radiative decays. Atoms in the $2p$ state reach the ground state when photons redshift through the $\text{Ly}\alpha$ line due to cosmological expansion, while those in the $2s$ level de-excite through a two-photon process. Direct recombination via the redshift of continuum photons is much slower (by a factor of $\sim 10^{-6}$) than through the $\text{Ly}\alpha$ channel [338]. Hence we set the direct recombination's contribution to zero in the background case. As Section 7.3 demonstrates,

this assumption is no longer valid in the perturbed case.

We add the recombination coefficients to the excited states to obtain an effective, or case B recombination coefficient, α_B . We also have an effective rate of photo-ionization from this state, β_B . With these definitions, the ionization fraction evolves according to

$$\dot{x}_e = -C \left(n_H x_e^2 \alpha_B - 4x_{1s} \beta_B e^{-E_{21}/k_B T} \right), \quad (6.11)$$

where C is the Peebles C -factor, which is the probability that an atom in the $n = 2$ state reaches the ground state [83]. It is defined in terms of the Ly α escape rate, the $2s$ - $1s$ two-photon transition rate, and the rate of photo-ionization from the $n = 2$ state. We derive explicit expressions for C and the population of the $n = 2$ state, x_2 , in Section 7.4.1.1.

The case B recombination coefficient and the effective photo-ionization rate are related by the principle of detailed balance [83, 84, 336]:

$$\beta_B(T) = \frac{(2\pi m_e k_B T)^{3/2}}{4h^3} e^{(E_2/k_B T)} \alpha_B(T). \quad (6.12)$$

We assume that the four sublevels of the $n = 2$ level are equally occupied. Thus their occupation fractions are related by $x_{2p} = 3x_{2s} = (3/4)x_2$. This is justified by the high effective $2p$ - $2s$ transition rate at these redshifts ($\Lambda_{2p,2s} \approx 2.5 \times 10^4 \text{ s}^{-1}$ [168, 169]). This is much faster than both the case B recombination rate per hydrogen atom, and the photo-ionization rate, which are $\sim 1.3 \times 10^2 \text{ s}^{-1}$, and the two-photon decay rate, $\Lambda_{2s,1s} = 8.22 \text{ s}^{-1}$ [339].

In deriving Eq. (6.11), we assume that the population of the $n = 2$ level is in steady state, i.e., we balance the net rate of recombination and photo-ionization against the escape of Ly α photons and two-photon decays. This is valid if the abundance of intermediate states is very small; in this case, x_2/x_{1s} can be estimated from the recombination codes themselves (e.g. Ref. [169]), and is typically of order $\sim 10^{-14}$.

The final piece needed is the spectrum of relative velocities between matter and radiation on large scales. We assume that velocities are irrotational, i.e., they are aligned with their wave vectors, \mathbf{k} . The velocity at any point in space is a Gaussian random variable, whose two-point correlation function is

$$\langle v_{0,i}(\mathbf{x}) v_{0,j}^*(\mathbf{x}) \rangle = \frac{1}{3} \delta_{ij} \int d \ln k \Delta_{v_0}^2(k), \quad (6.13)$$

where $\Delta_{v_0}^2$ is the dimensionless power per log wave-number of the component along the wave-vector. This power spectrum is given by [160]

$$\Delta_{v_0}^2(k) = \frac{k^3 P_{v_0}(k)}{2\pi^2} = \frac{1}{k^2} |\Theta_m(k) - \Theta_r(k)|^2 \Delta_\zeta^2(k), \quad (6.14)$$

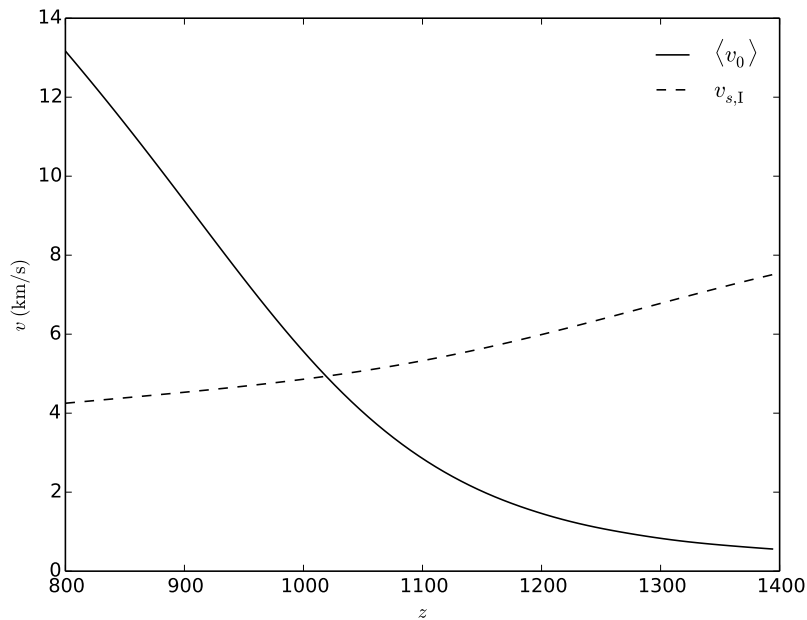


Figure 6.3: Speeds with redshift: the solid line shows the average magnitude of the background relative velocity between matter and radiation; the dashed line shows the isothermal sound speed.

where ζ is the primordial curvature perturbation, and Θ_m and Θ_r are the transfer functions for the matter and radiation velocity divergence respectively. We use the publicly available CLASS code to obtain these transfer functions [340]. Figure 6.2 shows the resulting power spectrum for the relative velocity. We observe that most of the power is in scales near $k \sim 0.1 \text{ Mpc}^{-1}$.

We estimate the typical velocities from the distribution of Eq. (6.13). Figure 6.3 shows both the average speed of the matter relative to the radiation, and the isothermal sound speed, as a function of redshift. We observe that these velocities are very small during the pre-recombination era: the matter-radiation response time, $\tau_{e\gamma}$, is much smaller than the expansion age due to rapid scattering, which suppresses the relative velocities. During recombination the free electron fraction drops, and the response time becomes comparable to the expansion age, i.e., recombination leads to decoupling.

Chapter 7

Calculation of growth rates

7.1 Linear analysis of density and velocity fluctuations

Small-scale fluctuations of the matter field perturb the density, velocity, and the ionization fraction. We denote the fractional matter overdensity by δ_m , the velocity by \mathbf{v}_m and the ionization fraction and its fluctuation by x_e and δx_e , respectively. In addition to these, we denote the perturbed gravitational potential by $\delta\phi$. In this section, we derive the evolution equations for the density and velocity. In what follows, \mathbf{x} is the position on a comoving grid, while a dot represents a derivative with respect to coordinate time.

There is a small amount of helium present in the early Universe: the He:H ratio by number, f_{He} , is given in terms of the Helium mass fraction, Y_{He} , by $f_{\text{He}} = Y_{\text{He}}/[4(1 - Y_{\text{He}})] \approx 0.08$. We consider late times, $z \lesssim 1800$, where the helium is fully neutral, so that it does not contribute to the ionization fraction. The hydrogen mass fraction $X_{\text{H}} = 0.76$ is also used in the equations below.

The matter density, velocity, and gravitational potential on sub-horizon scales are governed by the Newtonian equations of motion – the equation of continuity, the Navier-Stokes equation, and Poisson’s equation written in the comoving frame (as in Ref. [341]). The linearized forms of these equations are

$$\dot{\delta}_m + \frac{1}{a} \nabla \cdot \mathbf{v}_m = 0, \quad (7.1a)$$

$$\dot{\mathbf{v}}_m + H \mathbf{v}_m = -\frac{1}{a\rho_m} \nabla P - \frac{1}{a} \nabla \delta\phi + \mathbf{f}_{\text{rad}}, \quad (7.1b)$$

$$\frac{1}{a^2} \nabla^2 \delta\phi = -4\pi G \rho_m \delta_m. \quad (7.1c)$$

The quantity H is the Hubble rate of expansion, $H = \dot{a}/a$. The relative velocity force term, \mathbf{f}_{rad} , depends on the flux of background radiation in the local matter rest frame. We use Eqs. (6.2) and (6.3) to write the force as $\mathbf{f}_{\text{rad}} = -\Lambda_{e\gamma} X_{\text{H}} x_e (\mathbf{v}_m - \mathbf{v}_r)$, where $\Lambda_{e\gamma}$ is the inverse of the response time in the case where the hydrogen is completely ionized and the helium mass is neglected. Typical

large-scale relative velocities, \mathbf{v}_0 , on comoving scales $k \approx 0.1 \text{ Mpc}^{-1}$, appear nearly uniform to the small-scale matter fluctuations. By definition, the latter do not perturb the radiation field. Therefore the force associated with the relative velocity is

$$\mathbf{f}_{\text{rad}} = -\Lambda_{e\gamma} X_{\text{H}} x_e \mathbf{v}_m - \Lambda_{e\gamma} X_{\text{H}} \delta x_e \mathbf{v}_0. \quad (7.2)$$

We decompose the velocity into scalar (curl-free) and vector (divergence-free) parts:

$$\Theta_m = \nabla \cdot \mathbf{v}_m \quad \text{and} \quad \Omega_m = \nabla \times \mathbf{v}_m. \quad (7.3)$$

Under the equation of motion, (7.1b), the vector part's evolution depends on the scalar part through the latter's modulation of the free electron fraction in the force term, but the reverse is not true. We focus on the scalar part in the rest of this work.

We expand the restoring force due to the pressure up to first order in the fluctuation as follows:

$$\begin{aligned} -\frac{\nabla P}{a\rho_m} &= -\frac{1}{a\rho_m} \nabla(nk_{\text{B}}T) \\ &= -\frac{1}{a\rho_m} k_{\text{B}}T \nabla[n_{\text{H}}(1 + f_{\text{He}} + x_e + \delta x_e)] \\ &= -\frac{1}{a} \frac{k_{\text{B}}T}{m_{\text{H}}} X_{\text{H}} \nabla[(1 + \delta_m)(1 + f_{\text{He}} + x_e + \delta x_e)] \\ &= -i \frac{\mathbf{k}}{a} \frac{k_{\text{B}}T}{m_{\text{H}}} X_{\text{H}} [(1 + f_{\text{He}} + x_e) \delta_m + \delta x_e]. \end{aligned} \quad (7.4)$$

We substitute the pressure and relative velocity force terms [Eqs. (7.4) and (7.2)] in the Newtonian equations [Eq. (7.1)], and eliminate the gravitational potential, $\delta\phi$. Assuming plane-wave forms for the perturbed quantities, $\alpha(\mathbf{x}) = \int [d^3\mathbf{k}/(2\pi)^3] \alpha(\mathbf{k}) \exp(i\mathbf{k} \cdot \mathbf{x})$, the final forms of the evolution equations for the matter density and velocity are

$$\dot{\delta}_m = -\frac{1}{a} \Theta_m, \quad (7.5a)$$

$$\begin{aligned} \dot{\Theta}_m &= -\frac{k^2}{a} \left[\frac{4\pi G \rho_m}{k^2} a^2 - X_{\text{H}} (1 + f_{\text{He}} + x_e) \frac{k_{\text{B}}T}{m_{\text{H}}} \right] \delta_m \\ &\quad - (H + \Lambda_{e\gamma} X_{\text{H}} x_e) \Theta_m + X_{\text{H}} \left(\frac{k^2}{a} \frac{k_{\text{B}}T}{m_{\text{H}}} - i\Lambda_{e\gamma} \mathbf{k} \cdot \mathbf{v}_0 \right) \delta x_e. \end{aligned} \quad (7.5b)$$

7.2 Ionization fraction fluctuation: Saha equilibrium scaling

In order to get a complete picture of the ionization fraction's evolution, we need to study the transport of photons between different parts of the fluctuations. Before we deal with this problem in Sections 7.3 and 7.4, we make a simple first estimate following Ref. [162].

The simplifying assumption in this section is that the ionization fraction scales with matter

density in the same manner as the value calculated using local thermodynamic equilibrium (LTE, or Saha equilibrium). In subsequent sections, we consider non-equilibrium ionization. We note that perturbed non-equilibrium ionization in cosmology is one of the contributions to the CMB bispectrum and hence has been investigated as a potential contaminant to primordial non-Gaussianity studies [342–345] and probe of new physics [346]; however, these studies did not consider the very high k of interest in this work and hence did not have to solve the nonlocal radiative transfer problem considered in Sections 7.3 and 7.4.

Using the scaling of Eq. (6.5) for the ionization fraction fluctuation in Eq. (7.5b), we reduce the Newtonian evolution equations to

$$\dot{\delta}_m = -\frac{1}{a}\Theta_m, \quad (7.6a)$$

$$\begin{aligned} \dot{\Theta}_m = & -\left[H + \Lambda_{e\gamma}X_Hx_e\right]\Theta_m + \left\{\frac{(1-x_e)}{(2-x_e)}i\Lambda_{e\gamma}X_Hx_e\mathbf{k}\cdot\mathbf{v}_0\right. \\ & \left.-\frac{k^2}{a}\left[\frac{4\pi G\rho_m}{k^2}a^2 - \frac{2-f_{\text{He}}x_e}{2-x_e}X_H\frac{k_B T}{m_H}\right]\right\}\delta_m. \end{aligned} \quad (7.6b)$$

The instantaneous growth rate, \mathcal{G} , is the largest eigenvalue of the system of Eq. (7.6). Figure 7.1 plots this growth rate (normalized to a net elapsed coordinate time, τ_u , at the redshift of recombination, $z_0 = 1100$) for various values of the large-scale relative velocity, with the wave vector oriented along its direction. Modes with comoving wavenumbers satisfying $k > 2 \times 10^2 \text{ Mpc}^{-1}$ (or physical wavelength smaller than $\approx 30 \text{ pc}$) at recombination are unstable. The growth rate increases with wavenumber until it saturates on very large wavenumbers ($k \approx 10^5 \text{ Mpc}^{-1}$), or physical wavelength $\lambda_{\text{phys}} \approx 0.06 \text{ pc}$, or 10^4 AU . The modes at the saturation scale grow by a factor of a few hundred. Since there is a large number of small-scale modes, it is worth considering mechanisms that can cut off the growth on these scales.

Photons in the continuum and Ly α line interact strongly with matter during this epoch. We have briefly considered the aspects of this interaction relevant to background recombination in Section 6.3. Continuum photons produced in direct recombinations to the ground state are completely unimportant for the background at the level of accuracy of Section 6.3. Their interaction cross section with neutral hydrogen atoms is so large that they are promptly reabsorbed. However, we should keep track of them in the in-homogenous case, since they can stream from one part of the fluctuation to another.

Figure 7.2 is a schematic diagram of the radiative transport processes relevant to perturbed recombination. Before we study the various processes in detail in subsequent sections, we clarify a few general points.

Under the assumptions of the three level model of the hydrogen atom, we only need to consider a single spectral line (Ly α). This greatly simplifies our analysis. The Ly α photons can be decoupled

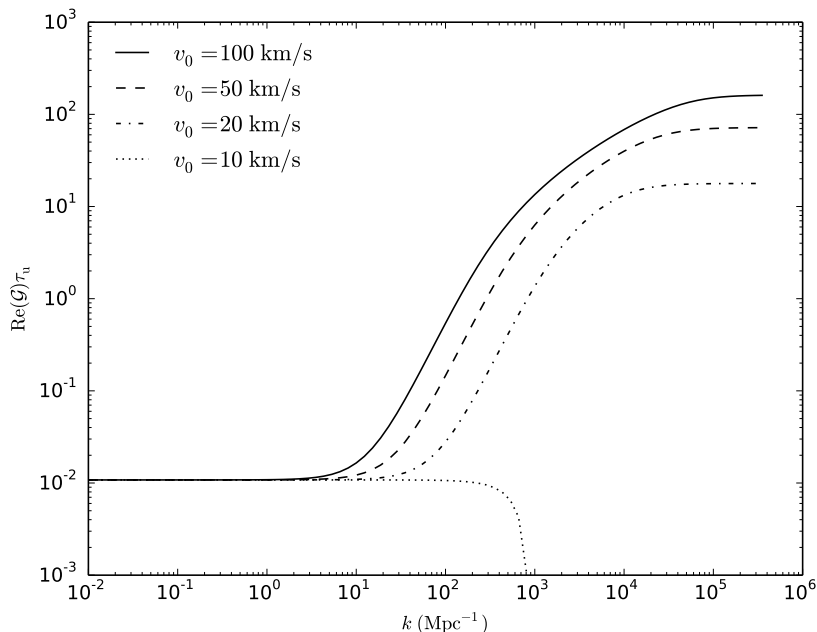


Figure 7.1: Maximum instantaneous growth rate for small-scale fluctuations in the matter field at recombination, normalized to the net elapsed coordinate time, τ_u . The wave-vector is oriented along the large-scale relative velocity between matter and radiation, \mathbf{v}_0 . This approximates the perturbed ionization fraction with the scaling relation of the Saha equilibrium value, given by Eq. (6.5).

from the continuum due to their wide separation in frequency. In the rest of this work, we neglect the homogenous population of the first excited state, x_2 (except in equations which compute transitions from the $n = 2$ level), and assume $x_e + x_{1s} \approx 1$. As discussed in Section 6.3, it is completely negligible compared to the other populations.

A first step towards judging the relative importance of various arms of Figure 7.2 is to look at the mean free paths (MFPs) of the photons at this redshift. If we use numbers for Ly α photons at the line center, the comoving wavenumbers corresponding to the MFPs are

$$k_{\text{cont}} = n_{1s} \sigma_{1s, \text{cont}} a \approx 3.6 \times 10^6 \text{ Mpc}^{-1} \quad (7.7)$$

and

$$k_{\text{Ly}\alpha} = n_{1s} \sigma_{1s, \text{Ly}\alpha} a \approx \frac{H \tau_S a}{c \Delta_H} \approx 10^{11} \text{ Mpc}^{-1}. \quad (7.8)$$

Here $\sigma_{1s, \text{cont}} \approx 6.3 \times 10^{-18} \text{ cm}^2$ is the photo-ionization cross section for a ground state hydrogen atom at the threshold frequency, while $\tau_S \approx 5.6 \times 10^8$ and $\Delta_H \approx 2.3 \times 10^{-5}$ are the Sobolev optical depth and the dimensionless Doppler width of the Ly α line at the redshift of recombination.

The MFP for continuum photons is very close to the saturation scale in Figure 7.1. Moreover, as we show in Appendix 7.A.1, the length scale for the diffusion of Ly α photons is much larger than this

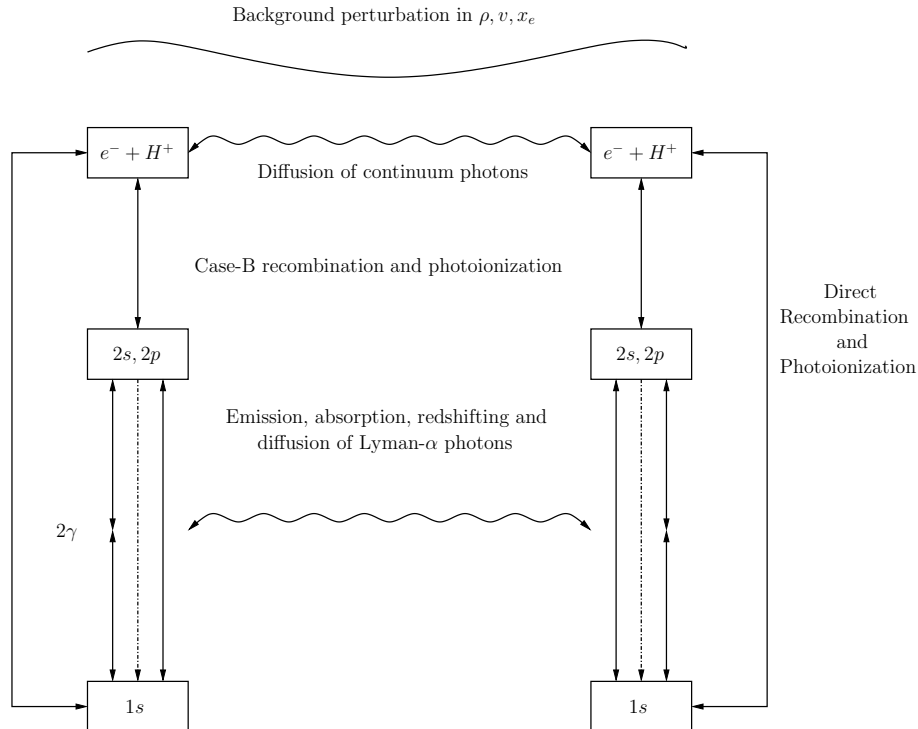


Figure 7.2: Schematic diagram showing the effect of continuum and Ly α photon transport on the evolution of the ionization fraction fluctuation associated with small-scale fluctuations.

naive estimate. In fact, we will see in Section 7.4 that Ly α transport is important for wavenumbers satisfying $k > 10^3 \text{ Mpc}^{-1}$. We begin by studying the outer arm of Figure 7.2 in the next section.

7.3 Radiative transfer in the continuum

We study the transport of continuum photons in two stages: we first determine their perturbed phase space density, and then calculate its effect on the recombination rate. We approach the problem using the Fourier-space Boltzmann equation (as used in previous sections and in modern CMB codes [160, 347–349]). We note that the similar problem of ultraviolet and X-ray radiative transfer in the literature on high-redshift 21 cm radiation is usually addressed by a Green’s function approach, i.e. by summing the contributions from individual point sources either analytically or numerically [350–353].

Let the phase space density (henceforth, the PSD) of continuum photons be $f(\nu, \mathbf{x}, \hat{\mathbf{n}}, t)$. It evolves via the Boltzmann equation

$$\frac{\partial f}{\partial t} - \left[H + \frac{n_i n_j}{a} \frac{\partial v_i}{\partial x_j} \right] \nu \frac{\partial f}{\partial \nu} + \frac{c}{a} \hat{\mathbf{n}} \cdot \nabla f = \sum_{\text{process}} \dot{f}|_{\text{process}}. \quad (7.9)$$

The second and third terms on the left-hand side account for the redshift of photons and their ad-

vection, respectively. Both the background cosmological expansion and the peculiar matter velocity contribute to the redshift term.

We assume that the PSD is not a dynamical variable and drop the explicit time-dependence. This is valid both in the unperturbed and perturbed cases: in the former, because photons redshift through the frequency range much faster than a Hubble time, and in the latter, because the advection term dominates below the Jeans scale.

We neglect the redshift term in Eq. (7.9). This is equivalent to neglecting the background rate of recombination through the continuum channel. We consider the contributions of the absorption and emission of continuum photons to the right hand side of Eq. (7.9), and neglect the redistribution of photons within the frequency range due to resonant scattering – this is important within the Lyman lines.

Let $\sigma_a(\nu)$, $\alpha_{1s}(\nu)$, and $\phi(\nu)$ denote the continuum photon absorption cross-section, the direct recombination coefficient, and the probability distribution for the emitted photons' frequency respectively. These quantities are functions of radiation (absorption) and matter (recombination) temperature. The integrated or total recombination coefficient to the ground state is defined by

$$\alpha_{1s} = \int_{\nu_c}^{\infty} d\nu \alpha_{1s}(\nu)\phi(\nu). \quad (7.10)$$

The rates of absorption and emission of continuum photons are

$$\dot{f}(\nu, \mathbf{x}, \hat{\mathbf{n}})|_{\text{abs}} = -cn_{1s}\sigma_a(\nu)f(\nu, \mathbf{x}, \hat{\mathbf{n}}), \quad (7.11)$$

$$\dot{f}(\nu, \mathbf{x}, \hat{\mathbf{n}})|_{\text{em}} = \frac{c^3}{2\nu^2}n_en_p\alpha_{1s}(\nu)\frac{\phi(\nu)}{4\pi}, \quad (7.12)$$

where we have used the fact that every direct recombination is accompanied by the emission of a continuum photon, and multiplied by a factor of $c^3n_{\text{H}}/(2\nu^2)$ to convert the contributions per hydrogen atom to those for the PSD. Substitution in the Boltzmann equation yields

$$\begin{aligned} & \frac{1}{a}\hat{\mathbf{n}} \cdot \nabla f(\nu, \mathbf{x}, \hat{\mathbf{n}}) \\ &= -n_{1s}\sigma_a(\nu)f(\nu, \mathbf{x}, \hat{\mathbf{n}}) + \frac{c^2}{8\pi\nu^2}n_en_p\alpha_{1s}(\nu)\phi(\nu). \end{aligned} \quad (7.13)$$

In the homogenous case, with just the background parameters, this reduces to the balance between absorption and recombination contributions:

$$0 = \frac{1}{a}\hat{\mathbf{n}} \cdot \nabla f(\nu) \quad (7.14)$$

$$= -(1 - x_e)n_{\text{H}}\sigma_a(\nu)f(\nu) + \frac{c^2}{8\pi\nu^2}(x_en_{\text{H}})^2\alpha_{1s}(\nu)\phi(\nu). \quad (7.15)$$

In the presence of small-scale fluctuations, we linearize the Boltzmann equation and simplify using the unperturbed solution, Eq. (7.15), and obtain

$$\begin{aligned} \frac{1}{a} \hat{\mathbf{n}} \cdot \nabla \delta f(\nu, \mathbf{x}, \hat{\mathbf{n}}) + (1 - x_e) n_{\text{H}} \sigma_{\text{a}}(\nu) \delta f(\nu, \mathbf{x}, \hat{\mathbf{n}}) = \\ \frac{c^2}{8\pi\nu^2} n_{\text{H}}^2 x_e \alpha_{1s}(\nu) \phi(\nu) \left[x_e \delta_{\text{m}} + \frac{2 - x_e}{1 - x_e} \delta x_e \right]. \end{aligned} \quad (7.16)$$

Let the total number flux of continuum photons in a direction be $N(\mathbf{x}, \hat{\mathbf{n}})$. In terms of the PSD, it is given by

$$N(\mathbf{x}, \hat{\mathbf{n}}) = \int_{\nu_c}^{\infty} d\nu \frac{8\pi\nu^2}{c^2} f(\nu, \mathbf{x}, \hat{\mathbf{n}}). \quad (7.17)$$

The photo-ionization cross-section, $\sigma_{\text{a}}(\nu)$, is discontinuous across the threshold frequency. It falls off with increasing frequency in a power-law fashion [354], while the PSD falls in an exponential manner in the UV part of the spectrum. Hence we neglect the frequency dependence of σ_{a} in all integrals. Using Eq. (7.16) and the definition (7.17), we get the equation for the transport of the number flux:

$$\frac{1}{a} \hat{\mathbf{n}} \cdot \nabla \delta N(\mathbf{x}, \hat{\mathbf{n}}) + A \delta N(\mathbf{x}, \hat{\mathbf{n}}) = n_{\text{H}} \left[B_1 \delta_{\text{m}} + B_2 \delta x_e \right], \quad (7.18)$$

where the coefficients are

$$A = (1 - x_e) n_{\text{H}} \sigma_{\text{a}}(\nu_c), \quad (7.19\text{a})$$

$$B_1 = n_{\text{H}} x_e^2 \alpha_{1s}, \quad (7.19\text{b})$$

$$B_2 = n_{\text{H}} x_e \alpha_{1s} \frac{2 - x_e}{1 - x_e}. \quad (7.19\text{c})$$

Note that the coefficient A is the inverse of the mean free path for continuum photons at the threshold for photo-ionization.

We assume a plane-wave dependence for the fluctuation, following which the solution to Eq. (7.18) is

$$\frac{\delta N(\mathbf{k}, \hat{\mathbf{n}})}{n_{\text{H}}} = \frac{B_1 \delta_{\text{m}} + B_2 \delta x_e}{A + i(\hat{\mathbf{n}} \cdot \mathbf{k}/a)}. \quad (7.20)$$

The photo-ionization from and recombinations to the ground state together cause the free electron fraction to evolve as

$$\dot{x}_{\text{e}}|_{\text{cont}} = x_{1s} \int_{\nu_c}^{\infty} d\nu \frac{8\pi\nu^2}{c^2} \sigma_{\text{a}}(\nu) f_0(\nu, \mathbf{x}) - n_{\text{H}} x_e^2 \alpha_{1s}. \quad (7.21)$$

In the homogenous case, we approximate the small contribution to be zero, which gives us a relation between the absorption cross-section and the recombination coefficient.

We can obtain this relation by considering the alternative scenario of local thermal equilibrium (LTE) between a population of ionized and 1s hydrogens, free electrons, and a blackbody distribution

of photons above the threshold frequency. The free electron fraction then equals the Saha equilibrium value of Eq. (6.4). As earlier, we neglect power-law frequency dependence of pre-factors in the integrals over frequency and obtain the relation

$$\alpha_{1s}(T) = 4 \frac{h\nu_c}{m_e c^2} \frac{h\nu_c}{(2\pi m_e k_B T)^{1/2}} \sigma_a(\nu_c, T). \quad (7.22)$$

In the inhomogenous case, we perturb Eq. (7.21) and retain terms up to the first order.

$$\begin{aligned} \delta\dot{x}_e|_{\text{cont}} &= x_{1s} \int_{\nu_c}^{\infty} d\nu \frac{8\pi\nu^2}{c^2} \sigma_a(\nu) \left[\frac{\delta x_{1s}}{x_{1s}} f_0(\nu) + \delta f_0(\nu, \mathbf{x}) \right] \\ &\quad - n_H x_e^2 \left[\delta_m + 2 \frac{\delta x_e}{x_e} \right] \alpha_{1s}. \end{aligned} \quad (7.23)$$

We use detailed balance in the homogenous case, and the definition of the total flux in Eq. (7.17) to simplify this contribution to

$$\begin{aligned} \delta\dot{x}_e|_{\text{cont}} &= (1 - x_e) \sigma_a(\nu_c) \delta N_0(\mathbf{x}) \\ &\quad - n_H x_e \left[x_e \delta_m + \frac{2 - x_e}{1 - x_e} \delta x_e \right] \alpha_{1s} \end{aligned} \quad (7.24)$$

$$= - \frac{1}{4\pi a n_H} \int d\hat{\mathbf{n}} \hat{\mathbf{n}} \cdot \nabla \delta N(\mathbf{x}, \hat{\mathbf{n}}). \quad (7.25)$$

To get to the second line, we used equation (7.18) for the the flux.

We use the solution (7.20) and evaluate the angular integral to obtain the final equation for the effect of continuum photon transport on the ionization fraction for a plane-wave fluctuation.

$$\begin{aligned} \delta\dot{x}_e|_{\text{cont}} &= - \left\{ \frac{1}{4\pi} \int d\hat{\mathbf{n}} \frac{i\hat{\mathbf{n}} \cdot \mathbf{k}}{Aa + i\hat{\mathbf{n}} \cdot \mathbf{k}} \right\} [B_1 \delta_m + B_2 \delta x_e] \\ &= - \left\{ 1 - \frac{Aa}{k} \arctan\left(\frac{k}{Aa}\right) \right\} [B_1 \delta_m + B_2 \delta x_e], \end{aligned} \quad (7.26)$$

where the coefficients A , B_1 , and B_2 are given in Eq. (7.19). The MFP of continuum photons is $1/A$; as expected the continuum photons' contribution goes to zero when the wavelength becomes much larger than this.

7.4 Radiative transfer in Lyman- α

This section works out the radiative transfer of Ly α photons in an inhomogenous universe. The subject and details of this calculation are self-contained, but impact the rest of the work through the resulting perturbed recombination rates. This sections' results are applicable over a wide range of length scales; we show that they reduce to expected values in the large- and small-scale limits in Appendices 7.A and 7.B.

The PSD of Ly α photons evolves via the Boltzmann equation of Eq. (7.9). It is simplest to work in the matter's rest frame, since the source terms on the right-hand side take on simple forms. Absorption, emission and resonant scattering contribute to this source term; we describe each of these processes in detail below.

The scattering of photons off a hydrogen atom in the ground state is a two step process, involving an excitation to a virtual excited state through the absorption of the incident photon, and subsequent decay through the emission of the outgoing one. When the first photon is of very low frequency, this corresponds to classical Rayleigh scattering. When its frequency approaches the Ly α frequency (henceforth $\nu_{\text{Ly}\alpha}$), the intermediate state is long lived and other processes which deplete it become important.

In particular, the excitation of the $2p$ state to higher bound states and its photo-ionization compete with spontaneous emission. We count the former as true absorptions, and the latter as coherent scattering events. The net photon number is unaffected by coherent scattering, but the frequency of the outgoing photon is related to that of the incident one.

The branching ratio for coherent scattering is set by the rate of spontaneous emission from the $2p$ state

$$p_{\text{sc}} = \frac{A_{\text{Ly}\alpha}}{\Gamma_{2p}} = 1 - p_{\text{ab}}, \quad (7.27)$$

where Γ_{2p} is the width due to all processes, and p_{ab} is the complementary branching ratio for absorption via two-photon processes. Coherent scattering is the dominant process, and the scattering probability p_{sc} is close to unity.

A useful definition is the Sobolev optical depth of the Ly α line. It is the net optical depth for the absorption of a photon over its path as it redshifts through the Ly α line due to cosmological expansion.

$$\tau_{\text{S}} = \frac{3}{8\pi} n_{1s} \left(\frac{c}{\nu_{\text{Ly}\alpha}} \right)^3 \frac{A_{\text{Ly}\alpha}}{H}. \quad (7.28)$$

The line is optically thick at the redshift of recombination, i.e. $\tau_{\text{S}} \approx 5.6 \times 10^8 \gg 1$. We divide this optical depth into true absorption and scattering contributions as

$$\tau_{\text{sc/ab}} = p_{\text{sc/ab}} \tau_{\text{S}}. \quad (7.29)$$

The rate of removal of Ly α photons per unit volume of phase space due to coherent scattering is

$$\dot{f}(\nu, \hat{\mathbf{n}})|_{\text{sc-}} = -H\nu\tau_{\text{sc}}\phi(\nu)e^{[h(\nu-\nu_{\text{Ly}\alpha})/k_{\text{B}}T]}f(\nu, \hat{\mathbf{n}}). \quad (7.30)$$

In the above expression, $\phi(\nu)$ is broadened from a delta function at the Ly α frequency, $\nu_{\text{Ly}\alpha}$, due to

the thermal motions of the absorbing atoms and the finite lifetime of the excited state. The resulting profile is a Voigt function, which is most easily expressed in terms of the deviation from the central frequency in Doppler widths [355]:

$$\phi(x, a) = \frac{a}{\pi^{3/2}} \int_{-\infty}^{\infty} du \frac{e^{-u^2}}{a^2 + (x - u)^2}, \quad (7.31)$$

$$x = \frac{\nu - \nu_{\text{Ly}\alpha}}{\nu_{\text{Ly}\alpha} \Delta_{\text{H}}}, \quad \Delta_{\text{H}} = \left(\frac{2k_{\text{B}}T}{m_{\text{H}}c^2} \right)^{1/2}. \quad (7.32)$$

The Voigt parameter, a , quantifies the relative strength of the radiative and Doppler broadening mechanisms, and is given by

$$a = \frac{\Gamma_{2p}}{4\pi\nu_{\text{Ly}\alpha}\Delta_{\text{H}}}. \quad (7.33)$$

The outgoing photon follows a redistribution function, $p(\nu, \hat{\mathbf{n}}|\nu', \hat{\mathbf{n}}')$. This is defined as the probability of an outgoing photon $(\nu, \hat{\mathbf{n}})$ conditioned on the incoming photon $(\nu', \hat{\mathbf{n}}')$ [355]. It is normalized as

$$\int d\nu \frac{d\hat{\mathbf{n}}}{4\pi} p(\nu, \hat{\mathbf{n}}|\nu', \hat{\mathbf{n}}') = 1. \quad (7.34)$$

The rate of injection per unit volume of phase space due to coherent scattering is

$$\begin{aligned} \dot{f}(\nu, \hat{\mathbf{n}})|_{\text{sc}+} &= H\nu\tau_{\text{sc}} \int d\nu' \frac{d\hat{\mathbf{n}}'}{4\pi} \phi(\nu') e^{[h(\nu' - \nu_{\text{Ly}\alpha})/k_{\text{B}}T]} \\ &\times p(\nu, \hat{\mathbf{n}}|\nu', \hat{\mathbf{n}}') f(\nu', \hat{\mathbf{n}}'). \end{aligned} \quad (7.35)$$

True absorptions are two-photon transitions to higher states, through an intermediate ‘virtual’ $2p$ state. Direct photo-ionization from the $2p$ state is formally included by letting the summation over the higher states run over the continuum states. However, the dominant transitions from $2p$ are to the $3s$ and $3d$ levels. To the first approximation, the resultant absorption probability is

$$\begin{aligned} p_{\text{ab}} &\approx \frac{A_{3s-2p} + 5A_{3d-2p}}{3A_{\text{Ly}\alpha}} e^{-(5h\nu_{\text{Ly}\alpha}/27k_{\text{B}}T)} \\ &\approx 10^{-4} \text{ at } z_0 = 1100. \end{aligned} \quad (7.36)$$

In the first line, we have neglected the absorption contribution in the denominator, and assumed that the PSD for the second photon of lower energy is that of a blackbody at the radiation temperature. The rate of removal of photons due to true absorption is

$$\dot{f}(\nu, \hat{\mathbf{n}})|_{\text{ab}} = -H\nu\tau_{\text{ab}}\phi(\nu) e^{[h(\nu - \nu_{\text{Ly}\alpha})/k_{\text{B}}T]} f(\nu, \hat{\mathbf{n}}). \quad (7.37)$$

In a similar manner, true emission of Ly α photons is a two-photon process, in which the first photon

is emitted in a transition from one of the higher levels (as earlier, largely from $3s$ and $3d$) to a ‘virtual’ $2p$ level, and the second one during a subsequent decay to the ground state. We neglect the stimulated component of both transitions since the PSDs involved are much smaller than unity. The rate of injection due to true emission is

$$\dot{f}(\nu, \hat{\mathbf{n}})|_{\text{em}} = \frac{c^3 n_{\text{H}}}{8\pi\nu^2} p_{\text{sc}} \sum_{i \neq 1s} x_i A_{i-2p} \phi(\nu). \quad (7.38)$$

In principle, two-photon transitions to and from the $2s$ state can also inject or remove photons within the $\text{Ly}\alpha$ line. Depending on the frequency of the more energetic photon involved, these are Raman scattering or two-photon transitions between $2s$ and the ground state. However, these transitions are much slower than those involving the $2p$ state; in particular, their cross-section goes to zero at the central frequency, since there is no phase space available for the second photon (see Figure 7.3). This statement is no longer true if we include stimulated emission, but the full transition rates are still much smaller than the ones to $2p$ within the $\text{Ly}\alpha$ line [356]. Thus, the majority of photons produced in this manner are on the far red side of the line. We can safely neglect this channel while calculating the spectral distortion within a few hundred Doppler widths of the $\text{Ly}\alpha$ line center.

Figure 7.3 shows the rates of the radiative processes described above which add or remove photons from the frequency range of interest.

7.4.1 Solution of the Boltzmann equation

We solve the Boltzmann equation under a number of simplifying assumptions.

1. The $2s$ - $2p$ transition rate is high enough so that all their sublevels are equally occupied. Consequently we neglect the fast transitions between these sublevels.
2. The line profile, $\phi(\nu)$, dominates the frequency dependence of the absorption and emission terms. Thus we replace all factors of ν multiplying the profile with the central frequency, $\nu_{\text{Ly}\alpha}$.
3. The rates of radiative processes are large compared to the Hubble rate, so the PSD and excited level populations are effectively in steady state. This is valid within the line profile due to the high scattering rate.
4. The absorption and emission profiles are identical. Under this approximation, factors of $\exp[h(\nu - \nu_{\text{Ly}\alpha})/k_{\text{B}}T]$ are approximately equal to unity. This is valid if we restrict ourselves to frequencies which satisfy

$$|\nu - \nu_{\text{Ly}\alpha}| \ll \nu_{\text{Ly}\alpha} \Delta_{\text{HX}}, \quad (7.39)$$

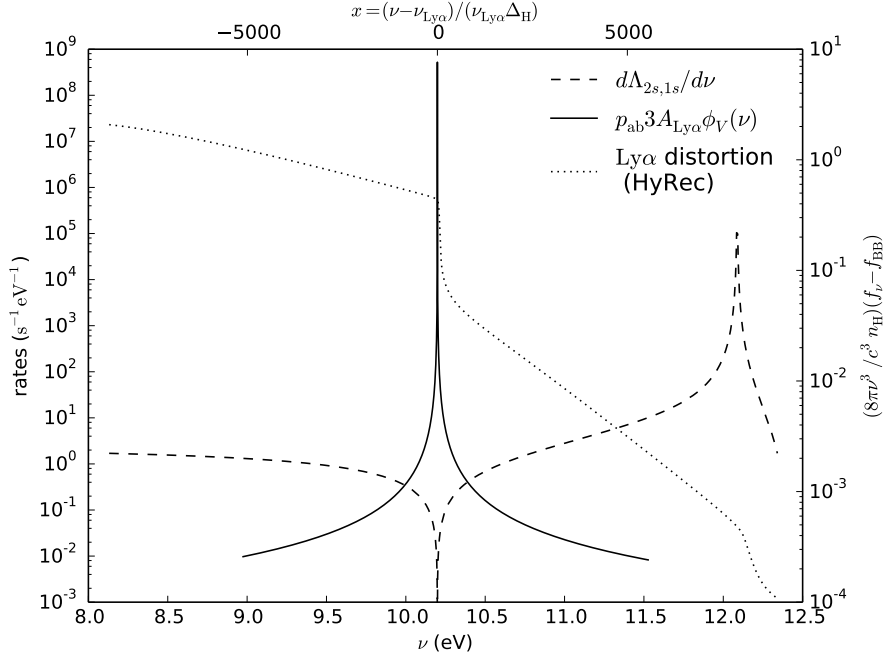


Figure 7.3: Rates of radiative processes. The solid and dashed lines show the rate coefficients per unit frequency for two-photon absorption via an intermediate $2p$ level, and two-photon absorption/Raman scattering to the $2s$ level, respectively. The lower and upper axes show the frequency in physical units, and Doppler widths from line center, respectively. Also shown on the same plot is the spectral distortion, as calculated by HyRec [169]. The dotted line shows the number of excess photons over a blackbody per hydrogen atom per logarithmic frequency interval. The plots are generated at redshift $z_0 = 1100$.

$$X = \frac{k_B T}{h \nu_{\text{Ly}\alpha} \Delta_H} \approx 1080, \text{ at } z_0 = 1100.$$

This is satisfied within the frequency range of interest, since the wings are optically thick to true absorption only up to ~ 20 Doppler widths at this redshift [357].

5. On the far blue side of the line, we take the PSD to equal that of a blackbody at the radiation temperature.
6. The redistribution function, $p(\nu, \hat{\mathbf{n}}|\nu', \hat{\mathbf{n}}')$, is isotropic. We condense it to the notation $p(\nu|\nu')$.

We use the steady state approximation to balance the rate of processes which populate the $2p$ level – downward transitions from higher levels and upward transitions from the $1s$ level – with its net rate of depletion:

$$\begin{aligned} 0 &= \dot{x}_{2p} \\ &= \sum_{i \neq 1s} x_i A_{i-2p} + 3x_{1s} A_{\text{Ly}\alpha} \bar{f} - \Gamma_{2p} x_{2p}, \end{aligned} \quad (7.40)$$

where \bar{f} is the average of the phase-space density over the line profile, $\bar{f} = \int d\nu \phi(\nu) f(\nu)$. We use this along with the definition of the scattering probability in Eq. (7.27) to rewrite the emission term of Eq. (7.38) as

$$\dot{f}(\nu, \hat{\mathbf{n}})|_{\text{em}} = H\nu\tau_{\text{S}}\phi(\nu) \left[f_{\text{eq}} - p_{\text{sc}}\bar{f} \right], \quad (7.41)$$

where we have introduced the equilibrium PSD, f_{eq} , which is defined as

$$f_{\text{eq}} = \frac{x_{2p}}{3x_{1s}} = \frac{x_2}{4x_{1s}}. \quad (7.42)$$

7.4.1.1 Homogenous case

If the background ionization state and density are homogenous, the PSD is independent of direction and position. Under the assumptions listed above, the Boltzmann equation of Eq. (7.9) reduces to

$$\begin{aligned} \frac{\partial f(\nu)}{\partial \nu} &= \tau_{\text{sc}} \left[\phi(\nu) f(\nu) - \int d\nu' \phi(\nu') p(\nu', \nu) f(\nu') \right] \\ &+ \tau_{\text{S}} \phi(\nu) \left[p_{\text{ab}} \bar{f}(\nu) - f_{\text{eq}} + p_{\text{sc}} \bar{f} \right]. \end{aligned} \quad (7.43)$$

This is easily solved if the redistribution due to coherent scattering is unimportant, i.e., $p_{\text{sc}} \approx 0$, or independent of the incoming frequency, i.e., $p(\nu', \nu) = \phi(\nu)$. The PSD is then given by the Sobolev solution. Complete redistribution is a good approximation within the Doppler core (up to ~ 40 Doppler widths away from $\nu_{\text{Ly}\alpha}$ at $z = 1100$ [357]).

However, redistribution due to coherent scattering is nontrivial in the wings, since the average change in frequency between the incident and outgoing photons is only a few Doppler widths. We implement the resulting diffusion in frequency using a second-order differential operator. This is commonly known as the Fokker-Planck approximation [165, 357, 358]. It is well suited for describing the partial redistribution in the wings. Due to the high scattering rates near the line center, the PSD sets itself to the equilibrium value, and the particular prescription used becomes unimportant, as long as it yields a small result. Under this approximation, the rates of injection and removal due to scattering are

$$\begin{aligned} \dot{f}(\nu)|_{\text{sc}} &= -H\nu\tau_{\text{sc}} \left[\phi(\nu) f(\nu) - \int d\nu' \phi(\nu') p(\nu', \nu) f(\nu') \right] \\ &= H\nu\tau_{\text{sc}} \frac{\nu_{\text{Ly}\alpha}^2 \Delta_{\text{H}}^2}{2} \frac{\partial}{\partial \nu} \left[\phi(\nu) \frac{\partial f}{\partial \nu} \right], \end{aligned} \quad (7.44)$$

The operator above does not account for the effect of atomic recoil; this is consistent with the approximation of equal absorption and emission profiles (assumption 4). Using this in Eq. (7.43),

we get a second-order ordinary differential equation (ODE) for the phase-space density

$$\begin{aligned} \frac{\partial f(\nu)}{\partial \nu} = & -\tau_{\text{sc}} \frac{\nu_{\text{Ly}\alpha}^2 \Delta_{\text{H}}^2}{2} \frac{\partial}{\partial \nu} \left[\phi(\nu) \frac{\partial f}{\partial \nu} \right] \\ & + \tau_{\text{S}} \phi(\nu) \left[p_{\text{ab}} f(\nu) - f_{\text{eq}} + p_{\text{sc}} \bar{f} \right]. \end{aligned} \quad (7.45)$$

We numerically solve this differential equation in a frequency range extending out to 1000 Doppler widths on either side of $\nu_{\text{Ly}\alpha}$, with 50 bins per Doppler width. We set the PSD to a blackbody on the far blue side, and use a Neumann boundary condition on the far red side, where we set the derivative to zero. The latter is designed to kill an unphysical solution where the PSD grows catastrophically as we approach the red side of the line.

Technically, this region is larger than the domain of validity for some of our approximations, but we formally extend the equation out to this region in order to reduce boundary effects. We evaluate the Voigt profile using Gubner's series in the core, and a fourth order asymptotic expansion in the wings [359].

In order to evaluate the equilibrium PSD, f_{eq} , we need the occupancies of the ground ($1s$) and excited ($2p$) states. The rates of their depletion and population depend on the PSD itself, so to be completely self-consistent, we need to solve for the level populations together with the PSD. Instead, we use the three level model of recombination of Section 6.3, which assumes the Sobolev solution. The error introduced by doing so is small, because the most significant effect of the redistribution is to broaden the jump in the PSD, rather than change its amplitude.

Figure 7.4 shows the resulting spectral distortion, which is defined via the PSD as the number of excess photons over a blackbody distribution per hydrogen atom per logarithmic frequency interval. Also shown are the true distortion (as calculated by the publicly available HyRec code [169]), and the Sobolev approximation to it, which neglects redistribution due to coherent scattering. HyRec's treatment of recombination and radiative processes is significantly more sophisticated than ours – it does not assume a steady state or equal emission and absorption profiles, follows the population of the higher levels, and accounts for two-photon and Raman transitions which are nonresonant with the Ly α transition.

The rate of recombination through the Ly α channel is the difference between the downward and upward transition rates:

$$\dot{x}_{1s}|_{\text{Ly}\alpha} = 3A_{\text{Ly}\alpha} x_{1s} \left[f_{\text{eq}} - \bar{f}_{00} \right]. \quad (7.46)$$

We get an expression for the average monopole, \bar{f}_{00} , and hence the recombination rate through the Ly α channel by integrating Eq. (7.43) over frequency, and using the normalization of the redistri-

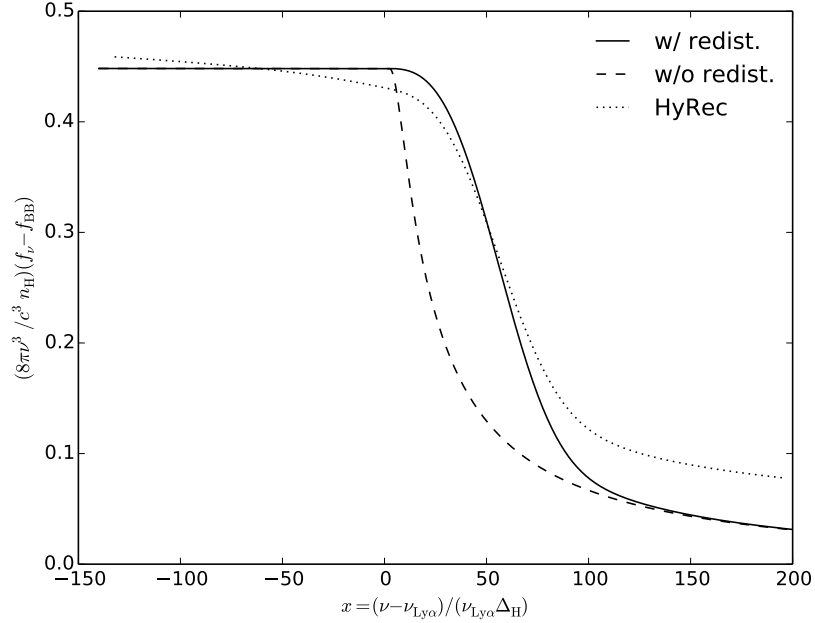


Figure 7.4: Ly α spectral distortion: This figure plots the number of excess photons over a blackbody distribution per hydrogen atom per logarithmic frequency interval, against the frequency offset from line center measured in Doppler widths, at redshift $z_0 = 1100$. The solid line is the solution of Eq. (7.45), which incorporates redistribution due to coherent scattering, while the dashed one is the Sobolev solution, which does not. Also shown for reference is the result of the full calculation of HyRec [169].

bution probability:

$$\Delta f = \tau_S [\bar{f} - f_{\text{eq}}], \quad (7.47)$$

where the notation ΔX represents the jump in a quantity X across the line, $\Delta X = X(\nu_+) - X(\nu_-)$. Using this in Eq. (7.46), we recover the background recombination rate in the Sobolev approximation with large optical depth

$$\dot{x}_{1s}|_{\text{Ly}\alpha} = -\frac{3A_{\text{Ly}\alpha}x_{1s}}{\tau_S} \Delta f. \quad (7.48)$$

Typically the PSD on the red side, f_{ν_-} , sets itself to the equilibrium value, f_{eq} , due to the high optical depth. On the far blue side, we take f_{ν_+} to equal the blackbody value to maintain consistency with assumption 5 and the numerical solution.

A significant fraction of atoms reach the ground state via two-photon decays from the $2s$ level. From Figure 7.3, we see that the more energetic of the emitted photons is largely on the far red side of the Ly α line. The effect of absorption of the background spectral distortion in this region is largely canceled by that of the stimulated emission of the low energy photon [356]. Thus, we compute the two-photon decay rate using the blackbody PSD.

$$\dot{x}_{1s}|_{2s} = \Lambda_{2s,1s}x_{1s} \left[f_{\text{eq}} - e^{-\{h\nu_{\text{Ly}\alpha}/k_B T\}} \right], \quad (7.49a)$$

$$\Lambda_{2s,1s} = \int_{\nu_{\text{Ly}\alpha}/2}^{\nu_{\text{Ly}\alpha}} d\nu \frac{d\Lambda_{2s}}{d\nu} = 8.22 \text{ s}^{-1}. \quad (7.49\text{b})$$

We neglect Raman scattering events involving photons above $\nu_{\text{Ly}\alpha}$. Their main impact on recombination is ‘nonlocal’ in time; they inject photons on the far blue side of Ly α which redshift into the line at a later time due to cosmological expansion and get absorbed [356].

Equations (7.48) and (7.49) together give the net rate of recombination to the ground state. The result depends on the equilibrium PSD, f_{eq} , which in turn depends on the $n = 2$ level’s population. We use the steady state assumption and balance its overall rates of population and depopulation.

One way of implementing this would be to follow the populations of all the levels which connect to it, in the manner of Eq. (7.40). Instead, we choose to work in the three level approximation of Section 6.3, which collects all the higher levels into a single block and assumes equal population for all the sublevels. The rates of case B recombination and photo-ionization add up to give the rate of the upper arms, which connect the fully ionized state with the $n = 2$ state.

$$\dot{x}_2|_{\text{rec/ion}} = n_{\text{H}} x_{\text{e}}^2 \alpha_{\text{B}} - x_2 \beta_{\text{B}}. \quad (7.50)$$

If we equate this expression to the sum of Eqs. (7.48) and (7.49), we recover Eq. (6.11) after some algebra. The explicit expressions for Peebles’ C factor and the $n = 2$ population are

$$C = \frac{3A_{\text{Ly}\alpha}/\tau_{\text{S}} + \Lambda_{2s,1s}}{3A_{\text{Ly}\alpha}/\tau_{\text{S}} + \Lambda_{2s,1s} + 4\beta_{\text{B}}}, \quad (7.51)$$

$$x_2 = 4 \frac{n_{\text{H}} x_{\text{e}}^2 \alpha_{\text{B}} + (3A_{\text{Ly}\alpha}/\tau_{\text{S}} + \Lambda_{2s,1s}) x_{1s} e^{-E_{21}/(k_{\text{B}}T)}}{3A_{\text{Ly}\alpha}/\tau_{\text{S}} + \Lambda_{2s,1s} + 4\beta_{\text{B}}}. \quad (7.52)$$

7.4.1.2 Inhomogenous case

The situation of interest in this investigation involves spatially varying hydrogen number density, ionization fraction, and matter velocity. The resulting phase-space density in Ly α is both inhomogenous, i.e., varies with position \mathbf{x} , and anisotropic, i.e., varies with direction $\hat{\mathbf{n}}$. We assume that these variations take the form of small fluctuations over a homogenous background, so that we can expand their spatial dependence into plane waves which evolve independently of each other. They obey the Boltzmann equation (7.9), whose linearized form is

$$\begin{aligned} & \frac{\partial \delta f}{\partial \nu} - \frac{ick}{H\nu a} (\hat{\mathbf{k}} \cdot \hat{\mathbf{n}}) \delta f - \frac{\delta \tau_{\text{S}}}{\tau_{\text{S}}} \frac{\partial f}{\partial \nu} \\ & = \tau_{\text{S}} \phi(\nu) \left[p_{\text{ab}} \delta f(\nu, \hat{\mathbf{n}}) - \delta f_{\text{eq}} + p_{\text{sc}} \delta \bar{f}_{00} \right] \\ & + \tau_{\text{sc}} \left[\phi(\nu) \delta f(\nu, \hat{\mathbf{n}}) - \int d\nu' \frac{d\hat{\mathbf{n}}'}{4\pi} \phi(\nu') p(\nu|\nu') \delta f(\nu', \hat{\mathbf{n}}') \right]. \end{aligned} \quad (7.53)$$

Here the perturbed source terms on the right hand side include the effects of absorption [Eq. (7.37)], emission [Eq. (7.41)], and scattering [Eqs. (7.30) and (7.35)], after applying the assumptions listed at the beginning of Section 7.4.1.

The fluctuation in the optical depth is

$$\frac{\delta\tau_S}{\tau_S} = \delta_m + \frac{\delta x_{1s}}{x_{1s}} - \frac{\Theta}{aH} (\hat{\mathbf{k}} \cdot \hat{\mathbf{n}})^2. \quad (7.54)$$

We decompose the angular dependence of quantities into their spherical harmonic components. (This – or some more sophisticated variant – is the standard approach for Boltzmann solvers that predict CMB anisotropies [160, 347–349, 360].) It is convenient to orient the z-axis, $\hat{\mathbf{z}}$, along the wave vector, \mathbf{k} . Due to azimuthal symmetry about this axis, quantities depend on direction only through $\mu = \hat{\mathbf{k}} \cdot \hat{\mathbf{n}}$, and the spherical harmonics reduce to the appropriate Legendre polynomials. The explicit forms of the decomposition and its inverse for the PSD are [160, 360]

$$\delta f(\nu, k, \mu) = \sum_j (-i)^j \delta f_j(\nu, k) P_j(\mu), \quad (7.55a)$$

$$\delta f_j(\nu, k) = \frac{2j+1}{2} \int d\mu i^j P_j(\mu) \delta f(\nu, k, \mu). \quad (7.55b)$$

We substitute the expansion (7.55) into Eq. (7.53) to get the Boltzmann equations for the moments. The equation for the zeroeth moment is

$$\begin{aligned} \frac{\partial \delta f_0}{\partial \nu} &= \frac{\delta\tau_{S,0}}{\tau_S} \frac{\partial f}{\partial \nu} - \tau_S \phi(\nu) \left[\delta f_{\text{eq}} - p_{\text{sc}} \delta \bar{f}_0 \right] \\ &+ \frac{ck}{3H\nu a} \delta f_1 + p_{\text{ab}} \tau_S \phi(\nu) \delta f_0 + \tau_{\text{sc}} \left\{ \phi(\nu) \delta f_0 \right. \\ &\left. - \int d\nu' \phi(\nu') p(\nu|\nu') \delta f_0(\nu') \right\}. \end{aligned} \quad (7.56)$$

The term within curly braces is the scattering contribution, which redistributes photons within the line. We replace it with a second-order differential operator under the Fokker-Planck approximation, in the same manner as in the homogenous case.

$$\begin{aligned} \frac{\partial \delta f_0}{\partial \nu} &= \frac{\delta\tau_{S,0}}{\tau_S} \frac{\partial f}{\partial \nu} - \tau_S \phi(\nu) \left[\delta f_{\text{eq}} - p_{\text{sc}} \delta \bar{f}_0 \right] + \frac{ck}{3H\nu a} \delta f_1 \\ &+ p_{\text{ab}} \tau_S \phi(\nu) \delta f_0 - \tau_{\text{sc}} \frac{\nu_{\text{Ly}\alpha}^2 \Delta_{\text{H}}^2}{2} \frac{\partial}{\partial \nu} \left[\phi(\nu) \frac{\partial \delta f_0}{\partial \nu} \right]. \end{aligned} \quad (7.57)$$

The Boltzmann equations for the higher moments, with $j \geq 1$, are of the form

$$\begin{aligned} \frac{\partial \delta f_j}{\partial \nu} &= \frac{ck}{H\nu a} \left[-\frac{j}{2j-1} \delta f_{j-1} + \frac{j+1}{2j+3} \delta f_{j+1} \right] \\ &+ \tau_S \phi(\nu) \delta f_j + \frac{\delta\tau_{S,2}}{\tau_S} \frac{\partial f}{\partial \nu} \delta_{j,2}, \end{aligned} \quad (7.58)$$

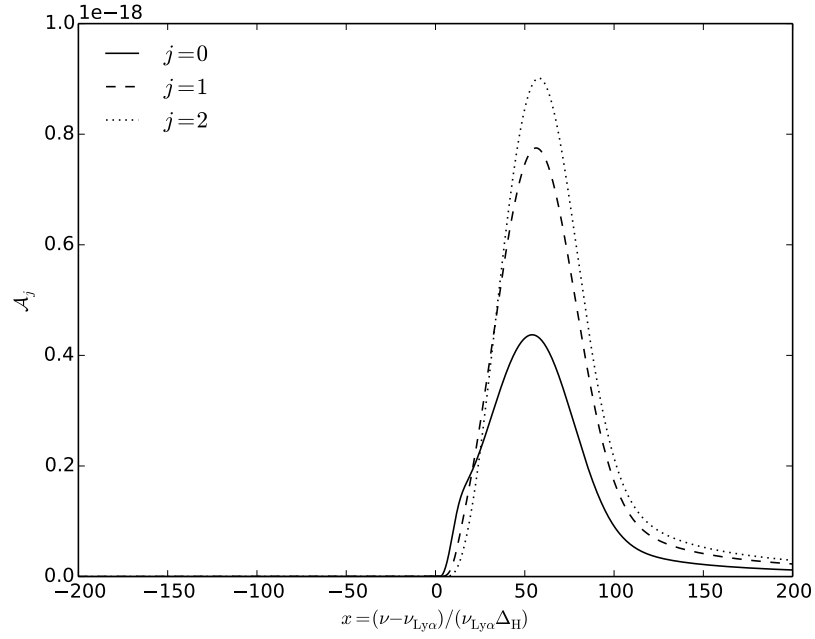
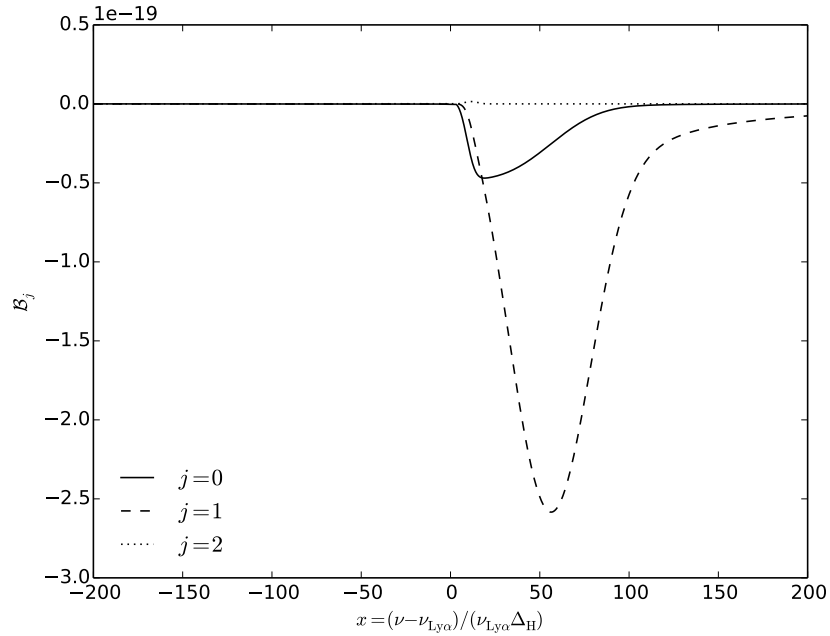
(a) Source: $\delta_m + \delta x_{1s}/x_{1s}$ (b) Source: Θ/aH

Figure 7.5: Basis solutions for the inhomogenous Boltzmann equation: (a) and (b) show the solutions \mathcal{A}_j and \mathcal{B}_j defined in Eq. (7.59). The source terms modulate the optical depth through the density and ground state population, and velocity gradient. This figure is generated for $k = 10^5 \text{ Mpc}^{-1}$ at redshift $z_0 = 1100$.

where the $\delta_{j,2}$ in the final term on the RHS equals unity if $j = 2$ and zero otherwise.

Equations (7.57)–(7.58) form a hierarchy for the moments of the PSD, δf_{j0} [160, 347]. Absorption, emission and redshifting of Ly α photons contribute to the evolution of each moment, while redistribution due to coherent scattering only contributes to the zeroeth moment. The latter is a direct consequence of the assumption of the isotropy of the redistribution function, $p(\nu, \hat{\mathbf{n}}|\nu', \hat{\mathbf{n}}')$ (assumption 6). In addition to this, free-streaming couples moments whose angular indices differ by unity [360].

We obtain the complete solution by adding the ones for each of the source terms as follows:

$$\begin{aligned} \delta f_j(\nu) = & \left(\delta_m + \frac{\delta x_{1s}}{x_{1s}} \right) \mathcal{A}_j(\nu) + \frac{\Theta}{aH} \mathcal{B}_j(\nu) \\ & + \left(\delta f_{\text{eq}} - p_{\text{sc}} \delta \bar{f}_0 \right) \mathcal{C}_j(\nu), \end{aligned} \quad (7.59)$$

where $\mathcal{A}_j, \mathcal{B}_j$, and \mathcal{C}_j are dimensionless solutions sourced by combinations of the first and second terms on the RHS of Eq. (7.57), and the last term on the RHS of (7.58). The notation for \mathcal{C}_j is used only in this section, and is not to be confused with Peebles' C factor.

We numerically solve the Boltzmann hierarchy of Eq. (7.57) and (7.58) for a set of multipoles from $j = 0$ to $j_{\text{max}} = 8$. We discretize a range of frequencies extending out to ± 1000 Doppler widths from the line center, with 50 bins per Doppler width, in the same manner as we did for the homogenous case. We assume that all the perturbed moments go to zero on the far blue side, i.e., a boundary condition of the Dirichlet type, with an additional Neumann boundary condition on the blue side for the zeroeth moment. We use a nonreflecting boundary condition at j_{max} to minimize the propagation of errors back to low values of j [160].

Figure 7.5 shows the resulting basis solutions \mathcal{A}_j and \mathcal{B}_j . These source terms for these solutions create regions of higher and lower optical depth, which accumulate over- and under-densities of photons in the blue damping wings of the Ly α line. The excess photons stream between these regions, which leads to characteristic features in higher moments as well. Since there is no injection of photons, the solutions go to zero on the red-side of the line-center.

Figure 7.6 shows the solution \mathcal{C}_j , whose source term includes δf_{eq} , which injects photons within the line. Due to these photons' large interaction cross section, local equilibrium between emission and absorption is achieved over a range of frequencies. This is reflected in the large and 'truncated' peak in the monopole. Also worth noting is the characteristic double peak in the dipole, which arises due to streaming away from the central frequency.

We solve for the perturbed monopole, $\delta \bar{f}_0$, by averaging Eq. (7.59) with $j = 0$ over the line profile.

$$\delta \bar{f}_0 = \frac{1}{1 + p_{\text{sc}} \bar{\mathcal{C}}_0} \left[\left(\delta_m + \frac{\delta x_{1s}}{x_{1s}} \right) \bar{\mathcal{A}}_0 + \frac{\Theta}{aH} \bar{\mathcal{B}}_0 + \delta f_{\text{eq}} \bar{\mathcal{C}}_0 \right]. \quad (7.60)$$

7.4.2 Perturbed recombination rate

Our goal is to compute the fluctuation in the recombination rate. We first consider the recombination rate within the Ly α line. The linearized form of Eq. (7.46) is

$$\delta\dot{x}_{1s}|_{\text{Ly}\alpha} = \frac{\delta x_{1s}}{x_{1s}} \dot{x}_{1s}|_{\text{Ly}\alpha} + 3x_{1s}A_{\text{Ly}\alpha} \left[\delta f_{\text{eq}} - \delta \bar{f}_0 \right]. \quad (7.61)$$

We substitute the expression (7.60) for the fluctuation in the monopole averaged over the line, to write this in terms of the dimensionless solutions defined in Eq. (7.59).

$$\begin{aligned} \delta\dot{x}_{1s}|_{\text{Ly}\alpha} &= \frac{\delta x_{1s}}{x_{1s}} \dot{x}_{1s}|_{\text{Ly}\alpha} + 3x_{1s}A_{\text{Ly}\alpha} \frac{1 - p_{\text{ab}}\bar{\mathcal{C}}_0}{1 + p_{\text{sc}}\bar{\mathcal{C}}_0} \delta f_{\text{eq}} - 3x_{1s}A_{\text{Ly}\alpha} \\ &\times \left[\left(\delta_m + \frac{\delta x_{1s}}{x_{1s}} \right) \frac{\bar{\mathcal{A}}_0}{1 + p_{\text{sc}}\bar{\mathcal{C}}_0} + \frac{\Theta}{aH} \frac{\bar{\mathcal{B}}_0}{1 + p_{\text{sc}}\bar{\mathcal{C}}_0} \right]. \end{aligned} \quad (7.62)$$

Next we consider the perturbation to the two-photon decay rate from the 2s level. This is only sourced by changes in the level populations, since the perturbed moments of the PSD go to zero on the far red side of the line [see Figs. 7.5 and 7.6]. The linearized form of Eq. (7.49) is

$$\delta\dot{x}_{1s}|_{2s} = \frac{\delta x_{1s}}{x_{1s}} \dot{x}_{1s}|_{2s} + \Lambda_{2s,1s} x_{1s} \delta f_{\text{eq}}. \quad (7.63)$$

To close Eqs. (7.62) and (7.63), we need to compute the fluctuation in the equilibrium PSD, δf_{eq} (or equivalently, the population of the $n = 2$ level). As in the homogenous case, we use the steady state assumption within the three level approximation, and balance the rates of the upper and lower arms of Figure 7.2.

For the upper arm, we perturb Eq. (7.50), which describes the change in the population of the $n = 2$ level due to photo-ionization and recombination from the continuum levels. We expect the fractional change in the population of the $n = 2$ level, x_2 , to be related to those in the other parameters of the system. The background value of x_2 is much smaller than the other states' populations [see discussion in Section 6.3]. Thus, it is a good approximation to set $\delta x_e + \delta x_{1s} = 0$. Using this,

$$\delta\dot{x}_2|_{\text{rec/ion}} = n_{\text{H}} x_e^2 \alpha_{\text{B}} \left[\delta_m + 2 \frac{\delta x_e}{x_e} \right] - \delta x_2 \beta_{\text{B}}. \quad (7.64)$$

$$\begin{aligned} &= n_{\text{H}} x_e^2 \alpha_{\text{B}} \delta_m - \left[2n_{\text{H}} x_e \alpha_{\text{B}} + 4f_{\text{eq}} \beta_{\text{B}} \right] \delta x_{1s} \\ &\quad - 4x_{1s} \beta_{\text{B}} \delta f_{\text{eq}}. \end{aligned} \quad (7.65)$$

The rate of the lower arm is the sum of the recombination rate in the Ly α line [Eq. (7.62)] and two-

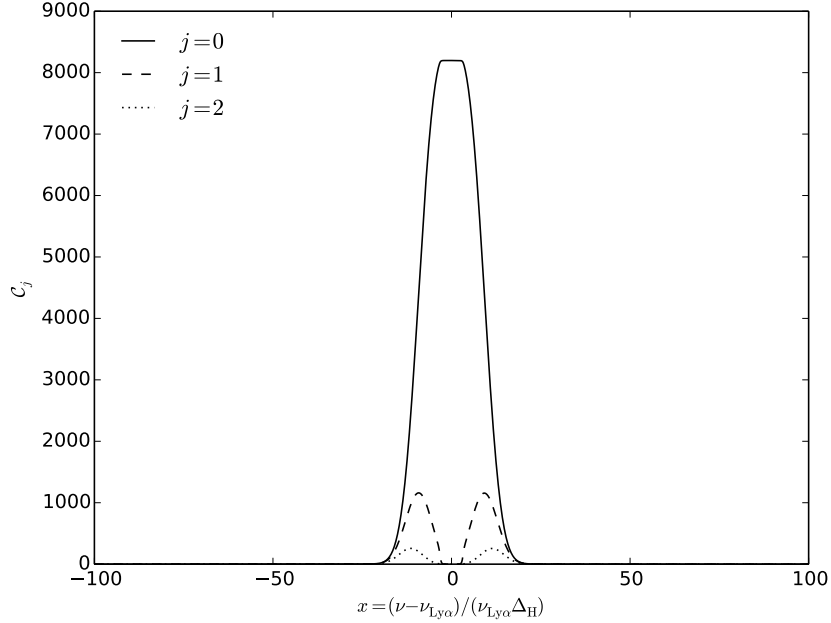


Figure 7.6: The case of injected photons: Shown above is the solution C_j as defined in Eq. (7.59), which perturbs the equilibrium PSD. This figure is generated for $k = 10^5 \text{ Mpc}^{-1}$ at redshift $z_0 = 1100$.

photon decays from the $2s$ state [(7.63)]. Using Eq. (7.50) for the background rate, and equating the sum with the RHS of Eq. (7.65), we get

$$\begin{aligned} \delta f_{\text{eq}} = & \left[3A_{\text{Ly}\alpha} \frac{1 - p_{\text{ab}}\bar{C}_0}{1 + p_{\text{sc}}\bar{C}_0} + \Lambda_{2s,1s} + 4\beta_{\text{B}} \right]^{-1} \\ & \times \left[n_{\text{H}} \frac{x_e^2}{x_{1s}} \alpha_{\text{B}} \left(\delta_{\text{m}} - \frac{\delta x_{1s}}{x_{1s}} \right) - 2n_{\text{H}} x_e \alpha_{\text{B}} \frac{\delta x_{1s}}{x_{1s}} + 3A_{\text{Ly}\alpha} \right. \\ & \left. \times \left\{ \left(\delta_{\text{m}} + \frac{\delta x_{1s}}{x_{1s}} \right) \frac{\bar{A}_0}{1 + p_{\text{sc}}\bar{C}_0} + \frac{\Theta}{aH} \frac{\bar{B}_0}{1 + p_{\text{sc}}\bar{C}_0} \right\} \right]. \end{aligned} \quad (7.66)$$

Before we compute the perturbed recombination rate, we define the quantity

$$\mathcal{P} = \frac{3A_{\text{Ly}\alpha} \frac{1 - p_{\text{ab}}\bar{C}_0}{1 + p_{\text{sc}}\bar{C}_0} + \Lambda_{2s,1s}}{3A_{\text{Ly}\alpha} \frac{1 - p_{\text{ab}}\bar{C}_0}{1 + p_{\text{sc}}\bar{C}_0} + \Lambda_{2s,1s} + 4\beta_{\text{B}}}. \quad (7.67)$$

This is the analog of Peebles' C factor [see Eq. (7.51)] in the perturbed case – it represents the probability that a fluctuation in the population of atoms in the $n = 2$ level translates into one in the ground state population.

Figure 7.7 plots \mathcal{P} as a function of the wavenumber. We observe that it asymptotes to a small value for large wavelengths. We expect this limiting value to be the Peebles C factor. It approaches

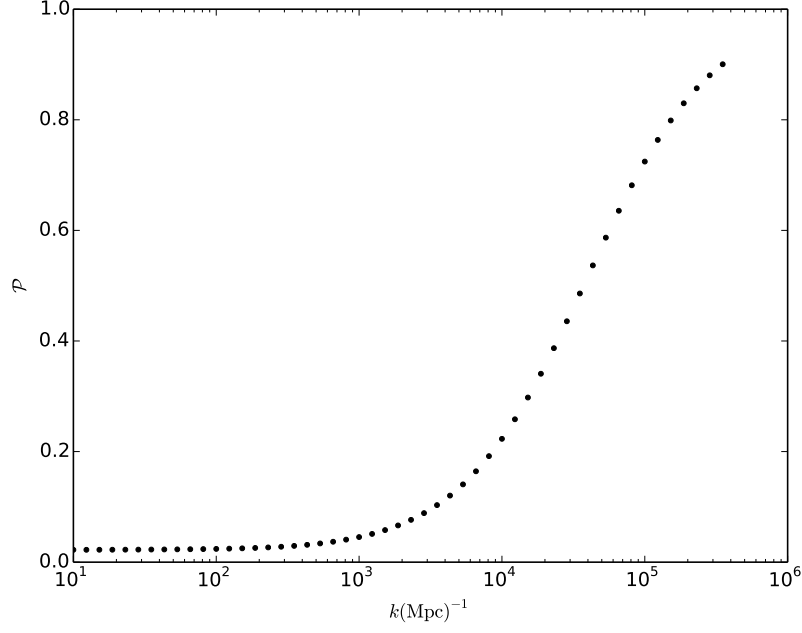


Figure 7.7: Inhomogenous analog of the Peebles C factor. The parameter \mathcal{P} defined in Eq. (7.67), as function of the wavenumber, k . It is the probability that a fluctuation in the population of $n = 2$ leads to one in that of $1s$. This figure plots values out to $k \approx 3.6 \times 10^5 \text{Mpc}^{-1}$, up to which matter fluctuations can be assumed to be isothermal.

unity in the complementary limit of small wavelengths, but we do not show this since the assumption of the isothermal nature of such small wavelength modes breaks down at low redshifts. This turnover happens on scales of $k \approx 10^3 \text{Mpc}^{-1}$, which is large compared to the diffusion scale at line center, which was calculated in Section 7.2. We give physical arguments for the large wavelength limit in Appendix 7.B, and the turnover scale for small wavelengths in Appendix 7.A.

We substitute Eq. (7.66) into Eqs. (7.62) and (7.63), and use the definition of \mathcal{P} to write the fluctuation in the net recombination rate as

$$\begin{aligned}
 \delta \dot{x}_{1s}|_{\text{Ly}\alpha, 2s} &= \mathcal{P} n_{\text{H}} x_e^2 \alpha_{\text{B}} \delta_{\text{m}} + \delta x_{1s} \left[(1 - \mathcal{P}) n_{\text{H}} \frac{x_e^2}{x_{1s}} \alpha_{\text{B}} \right. \\
 &\quad \left. - 2\mathcal{P} n_{\text{H}} x_e \alpha_{\text{B}} - 4f_{\text{eq}} \beta_{\text{B}} \right] - 3(1 - \mathcal{P}) x_{1s} A_{\text{Ly}\alpha} \\
 &\quad \times \left[\left(\delta_{\text{m}} + \frac{\delta x_{1s}}{x_{1s}} \right) \frac{\bar{\mathcal{A}}_0}{1 + p_{\text{sc}} \bar{\mathcal{C}}_0} + \frac{\Theta}{aH} \frac{\bar{\mathcal{B}}_0}{1 + p_{\text{sc}} \bar{\mathcal{C}}_0} \right]. \tag{7.68}
 \end{aligned}$$

In Appendix 7.A.2, we derive the expression for the perturbed recombination rate for wavelengths much smaller than the diffusion scale, and show that it is identical to the above expression in the limit $\mathcal{P} \rightarrow 1$.

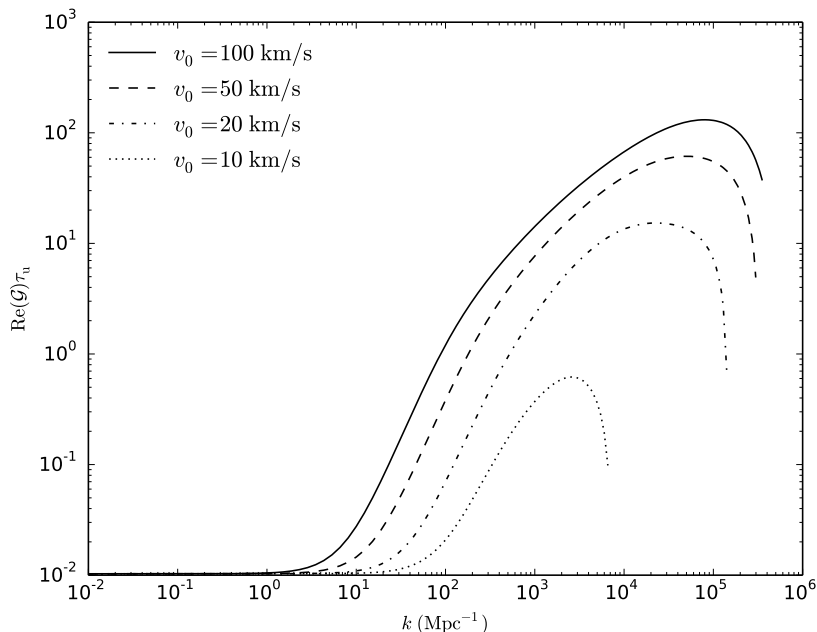


Figure 7.8: Maximum instantaneous growth rate for small-scale fluctuations in the matter field at recombination, normalized to the net elapsed coordinate time, τ_u . The scenario here is identical to that of Figure 7.1, except that perturbed recombination is treated with full radiative transport of Continuum and Lyman- α photons.

7.5 Solution for the local growth rates

We solve for the local growth rates by finding the fastest growing modes of the matter field. We use Eq. (7.5) for the evolution of the matter density and velocity, and obtain the evolution equation for the perturbed ionization fraction by adding the rates of perturbed recombination due to Ly α photons and two-photon decays from $2s$ [Eq. (7.68)] and Continuum photon transport [Eq. (7.26)]. We use case B recombination coefficients from [361] for numerical estimates.

Figure 7.8 plots the maximum instantaneous growth rate for small-scale matter fluctuations at recombination (normalized to the net elapsed coordinate time, τ_u at $z = 1100$) for various values of the large scale shear v_0 . Comparison with the results of Figure 7.1 shows that the instability persists, and even somewhat strengthened, on intermediate scales with wavenumber $k \approx 10^2 \text{ Mpc}^{-1}$. However, it is cut off on small scales due to the radiative processes described in Sections 7.3 and 7.4. The precise wavenumber at which it is cut off depends on the large-scale relative velocity, but is well before the saturation scale over the practically achievable range.

In the next section, we estimate the growth rates achieved due to a stochastic background relative velocity, the distribution for which was introduced in Section 6.3.

7.6 Distribution of growth factors

The growth rate shown in Figure 7.8 is a general property of the equations of motion calculated in the presence of a constant background relative velocity. In actuality, this background velocity at a given location and time is picked from the distribution of Eq. (6.13) of Section 6.3. Moreover, values at nearby redshifts are correlated with each other. Thus we should critically consider how this distribution is sampled over time.

Towards this end, we generalize the equal-time distribution of Eq. (6.13) to

$$\langle v_{0,i}(\mathbf{x}, t) v_{0,j}^*(\mathbf{x}, t') \rangle = \frac{1}{3} \delta_{ij} \int d \ln k \mathcal{F}(k; t, t') \Delta_{\zeta}^2(k), \quad (7.69)$$

$$\mathcal{F}(k; t, t') = \frac{1}{k^2} [\theta_m(k, t) - \theta_r(k, t)] [\theta_m(k, t') - \theta_r(k, t')]^*. \quad (7.70)$$

The direction of the relative velocity, $\mathbf{v}_0(\mathbf{x})$ at a given point \mathbf{x} , varies with time. The force term, \mathbf{f}_{rad} , in the equation of motion (7.1b), depends on the direction of the local wavevector relative to the background velocity. We proceed under the simplifying assumption that the fastest growing mode always aligns itself; this is true in the case where the timescale for growth is much smaller than that for change in the relative velocities. Thus the linear growth factors obtained are upper bounds to the actual ones achieved.

We use the notation $\mathcal{T}(\mathbf{k}, \mathbf{x})$ to denote the net growth factor of fluctuations with wave vector \mathbf{k} in a small region around a point \mathbf{x} . This quantity depends on the entire relative velocity history, $\mathbf{v}_0(\mathbf{x}, t)$. At any point on the history, the growth rate is the largest eigenvalue of the equations of motion [Eqns. (7.5b), (7.81), and (7.26)]. As earlier, we denote this eigenvalue by \mathcal{G} . The growth factor in a small region around a point, \mathbf{x} , due to linear physics, and over the velocity history, is

$$\mathcal{T}(\mathbf{k}, \mathbf{x}) = \exp \left[\int dt \operatorname{Re}(\mathcal{G})(\mathbf{k}, \mathbf{v}_0(\mathbf{x}, t)) \right]. \quad (7.71)$$

Note that $\mathcal{T}(\mathbf{k}, \mathbf{x})$ is normalized to unity in the absence of any growth or suppression. The relation in Eq. (7.71) endows the growth factor with a distribution that is inherited from that of the velocity histories. For a particular realization of the relative velocity field $\mathbf{v}_0(\mathbf{x}, t)$, the value of $\mathcal{T}(\mathbf{k}, \mathbf{x})$ varies when both its input wave-vector \mathbf{k} and position \mathbf{x} are varied. However, over the entire set of realizations, there is no dependence on the direction $\hat{\mathbf{k}}$ and the position \mathbf{x} , due to the isotropy and homogeneity of the fluctuations underlying the relative velocities. With this understanding, we use the condensed notation $\mathcal{T}(k)$ for the growth factors.

We generate a large number of these velocity histories in an efficient manner by sampling the distribution with the covariance matrix of Eq. (7.69). We numerically sample these velocity histories at 90 redshifts between $z = 800$ and $z = 1430$, and evaluate Eq. (7.71) by spline integration. In order to illustrate the tail of the growth distribution, we choose to plot the mean growth factor achieved

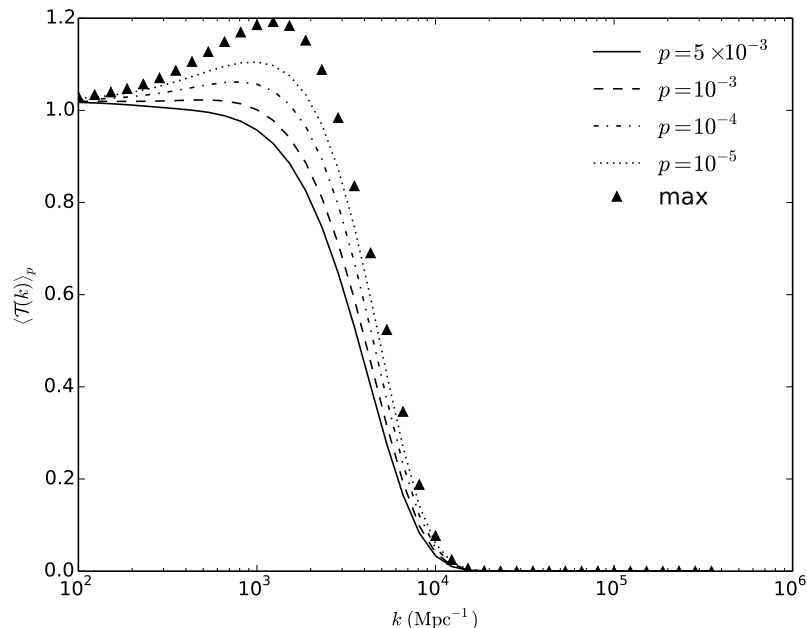


Figure 7.9: This figure plots the mean growth factor $\langle \mathcal{T}(k) \rangle_p$ achieved in the highest p^{th} fraction of a sample set of 10^7 velocity histories, for successively smaller p -values and a range of wavenumbers. The growth factor is normalized such that it is unity when there is no growth or suppression. Also shown is the largest growth factor for each wavenumber achieved in this sample set. Note that the growth is suppressed on scales on which the linear analysis predicts the strongest instability for large relative velocities ($k > 10^4 \text{ Mpc}^{-1}$, from Figure 7.8).

in the highest p^{th} fraction of the realizations. We formally define this as

$$\langle \mathcal{T}(k) \rangle_p = \frac{1}{Np} \sum_{i=N-Np+1}^N \mathcal{T}_i(k). \quad (7.72)$$

In this equation, N is the number of realizations of the relative velocity history, $\mathbf{v}_0(\mathbf{x}, t)$, which have been sorted in increasing order of the value of \mathcal{T} for the purpose of the summation. The p in this definition corresponds to the usual notion of p -value. This use of the symbols N and p is restricted to this section alone, and they do not represent the number flux and momentum here.

Figure 7.9 shows the tails $\langle \mathcal{T}(k) \rangle_p$ estimated from a set of 10^7 samples of the relative velocity history, for a range of wave numbers k . Note that Figure 7.8 predicts that small-scale modes of wavelengths $k \sim 10^5 \text{ Mpc}^{-1}$ are most unstable for a constant large-scale relative velocity. The growth factors estimated in Figure 7.8 are optimistic for two reasons: firstly, they depend on the distribution of the *histories*, i.e. time-series of large-scale relative velocities, and secondly and most importantly, the instability is only active during the time where the electrons and photons are coupled, and this is much smaller than the coordinate time due to the short duration of recombination.

7.7 Discussion

The analysis in this chapter accomplishes our primary goal of answering the question of the stability of small-scale fluctuations in the matter field at recombination. Our main conclusions in this regard is that *while growing sound wave modes exist, the amount of growth that occurs during the cosmic recombination epoch is only a fraction of an e -fold, and we do not expect the unstable modes to produce any phenomenological consequences.* Fluctuations with comoving wavenumbers satisfying $k > 10^2 \text{ Mpc}^{-1}$ are unstable in the presence of large-scale relative velocities between matter and radiation. On intermediate scales, this instability persists in the face of, and is even strengthened by the transport of continuum photons above the photo-ionization threshold, and photons within the Ly α line of neutral hydrogen. However, this transport cuts off the growth before the saturation scale of $k \approx 10^5 \text{ Mpc}^{-1}$.

The linear analysis of the fluctuations only yields instantaneous growth rates for a constant large-scale relative velocity; the true growth factor within a given patch depends on the local relative velocity over a range of redshifts, and occurs for a duration (the width of recombination) that is shorter than the coordinate time. Accounting for this, we find no appreciable growth within a large number of random realizations of the relative velocity history. The largest growth factor achieved in our sample set, which corresponds to a p -value of 10^{-7} , is slightly less than 1.2, for modes with wavenumber $k \approx 10^3 \text{ Mpc}^{-1}$.

Along the way, we made a number of simplifying assumptions to facilitate the solution of the complicated problem of perturbed recombination. We examine a few of them below.

The first, and most helpful one, is the three level model of the hydrogen atom, which assumes radiative equilibrium between upper levels of the true hydrogen atom. This is a good assumption at high redshifts, but becomes progressively worse as the redshift approaches $z \simeq 800$, at which point it is approximately a 10% correction. In the context of homogenous recombination, there have been two approaches to deal with this: follow the higher levels in a consistent manner [169], or multiply the case-B recombination coefficient, α_B , with a fudge factor [336]. We eschew this additional complication in our preliminary analysis; instead, we generate realizations and compute growth rates only for redshifts $z \geq 800$, where the instability is expected to be strongest.

A second assumption is the equality of matter and radiation temperatures, which allows us to compute the recombination and photo-ionization rates at the CMB temperature. This is an excellent approximation for the background temperatures during the redshifts of interest due to the high Thomson scattering rates [336]. Its validity is much less clear in the perturbed case; a detailed discussion of timescales can be found in Ref. [344]. In our case, the relevant comparison is the dimensionless ratio t_{sc}/t_C of the sound-crossing time $t_{sc} = a/(kv_{s,1})$ to the Compton cooling time $t_C = 3m_e c(1 + f_{\text{He}} + x_e)/(8\sigma_{\text{T}} a_{\text{rad}} T_{\gamma}^4 x_e)$. These timescales are equal at a critical wavenumber

k_{cr} : sound waves are isothermal for $k \ll k_{\text{cr}}$ and adiabatic (or at least decoupled from the CMB temperature) for $k \gg k_{\text{cr}}$. We find that k_{cr} decreases with time, equaling 10^8 Mpc^{-1} at $z = 1290$, 10^7 Mpc^{-1} at $z = 1020$, 10^6 Mpc^{-1} at $z = 870$, and 10^5 Mpc^{-1} at $z = 690$. Thus for the range of redshifts we consider in this investigation (up to $z = 800$), we can make the isothermal approximation for modes of wavenumbers up to $k \approx 3.6 \times 10^5 \text{ Mpc}^{-1}$.

Another factor we have not included in our analysis is the transport of the microwave background photons themselves between different parts of the fluctuations. Rather we have assumed that the CMB photons can freely stream through many perturbation wavelengths. At the earliest redshift considered herein, $z = 1430$, the photon comoving attenuation coefficient [inverse comoving mean free path: $1/(n_{\text{H}} a x_e \sigma_{\text{T}})]$ is 0.8 Mpc^{-1} . This is much smaller than the wave numbers k under consideration here, justifying the treatment of the CMB as uniform.

Finally, in a larger context, this work solves the problem of perturbed recombination for modes on very small scales. Previous work on large-scale modes relevant to the linear fluctuations in the CMB [344, 362, 363] has shown that the ionization fraction obtained by perturbing the ODE resulting from the three-level model of the hydrogen atom is accurate enough for all practical purposes. This breaks down for very small-scale modes; modulo the proper prescription for the perturbed kinetic temperature, the method outlined in Sections 7.3 and 7.4 helps solve the problem in this limit.

7.A Lyman- α transport: Diffusion-dominated regime

In this section, we study the diffusion of Ly α photons during the epoch of recombination. In the first part of this section, we demonstrate that the length scale for their transport is much larger than the simple estimate of Eq. (7.8). In the second part, we derive a simple expression for the perturbed rate of recombination in the Ly α and two-photon channels when the wavelength of the fluctuations is much smaller than this scale.

7.A.1 Length scale for diffusion

We begin by studying the redistribution of Ly α photons' frequency due to resonant scattering off ground-state hydrogen atoms.

The Sobolev optical depth, τ_{S} , is much greater than unity at the redshift of recombination [see the estimate following Eq. (7.28)]. The overwhelming majority of absorptions are followed by the spontaneous de-excitation of the excited atom [see Eq. (7.27)]. Thus the timescale for coherent scattering is much shorter than the Hubble time for a photon in the Doppler core of the Ly α line. A large number of scattering events effectively scrambles the initial frequency over a short time, and the emitted photon's frequency is well described by a distribution over the line profile which is

incoherent with the initial one.

$$p(\nu_{\text{out}}|\nu_{\text{in}}) = \phi(\nu_{\text{out}}), \quad (7.73)$$

where we have adopted a suggestive notation for the probability distribution.

The mean free path of the scattered photon is obtained by averaging over this frequency distribution

$$\langle l_{\text{mfp}}(\nu) \rangle = \left\langle \frac{1}{n_{1s}\sigma_{\text{sc}}(\nu)} \right\rangle = \frac{1}{\tau_{\text{S}}H} \frac{c}{\nu_{\text{Ly}\alpha}} \left\langle \frac{1}{\phi(\nu)} \right\rangle \rightarrow \infty. \quad (7.74)$$

Physically, this is a consequence of the Ly α photon rapidly scattering out of the core into the wings, where the probability of further scattering is very small. The repeated scattering and resulting diffusion is not described by typical Brownian motion with the steps drawn from a globally Gaussian distribution. Thus the mean free path at line center, in Eq. (7.8), is a poor guide to the Ly α transport scale.

In the rest of this section, we look at this random walk's step size distribution in more detail, and estimate a scale for the Ly α photon transport.

A general random walk is studied by following a collection of walkers starting at the origin. It is characterized by the distribution of their density after a given number of steps. The asymptotic form of this distribution is [364]

$$p_N(\mathbf{x}) = \frac{1}{N^{(d/\alpha)}} L_\alpha \left[\frac{\mathbf{x}}{N^{(1/\alpha)}} \right], \quad 0 < \alpha \leq 2, \quad (7.75)$$

where d is the dimensionality of the random walk ($d = 3$ in our case), and $L_\alpha[\mathbf{x}]$ is a stable distribution. Its index, α , is fixed by the tail of the distribution of the step size:

$$\lim_{x \rightarrow \infty} p(x) \sim \frac{1}{x^{1+\alpha}}. \quad (7.76)$$

We estimate the index in our case by marginalizing over the frequency of the scattered photon.

$$\begin{aligned} p(x) &= \int d\nu p(\nu) p(x|\nu) \\ &\sim \int d\nu \phi^4(\nu) x^2 \exp[-x^2 \phi^2(\nu)] \xrightarrow{x \rightarrow \infty} x^{-2}. \end{aligned} \quad (7.77)$$

The argument for the scaling in Eq. (7.77) is that the dominant contribution to the integral at large step sizes, i.e., when $x \rightarrow \infty$, is from frequencies satisfying $\phi(\nu) \leq x^{-1}$; the prefactor is exponentially suppressed when we move a few Doppler widths away. Through Eq. (7.76), this implies a distribution of the form Eq. (7.75) for the density distribution, with an index of around unity.

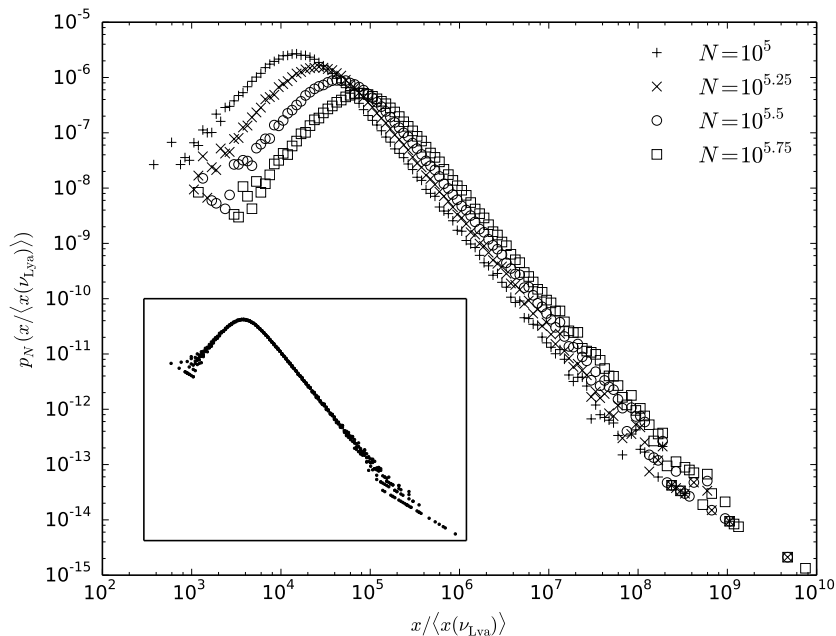


Figure 7.10: Histograms of the displacements of 10^5 photons after N scattering events, in units of the mean step size at the Ly α line-center, $\langle x(\nu_{Ly\alpha}) \rangle$. They are normalized to integrate to unity. **Inset:** Demonstration of their scaling property. The histograms collapse onto a common form when the displacement, \mathbf{x} , is rescaled by a factor of $N^{1/\alpha}$, with the index $\alpha = 1.06$.

We confirm this observation by following a large number of photons through simulated scattering events. Following each event, we redistribute the frequency incoherently according to Eq. (7.73), neglect any direction dependence, and pick the subsequent step with a Gaussian distribution for its size, with the MFP at that frequency.

Figure 7.10 shows the density distributions following a large number of scattering events, N , and the collapse of these distributions onto a universal form when the displacements are scaled appropriately.

The displacement does not follow the usual \sqrt{N} law of Brownian motion – instead, the histograms collapse onto a universal form when the independent variable is scaled as $N^{1/\alpha}$ with $\alpha = 1.06$. Also notable is the fact that the resulting universal form is a fat-tailed distribution which exhibits power law scaling, rather than the usual exponential falloff of the Gaussian distribution.

The quantity of direct interest for transport properties is the spread in a given time, t . The diverging mean-free path leads to a spread which approaches ballistic transport, and hence the distributions are significantly cut off by the maximum distance ct .

As before, we directly sample the distributions through a large number of simulated scattering events. Their spread is fit by a power-law dependence of the form $\langle x^2(t) \rangle \sim t^{1.88}$.

To gauge the implications for the importance of Ly α photon transport, we consider the various

processes involved in perturbed recombination, schematically represented in Figure 7.2. The response time to a fluctuation in the ionization fraction is set by the speed of the case B recombination arm, $t_r = (1/n_e\alpha_B)$. From the near-ballistic transport discussed above, the time taken by a Ly α photon to diffuse across the fluctuation is comparable to the wave crossing time $t_d \approx (\lambda_{\text{phys}}/c)$. From Figure 7.1, we see that comoving wave-numbers of $k \sim 10^5 \text{ Mpc}^{-1}$ are most relevant for the instability. On these length scales, the wave crossing time and response time are

$$t_d \approx \frac{2\pi a}{kc} = 0.2 \text{ yr} \ll t_r \approx 200 \text{ yr} \text{ at } z = 1100. \quad (7.78)$$

These two timescales become comparable for wavenumbers $k \approx 10^2 \text{ Mpc}^{-1}$ at the redshift of recombination, which is when the nonlocal radiative transport starts to matter. These wavelengths are significantly larger than the simple estimate of Eq. (7.8). This is borne out by Figure 7.7. The practical consequence is that for modes with wavelengths smaller than this, perturbed recombination cannot be modeled by simply varying the cosmological parameters of the homogenous solution.

7.A.2 Recombination rate in diffusion-dominated regime

This section uses the notation of Section 7.4 for the moments of the photons' phase space density. In particular, inhomogeneities in the zeroeth moment, $\delta f_0(\nu_{\text{Ly}\alpha}, \mathbf{x})$, drive transport of Ly α photons. We consider fluctuations with small enough wavelengths so that the Ly α photons easily diffuse between the peaks and troughs. In this case, the Ly α flux adjusts itself to wash out inhomogeneities in the zeroeth moment.

The population of the first excited level is set by balancing the transition rates to and from the ground state. The condition that the Ly α phase space density is uniform yields

$$\delta f_0(\nu_{\text{Ly}\alpha}, \mathbf{x}) = \delta(f_{\text{eq}}) = 0, \quad (7.79)$$

$$\delta x_2 = 4f_{\text{eq}}\delta x_{1s}. \quad (7.80)$$

The precise details of the radiative transfer determine the adjustment in the Ly α flux — we avoid studying that part of the mechanism by considering the case B recombination arm of Fig 7.2. All that is needed to solve the recombination arm is the fluctuation in the population of the $n = 2$ level, which is given by Eq. (7.80):

$$\begin{aligned} \delta \dot{x}_e|_{\text{Ly}\alpha, 2s} &= \delta(-n_{\text{H}}x_e^2\alpha_{\text{B}} + x_2\beta_{\text{B}}) \\ &= -n_{\text{H}}x_e^2\alpha_{\text{B}} \left[\delta_{\text{m}} + 2\frac{\delta x_e}{x_e} \right] + \beta_{\text{B}}\delta x_2 \\ &= -n_{\text{H}}x_e^2\alpha_{\text{B}}\delta_{\text{m}} - \left[2n_{\text{H}}x_e\alpha_{\text{B}} + 4f_{\text{eq}}\beta_{\text{B}} \right] \delta x_e. \end{aligned} \quad (7.81)$$

This matches the $\mathcal{P} \rightarrow 1$ limit of the result of the complete analysis, Eq. (7.68).

7.B Limit of weak diffusion

In this section we work out an analytical solution to the Boltzmann hierarchy in a situation with weak diffusion. This is the complementary limit to that considered in Appendix 7.A, and is realized when the wavelength of the fluctuations is much larger than the length scale for the diffusion of the $\text{Ly}\alpha$ photons. We restrict ourselves to the source term in Eq. (7.57) involving δf_{eq} .

7.B.1 Anisotropic part of hierarchy

Let us consider the hierarchy of equations for the moments with $j \geq 1$, Eq. (7.58). If the range of frequencies $\Delta\nu_{\nu}$ over which δf_{j0} varies is larger than

$$\Delta\nu_{\text{mfp}} = \frac{1}{\tau_{\text{S}}\phi(\nu)} \approx \frac{4\pi^2(\nu - \nu_{\text{Ly}\alpha})^2}{A_{\text{Ly}\alpha}\tau_{\text{S}}} \quad (7.82)$$

(where the approximation is in the damping wings), the photons' scattering rate is faster than that of their redshift through the frequency range of interest, and we may drop the left hand side. We expect this to be valid since $\Delta\nu_{\text{mfp}} < |\nu - \nu_{\text{Ly}\alpha}|$ in the damping wings, even out to $|\nu/\nu_{\text{Ly}\alpha} - 1|$ of order unity.

This condition is satisfied very easily in the Doppler core due to the high scattering rates:

$$\Delta\nu_{\text{mfp,core}} = \nu_{\text{Ly}\alpha}\Delta_{\text{H}}\frac{\sqrt{\pi}}{\tau_{\text{S}}}e^{(\nu - \nu_{\text{Ly}\alpha}/\nu_{\text{Ly}\alpha}\Delta_{\text{H}})^2} \ll \nu_{\text{Ly}\alpha}\Delta_{\text{H}}. \quad (7.83)$$

Dropping the left-hand side of Eq. (7.58) converts the system of ODEs into an algebraic hierarchy. We can define the frequency-dependent parameter

$$q = q(\nu, k) \equiv \frac{H\nu\alpha\tau_{\text{S}}\phi(\nu)}{ck} \quad (7.84)$$

$$= 1.1 \times 10^6 \left(\frac{k}{10^5 \text{ Mpc}^{-1}} \right)^{-1} \phi_{\text{V}}(x) \text{ at } z = 1100, \quad (7.85)$$

which is the optical depth for photons to travel a comoving distance k^{-1} at that frequency. We then reduce Eq. (7.58) to

$$0 = q^{-1} \left[-\frac{j}{2j-1} \delta f_{j-1} + \frac{j+1}{2j+3} \delta f_{j+1} \right] + \delta f_j \quad (7.86)$$

(for $j \geq 1$). It is convenient at this point to transform back to angle-space, i.e. to work with the function $\delta f(\nu, k, \mu)$. Multiplying Eq. (7.86) by 2 and using the inverse transformation of Eq. (7.55),

we see that

$$0 = \int_{-1}^1 d\mu \delta f(\mu) \left[iq^{-1} j P_{j-1}(\mu) + iq^{-1} (j+1) P_{j+1}(\mu) + (2j+1) P_j(\mu) \right]. \quad (7.87)$$

Using the multiplication formula for the Legendre polynomials gives

$$0 = (2j+1) \int_{-1}^1 d\mu P_j(\mu) \delta f(\mu) (iq^{-1} \mu + 1). \quad (7.88)$$

This holds for all $j \geq 1$, hence the solution is that the combination $(iq^{-1} \mu + 1) \delta f(\mu)$ must be a constant independent of μ :

$$\delta f(\mu) = \mathcal{F} \frac{1}{1 + iq^{-1} \mu}. \quad (7.89)$$

In particular, the relation between the first and zeroth moments is

$$\begin{aligned} \frac{\delta f_1(\nu, k)}{\delta f_0(\nu, k)} &= 3i \frac{\int_{-1}^1 d\mu \mu \delta f(\nu, k, \mu)}{\int_{-1}^1 d\mu \delta f(\nu, k, \mu)} \\ &= 3i \frac{\int_{-1}^1 d\mu \mu (1 + iq^{-1} \mu)^{-1}}{\int_{-1}^1 d\mu (1 + iq^{-1} \mu)^{-1}} \\ &= -3q \left[1 - \frac{1/q}{\arctan(1/q)} \right]. \end{aligned} \quad (7.90)$$

7.B.2 The isotropic part

It remains to solve the equation for $\delta f_0(\nu, k)$. We substitute the relation (7.90) into Eq. (7.57), and retain the source term of interest to get the Boltzmann equation for this moment

$$\begin{aligned} \frac{\partial \delta f_0}{\partial \nu} &= -\tau_S \phi(\nu) [\delta f_{\text{eq}} - p_{\text{sc}} \delta \bar{f}_0] - \tau_{\text{sc}} \frac{\nu_{\text{Ly}\alpha}^2 \Delta_{\text{H}}^2}{2} \frac{\partial}{\partial \nu} \left[\phi(\nu) \frac{\partial \delta f_0}{\partial \nu} \right] \\ &\quad + \tau_S \phi(\nu) \left[p_{\text{ab}} - \left\{ 1 - \frac{1/q}{\arctan(1/q)} \right\} \right] \delta f_0. \end{aligned} \quad (7.91)$$

The boundary condition is that $\delta f_{00,+} = 0$ (i.e. no perturbation to the incoming radiation on the blue side of the line). The solution $\mathcal{C}_0(\nu)$ of Eq. (7.59) is determined by setting $\delta f_{\text{eq}} - p_{\text{sc}} \delta \bar{f}_{00} = 1$ in Eq. (7.91).

We examine the simplest case, where the frequency diffusion term is negligible. In the limit we are considering in this section, the wave-number $k \rightarrow 0$. In that case, the parameter $q \rightarrow \infty$, and

the term in curly braces on the RHS of Eq. (7.91) approaches zero. Taking this limit, we have

$$\frac{\partial \delta f_0}{\partial \nu} = \tau_S \phi(\nu) p_{\text{ab}} \delta f_0 - \tau_S \phi(\nu). \quad (7.92)$$

Defining the cumulative distribution function of the profile $\mathcal{X} = \int d\nu \phi(\nu)$ (so that \mathcal{X} ranges from 0 at the red side of the line to 1 at the blue side), we may solve this equation to yield

$$\delta f_0(\nu) = \frac{1}{p_{\text{ab}}} \left[1 - e^{p_{\text{ab}} \tau_S (\mathcal{X} - 1)} \right]. \quad (7.93)$$

Averaging over the line profile is equivalent to the integration $\int_0^1 d\mathcal{X}$:

$$\bar{\mathcal{C}}_0 = \delta \bar{f}_0 = \frac{1}{p_{\text{ab}}} \left(1 - \frac{1 - e^{-\tau_S p_{\text{ab}}}}{\tau_S p_{\text{ab}}} \right). \quad (7.94)$$

It follows that

$$\frac{1 - p_{\text{ab}} \bar{\mathcal{C}}_0}{1 + p_{\text{sc}} \bar{\mathcal{C}}_0} = \frac{1}{\tau_S} \frac{1 - e^{-\tau_S p_{\text{ab}}}}{1 - p_{\text{sc}} (1 - e^{-\tau_S p_{\text{ab}}}) / (\tau_S p_{\text{ab}})}. \quad (7.95)$$

In the relevant optically thick limit of $\tau_S p_{\text{ab}} \gg 1$, this becomes equivalent to the usual Sobolev escape probability, $\approx 1/\tau_S$. Substitution into the definition of \mathcal{P} in Eq. (7.67) recovers the standard Peebles' C factor of Eq. (7.51).

Part III

A new probe of magnetic fields in the pre-reionization epoch

Chapter 8

Preliminaries¹

8.1 Introduction

Magnetic fields (MFs) are seen in astrophysical structures on a wide range of observable scales, both in the local universe [365, 366] and at high redshifts [367]. Typical field strengths in galaxies and galaxy clusters are a few to a few tens of μG , with coherence lengths of up to hundreds of kpc [368]. In contrast, the properties of the intergalactic magnetic field, i.e. that on larger length scales, are largely unknown.

The leading paradigm for the origin of large-scale cosmic MFs assumes some kind of amplification and dynamo-based sustaining of weak seed fields [369]. These seed fields may originate from mechanisms effective during structure formation, or could be primordial remnants from the early universe (see, for example, Refs. [369–373]). The search for primordial magnetic fields (PMFs) is an active area of investigation in astrophysics and cosmology, as their observation would open up a new window into the physics of the early universe and possibly provide an entirely unexplored source of information about inflationary and pre-reheating processes.

Current upper limits on large-scale MFs come from several different observations, and are on the order of 10^{-9} G. They are derived from the limits on Faraday rotation of the cosmic-microwave-background (CMB) polarization [188] and of the radio emission from distant quasars [189], measurements of the CMB temperature anisotropies [191], limits on CMB spectral distortions [192], and various observations of large scale structure [190].

More recently, observations of TeV sources by the Fermi mission have been interpreted as implying the existence of magnetic fields stronger than 10^{-15} G with Mpc scale coherence lengths, in local large-scale-structure (LSS) voids [193–195]. Plasma instabilities might avoid these bounds by eliminating the expected cascade of lower-energy gamma rays [196], but recent calculations indicate

¹The material in Chapters 8–10 was adapted from the manuscript *A new probe of magnetic fields in the pre-reionization epoch: Formalism*, Venumadhav, T., Oklopčić, A., Gluscevic, V., Mishra, A., & Hirata, C. M. 2014, arXiv:1410.2250, currently under consideration for publication in Physical Review D. Reproduced here with permission, copyright (2014) by the American Physical Society.

these instabilities might saturate, and thus challenge the viability of this argument [197, 198] (but see also Ref. [199])). The lower limit may also be reduced if the TeV emission timescale is short, since the arrival of the lower-energy cascade photons is delayed relative to the direct TeV photons [200, 201].

All these methods have their advantages, but share the common feature of being sensitive to the integrated effect of any MFs along a line of sight. Thus their measurements can be contaminated by low-redshift magnetic fields of astrophysical origin, for instance, those carried by galactic winds. Moreover, these methods optimally detect only fields which are much stronger than typical expectations for PMFs. Thus a definitive probe of PMFs needs to have the following features:

- The ability to isolate the effects of fields at different redshifts. In particular, sensitivity at high redshifts (prior to, or at the dawn of structure formation).
- Sensitivity to extremely low field strengths. Inflationary, post-inflationary, and structure-formation related mechanisms typically generate seed fields with strengths in the range 10^{-30} – 10^{-15} G [371, 373].
- The ability to recover the MF power spectrum, whose features might give insight into the specifics of the process of magnetogenesis.

This is the first part of a series that proposes a new observational probe of magnetic fields, which has all the desired properties listed above. In this work, we lay out the details of the microphysics behind it, while upcoming work [Gluscevic et al., in prep] evaluates detectability for various PMF models and experimental setups.

The method discussed here is based on the effect of global MFs on the redshifted 21-cm emission from neutral hydrogen prior to and during the epoch of cosmic reionization (EoR), whose measurement is the goal of a number of low-frequency radio arrays, such as MWA [183], LOFAR [184], PAPER [185], LEDA [186], SKA [187], and others. The 21-cm signal allows insight into very high redshifts (in the approximate range $7 < z < 30$), including early epochs where the intergalactic medium (IGM) was just beginning to be affected by stellar feedback.

This method relies on the availability of internal (spin) degrees of freedom to hydrogen atoms in the triplet state of the ground hyperfine transition. As we show in the body of the work, an anisotropic radiation field spin-polarizes these levels (also see previous work in Refs. [374–378]). Such anisotropies are naturally present in the early universe due to density fluctuations in the neutral gas. In the presence of a background magnetic field, the Larmor precession of the atoms leads to a characteristic signature in the 21-cm brightness temperature. In particular, the magnetic field breaks the statistical isotropy of the measured two-point correlation functions of the brightness temperature, which encapsulates information about both the MF’s coherence length and strength.

This effect is inherently sensitive to extremely weak MFs, smaller than $\sim 10^{-19}$ G.¹ This remarkable sensitivity is due to the long lifetime of the excited state, during which even very slow precession results in a substantial change in the direction of the emitted radiation.

We organize the presentation as follows: the rest of this chapter is devoted to background material, and introduces the effect. We introduce 21-cm cosmology, and the Hanle effect (which is closely related to the effect considered in this work) in Sections 8.2.1 and 8.2.2. We then introduce the effect in a simple, semi-classical manner in Section 8.3. We lay out the notation and formalism we use in Section 8.4, including our description of spin-polarized atoms in 8.4.1 and the anisotropic radiation field in the vicinity of the 21-cm transition in 8.4.2.

Next, we study the microphysics of the 21-cm transition in Chapter 9. Section 9.1 studies the excitation and de-excitation of the atoms by the 21-cm radiation itself, while Section 9.2 focuses on de-polarization by competing non-radiative processes: Sections 9.2.2 and 9.2.3 deal with spin-exchange collisions and optical pumping by Lyman- α photons, respectively.

Finally, Chapter 10 calculates the observables at late times; Section 10.1 describes the radiative transfer of 21-cm photons, and Section 10.2 puts together all the results and calculates the resulting change in the brightness temperature fluctuations. We summarize the work and lay out our conclusions in Section 10.3, and collect various technical details into the appendices.

8.2 Background

8.2.1 21-cm cosmology basics

The 21-cm line of neutral hydrogen corresponds to the transition between the hyperfine sublevels of its ground state, whose origin is the interaction between the spins of the proton and the electron. This interaction reorganizes the four possible spin states of the electron and proton into singlet and triplet levels, which are separated by an energy gap of 5.9×10^{-6} eV, which corresponds to radiation with a wavelength of 21.1 cm or a frequency of 1420 MHz in the rest frame.

In the early stages of the EoR, the universe was still mostly neutral, and fluctuations in the brightness temperature of the 21-cm line were mainly driven by (mostly Gaussian) density fluctuations. This stage lends itself to a very precise statistical description, allowing us to get a good handle on the expected 21-cm signal from these redshifts [181, 182].

The first generation of EoR experiments, such as the MWA, PAPER, and LOFAR, aim to achieve a statistical detection of the 21-cm signal from the EoR. Second generation experiments, such as the SKA, are planned to come online within the next couple of decades. They aim to perform detailed tomography of the IGM out to $z \sim 30$. Future 21-cm observations of the high-redshift universe

¹Note that a frozen magnetic field should scale as $\propto (1+z)^2$ due to flux conservation; the “comoving” field strength, defined by extrapolation to the present day, would be 10^{-21} G.

can open up a new frontier in cosmology, with a sample volume far exceeding that probed with current observations. Several authors have suggested that cosmological 21-cm radiation could be used to detect primordial magnetic fields via their dynamical effects on density and gas temperature fluctuations [379–381]. The method proposed here using radiative transfer is sensitive to much weaker fields than those investigated by these authors.

The conventional appeal of 21-cm observations is the availability of redshift information (in contrast to other probes of the very early universe such as the CMB), the access to small-scale modes (Silk damped in the CMB and washed out by nonlinear evolution today), and the consequent large number of accessible modes [382]. The effect studied in this work relies on another aspect of the transition: in the triplet state, the net magnetic moment of the atom (which is dominated by the magnetic moment of the electron), takes on different values depending on the magnetic quantum number. It is through this magnetic moment that the 21-cm emission is sensitive to ambient MFs, as explained in the following sections.

For unpolarized atoms, the detectability of the 21-cm signal hinges on the spin temperature T_s , which quantifies the relative number densities of atoms in the two hyperfine levels of the electronic ground state:

$$\frac{n(F=1)}{n(F=0)} = 3e^{-T_*/T_s}. \quad (8.1)$$

Here $F=0$ denotes the lower (spin-antiparallel) hyperfine level, $F=1$ denotes the upper (spin-parallel) level, 3 is the ratio of statistical weights, and $T_* = \hbar\omega_{\text{hf}}/k_B = 68 \text{ mK}$ is the hyperfine splitting in temperature units. A signal is detected if the spin temperature of the gas deviates from the temperature of the background CMB T_γ at that redshift: net emission occurs if $T_s > T_\gamma$ and absorption if $T_s < T_\gamma$. The spin temperature is determined by three major processes: (1) absorption/emission of 21-cm photons from/to the radio background at that redshift (primarily the CMB), (2) collisional excitation and de-excitation of hydrogen atoms, and (3) resonant scattering of Ly α photons from the first stars and galaxies, which can change the spin state via the spin-orbit interaction while the atom is in the excited state.

The fundamental quantity of interest observationally is the *brightness temperature* of the H I 21-cm line [383]. In the optically thin approximation, the brightness temperature *fluctuation* relative to the CMB at redshift z and hence observed frequency $\omega_{\text{obs}} = \omega_{\text{hf}}/(1+z)$ is

$$\delta T_b \approx 27x_{1s}(1+\delta)\frac{T_s - T_\gamma}{T_s} \left(\frac{1+z}{10}\right)^{1/2} \frac{(1+z)H(z)}{\partial_{\parallel}v_{\parallel}} \text{ mK} \quad (8.2)$$

(see e.g. Ref. [182]).² Here x_{1s} is the hydrogen neutral fraction (essentially all in the ground state), $1+\delta$ is the matter density contrast, T_s is the spin temperature, and the line-of-sight velocity gradient $\partial_{\parallel}v_{\parallel}$ accounts for deviations from the expansion rate of the homogeneous universe.

²Note that Eq. (7) in Ref. [182] is missing a -1 exponent.

In this investigation, we take account of the spin-polarization of atoms, and hence we need the full atomic density matrix and not just T_s . We will extend the formalism of 21-cm cosmology as needed to derive an equation for ΔT_b valid in this case. Several previous analyses have considered polarized 21-cm radiation from high redshift and its “scrambling” by Faraday rotation in passing through the interstellar medium of our own galaxy [384, 385]; however, they did not study polarization of the emitting atoms³, and thus did not need to develop the formalism here.

8.2.2 Related methods: Hanle effect and ground-state alignment

The effect considered in this work is closely related to the Hanle effect [386], which refers to the change in the polarization of resonant-scattering radiation in the presence of external MFs. In solar research, techniques based on the Hanle effect are used for measuring weak MFs in solar prominences and the upper solar atmosphere (see e.g. Refs. [387–390]).

The subject of this work relies on atomic alignment, whose significance in the astrophysical context was first realized in the early days of maser studies. The theory of alignment in astrophysical environments was further developed in the pioneering work of Varshalovich [374, 375]. Other significant milestones were the work of Goldreich, Keeley, and Kwan [391, 392], who considered the polarization of maser emission due to aligned molecules, and Goldreich and Kylafis [393], who proposed using linear polarization in radio lines as probes of magnetic fields in molecular clouds.

More recently, Yan & Lazarian [376–378] proposed a suite of methods to probe weak MFs in diffuse media using atomic alignment. Since the method discussed in this work relies on the same atomic physics as these previous studies, we briefly summarize the main idea behind them. Their methods rely on the polarization and intensity of radiation interacting with atoms or ions with fine (or hyperfine) structure in the ground state. When these species are immersed in an anisotropic flux of photons, the orientation of the total atomic angular momentum vector gets a preferred direction since photons carry angular momentum and transfer it via interactions. If aligned atoms are further placed in an external MF, their orientations change due to Larmor precession. As a result, the output radiation’s intensity and polarization changes in a manner depending on the direction and strength of the MF. The main advantage of using atomic species with (hyper)fine structure in their ground or metastable states is these states’ long lifetimes. Longer lifetimes are associated with longer baselines for Larmor precession, which make the effect sensitive to very weak MFs. These authors recognize the relevance of this effect for studying magnetic fields during the EoR via the 21-cm line of neutral hydrogen [378] and the fine-structure lines of the first metals [394], but they do not include its calculation in the cosmological context.

This work distills elements from the physics of all the previous work on astrophysical alignment,

³These works focused on polarization produced by re-scattering of 21-cm radiation by electrons in ionized regions. There is no anisotropy of the spins of the hydrogen atoms involved in this mechanism.

and uses features unique to the study of the 21-cm line in the cosmological context in order to synthesize a new method for measuring MFs. In order to align the excited state of the 21-cm transition, our method relies on ‘resonant’ anisotropies (at frequencies $\nu = 1.42$ GHz) that are sourced by fluctuations of Large Scale Structure (LSS). This is closely related to the mechanism of Refs. [391–393], in that it uses anisotropies in optical depth sourced by velocity gradients in order to achieve alignment. The mechanism studied in [376–378] aligns the triplet via optical pumping by anisotropies in the incident Lyman- α radiation field, i.e. at frequencies $\nu \approx 2.46 \times 10^{15}$ GHz.

Our method also differs from these previous methods in the respect that it uses relatively subtle changes in the intensity of the outgoing radiation to detect MFs. Refs. [376–378] recognize the change in the net emissivity, and propose using the emissivity ratio of multiple lines to probe MFs. As we show in this work, it is possible to use *solely* the 21cm transition, due to the statistical nature of its measurement in cosmology. The cosmic density field contains perturbation modes with a variety of wave vectors \mathbf{k} , whose amplitudes obey the underlying statistical isotropy of the Universe. The anisotropy in the scattering properties caused by the MF can then be probed using the varying illumination conditions (depending on the direction of $\hat{\mathbf{k}}$), rather than the polarization of outgoing radiation.

8.3 Illustration and simple estimate of the effect

Consider a hydrogen atom in the ground state of the hyperfine transition, located in the overdense part of a growing Fourier mode at a suitably high redshift. Moreover, let us assume that the 21-cm line is visible in emission. The brightness temperature fluctuation δT_b seen by this atom along a particular line of sight (LOS) $\hat{\mathbf{n}}$ is largely due to stimulated emission and absorption by a thermal background of excited atoms, and is proportional to the optical depth τ integrated along that direction:

$$\delta T_b(\hat{\mathbf{n}}) \approx \tau(\hat{\mathbf{n}})(T_s - T_\gamma), \quad (8.3)$$

where T_s and T_γ are the spin- and CMB-temperatures, respectively.

The optical depth, in turn, depends on the path length over which photons stay within the line:

$$\tau(\hat{\mathbf{n}}) \sim n \int \sigma(\nu) dl = n \int \sigma(\nu) \frac{dl}{d\nu} d\nu \sim \frac{n\sigma(\nu_0)c\Delta}{dv_{\parallel}/dr_{\parallel}(\hat{\mathbf{n}})}, \quad (8.4)$$

where $\sigma(\nu)$ is the absorption cross-section at frequency ν , ν_0 is the frequency at line-center, Δ is the dimensionless Doppler width of the line, c is the speed of light, and $dv_{\parallel}/dr_{\parallel}(\hat{\mathbf{n}})$ is the velocity gradient along the LOS. The velocity gradient term equals the Hubble rate when the LOS is orthogonal to the wave-vector \mathbf{k} of the Fourier mode, but it picks up a contribution from the infall into the growing overdensity when the LOS has a component along \mathbf{k} . For an arbitrary direction of the LOS, the

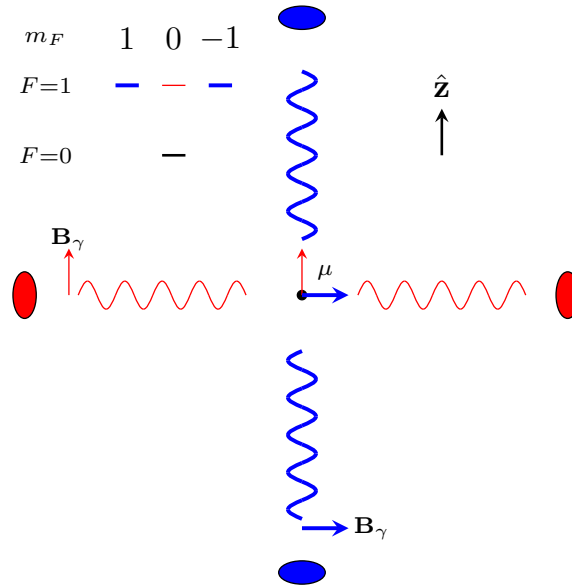


Figure 8.1: An illustration of how an incident quadrupole spin-polarizes the triplet level of the hyperfine transition. The hydrogen atom (at the center) is surrounded by a quadrupole intensity pattern with hot (blue, thick lines) and cold (red, thin lines) spots. Absorption of 21-cm photons produces a state with a magnetic moment μ aligned with the magnetic field \mathbf{B}_γ of the incident radiation. The incident anisotropy is transferred to the direction of the magnetic moment. **Inset:** The resulting unequal population of the triplet sublevels. For the orientation of this figure, the levels with magnetic quantum number $m_F = \pm 1$ (thick blue lines) are preferentially populated due to the hot spots.

velocity gradient term equals

$$\frac{dv_{\parallel}}{dr_{\parallel}}(\hat{\mathbf{n}}) = H + \frac{dv_{\text{infall},\parallel}}{dr_{\parallel}}(\hat{\mathbf{n}}) = H \left[1 - (\hat{\mathbf{k}} \cdot \hat{\mathbf{n}})^2 \delta \right]. \quad (8.5)$$

Hence the optical depth of the medium around the atom has a quadrupole dependence with a fractional size proportional to the overdensity, or an absolute size of $\mathcal{O}(\delta\tau)$. This leads to a quadrupole in the incident brightness temperature, oriented such that directions along the wave-vector are hotter.

Atoms that are excited by absorption have magnetic moments that are aligned with the exciting radiation's magnetic field. For anisotropic incident radiation, this leads to a preference for directions orthogonal to that of hot spots in the incident radiation field. Thus an incident quadrupole spin-polarizes the atoms, i.e. unequally populates the states within the hyperfine triplet. Figure 8.1 illustrates this effect.

These excited atoms de-excite to the ground state mainly by stimulated emission or non-radiative processes. The former leads to an output quadrupole pattern with the same orientation as the incident one, but a smaller size of $\mathcal{O}(\tau \delta\tau)$. This is illustrated in Fig. 8.2.

The angular structure of the observed brightness temperature fluctuations is dominated by the contribution of the pre-existing thermal background of excited atoms, and is $\mathcal{O}(\delta\tau)$ in size, as can

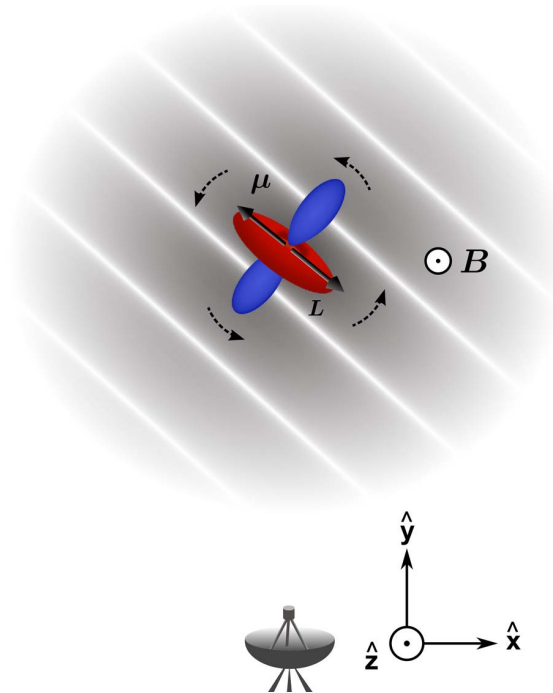


Figure 8.2: A hydrogen atom in a growing plane wave density fluctuation: The atom is excited to the spin-polarized state of Fig. 8.1, which produces the quadrupolar radiation pattern shown above when it de-excites. Also shown is one possible orientation of the intermediate magnetic moment μ , and the associated angular momentum \mathbf{L} . If an external magnetic field \mathbf{B} is present, the torque it exerts ($\mu \times \mathbf{B}$) causes the moment to precess around it before it de-excites. If the field has a component in the plane of the observer's sky, this changes the brightness temperature for a plane wave oriented in a general direction.

be seen from Eq. (8.3). The secondary emission described above is much smaller (by a factor of the optical depth, τ), and does not correspond to a qualitatively different pattern.

The presence of a background magnetic field breaks isotropy and leads to a unique signature in the angular pattern of this secondary emission. To see this, consider the effect of the magnetic field on the intermediate magnetic moment, which has a finite lifetime t_d . This lifetime is mainly due to stimulated emission and non-radiative processes such as collisions and optical pumping by Lyman- α photons. Additionally, the moment precesses about the background magnetic field \mathbf{B} with the Larmor frequency ω_L .

Due to these effects, the moment μ evolves as

$$\frac{d}{dt}\mu \approx -\frac{\mu}{t_d} - \omega_L \mu \times \hat{\mathbf{B}}. \quad (8.6)$$

In a coordinate system with the background magnetic field along the z -axis, the solution is

$$\mu(t) = e^{-t/t_d} \begin{pmatrix} \cos(\omega_L t) & -\sin(\omega_L t) & 0 \\ \sin(\omega_L t) & \cos(\omega_L t) & 0 \\ 0 & 0 & 1 \end{pmatrix} \mu_0. \quad (8.7)$$

Thus the moment precesses through an angle $\theta_B \approx \omega_L t_d$ before the atom de-excites. If the de-excitation occurs only via radiative processes, the lifetime is

$$t_d^{-1} \approx A \frac{k_B T_\gamma}{\Delta E_{\text{hf}}}, \quad (8.8)$$

where k_B is the Boltzmann constant, ΔE_{hf} is the hyperfine energy gap, and A is the Einstein A -coefficient or intrinsic width of the line, which is broadened due to stimulated emission by the background CMB with a temperature T_γ .

We estimate the angle of precession to be

$$\theta_B \approx \omega_L t_d = \frac{\gamma_e \Delta E_{\text{hf}}}{A k_B T_\gamma} B = 1.5 \times \left(\frac{B}{10^{-19} \text{G}} \right) \left(\frac{1+z}{10} \right)^{-1}, \quad (8.9)$$

where γ_e is the gyromagnetic ratio of the electron. Figure 8.2 illustrates the precession of the magnetic moment, and that of the quadrupole associated with the secondary emission. From the geometry of the figure with the magnetic field along the z -axis, the change in a mode's brightness temperature depends on which quadrant of the $x-y$ plane the projection of \mathbf{k} lies in. Keeping the line of sight along $\hat{\mathbf{y}}$ and assuming the precession angle is small,

$$\delta T_b|_{\text{pr}} \sim (T_s - T_\gamma) \tau \delta \tau \left(\theta_{B_z} \hat{\mathbf{k}}_x \hat{\mathbf{k}}_y - \theta_{B_x} \hat{\mathbf{k}}_y \hat{\mathbf{k}}_z \right). \quad (8.10)$$

The precession-induced correction shown in Eq. (8.10) distorts the angular structure of the 21-cm emission in a manner unlike any of the usually considered effects – it breaks the symmetry around the line of sight. This distinguishes it from corrections like the usual redshift space distortions due to peculiar velocities. Fig. 8.3 illustrates this.

In the rest of the work we go beyond this simple semi-classical treatment of the spin-polarization, and compute the rates of de-polarization by other non-radiative channels.

8.4 Notation and Basic Formalism

Table 8.1 lists the symbols used throughout this work and the physical quantities they represent.

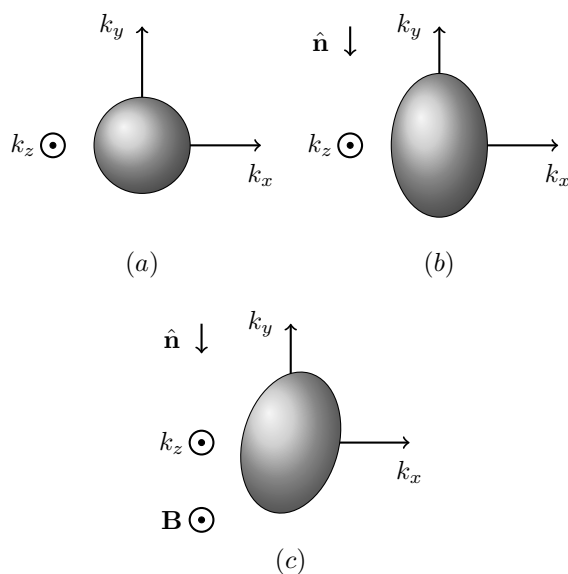


Figure 8.3: This figure illustrates the effect on the power-spectrum of the brightness temperature fluctuations. The sub-figures show contours of constant power in \mathbf{k} -space. (a) Fluctuations of the 21-cm emissivity (photons per cm^3 per s emitted over all solid angles) in the rest-frame of the emitting atoms. (b) Fluctuations as seen by a distant (present-day) observer. Note the elongation in the direction of the line of sight to the observer, $\hat{\mathbf{n}}$, due to peculiar velocities. This manifests as a “compression” in the real-space correlation function, but as a power enhancement (“stretching” of the $P(\mathbf{k})$ contours) in Fourier-space. (c) Fluctuations with an external magnetic field added. The effect of the precession is to break the symmetry around $\hat{\mathbf{n}}$. The size of the effects has been exaggerated in (b) and (c).

Table 8.1: Glossary of symbols used in this work.

Symbol	Physical quantity
ρ	Density matrix of neutral hydrogen atoms
ρ_{aa}	Singlet state sub-matrix of ρ . It is a scalar which corresponds to the occupancy of the singlet state
ρ_{mn}	Triplet state sub-matrix of ρ
\mathcal{P}_{jm}	Irreducible components of ρ_{mn}
ω_{hf}	Angular frequency of the hyperfine transition
T_*	Hyperfine gap expressed in temperature units
A	Einstein A -coefficient for the hyperfine transition
k^\pm	Averaged cross-sections for collisional transitions
$\kappa(1-0)$	Collisional rate for transition from triplet to singlet state
$\kappa(0-1)$	Collisional rate for transition from singlet to triplet state
$\kappa^{(j)}(1-0)$	Collisional depolarization rates for rank- j irreducible components
n	Principal quantum number
l	Azimuthal quantum number
m	Magnetic quantum number
F	Total angular momentum (nuclear + electronic)
m_F	Total magnetic quantum number
J_α	Flux of Lyman- α photons on the blue side of the line (in $\text{cm}^{-2}\text{s}^{-1}\text{Hz}^{-1}\text{sr}^{-1}$)
$T_{\text{c,eff}}$	Effective color temperature in the vicinity of the Lyman- α resonance
Γ_{2p}	Einstein A -coefficient for the Lyman- α transition
γ_{2p}	$= \Gamma_{2p}/4\pi$, HWHM of the Lyman- α transition
$\phi_{\text{AB}}(\nu)$	Interference profiles for the lines A and B
$\sigma_{F_I \rightarrow F_J, (j)}(\nu)$	Cross section for the transition between the rank- j components of multiplets with $F = F_I, F_J$ due to optical pumping by incident Lyman- α photons of frequency ν
$\tilde{S}_\alpha, \tilde{S}_{\alpha, (2)}$	Correction factors for the detailed frequency dependence of Lyman- α flux, entering the rate equations for \mathcal{P}_{00} and \mathcal{P}_{2m}
\mathbf{k}_γ	Wave-vector of the radiation
$\hat{\mathbf{n}}$	Direction of the radiation's propagation (line-of-sight from the emitter to the observer)
$f_{\alpha\beta}(\omega)$	Phase space density (p.s.d) matrix for the radiation
$f_X(\omega)$	Parity invariants of the radiation's p.s.d
$\mathcal{F}_{jm}(\omega)$	Irreducible components of the radiation's p.s.d
$\phi(\omega)$	Absorption profile for the hyperfine transition
$\mathcal{X}(\omega)$	Cumulative function for $\phi(\omega)$
$\sigma(\omega)$	Absorption cross-section for the hyperfine transition
τ	Optical depth of the medium
δT_{b}	Brightness temperature fluctuation of the 21-cm line relative to the CMB
$x_{\alpha, (2)}$	Relative strength of depolarization through optical pumping and radiative channels
$x_{\text{c}, (2)}$	Relative strength of depolarization through collisions and radiative channels
x_{B}	Relative rates of precession and radiative depolarization
δ	Local overdensity
\mathbf{v}	Bulk matter velocity
\mathbf{k}	Wave-vector of the growing mode of the matter density
z	Redshift
T_{s}	Spin temperature
T_γ	CMB temperature
T_{k}	Kinetic temperature
n_{H}	Number density of hydrogen atoms
$x_{1\text{s}}$	Fraction of hydrogen atoms in the 1s state
H	Hubble expansion rate
\mathbf{B}	External magnetic field in the region of interest

8.4.1 Atomic Density Matrix

We study the level populations of the hydrogen ground state using the density matrix formalism [395]. If we consider an ensemble of atoms consisting of a mixture of states $|\psi_\alpha\rangle$ with statistical weights W_α , then the density operator is defined as

$$\rho = \sum_{\alpha} W_{\alpha} |\psi_{\alpha}\rangle \langle \psi_{\alpha}|. \quad (8.11)$$

Given the density matrix ρ , the expectation value of a general dynamical operator \mathcal{M} is

$$\langle \mathcal{M} \rangle = \text{Tr} [\rho \mathcal{M}]. \quad (8.12)$$

In order to express the density operator in matrix form, we choose a set of basis states $|\phi_I\rangle$ which are orthonormal and complete, i.e.,

$$\langle \phi_I | \phi_J \rangle = \delta_{IJ}, \quad \text{and} \quad (8.13)$$

$$\sum_I |\phi_I\rangle \langle \phi_I| = \mathbb{1}, \quad (8.14)$$

where δ_{IJ} is the Kronecker delta. The matrix elements of ρ are then given by

$$\rho_{IJ} = \langle \phi_J | \rho | \phi_I \rangle = \sum_{\alpha} W_{\alpha} \langle \phi_I | \psi_{\alpha} \rangle \langle \psi_{\alpha} | \phi_J \rangle. \quad (8.15)$$

The interaction between the electronic and the nuclear spin splits the ground state of the hydrogen atom into a superposition of two hyperfine levels, a singlet with quantum numbers ($F = 0, m_F = 0$), and a triplet with ($F = 1, m_F = 0, \pm 1$). As long as we consider the subset of neutral hydrogen atoms in the 1s electronic state, these states form a complete basis. In the ket notation, these states are represented by $|Fm_F\rangle$.

We will henceforth adopt the convention that indices of the kind I, J, \dots , when used as subscripts for the density matrix ρ or as state labels, run over all four of the hyperfine states of the 1s type. They are purely abstract indices. Depending on the context, their instantiations are either the lower-case roman letters a, b, c , and d or the numbers 1, 0, and -1 . Table 8.2 maps the various indices to states. Note that numerical subscripts, referred to by m, n, \dots in the text, run over only the triplet states. They equal the magnetic quantum numbers of the respective states. Thus summations over these numeric indices represent ones over only the triplet states.

Within the basis of the two hyperfine levels, the density matrix is of the form

$$\rho = \rho_{IJ} = \begin{pmatrix} \overbrace{\rho_{aa}}^{1 \times 1} & \rho_{am} \\ \rho_{ma} & \underbrace{\rho_{mn}}_{3 \times 3} \end{pmatrix}. \quad (8.16)$$

This density matrix consists of four submatrices. The upper diagonal submatrix has only one element (ρ_{aa}) that describes the probability of finding an atom in the singlet state. The lower diagonal submatrix describes the triplet state. Its diagonal elements represent the probabilities of finding atoms with $F = 1$ in the states with the corresponding quantum number m_F . The off-diagonal elements describe coherences between states of different m_F . The remaining two submatrices, with elements in the first row or column, describe the interference between $F = 0$ and $F = 1$ levels. The time evolution of these terms is proportional to $\exp(i\omega_{\text{hf}}t)$, where $\omega_{\text{hf}} = 2\pi \times 1420$ MHz is the angular frequency corresponding to the hyperfine gap. These terms rapidly oscillate on macroscopic timescales with average values of zero, and thus we do not need to follow them in the calculation.

The processes we are interested in only redistribute atoms between the levels, and hence the trace of the density matrix is preserved by them. The trace can be taken to be unity as long as we are interested in the population of atoms in the ground electronic state i.e. $\rho_{aa} + \text{Tr}(\rho_{mn}) = 1$.

The 4×4 Hermitian matrix ρ is described by sixteen real numbers. Removing the six real degrees of freedom constituting the sub-matrix ρ_{am} , and the singlet sub-matrix ρ_{aa} , leaves nine real numbers describing the triplet state sub-matrix ρ_{mn} .

In order to take advantage of the symmetries of the problem, it is convenient to express the density matrix in terms of irreducible tensor operators. We construct irreducible components of ranks $j = \{0, 1, 2\}$ from the elements of the triplet sub-matrix, in the manner of Ref. [396]:⁴

$$\mathcal{P}_{jm} = \sqrt{3(2j+1)} \sum_{m_1, m_2} (-1)^{1-m_2} \begin{pmatrix} 1 & j & 1 \\ -m_2 & m & m_1 \end{pmatrix} \times \rho_{m_1 m_2}, \quad (8.17)$$

where the expression in large parentheses is the Wigner 3-j symbol. The indices j and m indicate that the irreducible component \mathcal{P}_{jm} transforms in the same way as the corresponding spherical harmonic Y_{jm} does under a rotation of the axes – only components with the same rank j mix. The Hermiticity of the density matrix leads to the characteristic behavior of these components under complex conjugation:

$$\mathcal{P}_{j-m} = (-1)^m \mathcal{P}_{jm}^*. \quad (8.18)$$

The components of rank zero, one, and two are described by one, three, and five real numbers, respectively. As expected, both descriptions of the triplet state density sub-matrix have the same total number of real degrees of freedom.

⁴Note that the definition in Ref. [396] differs from ours by a factor of i^j , due to their usage of a different convention for spherical tensors.

Table 8.2: Notation for hyperfine states.

$ Fm_F\rangle$	Roman	Numeric
$ 0\ 0\rangle$	a	-
$ 1\ -1\rangle$	b	-1
$ 1\ 0\rangle$	c	0
$ 1\ 1\rangle$	d	1

We recover the density matrix in the standard basis from the irreducible components using the following relation:

$$\rho_{m_1 m_2} = \sum_{jm} \sqrt{\frac{2j+1}{3}} (-1)^{1-m_2} \begin{pmatrix} 1 & j & 1 \\ -m_2 & m & m_1 \end{pmatrix} \mathcal{P}_{jm}. \quad (8.19)$$

The explicit forms of the irreducible components are as follows:

$$\mathcal{P}_{00} = \rho_{11} + \rho_{00} + \rho_{-1-1} = \text{Tr}(\rho_{mn}), \quad (8.20a)$$

$$\mathcal{P}_{11} = -\sqrt{\frac{3}{2}}(\rho_{01} + \rho_{-10}),$$

$$\mathcal{P}_{10} = \sqrt{\frac{3}{2}}(\rho_{11} - \rho_{-1-1}), \quad (8.20b)$$

$$\mathcal{P}_{1-1} = \sqrt{\frac{3}{2}}(\rho_{10} + \rho_{0-1}),$$

$$\mathcal{P}_{22} = \sqrt{3}\rho_{-11},$$

$$\mathcal{P}_{21} = -\sqrt{\frac{3}{2}}(\rho_{01} - \rho_{-10}),$$

$$\mathcal{P}_{20} = \frac{1}{\sqrt{2}}(\rho_{11} - 2\rho_{00} + \rho_{-1-1}), \quad (8.20c)$$

$$\mathcal{P}_{2-1} = \sqrt{\frac{3}{2}}(\rho_{10} - \rho_{0-1}), \quad \text{and}$$

$$\mathcal{P}_{2-2} = \sqrt{3}\rho_{1-1}.$$

The operator of rank zero is a scalar representing the net probability of finding an atom in the triplet, or $F = 1$, state. The operator of rank one is a vector with three components, and is often called the *orientation vector*. It is proportional to the internal angular momentum of the ensemble. The operator of rank two is the so-called *alignment tensor*, which has five components that are quadratic in angular momentum – they are related to the spherical components of the electric quadrupole tensor.

In many applications, excitations between the singlet and the triplet are isotropic. In such cases, only the operator of rank zero, or the net excited-state occupancy, is relevant. The scenario of interest in this work involves anisotropic excitations, and thus we need to use operators of higher

rank to describe the spin state of the atoms, which are said to be *spin-polarized*.

For a system in equilibrium with a heat bath with temperature T , the elements of the density matrix take the form

$$\rho_{IJ}^{\text{th}} = \frac{e^{-\beta E_I}}{Z} \delta_{IJ}, \quad (8.21)$$

where $\beta = (k_B T)^{-1}$, and $Z = \sum_I e^{-\beta E_I}$ is the partition function of the ensemble.

Given a general density matrix ρ_{IJ} , the spin temperature T_s is defined using this equilibrium formula:

$$\frac{\mathcal{P}_{00}}{1 - \mathcal{P}_{00}} = \frac{\rho_{11} + \rho_{00} + \rho_{-1-1}}{\rho_{aa}} = 3e^{-(\hbar\omega_{\text{hf}}/k_B T_s)}. \quad (8.22)$$

In the regimes of interest, the spin temperature is much larger than the temperature associated with the gap, which is $T_* = \hbar\omega_{\text{hf}}/k_B = 68.2$ mK. In this limit, the occupancy of the excited state is

$$\mathcal{P}_{00} \approx \frac{3}{4} - \frac{3T_*}{16T_s}. \quad (8.23)$$

8.4.2 Phase-space density matrix for radiation

In this section and subsequent sections, we use the Coulomb gauge to describe the electromagnetic field. It is defined by the condition that

$$\nabla \cdot \mathbf{A} = 0, \quad (8.24)$$

where \mathbf{A} is the vector potential. In this gauge, the electric and magnetic fields are functions only of the vector potential in the absence of free charges.

As long as we can approximate the electromagnetic field to be Gaussian, we can describe its general state by a density matrix or two-point function, in the same manner as the spin-states of the hydrogen atoms in Section 8.4.1. In order to explicitly realize this, we use the Fourier modes of the vector potential as an orthogonal and complete basis set:

$$\mathbf{A}(\mathbf{r}) = \sum_{\mathbf{k}_\gamma, \alpha} \left[a_\alpha(\mathbf{k}_\gamma) \mathbf{A}_{\mathbf{k}_\gamma, \alpha}(\mathbf{r}) + a_\alpha^\dagger(\mathbf{k}_\gamma) \mathbf{A}_{\mathbf{k}_\gamma, \alpha}^*(\mathbf{r}) \right], \quad (8.25)$$

with mode functions given by

$$\mathbf{A}_{\mathbf{k}_\gamma, \alpha}(\mathbf{r}) = \left(\frac{2\pi\hbar c^2}{\omega} \right)^{1/2} \mathbf{e}_{(\alpha)}(\hat{\mathbf{k}}) e^{i\mathbf{k}_\gamma \cdot \mathbf{r}}, \quad (8.26)$$

where \mathbf{k}_γ is the wave-vector of the radiation. We use a subscript on the wave-vector to avoid confusing it with that of the density fluctuations. The summation over \mathbf{k}_γ is shorthand for the integral $\int d^3\mathbf{k}_\gamma / (2\pi)^3$, and the angular frequency is given by $\omega = ck_\gamma$. The symbol $\mathbf{e}_{(\alpha)}(\hat{\mathbf{k}}_\gamma)$ represents

polarization vectors for modes propagating in the direction $\hat{\mathbf{k}}_\gamma$, where $\alpha = \pm 1$ indicates right- and left-circularly polarized radiation, respectively, with the phase convention in terms of the unit vectors $\hat{\theta}$ (north-south polarization) and $\hat{\phi}$ (east-west polarization):

$$\mathbf{e}_{(\pm 1)}(\hat{\mathbf{k}}_\gamma) = \mp \frac{1}{\sqrt{2}} (\hat{\theta} \pm i\hat{\phi})|_{(\theta, \phi) = (\theta_{\mathbf{k}_\gamma}, \phi_{\mathbf{k}_\gamma})}. \quad (8.27)$$

The expansion coefficients in Eq. (8.25) are annihilation and creation operators for photons with momentum $\hbar\mathbf{k}_\gamma$, with the following commutation relations:

$$[a_\alpha(\mathbf{k}_\gamma), a_\beta^\dagger(\mathbf{k}'_\gamma)] = (2\pi)^3 \delta(\mathbf{k}_\gamma - \mathbf{k}'_\gamma) \delta_{\alpha\beta}, \quad (8.28)$$

$$[a_\alpha(\mathbf{k}_\gamma), a_\beta(\mathbf{k}'_\gamma)] = [a_\alpha^\dagger(\mathbf{k}_\gamma), a_\beta^\dagger(\mathbf{k}'_\gamma)] = 0. \quad (8.29)$$

We define the density matrix for radiation in a manner almost exactly paralleling that of Eq. (8.15), which defined it for the atoms:

$$\langle a_\alpha^\dagger(\mathbf{k}_\gamma) a_\beta(\mathbf{k}'_\gamma) \rangle = (2\pi)^3 \delta(\mathbf{k}_\gamma - \mathbf{k}'_\gamma) f_{\beta\alpha}(\omega, \hat{\mathbf{n}} = \hat{\mathbf{k}}_\gamma), \quad (8.30)$$

where $\hat{\mathbf{n}}$ denotes the direction of propagation. The phase-space density matrix $f_{\alpha\beta}(\omega, \hat{\mathbf{n}})$ generalizes the scalar phase-space density for photons to the polarized case:

$$f_{\alpha\beta} = \begin{pmatrix} f_{++} & f_{+-} \\ f_{-+} & f_{--} \end{pmatrix} = f_{\text{I}} \mathbb{1} + f_{\text{V}} \sigma_z - f_{\text{Q}} \sigma_x - f_{\text{U}} \sigma_y = \begin{pmatrix} f_{\text{I}} + f_{\text{V}} & -f_{\text{Q}} + if_{\text{U}} \\ -f_{\text{Q}} - if_{\text{U}} & f_{\text{I}} - f_{\text{V}} \end{pmatrix}. \quad (8.31)$$

The decomposition of the elements of the phase-space density matrix in Eq. (8.31) using the Pauli matrices connects them to the Stokes parameters:

$$X(\omega, \hat{\mathbf{n}}) = \frac{\hbar}{c^2} \frac{\omega^3}{4\pi^3} f_X(\omega, \hat{\mathbf{n}}), \quad X \in \{\text{I}, \text{Q}, \text{U}, \text{V}\}, \quad (8.32)$$

where the quantities are defined per unit angular frequency ω .

The elements of the phase-space density matrix transform in different ways under a rotation of the axes. The diagonal elements transform as scalars, while the off-diagonal elements transform as quantities with spin weights of ± 2 [397]. Hence, their decomposition into moments is of the form

$$f_{\alpha\beta}(\omega, \hat{\mathbf{n}}) = \sum_{j,m} \sqrt{\frac{4\pi}{2j+1}} (f_{\alpha\beta})_{jm}(\omega) [{}_{\alpha-\beta}Y_{jm}(\hat{\mathbf{n}})]^*. \quad (8.33)$$

The quantity ${}_s Y_{jm}(\hat{\mathbf{n}})$ is the spin-weighted spherical harmonic with spin-weight s . The convention of Eq. (8.33) is slightly different from that in the standard cosmology literature. Appendix 10.A expands on the difference and the reason for adopting the current convention.

Inversion of the coordinate axes (a so-called parity transformation) transforms quantities with spin weights of ± 2 into each other. We further split the moments into parity invariants as follows:

$$(f_{++/--})_{jm} = f_{\text{I},jm} \pm f_{\text{V},jm} , \quad (8.34a)$$

$$(f_{+-/-+})_{jm} = -f_{\text{E},jm} \pm i f_{\text{B},jm} . \quad (8.34b)$$

The quantities $f_{\text{I},jm}$ and $f_{\text{V},jm}$ are moments of the intensity and circular polarization, respectively. A parity transformation multiplies the quantities $f_{\text{E},jm}$ and $f_{\text{B},jm}$ by factors of $(-1)^j$ and $(-1)^{j+1}$ respectively. Hence, the nomenclature of “electric-type” and “magnetic-type” moments.

In this section, we used the plane wave basis to define the phase-space density matrix and its moments. The interaction of partially polarized light and atoms takes on a particularly simple form if we describe the EM field in the alternate spherical wave basis [398]. We use this basis to perform calculations with an atomic physics flavor, due to the simplicity and transparency of the resulting equations. If needed, we can also perform all the calculations in the plane wave basis, with the investment of some extra effort. The substance of the final results does not depend on the choice of basis; when we use the results as inputs to calculations with a cosmology flavor, we use their form in the conventional plane wave basis of this section.

Appendix 10.B expands on the details of the spherical wave basis, and the steps involved in moving back and forth between it and the plane wave basis.

Chapter 9

Microphysics of the 21-cm line

9.1 Interaction Between Hydrogen Atoms and 21-cm Radiation

In this section, we work out the effect of radiative transitions to and from spin-polarized states of the atom. We generalize the usual treatment of absorption, and spontaneous and stimulated emission, to account for the evolution of the full density matrix ρ rather than just the level occupation probabilities. Our description of the atom-radiation interaction Hamiltonian is similar, in principle if not in detail, to Sections 14.1 and 15.4 of Mandel & Wolf [399].

Radiative transitions between the singlet and triplet states of neutral hydrogen atoms are accompanied by the emission or absorption of radio photons at or near the frequency of the hyperfine gap. The electronic wavefunctions of both states are of the 1s type in position space, so an electric dipole transition between them is forbidden. The dominant channel is a magnetic dipole transition, which involves the emission or absorption of $j = 1$ photons of the magnetic type.

The matrix element for the transition from an initial state I to a final state J , via the absorption of a photon of the magnetic type, with angular frequency ω and angular momentum indices $j = 1, m$ is [396]

$$V_{JI,m}(\omega) = -i\sqrt{\frac{2}{3\pi}} \left(\frac{\hbar\omega^3}{c^3}\right)^{1/2} \left[-e\{Q_{1,m}^{(M)}\}_{JI}\right], \quad (9.1)$$

where $\{Q_{1m}^{(M)}\}_{JI}$ is a component of the magnetic dipole transition moment $\mathbf{Q}_{JI}^{(M)}$ in the spherical coordinate system. Given the initial and final states, rotational invariance fixes the magnetic quantum number m of the photon.

The magnetic dipole moment is related to the electron's spin-angular momentum by the gyromagnetic ratio, i.e., $-e\mathbf{Q}^{(M)} = -(g_e\mu_B/\hbar)\mathbf{S}_e$, where g_e is the Landé g -factor for the electron spin and μ_B is the Bohr magneton.

The initial state I is the singlet state a , and the final state J lies within the triplet. We appeal to

the Wigner-Eckart theorem to write the various absorption matrix elements in terms of the reduced (or double-barred) matrix element:

$$V_{m_F a, m}(\omega) = (-1)^{1-m_F} \begin{pmatrix} 1 & 1 & 0 \\ -m_F & m & 0 \end{pmatrix} \langle 1 \| V(\omega) \| 0 \rangle, \quad (9.2)$$

$$\langle 1 \| V(\omega) \| 0 \rangle = i \left(\frac{\hbar \omega^3}{2\pi c^3} \right)^{1/2} g_e \mu_B. \quad (9.3)$$

The Hamiltonian for the interaction between the atoms and EM radiation is¹

$$H_{\text{hf}, \gamma} = \sum_{m_F m} \int d\omega V_{m_F a, m}(\omega) |1m_F\rangle \langle 00| a_{1m}^{(M)}(\omega) + \text{h.c.} \quad (9.4)$$

Here ‘‘h.c.’’ stands for Hermitian conjugation. The Hamiltonian uses the notation for the annihilation operator for a photon of the magnetic type, expanded upon in Appendix 10.B.

From here onwards, we use a dot over a quantity to represent its rate of change with respect to coordinate time. Equation (8.15) enables us to write down the evolution of the triplet state sub-matrix ρ_{m_n} due to the interaction with the EM field. The underlying operator commutes with the matter Hamiltonian, so its evolution is solely due to the interaction $H_{\text{hf}, \gamma}$, specifically:

$$\dot{\rho}_{m_1 m_2} |_{\gamma} = \frac{i}{\hbar} \langle [H_{\text{hf}, \gamma}, |1m_2\rangle \langle 1m_1|] \rangle = \frac{i}{\hbar} \sum_m \int d\omega V_{m_2 a, m}^*(\omega) \langle |00\rangle \langle 1m_1| a_{1m}^{(M)\dagger}(\omega) \rangle + \text{c.c.s.} \quad (9.5)$$

Here ‘‘c.c.s.’’ stands for complex conjugation with a swap (i.e. swap $m_1 \leftrightarrow m_2$).

The three-point functions of the atom and the radiation field represent transitions between the singlet and the triplet levels. Appendix 10.C derives expressions for such three-point functions. Plugging in Eq. (10.60) gives the evolution equation

$$\dot{\rho}_{m_1 m_2} |_{\gamma} = -\frac{\pi}{\hbar^2} \sum_{m, m', m_3} V_{m_2 a, m}^* V_{m_3 a, m'} \left[\rho_{m_1 m_3} \left\{ \delta_{mm'} + f_{m', m}^{(M1)(M1)} \right\} - \delta_{m_3 m_1} \rho_{aa} f_{m', m}^{(M1)(M1)} \right] + \text{c.c.s.} \quad (9.6)$$

This uses the notation for the radiation’s phase-space density matrix in the spherical basis, defined in Eq. (10.49) of Appendix 10.B. The transition matrix elements and phase-space density moments are evaluated at ω_{hf} , the angular frequency of the hyperfine transition. However, the frequency in the bulk-rest frame corresponding to ω_{hf} in the interacting atoms’ frame is distributed over a broadened profile due to the thermal motions of the atoms.

In this calculation, we assume that the atom density matrix is independent of the velocity. The practical consequence of this assumption is that Eq. (9.6) can be used as is, with the radiation’s phase

¹Compare Eq.(15.4-3) of Ref. [399]. Their interaction Hamiltonian is for a single plane wave mode of the radiation field, and is written in the interaction rather than the Heisenberg picture.

space density averaged over a Doppler-broadened profile centered around ω_{hf} . The consequences of relaxing this assumption have been explored in a different context before [400]. In subsequent equations, a bar over quantities is used to indicate averages over the line profile.

In order to simplify the evolution given by Eq. (9.6), it is convenient to divide the terms into spontaneous and stimulated emission, and photo-absorption contributions.

Spontaneous emission is described by the terms in Eq. (9.6) connecting the excited state density sub-matrix ρ_{mn} to itself. We write these terms in terms of the irreducible components \mathcal{P}_{jm} using Eqs. (8.17) and (8.19):

$$\dot{\mathcal{P}}_{jm}|_{\text{sp.em}} = -A\mathcal{P}_{jm}, \quad (9.7)$$

$$A = \frac{2\pi}{3\hbar^2} |\langle 1||V(\omega_{\text{hf}})||0\rangle|^2 = 2.86 \times 10^{-15} \text{s}^{-1}. \quad (9.8)$$

The quantity A is the Einstein A -coefficient for the hyperfine transition. We use Eqs. (9.2), (9.3) and (9.8) to express the transition matrix element in terms of A as follows:

$$V_{m_F a, m}(\omega_{\text{hf}}) = i\hbar\sqrt{\frac{A}{2\pi}}\delta_{mm_F}. \quad (9.9)$$

Absorption is described by the terms in Eq. (9.6) connecting the excited state density sub-matrix ρ_{mn} to the ground state occupancy ρ_{aa} . Using Eq. (9.9), we write this contribution as

$$\dot{\rho}_{m_1 m_2}|_{\text{ab}} = A\rho_{aa}\overline{f_{m_1, m_2}^{(M1)(M1)}}. \quad (9.10)$$

We can define irreducible components, \mathcal{F}_{jm} , of the M1–M1 block of the photon phase-space density matrix in the same manner as those of the triplet state density sub-matrix [see Eq. (10.53)]. Hence, the photo absorption contribution retains its form when expressed in terms of the irreducible components:

$$\dot{\mathcal{P}}_{jm}|_{\text{ab}} = A\rho_{aa}\overline{\mathcal{F}_{jm}} = A(1 - \mathcal{P}_{00})\overline{\mathcal{F}_{jm}}. \quad (9.11)$$

Stimulated emission is described by the terms in Eq. (9.6) connecting the excited state density sub-matrix ρ_{mn} to itself, via the photon phase-space density moments $f_{m,n}^{(M1)(M1)}$. Using Eq. (9.9), this contribution is

$$\dot{\rho}_{m_1 m_2}|_{\text{st.em}} = -\frac{A}{2} \sum_{m_3} \rho_{m_1 m_3} f_{m_3, m_2}^{(M1)(M1)} + \text{c.c.s.} \quad (9.12)$$

Using Eqs. (8.17), (8.19) and (10.54), we rewrite this in terms of the irreducible components \mathcal{P}_{jm} and \mathcal{F}_{jm} :

$$\dot{\mathcal{P}}_{jm}|_{\text{st.em}} = -\frac{A}{2} \sum_{m_1 m_2 m_3} \sum_{j' m' j'' m''} \sqrt{\frac{(2j+1)(2j'+1)(2j''+1)}{3}}$$

$$\times (-1)^{1-m_3} \left[\begin{pmatrix} 1 & j & 1 \\ -m_2 & m & m_1 \end{pmatrix} \begin{pmatrix} 1 & j' & 1 \\ -m_3 & m' & m_1 \end{pmatrix} \begin{pmatrix} 1 & j'' & 1 \\ -m_2 & m'' & m_3 \end{pmatrix} + (j'm' \leftrightarrow j''m'') \right] \mathcal{P}_{j'm'} \overline{\mathcal{F}_{j''m''}}. \quad (9.13)$$

The summations over angular indices for products of three 3-j symbols, when evaluated, yield the product of a Wigner 6-j symbol along with a 3-j symbol [401]. Thus the evolution of the irreducible components \mathcal{P}_{jm} due to stimulated emission is

$$\dot{\mathcal{P}}_{jm}|_{\text{st.em}} = -A \sum_{j',j''} \sqrt{\frac{(2j'+1)(2j''+1)}{3}} \begin{Bmatrix} j'' & j' & j \\ 1 & 1 & 1 \end{Bmatrix} \left[\frac{(-1)^j + (-1)^{j''-j'}}{2} \right] (\mathcal{P}_{j'} \otimes \overline{\mathcal{F}_{j''}})_{jm}. \quad (9.14)$$

The expression enclosed in curly braces is the 6-j symbol, and the notation $(\mathcal{P}_{j_1} \otimes \mathcal{F}_{j_2})_{jm}$ denotes the sum of products of the irreducible quantities $\mathcal{P}_{j_1 m_1}$ and $\mathcal{F}_{j_2 m_2}$, weighted with appropriate 3-j symbols, to yield a quantity which transforms in the (jm) representation.

In the absence of a density fluctuation, the excited states are isotropically occupied. Thus only the irreducible moment \mathcal{P}_{00} has a zeroth-order contribution. The radiation field is unpolarized in this case, so only the intensity monopole has a zeroth-order contribution. Thus the only relevant radiation moment in the unperturbed case is \mathcal{F}_{00} .

As discussed in Section 8.3, a growing density fluctuation leads to an incident quadrupole on the atoms. Hence the extra radiation moment exciting the atoms is of the \mathcal{F}_{2m} type. The spin-polarization due to this quadrupole is described by the alignment tensor \mathcal{P}_{2m} . The orientation tensor \mathcal{P}_{1m} can be neglected to the first order in the fluctuations. (The CMB dipole in the baryon rest frame is first-order in perturbation theory, and thus in principle should be considered; however, it has the wrong parity to contribute to \mathcal{P}_{1m} .)

When we sum up the contributions of absorption and emission from Eqs. (9.7), (9.11), and (9.14), we get the net rate of change of the atom density matrix due to radiative processes. Using explicit expressions for the irreducible components \mathcal{F}_{jm} of the phase-space density matrix from Eq. (10.53), we find that

$$\dot{\mathcal{P}}_{00}|_{\gamma} = -A [\mathcal{P}_{00} - (3 - 4\mathcal{P}_{00}) \overline{f_{1,00}}] \quad \text{and} \quad (9.15a)$$

$$\dot{\mathcal{P}}_{2m}|_{\gamma} = -A \left[(1 + \overline{f_{1,00}}) \mathcal{P}_{2m} - \frac{3 - 4\mathcal{P}_{00}}{5\sqrt{2}} (\overline{f_{1,2m}} + \sqrt{6} \overline{f_{E,2m}}) \right]. \quad (9.15b)$$

9.2 Other Processes Affecting the Atomic Density Matrix

The level populations or spin-polarization of the hydrogen ground state can be altered by mechanisms other than emission/absorption of the 21-cm photons. The ones relevant to the subject of this work

are background magnetic fields, hydrogen-hydrogen collisions, optical pumping by Lyman- α photons. Of these, the effect of the magnetic fields is simplest to evaluate.

The transition rates for the isotropically occupied cases due to the other processes have been calculated previously [402, 403]. In this section, we generalize these results to the case of spin-polarized hydrogen atoms – in particular we calculate the rates of de-polarization due to collisions and optical pumping, which are important for determining the lifetime of the excited state of Section 8.3.

9.2.1 Background magnetic field

The precession of an atom in an external magnetic field \mathbf{B} is the result of the perturbing Hamiltonian

$$H_B = -\boldsymbol{\mu} \cdot \mathbf{B} = \frac{\mu_B}{\hbar} (\mathbf{L}_e + g_e \mathbf{S}_e - g_p \frac{m_e}{m_p} \mathbf{S}_p) \cdot \mathbf{B}. \quad (9.16)$$

The orbital angular momentum \mathbf{L}_e vanishes for electronic wavefunctions in the 1s subspace. The spin angular momenta of the electron and proton are comparable, but their masses differ by three orders of magnitude. Hence we neglect the third term in Eq. (9.16) (the interaction of the nuclear spin with the external magnetic field, since $g_e/m_e \gg g_p/m_p$).

It is simplest to choose a coordinate system such that the z -axis is oriented along the external magnetic field. If we retain only the second term in Eq. (9.16), we have the following evolution equation for the density matrix:

$$\dot{\rho}_{m_1 m_2 | B} = \frac{i}{\hbar} \langle [H_B, |1m_2\rangle \langle 1m_1|] \rangle = \frac{i}{\hbar} g_e \mu_B B [\rho_{m_1 m_3} \langle m_3 | S_{e,z} | m_2 \rangle - (m_1 \leftrightarrow m_2)^*]. \quad (9.17)$$

In terms of the irreducible components \mathcal{P}_{jm} , this takes the form

$$\dot{\mathcal{P}}_{jm | B} = i \frac{m}{2} \frac{g_e \mu_B}{\hbar} B \mathcal{P}_{jm}. \quad (9.18)$$

9.2.2 Spin-exchange Collisions

Spin-exchange collisions can occur between a pair of hydrogen atoms (atoms A and B) with antiparallel spins (spin up \uparrow and down \downarrow):



Collisions often result in spin-exchange due to the large energy difference between the singlet state of a pair of hydrogen atoms $X^1\Sigma_g^+$, which has an antisymmetrical spin wave function and corresponds to the ground state of a stable H_2 molecule, and the unbound triplet $b^3\Sigma_u^+$ state. The change in

the electronic spin induces a hyperfine transition in the atom because the electron and nuclear spins are coupled by the hyperfine interaction. Since the energy difference between the triplet and singlet state is large, the cross sections for the spin-exchange collisions are much greater than those of spin-flipping transitions induced by magnetic interactions between atoms, in which only one atom can change its spin [404]. We do not consider the latter type of transitions in this analysis.

The rates of spin-exchange hydrogen collisions have been calculated by Ref. [403] for a range of temperatures. We will follow their procedure for obtaining the rate equations for populations of hyperfine levels, which we briefly describe here.

The total azimuthal spin angular momentum of the atomic pair is conserved in spin-exchange collisions. However, the collision cross section depends on how many atoms involved in the collision change their value of the quantum number F . If both atoms change their value of F , making the total change $\Delta F = 2$, the cross section is equal to

$$\sigma^+ = \frac{\pi}{2k^2} \sum_{L=0,2,\dots} (2L+1) \sin^2(\delta_t - \delta_s), \quad (9.20)$$

where $k^2/2\mu$ is the kinetic energy in the entrance channel ($\mu = m_H/2$ is the reduced mass), and δ_t and δ_s are the phase shifts for elastic scattering in the triplet $b^3\Sigma_u^+$ and singlet $X^1\Sigma_g^+$ configurations, respectively. On the other hand, if $\Delta F = 1$, that is if only one atom changes its value of F , then the cross section is given by

$$\sigma^- = \frac{\pi}{2k^2} \sum_{L=1,3,\dots} (2L+1) \sin^2(\delta_t - \delta_s). \quad (9.21)$$

For transitions with no change in the total angular momentum of both atoms involved ($\Delta F = 0$), the cross section equals $\sigma^0 = \sigma^+$.

To get the de-excitation rate of hydrogen atoms, we need to average the cross sections over a Maxwellian velocity distribution. The rates $k^\pm = \langle \sigma^\pm v \rangle$ evaluate to

$$k^\pm = \sqrt{\frac{8k_B T_k}{\pi\mu}} \frac{1}{(k_B T_k)^2} \int_0^\infty dE E \sigma^\pm(E) \exp\left(-\frac{E}{k_B T_k}\right), \quad (9.22)$$

where T_k is the kinetic temperature. We can take $k^0 \approx k^+$. The excitation rate coefficients are given by

$$k_x^\pm = \exp(-\omega^\pm) k^\pm, \quad (9.23)$$

where $\omega^+ = 2\Delta E_{\text{hf}}/k_B T_k = 2T_*/T_k$, $\omega^- = \Delta E_{\text{hf}}/k_B T_k = T_*/T_k$. The values of coefficients k^\pm as functions of temperature are given in Ref. [403] and we use them in our calculations.

The final rate equations in Ref. [403] are applicable to the case of isotropically excited hydrogen

atoms. The collisional evolution of a general density matrix has been studied earlier in Ref. [405].

We perform the calculation by choosing a basis where the density matrix is diagonal, and using rate equations with the coefficients k^\pm for the level populations. This works because different irreducible moments \mathcal{P}_{jm} of the atomic density matrix do not mix due to collisions in linear theory. Schematically,

$$\dot{\mathcal{P}}_{jm}|_c \sim C_j \mathcal{P}_{jm}. \quad (9.24)$$

The collision coefficients C_j depend only on the rank of the polarization moment j , and not on its projection m . Because of this general property, we only need to calculate the coefficients in the basis where the density matrix is diagonal, i.e., only the irreducible components \mathcal{P}_{jm} with $m = 0$ are non-zero [see Eq. (8.20)]. The equations for the scalar components are slightly more complicated because there are two rank-0 objects that come into play: the occupancies of the singlet and the triplet.

We refer to the analysis of Ref. [403] to write down the evolution equations in such a basis:

$$\begin{aligned} \dot{\rho}_{aa}|_c = & -3k_x^+ n_{\text{H}} \rho_{aa}^2 + 2(k^- + k^+) n_{\text{H}} \rho_{bb} \rho_{dd} + 2k^- n_{\text{H}} (\rho_{bb} + \rho_{dd}) \rho_{cc} + k^+ n_{\text{H}} \rho_{cc}^2 \\ & - 2k_x^- n_{\text{H}} \rho_{aa} (\rho_{bb} + \rho_{cc} + \rho_{dd}), \end{aligned} \quad (9.25a)$$

$$\dot{\rho}_{bb}|_c = \dot{\rho}_{dd}|_c = k_x^+ n_{\text{H}} \rho_{aa}^2 + 2k_x^- n_{\text{H}} \rho_{aa} \rho_{cc} + k^0 n_{\text{H}} \rho_{cc}^2 - (k^0 + k^+ + 2k^-) n_{\text{H}} \rho_{bb} \rho_{dd}, \text{ and} \quad (9.25b)$$

$$\begin{aligned} \dot{\rho}_{cc}|_c = & k_x^+ n_{\text{H}} \rho_{aa}^2 + 2k_x^- n_{\text{H}} \rho_{aa} (\rho_{bb} - \rho_{cc} + \rho_{dd}) - 2k^- n_{\text{H}} (\rho_{bb} + \rho_{dd}) \rho_{cc} - (k^+ + 2k^0) n_{\text{H}} \rho_{cc}^2 \\ & + 2(k^- + k^0) n_{\text{H}} \rho_{bb} \rho_{dd}. \end{aligned} \quad (9.25c)$$

Since the level of anisotropy is very small, the occupation of a state I can be written as $\rho_{II} = \rho_{II}^{\text{th}} + \epsilon_I$, where ρ_{II}^{th} is the thermal occupation of that state ($\rho_{bb}^{\text{th}} = \rho_{cc}^{\text{th}} = \rho_{dd}^{\text{th}} = \mathcal{P}_{00}^{\text{th}}/3$, $\rho_{aa}^{\text{th}} = 1 - \mathcal{P}_{00}^{\text{th}}$), and ϵ_I is a small perturbation. Retaining only quantities linear in ϵ , the above equations become:

$$\begin{aligned} \dot{\epsilon}_a|_c = & - \left[6k_x^+ (1 - \mathcal{P}_{00}^{\text{th}}) + 2k_x^- \mathcal{P}_{00}^{\text{th}} \right] n_{\text{H}} \epsilon_a + \left[-2k_x^- (1 - \mathcal{P}_{00}^{\text{th}}) + (4k^- + 2k^+) \frac{\mathcal{P}_{00}^{\text{th}}}{3} \right] \\ & \times n_{\text{H}} (\epsilon_b + \epsilon_c + \epsilon_d), \end{aligned} \quad (9.26a)$$

$$\begin{aligned} \dot{\epsilon}_b|_c = \dot{\epsilon}_d|_c = & \left[2k_x^+ (1 - \mathcal{P}_{00}^{\text{th}}) + \frac{2}{3} k_x^- \mathcal{P}_{00}^{\text{th}} \right] n_{\text{H}} \epsilon_a - \frac{1}{3} k^0 \mathcal{P}_{00}^{\text{th}} n_{\text{H}} (\epsilon_b + \epsilon_d - 2\epsilon_c) + 2k_x^- (1 - \mathcal{P}_{00}^{\text{th}}) n_{\text{H}} \epsilon_c \\ & - \frac{1}{3} (k^+ + 2k^-) \mathcal{P}_{00}^{\text{th}} n_{\text{H}} (\epsilon_b + \epsilon_d), \text{ and} \end{aligned} \quad (9.26b)$$

$$\begin{aligned} \dot{\epsilon}_c|_c = & \left[2k_x^+ (1 - \mathcal{P}_{00}^{\text{th}}) + \frac{2}{3} k_x^- \mathcal{P}_{00}^{\text{th}} \right] n_{\text{H}} \epsilon_a + 2k_x^- (1 - \mathcal{P}_{00}^{\text{th}}) n_{\text{H}} (\epsilon_b - \epsilon_c + \epsilon_d) - (4k^- + 2k^+) \frac{\mathcal{P}_{00}^{\text{th}}}{3} n_{\text{H}} \epsilon_c \\ & + \frac{2}{3} k^0 \mathcal{P}_{00}^{\text{th}} n_{\text{H}} (\epsilon_b + \epsilon_d - 2\epsilon_c). \end{aligned} \quad (9.26c)$$

We convert these equations to ones for the irreducible components \mathcal{P}_{jm} following the argument leading to the Eq. (9.24) and the explicit forms of Eq. (8.20). The resulting equations are of the

form:

$$\dot{\rho}_{aa}|_c = -n_{\text{H}}\kappa(0-1)\rho_{aa} + n_{\text{H}}\kappa(1-0)\mathcal{P}_{00}, \quad (9.27)$$

$$\dot{\mathcal{P}}_{00}|_c = n_{\text{H}}\kappa(0-1)\rho_{aa} - n_{\text{H}}\kappa(1-0)\mathcal{P}_{00} = n_{\text{H}}\kappa(0-1) - n_{\text{H}}[\kappa(0-1) + \kappa(1-0)]\mathcal{P}_{00}, \quad (9.28)$$

$$\dot{\mathcal{P}}_{1m}|_c = -n_{\text{H}}\kappa^{(1)}(1-0)\mathcal{P}_{1m}, \text{ and} \quad (9.29)$$

$$\dot{\mathcal{P}}_{2m}|_c = -n_{\text{H}}\kappa^{(2)}(1-0)\mathcal{P}_{2m}, \quad (9.30)$$

where we have extended the notation of Ref. [403] to include both transition and de-polarization rates, which we read off from Eq. (9.26):

$$\kappa(0-1) = 6k_{\text{x}}^+(1 - \mathcal{P}_{00}^{\text{th}}) + 2k_{\text{x}}^-\mathcal{P}_{00}^{\text{th}}, \quad (9.31a)$$

$$\kappa(1-0) = -2k_{\text{x}}^-(1 - \mathcal{P}_{00}^{\text{th}}) + (4k^- + 2k^+) \frac{\mathcal{P}_{00}^{\text{th}}}{3}, \quad (9.31b)$$

$$\kappa^{(1)}(1-0) = 0, \text{ and} \quad (9.31c)$$

$$\kappa^{(2)}(1-0) = 4k_{\text{x}}^-(1 - \mathcal{P}_{00}^{\text{th}}) + \frac{2}{3}(3k^0 + 2k^- + k^+)\mathcal{P}_{00}^{\text{th}}. \quad (9.31d)$$

The de-polarization rate $\kappa^{(1)}(1-0)$ vanishes because the total spin angular momentum of the ensemble, corresponding to the orientation vector \mathcal{P}_{1m} , is conserved in collisions.

If the spin temperature is much larger than $T_* = 68$ mK, the states are nearly equally occupied and $\mathcal{P}_{00}^{\text{th}} \approx 3/4$ [see Eq. (8.23)]. Using this in the rates of Eq. (9.31), we write down the collisional contributions to the evolution of the relevant pieces of the atom density matrix as follows:

$$\dot{\mathcal{P}}_{00}|_c = -4n_{\text{H}}\kappa(1-0) \left(\mathcal{P}_{00} - \frac{3}{4} + \frac{3T_*}{16T_{\text{k}}} \right) \text{ and} \quad (9.32a)$$

$$\dot{\mathcal{P}}_{2m}|_c = -n_{\text{H}}\kappa^{(2)}(1-0)\mathcal{P}_{2m}, \quad (9.32b)$$

with

$$\kappa^{(2)}(1-0) = 4\kappa(1-0) = 2(k^+ + k^-). \quad (9.33)$$

These equations assume that the kinetic temperature $T_{\text{k}} \gg T_*$, which is valid over the entire range of redshifts.

9.2.3 Optical pumping by Lyman- α photons

Optical pumping by Lyman- α ($\text{Ly}\alpha$) photons, or the Wouthuysen-Field effect, is another process which significantly affects the level populations within the hydrogen ground state (see e.g. Ref. [406]). An atom in the ground (1s) state absorbs a $\text{Ly}\alpha$ photon and gets excited to the 2p state. Subsequently, the atom re-emits a photon and returns to the ground state. However, it does not necessarily

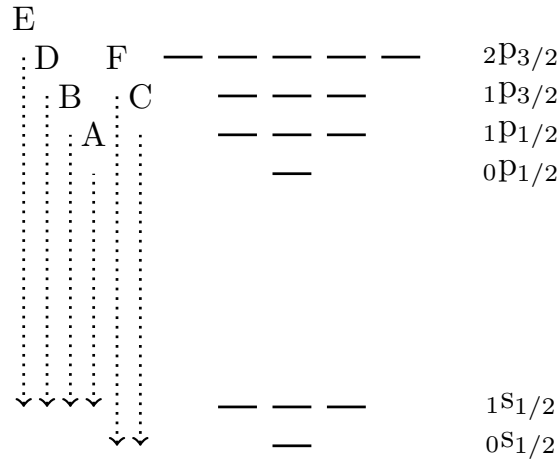


Figure 9.1: The hyperfine structure of the ground and first excited electronic levels of the hydrogen atom. The levels are labeled by term symbols ${}_{F}l_J$, where l is the spectroscopic notation for the orbital angular momentum, and J and F are the net electronic and total angular momentum, respectively. Also shown are all the allowed single photon transitions between the 1s and 2p levels, along with their labels; these involve photons in the Ly α frequency range. Only the downward transitions are shown. Needless to say, the gaps between the levels are not drawn to scale.

de-excite to the same ground-state level it originated from. Thus, interactions with Ly α photons can change the density matrix of hydrogen atoms within the ground state basis.

The excited state consists of four levels: ${}_{0}p_{1/2}$, ${}_{1}p_{1/2}$, ${}_{1}p_{3/2}$, and ${}_{2}p_{3/2}$, where we use the notation ${}_{F}l_J$ for the state in terms of its quantum numbers. The Roman index J here is not a state label, rather it is the quantum number for the net electronic angular momentum. Figure 9.1 shows the levels with their multiplicities, and the single-photon transitions which occur between them. Since we will study the effects of these transitions in detail, we adopt the convention that Greek indices represent the excited levels, i.e., those within 2p, when used as state labels.

The electric dipole interaction between hydrogen atoms and Ly α photons as a function of time is governed by the Hamiltonian (in the interaction picture)²:

$$H_{\text{Ly}\alpha}^{\text{int}}(t) = \sum_{I,\mu,\alpha,\mathbf{k}_\gamma} Q_{\mu I}(\mathbf{k}_\gamma, \alpha) |\mu\rangle \langle I| a_\alpha(\mathbf{k}_\gamma) e^{-i(\omega - \omega_{\mu I})t} + \text{h.c.}, \quad (9.34)$$

where the matrix element $Q_{\mu I}(\mathbf{k}_\gamma, \alpha)$ is given by

$$Q_{\mu I}(\mathbf{k}_\gamma, \alpha) = -i\sqrt{2\pi\hbar\omega} \langle \mu | \mathbf{d} \cdot \mathbf{e}_\alpha(\hat{\mathbf{k}}_\gamma) | I \rangle. \quad (9.35)$$

As in the case of the EM field in the radio frequency (see Section 8.4.2), the symbol \mathbf{k}_γ is the

²This is in contrast with the rest of the work, which uses the Heisenberg picture. We choose this to make contact with previous work on this topic, in particular Ref. [407]. Of course, the final answer does not depend on which picture is used to perform the calculation.

photon wave-vector, ω is its frequency, \mathbf{e}_α is the radiation polarization vector and $a_\alpha(\mathbf{k}_\gamma)$ is the photon annihilation operator. The quantity \mathbf{d} is the electric dipole moment of the atom, which is proportional to the position vector \mathbf{r} of the electron. The frequency corresponding to the energy difference between the upper (μ) and lower (I) state is $\omega_{\mu I} = (E_\mu - E_I)/\hbar$.

We divide the changes to the ground-state density matrix due to interactions with the Ly α photons into two categories: (i) depopulation pumping which describes how the ground state is depleted due to absorption of incident Ly α photons, and (ii) repopulation pumping which describes how the ground state is repopulated due to spontaneous emission from the excited 2p state.

To obtain the expressions for the evolution of the ground state density matrix, we follow the derivation presented in Ref. [407], with slightly modified notation for the purposes of clarity. We start by writing the wave function of an ensemble of hydrogen atoms and the radiation field γ_0 in the interaction picture:

$$\begin{aligned} \Phi(t) = & \sum_I b_I(t) |I, \gamma_0\rangle + \sum_{\mu, \mathbf{k}_\gamma, \alpha} b_{\mu, (\mathbf{k}_\gamma, \alpha)}(t) |\mu, \gamma_0 - (\mathbf{k}_\gamma, \alpha)\rangle \\ & + \sum_{I, \mathbf{k}_\gamma, \alpha, \mathbf{k}'_\gamma, \beta} b_{I, (\mathbf{k}_\gamma, \alpha), (\mathbf{k}'_\gamma, \beta)}(t) |I, \gamma_0 - (\mathbf{k}_\gamma, \alpha) + (\mathbf{k}'_\gamma, \beta)\rangle, \end{aligned} \quad (9.36)$$

The first term describes the population of atoms in the ground (1s) state and a background population of photons represented by γ_0 . The second term describes the ensemble in which one of the atoms was excited to the 2p state by absorbing a photon characterized by wave-vector \mathbf{k}_γ and polarization α (the sum is taken over all possible realizations of \mathbf{k}_γ and α). The third term describes the ensemble in which one of the atoms was excited by absorption of a Ly α photon (with \mathbf{k}_γ and α) and then de-excited back to the ground state through spontaneous emission of a photon with wave-vector \mathbf{k}'_γ and polarization β .

Using the Schrödinger equation, we get the following set of equations for the time-dependent coefficients b in the wave function. For the initial photon state, we find

$$\dot{b}_I = \frac{-i}{\hbar} \sum_{\mu, \mathbf{k}_\gamma, \alpha} \langle I, \gamma_0 | H_{\text{Ly}\alpha}^{\text{int}} | \mu, \gamma_0 - (\mathbf{k}_\gamma, \alpha) \rangle b_{\mu, (\mathbf{k}_\gamma, \alpha)}; \quad (9.37)$$

for the states with one photon removed,

$$\begin{aligned} \dot{b}_{\mu, (\mathbf{k}_\gamma, \alpha)} = & \frac{-i}{\hbar} \sum_I \langle \mu, \gamma_0 - (\mathbf{k}_\gamma, \alpha) | H_{\text{Ly}\alpha}^{\text{int}} | I, \gamma_0 \rangle b_I \\ & - \frac{\Gamma_{2\text{p}}}{2} b_{\mu, (\mathbf{k}_\gamma, \alpha)}; \end{aligned} \quad (9.38)$$

and for the states with a scattered photon,

$$\dot{b}_{I,(\mathbf{k}_\gamma,\alpha),(\mathbf{k}'_\gamma,\beta)} = \frac{-i}{\hbar} \sum_{\mu} \langle I, \gamma_0 - (\mathbf{k}_\gamma, \alpha) + (\mathbf{k}'_\gamma, \beta) | H_{\text{Ly}\alpha}^{\text{int}} | \mu, \gamma_0 - (\mathbf{k}_\gamma, \alpha) \rangle b_{\mu,(\mathbf{k}_\gamma,\alpha)}. \quad (9.39)$$

The coefficient Γ_{2p} is the Einstein A -coefficient of the $\text{Ly}\alpha$ transition, and the term containing it describes de-excitation of the $2p$ state through spontaneous emission.

We write the density matrix of the hydrogen ground state in terms of the b coefficients describing the contribution of different levels to the total population of hydrogen atoms. In general, the IJ element of the density matrix in the interaction picture is

$$\rho_{IJ}^{\text{int}} = b_I b_J^* + \sum_{\alpha,\beta,\mathbf{k}_\gamma,\mathbf{k}'_\gamma} b_{I,(\mathbf{k}_\gamma,\alpha),(\mathbf{k}'_\gamma,\beta)} b_{J,(\mathbf{k}_\gamma,\alpha),(\mathbf{k}'_\gamma,\beta)}^*. \quad (9.40)$$

The time derivative of the first term describes the depletion of the ground state population due to $\text{Ly}\alpha$ absorption, whereas that of the second term describes how the ground state is repopulated by spontaneous emission of $\text{Ly}\alpha$ photons by atoms that were once excited. In the remainder of this section we derive the expressions for the time change of the density matrix due to these two processes.

9.2.3.1 Depopulation pumping

Following Ref. [407], we begin our calculation by writing the expression for the excited state coefficient $b_{\mu,(\mathbf{k}_\gamma,\alpha)}$, which we get by integrating Eq. (9.38):

$$b_{\mu,(\mathbf{k}_\gamma,\alpha)}(t) = -\frac{i}{\hbar} \sum_J \int_{t_0}^t dt' e^{-\Gamma_{2p}(t-t')/2} \langle \mu, \gamma_0 - (\mathbf{k}_\gamma, \alpha) | H_{\text{Ly}\alpha}^{\text{int}}(t') | J, \gamma_0 \rangle b_J(t'). \quad (9.41)$$

We plug this expression into Eq. 9.37 to get

$$\begin{aligned} \dot{b}_I = & -\frac{1}{\hbar^2} \sum_{\mu,\mathbf{k}_\gamma,\alpha,K} \langle I, \gamma_0 | H_{\text{Ly}\alpha}^{\text{int}}(t) | \mu, \gamma_0 - (\mathbf{k}_\gamma, \alpha) \rangle \int_{t_0}^t dt' e^{-\Gamma_{2p}(t-t')/2} \langle \mu, \gamma_0 - (\mathbf{k}_\gamma, \alpha) | H_{\text{Ly}\alpha}^{\text{int}}(t') | K, \gamma_0 \rangle \\ & \times b_K(t'). \end{aligned} \quad (9.42)$$

Taking the integral over time and keeping only the leading term in the expansion of the exponential gives

$$\dot{b}_I = \sum_{\mu,\mathbf{k}_\gamma,\alpha,K} \frac{f(\mathbf{k}_\gamma)}{\hbar^2} \frac{Q_{\mu I}^*(\mathbf{k}_\gamma, \alpha) Q_{\mu K}(\mathbf{k}_\gamma, \alpha)}{i(\omega - \omega_{\mu I}) - \Gamma_{2p}/2} e^{i\omega_{IK}t} b_K, \quad (9.43)$$

where $f(\mathbf{k}_\gamma)$ is the phase-space density of photons. In order to write this equation, we used the following identity to simplify the Lyman- α radiation field's contribution to the matrix elements in

Eq. (9.42):

$$\begin{aligned} f(\mathbf{k}_\gamma) &= \langle \gamma_0 | a_\alpha^\dagger(\mathbf{k}_\gamma) a_\alpha(\mathbf{k}_\gamma) | \gamma_0 \rangle = \sum_{\mathbf{k}'_\gamma, \beta} \langle \gamma_0 | a_\alpha^\dagger(\mathbf{k}_\gamma) | \gamma_0 - (\mathbf{k}'_\gamma, \beta) \rangle \langle \gamma_0 - (\mathbf{k}'_\gamma, \beta) | a_\alpha(\mathbf{k}_\gamma) | \gamma_0 \rangle \\ &= \langle \gamma_0 | a_\alpha^\dagger(\mathbf{k}_\gamma) | \gamma_0 - (\mathbf{k}_\gamma, \alpha) \rangle \langle \gamma_0 - (\mathbf{k}_\gamma, \alpha) | a_\alpha(\mathbf{k}_\gamma) | \gamma_0 \rangle. \end{aligned} \quad (9.44)$$

The time evolution of the ground state density matrix in the interaction picture due to depopulation pumping is given by

$$\dot{\rho}_{IJ}^{\text{int}}|_{\text{depop}} = \dot{b}_I b_J^* + b_I \dot{b}_J^*. \quad (9.45)$$

Hence, in the Schrödinger picture, this becomes

$$\dot{\rho}_{IJ}^{\text{Sch}}|_{\text{depop}} = \dot{\rho}_{IJ}^{\text{int}}|_{\text{depop}} e^{-i\omega_{IJ}t} = \sum_{\mu, \mathbf{k}_\gamma, \alpha, K} \frac{f(\mathbf{k}_\gamma)}{\hbar^2} \frac{Q_{\mu I}^*(\mathbf{k}_\gamma, \alpha) Q_{\mu K}(\mathbf{k}_\gamma, \alpha)}{i(\omega - \omega_{\mu K}) - \Gamma_{2p}/2} \rho_{KJ}^{\text{Sch}} + \text{c.c.s.} \quad (9.46)$$

As in Section 9.1, “c.c.s” stands for complex conjugation along with a swap; the indices to be swapped in this case are I and J .

9.2.3.2 Repopulation pumping

The ground state density matrix also evolves with time due to the repopulation of the ground state via spontaneous emission of photons from the excited state. To find the rate equation for this repopulation, we follow the same approach as in the previous section.

We begin by plugging the expression for the excited state coefficient $b_{\mu, (\mathbf{k}_\gamma, \alpha)}$, which we obtained by evaluating the integral in Eq. (9.41), into Eq. (9.39):

$$\begin{aligned} \dot{b}_{I, (\mathbf{k}_\gamma, \alpha), (\mathbf{k}'_\gamma, \beta)} &= \frac{1}{\hbar^2} \sum_{\mu, K} Q_{\mu I}^*(\mathbf{k}'_\gamma, \beta) Q_{\mu K}(\mathbf{k}_\gamma, \alpha) e^{i(\omega' - \omega + \omega_{IK})t} b_K(0) \\ &\quad \times \frac{\langle \gamma - (\mathbf{k}_\gamma, \alpha) + (\mathbf{k}'_\gamma, \beta) | a_\beta^\dagger | \gamma - (\mathbf{k}_\gamma, \alpha) \rangle}{i(\omega - \omega_{\mu K}) - \Gamma_{2p}/2} \langle \gamma - (\mathbf{k}_\gamma, \alpha) | a_\alpha | \gamma \rangle. \end{aligned} \quad (9.47)$$

Integrating this gives

$$\begin{aligned} b_{J, (\mathbf{k}_\gamma, \alpha), (\mathbf{k}'_\gamma, \beta)} &= -\frac{1}{\hbar^2} \sum_{\nu, L} Q_{\nu J}^*(\mathbf{k}'_\gamma, \beta) Q_{\nu L}(\mathbf{k}_\gamma, \alpha) \frac{1 - e^{i(\omega' - \omega + \omega_{JL})t}}{i(\omega' - \omega + \omega_{JL})} \\ &\quad \times b_L(0) \frac{\langle \gamma - (\mathbf{k}_\gamma, \alpha) + (\mathbf{k}'_\gamma, \beta) | a_\beta^\dagger | \gamma - (\mathbf{k}_\gamma, \alpha) \rangle}{i(\omega - \omega_{\nu L}) - \Gamma_{2p}/2} \langle \gamma - (\mathbf{k}_\gamma, \alpha) | a_\alpha | \gamma \rangle. \end{aligned} \quad (9.48)$$

Combining the results in Eq. (9.47) and (9.48), we get:

$$\dot{b}_{I, (\mathbf{k}_\gamma, \alpha), (\mathbf{k}'_\gamma, \beta)} b_{J, (\mathbf{k}_\gamma, \alpha), (\mathbf{k}'_\gamma, \beta)}^* = \frac{1}{\hbar^4} \sum_{\mu, K, \nu, L} Q_{\mu I}^*(\mathbf{k}'_\gamma, \beta) Q_{\mu K}(\mathbf{k}_\gamma, \alpha) Q_{\nu J}(\mathbf{k}'_\gamma, \beta) Q_{\nu L}^*(\mathbf{k}_\gamma, \alpha)$$

$$\times \frac{f(\mathbf{k}_\gamma) b_K(0) b_L^*(0) e^{i(\omega_{IJ} - \omega_{KL})t}}{[i(\omega - \omega_{\mu K}) - \Gamma_{2p}/2] [-i(\omega - \omega_{\nu L}) - \Gamma_{2p}/2]} \frac{e^{i(\omega' - \omega + \omega_{JL})t} - 1}{i(\omega' - \omega + \omega_{JL})}. \quad (9.49)$$

In deriving this expression we used the definition of the phase-space density in Eq. (9.44) and the commutation relations of the creation and annihilation operators:

$$a_\alpha^\dagger a_\alpha a_\beta^\dagger a_\beta = a_\alpha^\dagger (a_\beta^\dagger a_\alpha + \delta_{\alpha\beta}) a_\beta \approx a_\alpha^\dagger a_\beta \delta_{\alpha\beta},$$

where we assume that the photon number operator $a^\dagger a \ll 1$, which is valid for the UV part of the spectrum, including the Ly α photons.

We can further simplify Eq. (9.49) by giving level L a small width, i.e. $\omega_L \rightarrow \omega_L - i\epsilon$. Due to this width, at large times, the numerator of the final factor on the RHS of Eq. (9.49) approaches -1 . For a given frequency of the incoming photon, ω , this factor is dominated by frequencies of the outgoing photon, ω' , for which the denominator is small. In other words, the last factor is dominated by its behavior near its pole, which manifests as a delta function in integrals over the outgoing frequency.

The evolution of the density matrix due to repopulation, in the Schödinger picture is then given by:

$$\begin{aligned} \dot{\rho}_{IJ}^{\text{Sch}}|_{\text{repop}} &= \sum_{\mathbf{k}_\gamma, \mathbf{k}'_\gamma, \alpha, \beta} \dot{b}_{I,(\mathbf{k}_\gamma, \alpha), (\mathbf{k}'_\gamma, \beta)} b_{J,(\mathbf{k}_\gamma, \alpha), (\mathbf{k}'_\gamma, \beta)}^* e^{-i\omega_{IJ}t} + \text{c.c.s} \\ &= \hbar^{-4} \sum_{\mathbf{k}_\gamma, \mathbf{k}'_\gamma, \alpha, \beta, \mu, K, \nu, L} f(\mathbf{k}_\gamma) Q_{\mu I}^*(\mathbf{k}'_\gamma, \beta) Q_{\mu K}(\mathbf{k}_\gamma, \alpha) \\ &\quad \times \frac{Q_{\nu J}(\mathbf{k}'_\gamma, \beta) Q_{\nu L}^*(\mathbf{k}_\gamma, \alpha) \pi \delta(\omega' - \omega + \omega_{JL})}{[i(\omega - \omega_{\mu K}) - \Gamma_{2p}/2] [-i(\omega - \omega_{\nu L}) - \Gamma_{2p}/2]} \rho_{KL}^{\text{Sch}} + \text{c.c.s.} \end{aligned} \quad (9.50)$$

We rewrite the phase-space density in terms of the flux per unit frequency, and use Eq. (9.50) to infer a cross-section for the KL^{th} component of the density matrix ρ to go to the IJ^{th} component. We simplify Eq. (9.50) by using Eq. (9.35) for the dipole matrix elements, and approximating the incident Ly α radiation field to be isotropic for performing integrals over the directions $\hat{\mathbf{k}}_\gamma$ and $\hat{\mathbf{k}}'_\gamma$. This is an excellent approximation due to the large value of the cross-section, and low mean free path for incident Ly α photons. Thus we conclude that Eq. (9.50) connects only irreducible components of the same rank within the initial and final density matrix.

Let the initial and final states, (I and J), belong to multiplets with total angular momentum quantum numbers F_I and F_J , respectively. We implement the above program to infer the cross-section for a general irreducible component of rank- j within the initial state sub-matrix to go to the corresponding component within the final state sub-matrix. We use the suggestive notation $\sigma_{F_I \rightarrow F_J, (j)}$ to represent this cross-section, the expression for which we read off from Eq. (9.50). We approximate all multiplicative factors of frequencies by the value of the Ly α line-center, and get

(using, e.g., the methodology of Ref. [402])

$$\begin{aligned} \sigma_{F_I \rightarrow F_J, (j)}(\omega) = & \frac{8\pi}{9} \frac{\omega_{\text{Ly}\alpha}^4}{c^4} \frac{e^4}{\hbar^2} \sqrt{2j+1} \sqrt{\frac{2F_J+1}{2F_I+1}} \sum_{m_{J_1}, m_{J_2}} \sum_{m_{I_1}, m_{I_2}} \\ & \sum_{j', m'} \sum_{p, q} \sum_{r, s} \sum_{\mu, \nu} (-1)^{F_J - m_{J_2}} \begin{pmatrix} F_J & j & F_J \\ -m_{J_2} & m & m_{J_1} \end{pmatrix} (-1)^{F_I - m_{I_2}} \begin{pmatrix} F_I & j' & F_I \\ -m_{I_2} & m' & m_{I_1} \end{pmatrix} g_{pr} g_{qs} \\ & \times \frac{\langle F_J m_{J_1} | r^p | \mu \rangle \langle \mu | r^q | F_I m_{I_1} \rangle \langle F_I m_{I_2} | r^s | \nu \rangle \langle \nu | r^r | F_J m_{J_2} \rangle}{\Delta\omega_{\mu I} + i\Gamma_{\mu}/2} \frac{1}{\Delta\omega_{\nu I} - i\Gamma_{\nu}/2}, \end{aligned} \quad (9.51)$$

where the symbol $\Delta\omega_{\mu I}$ is shorthand for $\omega - \omega_{\mu I}$, which is the frequency offset from the line-center of the $\mu \rightarrow I$ transition. The two 3-j symbols project the irreducible components of rank j and j' (which equals j) in the initial and final density sub-matrices in Eq. (9.50). We further simplify this result using the Wigner-Eckart theorem, following which each factor of a matrix element of the electron's position vector \mathbf{r} on the RHS of Eq. (9.51) yields another 3-j symbol.

Using the identity for sums of products of three 3-j symbols, and their orthogonality property, we get the following expression for the cross-section:

$$\begin{aligned} \sigma_{F_I \rightarrow F_J, (j)}(\omega) = & \frac{8\pi}{9} \frac{\omega_{\text{Ly}\alpha}^4}{c^4} \frac{e^4}{\hbar^2} \sqrt{\frac{2F_J+1}{2F_I+1}} \sum_{\mu, \nu} (-1)^{F_I - F_J} \frac{\langle \mu || r || J \rangle^* \langle \mu || r || I \rangle \langle \nu || r || I \rangle^* \langle \nu || r || J \rangle}{(\Delta\omega_{\mu I} + i\Gamma_{\mu}/2)(\Delta\omega_{\nu I} - i\Gamma_{\nu}/2)} \\ & \times \begin{Bmatrix} F_{\mu} & F_{\nu} & j \\ F_I & F_I & 1 \end{Bmatrix} \begin{Bmatrix} F_{\mu} & F_{\nu} & j \\ F_J & F_J & 1 \end{Bmatrix}. \end{aligned} \quad (9.52)$$

When we perform the summation over the upper levels (μ and ν), the terms with $\mu = \nu$ and $\mu \neq \nu$ give Lorentzian line and interference profiles, respectively. In this calculation, we assumed that the only factor involved in broadening the lines shown in Fig. 9.1 is their finite lifetime; in reality, the lines are broadened due to a combination of this and the Doppler effect, owing to which we need to convolve these profiles with the appropriate velocity distributions.

In the case where the triplet sublevels are equally occupied, the only relevant components of the density sub-matrices are those of rank zero. For $j = 0$, Eq. (9.52) gives net transition cross-sections from $F = 1 \rightarrow F = 0$ and $F = 0 \rightarrow F = 1$, which have been previously worked out. We use the notation and list of line strengths in Appendix B of Ref. [402]. In particular, Fig. 9.1 shows their choice of labels for the various lines making up the fine-structure of the Ly α line, which we will use in subsequent expressions.

Using the line-strengths in Ref. [402] for the irreducible matrix elements in Eq. (9.52), the isotropic cross-sections are

$$\sigma_{0 \rightarrow 0, (0)} = \frac{3}{2} \lambda_{\text{Ly}\alpha}^2 \gamma_{2p} \left(\frac{1}{9} \phi_{\text{CC}} + \frac{4}{9} \phi_{\text{FF}} + \frac{4}{9} \phi_{\text{CF}} \right), \quad (9.53a)$$

$$\sigma_{1 \rightarrow 1, (0)} = \frac{3}{2} \lambda_{\text{Ly}\alpha}^2 \gamma_{2p} \left(\frac{1}{9} \phi_{\text{AA}} + \frac{4}{27} \phi_{\text{BB}} + \frac{1}{27} \phi_{\text{DD}} + \frac{5}{9} \phi_{\text{EE}} + \frac{4}{27} \phi_{\text{BD}} \right), \quad (9.53\text{b})$$

$$\sigma_{0 \rightarrow 1, (0)} = \frac{3}{2} \lambda_{\text{Ly}\alpha}^2 \gamma_{2p} \left(\frac{2}{9} \phi_{\text{CC}} + \frac{2}{9} \phi_{\text{FF}} - \frac{4}{9} \phi_{\text{CF}} \right), \text{ and} \quad (9.53\text{c})$$

$$\sigma_{1 \rightarrow 0, (0)} = \frac{3}{2} \lambda_{\text{Ly}\alpha}^2 \gamma_{2p} \left(\frac{2}{27} \phi_{\text{BB}} + \frac{2}{27} \phi_{\text{DD}} - \frac{4}{27} \phi_{\text{BD}} \right), \quad (9.53\text{d})$$

where $\gamma_{2p} = \Gamma_{2p}/4\pi = 50$ MHz is the HWHM of the Ly α transition, and ϕ_{AB} etc. are the interference or line-profiles for the various lines shown in Fig. 9.1.

$$\phi_{\text{AB}}(\nu) = \frac{\gamma_{2p}}{\pi} \frac{\Delta\nu_{\text{A}} \Delta\nu_{\text{B}} + \gamma_{2p}^2}{(\Delta\nu_{\text{A}}^2 + \gamma_{2p}^2)(\Delta\nu_{\text{B}}^2 + \gamma_{2p}^2)}. \quad (9.54)$$

In the situation of interest in this work, the triplet is spin-polarized i.e. it has an irreducible component of rank-2. The one extra cross-section which involves this component is

$$\sigma_{1 \rightarrow 1, (2)} = \frac{3}{2} \lambda_{\text{Ly}\alpha}^2 \gamma_{2p} \left(\frac{1}{27} \phi_{\text{BB}} + \frac{1}{108} \phi_{\text{DD}} + \frac{7}{36} \phi_{\text{EE}} + \frac{2}{9} \phi_{\text{AE}} + \frac{1}{27} \phi_{\text{BD}} + \frac{1}{3} \phi_{\text{BE}} + \frac{1}{6} \phi_{\text{DE}} \right). \quad (9.55)$$

Note that this calculation also gives us the depopulation rates (or equivalent cross-section) of Section 9.2.3.1. These rates are independent of the rank of the irreducible component (or the magnetic quantum numbers) by isotropy. Since the net population of the 2p levels is always negligible, the rate of depopulation from a level is given by the sum of the rates of all repopulations which start from that level:

$$\sigma_{F_I} |_{\text{depop}} = \sum_{F_J} \sigma_{F_I \rightarrow F_J, (0)}. \quad (9.56)$$

We obtain the following evolution equations for the irreducible components of interest by subtracting the contribution of depopulation from that of repopulation:

$$\dot{\mathcal{P}}_{00} |_{\text{Ly}\alpha} = -4\pi \int d\nu J_{\text{Ly}\alpha}(\nu) \left[\sigma_{1 \rightarrow 0, (0)}(\nu) \mathcal{P}_{00} - \sigma_{0 \rightarrow 1, (0)}(\nu) \rho_0 \right], \quad (9.57)$$

$$\dot{\mathcal{P}}_{2m} |_{\text{Ly}\alpha} = -4\pi \int d\nu J_{\text{Ly}\alpha}(\nu) \left[\sigma_{1 \rightarrow 1, (0)}(\nu) + \sigma_{1 \rightarrow 0, (0)}(\nu) - \sigma_{1 \rightarrow 1, (2)}(\nu) \right] \mathcal{P}_{2m}. \quad (9.58)$$

To simplify these equations, we use the relation $\rho_0 = 1 - \mathcal{P}_{00}$, and substitute the repopulation cross-sections for the rank-zero components from Eq. (9.53), and the rank-two component of the triplet from Eq. (9.55).

The effect of optical pumping by Ly α photons on the rank zero component (net triplet occupancy) is complicated by a source term. In the approximation of a very high cross-section (or $T > \infty$), the states are driven to equal occupancy, i.e., $\mathcal{P}_{00} \rightarrow 3/4$. In order to correct the populations for a finite temperature, we need to consider the frequency dependence of the flux $J_{\text{Ly}\alpha}$. This motivates

the definition of the flux correction factor \tilde{S}_α ³ and the effective color temperature $T_{c,\text{eff}}$, which are given by

$$T_{c,\text{eff}} = -\frac{h}{k_B} \frac{d}{d\nu} \ln J_{\text{Ly}\alpha}(\nu) \quad (9.59)$$

and

$$\tilde{S}_\alpha = \frac{9}{8\lambda_{\text{Ly}\alpha}^2 \gamma_{2p}} \int d\nu \frac{J_{\text{Ly}\alpha}(\nu)}{J_\alpha} [\sigma_{1 \rightarrow 0,(0)}(\nu) + \sigma_{0 \rightarrow 1,(0)}(\nu)], \quad (9.60)$$

where J_α is the flux on the blue side of the Lyman- α line, before it is processed by any radiative transfer. Substitution of these definitions in Eq. (9.57) gives us the evolution equation for the occupancy:

$$\dot{\mathcal{P}}_{00}|_{\text{Ly}\alpha} = -\frac{32}{9} \pi \lambda_{\text{Ly}\alpha}^2 \gamma_{2p} \tilde{S}_\alpha J_\alpha \left[\mathcal{P}_{00} - \frac{3}{4} + \frac{3T_*}{16T_{c,\text{eff}}} \right]. \quad (9.61)$$

The evolution of the rank two irreducible component of the triplet state density sub-matrix is easier to evaluate, since it has no source term. The detailed frequency dependence of the flux $J_{\text{Ly}\alpha}$ is not crucial. Substituting the expressions for the cross-sections, we obtain the following depolarization rate:

$$\dot{\mathcal{P}}_{2m}|_{\text{Ly}\alpha} = -0.601 \times 6\pi \lambda_{\text{Ly}\alpha}^2 \gamma_{2p} \tilde{S}_{\alpha,(2)} J_\alpha \mathcal{P}_{2m}, \quad (9.62)$$

where the flux correction factor $\tilde{S}_{\alpha,(2)}$ for the rank-two tensor is defined such that

$$0.601 \tilde{S}_{\alpha,(2)} J_\alpha = \int d\nu J_{\text{Ly}\alpha}(\nu) \left(\frac{1}{9} \phi_{AA} + \frac{5}{27} \phi_{BB} + \frac{11}{108} \phi_{DD} + \frac{13}{36} \phi_{EE} - \frac{2}{9} \phi_{AE} - \frac{1}{27} \phi_{BD} - \frac{1}{3} \phi_{BE} - \frac{1}{6} \phi_{DE} \right), \quad (9.63)$$

and the numerical pre-factor is the integral over frequency of the term enclosed in braces on the RHS of the above equation.

³The tilde is to avoid conflict with the usual definition of S_α in the literature, which approximates the color temperature, $T_{c,\text{eff}}$ with the kinetic temperature, T_k . It is consistent with the notation of Ref. [402].

Chapter 10

From microphysics to observables

10.1 Radiative Transfer

Sections 9.1 and 9.2 dealt with the evolution of the atom's density matrix due to various processes. In this section, we study the evolution of the components of the 21-cm radiation's phase-space density matrix $f_{X,jm}(\omega)$. In particular, the intensity monopole $f_{1,00}$ and quadrupole $f_{1,2m}$ are the relevant multipoles to study for the effect on the brightness temperature.

The baryon rest frame simplifies the details of the matter-radiation interaction, and hence we use it throughout this calculation. We restrict ourselves to quantities which are at most of the first order in smallness in terms of the matter overdensity δ .

The only quantity related to the radiation field with a zeroth-order piece is the intensity monopole $f_{1,00}$. From the discussion in Section 8.1, we expect the matter velocity \mathbf{v} and the intensity and polarization quadrupoles, $f_{1,2m}$ and $f_{E,2m}$, to be quantities of the first order in smallness.

The Boltzmann equation for a generic component of the phase space density f_X is

$$\frac{Df_X}{Dt} = \dot{f}_X|_s. \quad (10.1)$$

The left hand side is the material derivative with respect to the flow of points in phase space, which represents the effect of free-streaming. The right hand side is the source term for the phase-space density, due to interaction with atoms.

10.1.1 Free-streaming term

The material derivative of the phase-space density expands to

$$\frac{Df}{Dt} = \dot{f} + \frac{d\mathbf{x}}{dt} \cdot \nabla f + \frac{d\omega}{dt} \frac{\partial f}{\partial \omega} + \frac{d\hat{\mathbf{n}}}{dt} \cdot \nabla_{\hat{\mathbf{n}}} f, \quad (10.2)$$

where, as earlier, $\hat{\mathbf{n}}$ is the radiation's direction of propagation. The second, third, and fourth terms represent advection, time-dependent redshift, and lensing, respectively. Since we are interested only in terms up to the first order in the density fluctuations, we neglect lensing (since it is a second-order effect), and replace the coefficient of ∇f in the advection term with its zeroth-order value, which is

$$\frac{d\mathbf{x}}{dt} = c \hat{\mathbf{n}}. \quad (10.3)$$

In order to expand the redshift term, we use the relation between the angular frequency of a photon in the baryon rest frame (ω) and in the Newtonian frame (ω_N):

$$\omega = \omega_N \left(1 - \frac{\mathbf{v} \cdot \hat{\mathbf{n}}}{c} \right), \quad (10.4)$$

where \mathbf{v} and $\hat{\mathbf{n}}$ are the bulk matter velocity and the direction of the photon's travel, respectively. The coefficient of the time-dependent redshift term is

$$\frac{1}{\omega} \frac{d\omega}{dt} = \frac{1}{\omega_N} \frac{d\omega_N}{dt} - \frac{1}{c} \frac{d}{dt} (\mathbf{v} \cdot \hat{\mathbf{n}}) + \dots = \frac{1}{\omega_N} \frac{d\omega_N}{dt} - \frac{1}{c} \dot{v}_i n_i - \frac{\partial v_i}{\partial x_j} n_i n_j + \dots \quad (10.5)$$

The first term, which is the rate of redshifting in the Newtonian frame, has contributions both from large-scale Hubble flow and gravitational redshifting in the presence of local potential wells. The latter contribution is the Sachs-Wolfe effect. The second term is the time-dependent redshift due to local acceleration, and is of the same size as the Sachs-Wolfe term. The final term, which is the origin of the effect of interest, is the contribution of the local matter velocity gradient $\nabla \mathbf{v}$.

The effect of local velocity gradients is much larger than that of acceleration, which scales as the depth of the potential wells, as long as the modes under consideration are sub-horizon sized. We estimate their relative sizes as

$$\frac{(1/c)\dot{v}_i n_i}{(\partial v_i / \partial x_j) n_i n_j} \approx \frac{aH}{kc} \approx 4 \times 10^{-4} \times \left(\frac{1+z}{10} \right)^{1/2} \left(\frac{k}{1 \text{ Mpc}^{-1}} \right)^{-1} \left(\frac{\Omega_m h^2}{0.143} \right)^{1/2}. \quad (10.6)$$

The second term in Eq. (10.2) is the advection term. On free streaming, it causes mixing of multipoles on a characteristic timescale $\sim (a/kc)$ [397]. The size of this contribution relative to the time-dependent redshift term is set by the comparison with the timescale for the photons to redshift through the line. We can safely neglect the advection term as long as we restrict ourselves to modes of wavelengths much larger than the Jeans length, r_J , at this epoch. This is a good approximation for the modes under consideration:

$$\frac{c(\partial f / \partial x_i) n_i}{H\omega(\partial f / \partial \omega)} \sim \frac{k v_s}{a H} \sim \frac{kr_J}{a} \approx 5.8 \times 10^{-3} \times \left(\frac{T_k}{T_\gamma} \right)^{1/2} \left(\frac{k}{1 \text{ Mpc}^{-1}} \right) \left(\frac{\Omega_m h^2}{0.143} \right)^{-1/2}. \quad (10.7)$$

Hence the most important contribution to the time-dependent redshift term is the velocity gradient

term. We assume that the fluctuation is a plane wave with co-moving wave-vector \mathbf{k} , and use the continuity equation to express the velocity gradient in terms of the overdensity as follows:

$$\frac{1}{\omega} \frac{d\omega}{dt} \approx -H - \frac{\partial v_i}{\partial x_j} n_i n_j = -H \left[1 - \delta (\hat{\mathbf{k}} \cdot \hat{\mathbf{n}})^2 \right], \quad (10.8)$$

where H is the Hubble rate at the redshift under consideration and δ is the local overdensity. In writing this equation, we used the standard scaling of the growth factor for a matter dominated universe, i.e. $d(\log \delta)/d(\log a) = 1$.

Thus the free-streaming term of Eq. (10.2) is

$$\frac{Df}{Dt} = \dot{f} - H \left[1 - \delta (\hat{\mathbf{k}} \cdot \hat{\mathbf{n}})^2 \right] \omega \frac{\partial f}{\partial \omega}. \quad (10.9)$$

In a coordinate system with an arbitrary orientation,

$$(\hat{\mathbf{k}} \cdot \hat{\mathbf{n}})^2 = \frac{8\pi}{15} \sum_m Y_{2m}(\hat{\mathbf{k}}) [Y_{2m}(\hat{\mathbf{n}})]^* + \frac{1}{3}. \quad (10.10)$$

Using this identity, we write down the free-streaming terms for the relevant moments in a general coordinate system.

In order to expand Eq. (10.9) into moments, we note that the only relevant moments, i.e., those which are non-zero up to first order in the matter density fluctuation δ , are the intensity monopole $f_{I,00}$ (which has a zeroth-order piece too) and quadrupole $f_{I,2m}$, and the polarization quadrupole $f_{E,2m}$ (vide Section 8.3 and Table 10.1). Thus, up to first order in δ , the equations describing the free-streaming of the relevant moments are

$$\frac{Df_{I,00}}{Dt} = \dot{f}_{I,00} - H \left[1 - \frac{\delta}{3} \right] \omega \frac{\partial f_{I,00}}{\partial \omega}, \quad (10.11a)$$

$$\frac{Df_{I,2m}}{Dt} = \dot{f}_{I,2m} - H\omega \frac{\partial f_{I,2m}}{\partial \omega} + \frac{2}{3} \sqrt{\frac{4\pi}{5}} \delta H\omega \frac{\partial f_{I,00}}{\partial \omega} Y_{2m}(\hat{\mathbf{k}}), \text{ and} \quad (10.11b)$$

$$\frac{Df_{E,2m}}{Dt} = \dot{f}_{E,2m} - H\omega \frac{\partial f_{E,2m}}{\partial \omega}. \quad (10.11c)$$

10.1.2 Source term

The source term describes the evolution of the 21-cm radiation's phase-space density matrix due to interaction with neutral hydrogen atoms. In this section, we generalize the usual treatment of spontaneous and stimulated emission, and photo-absorption to the case of spin-polarized atoms.

We complete construction of the plane wave source term $\dot{f}_{\alpha\beta}(\hat{\mathbf{n}}, \omega)|_s$ in several steps. First, we find the contribution to the plane wave source term from a single atom in terms of spherical operators. Then we sum this contribution over all atoms, with the specified number density $n_{\text{H}x_{1s}}$.

Finally, we turn the required expectation values of spherical operators into photon phase space densities, and re-express them in terms of the radiation multipoles and atomic polarizations.

We write the second-order moments of the photon field in the plane wave basis in terms of the spherical basis by inversion of Eq. (10.45):

$$a_\alpha(\mathbf{k}_\gamma) = \frac{(2\pi c)^{3/2}}{\omega} e^{-i\mathbf{k}_\gamma \cdot \mathbf{R}} \sum_{jm\lambda} \left[\mathbf{e}_{(\alpha)}^* \cdot \mathbf{Y}_{jm}^{(\lambda)} \right] (\hat{\mathbf{k}}_\gamma) a_{jm}^{(\lambda)}(\omega), \quad (10.12)$$

where $\omega = k_\gamma/c$ and $\lambda \in \{E, M\}$. We have inserted a factor of $e^{-i\mathbf{k}_\gamma \cdot \mathbf{R}}$ here to place the atom (which is the center around which we expand the spherical waves) at position \mathbf{R} rather than the origin. It follows that the time evolution of the photon density matrix is

$$\begin{aligned} \frac{d}{dt} \langle a_\alpha^\dagger(\mathbf{k}_\gamma) a_\beta(\mathbf{k}'_\gamma) \rangle &= \frac{(2\pi c)^3}{\omega^2} \sum_{jm\lambda j'm'\lambda'} \left[\mathbf{e}_{(\alpha)} \cdot \mathbf{Y}_{jm}^{(\lambda)*} \right] (\hat{\mathbf{k}}_\gamma) \left[\mathbf{e}_{(\beta)}^* \cdot \mathbf{Y}_{j'm'}^{(\lambda')} \right] (\hat{\mathbf{k}}'_\gamma) \\ &\quad \times e^{i(\mathbf{k}_\gamma - \mathbf{k}'_\gamma) \cdot \mathbf{R}} \frac{d}{dt} \langle a_{jm}^{(\lambda)\dagger}(\omega) a_{j'm'}^{(\lambda')}(\omega') \rangle. \end{aligned} \quad (10.13)$$

This result is valid if the electromagnetic field interacts with a single atom. However, in the scenario under consideration, it interacts with an ensemble of atoms of number density $n_{\text{H}x_{1s}}$. We obtain such an ensemble by integrating Eq. (10.13) over volume $d^3\mathbf{R}$ and multiplying by $n_{\text{H}x_{1s}}$. Using the rule that $\int e^{i(\mathbf{k}_\gamma - \mathbf{k}'_\gamma) \cdot \mathbf{R}} d^3\mathbf{R} = (2\pi)^3 \delta^{(3)}(\mathbf{k}_\gamma - \mathbf{k}'_\gamma)$, we obtain a δ -function on the right hand side and hence the result:

$$\dot{f}_{\beta\alpha}(\omega, \hat{\mathbf{k}}_\gamma)|_s = \frac{(2\pi c)^3}{\omega^2} n_{\text{H}x_{1s}} \sum_{jm\lambda j'm'\lambda'} \left[\mathbf{e}_{(\alpha)} \cdot \mathbf{Y}_{jm}^{(\lambda)*} \right] (\hat{\mathbf{k}}_\gamma) \left[\mathbf{e}_{(\beta)}^* \cdot \mathbf{Y}_{j'm'}^{(\lambda')} \right] (\hat{\mathbf{k}}_\gamma) \frac{d}{dt} \langle a_{jm}^{(\lambda)\dagger}(\omega) a_{j'm'}^{(\lambda')}(\omega) \rangle. \quad (10.14)$$

Note that in Eq. (10.14), the derivative on the right-hand side is the contribution of a single atom.

Since the operator $a_{jm}^{(\lambda)\dagger}(\omega) a_{j'm'}^{(\lambda')}(\omega)$ commutes with the radiation's Hamiltonian H_γ , it evolves only in accordance with the interaction Hamiltonian $H_{\text{hf},\gamma}$, specifically:

$$\begin{aligned} \frac{d}{dt} \langle a_{jm}^{(\lambda)\dagger}(\omega) a_{j'm'}^{(\lambda')}(\omega) \rangle &= \frac{i}{\hbar} \left\langle \left[H_{\text{hf},\gamma}, a_{jm}^{(\lambda)\dagger}(\omega) a_{j'm'}^{(\lambda')}(\omega) \right] \right\rangle \\ &= \frac{i}{\hbar} \sum_{m_F} V_{m_F a, m}(\omega) \left\langle |1m_F\rangle \langle 00| a_{j'm'}^{(\lambda')}(\omega) \right\rangle \delta_{M\lambda} \delta_{j1} + \text{c.c.s.} \\ &= -\frac{\pi}{\hbar^2} \sum_{m_F m_2 m_3} V_{m_F a, m}(\omega) V_{m_2 a, m_3}^*(\omega) \delta(\omega - \omega_{\text{hf}}) \delta_{M\lambda} \delta_{j1} \\ &\quad \times \left[\delta_{m_2 m_F} \rho_{aa} f_{j'm_3}^{(\lambda'j')(\text{M}1)}(\omega) - \rho_{m_2 m_F} (\delta_{\lambda'M} \delta_{j'1} \delta_{m'm} + f_{m'm_3}^{(\lambda'j')(\text{M}1)}(\omega)) \right] + \text{c.c.s.} \end{aligned} \quad (10.15)$$

Here again ‘‘c.c.s.’’ stands for complex conjugation with a swap (i.e. swap $\lambda jm \leftrightarrow \lambda' j' m'$). In the

second equality we used Eq. (9.4) for $H_{\text{hf},\gamma}$, and in the third we use the results of Appendix 10.C for the atom-radiation three-point function.

We next use Eq. (9.9) for the interaction matrix elements, with which Eq. (10.15) simplifies to

$$\begin{aligned} \frac{d}{dt} \langle a_{jm}^{(\lambda)\dagger}(\omega) a_{j'm'}^{(\lambda')}(\omega) \rangle &= -\frac{A}{2} \delta(\omega - \omega_{\text{hf}}) \delta_{M\lambda} \delta_{j1} \sum_{m_2} \left\{ \delta_{m_2 m} \rho_{aa} f_{m'm_2}^{(\lambda'j')(\text{M1})}(\omega) \right. \\ &\quad \left. - \rho_{m_2 m} [\delta_{\lambda'M} \delta_{j'1} \delta_{m'm_2} + f_{m'm_2}^{(\lambda'j')(\text{M1})}(\omega)] \right\} + \text{c.c.s.} \end{aligned} \quad (10.16)$$

A useful definition is the isotropic absorption cross-section $\sigma(\omega)$ for radiation whose wavelength is close to 21-cm:

$$\sigma(\omega) = 3\pi^2 \frac{c^2}{\omega^2} A \phi(\omega), \quad (10.17)$$

where $\phi(\omega)$ is the absorption profile centered at ω_{hf} . It is broadened from the delta function of Eq. (10.16) due to the thermal motions of the hydrogen atoms.

Substituting Eq. (10.16) into Eq. (10.14), using the definition (10.17) and the notation $\hat{\mathbf{n}}$ for the direction of propagation, we get

$$\begin{aligned} \dot{f}_{\beta\alpha}(\omega, \hat{\mathbf{n}})|_{\text{s}} &= -\frac{4\pi}{3} n_{\text{H}} x_{1\text{s}} \sigma(\omega) c \sum_{m_2 m j' m' \lambda'} \left[\mathbf{e}_{(\alpha)} \cdot \mathbf{Y}_{1m}^{(\text{M1})*}(\hat{\mathbf{n}}) \left[\mathbf{e}_{(\beta)}^* \cdot \mathbf{Y}_{j'm'}^{(\lambda')}(\hat{\mathbf{n}}) \left\{ \delta_{m_2 m} \rho_{aa} f_{m'm_2}^{(\lambda'j')(\text{M1})}(\omega) \right. \right. \right. \\ &\quad \left. \left. - \rho_{m_2 m} [\delta_{\lambda'M} \delta_{j'1} \delta_{m'm_2} + f_{m'm_2}^{(\lambda'j')(\text{M1})}(\omega)] \right\} + [\alpha \leftrightarrow \beta]^* \right]. \end{aligned} \quad (10.18)$$

(Note that because of the symmetry of Eq. 10.14 under $\lambda j m \leftrightarrow \lambda' j' m'$ symmetry, the ‘‘c.c.s.’’ term simply results in the complex conjugate of the contribution with α and β switched, thereby guaranteeing the Hermiticity of the phase-space density matrix).

It is profitable to break Eq. (10.18) into the three terms in braces: these correspond to absorption, spontaneous emission, and stimulated emission, respectively. Each one may be converted back into radiation multipole moments using the inverse of Eq. (8.33):

$$(\dot{f}_{\beta\alpha})_{jm}(\omega)|_{\text{s}} = \sqrt{\frac{2j+1}{4\pi}} \int \dot{f}_{\beta\alpha}(\omega, \hat{\mathbf{n}})|_{\text{s}} [\beta - \alpha Y_{jm}(\hat{\mathbf{n}})] d^2 \mathbf{n}. \quad (10.19)$$

This conversion entails the angular integral of products of three spherical harmonics, and results in appropriate sets of 3-j symbols [401].

The absorption term is

$$(\dot{f}_{\alpha\beta})_{jm}(\omega)|_{\text{ab}} = -n_{\text{H}} x_{1\text{s}} \sigma(\omega) c \rho_{aa} (f_{\alpha\beta})_{jm}(\omega). \quad (10.20)$$

The emission terms involve elements of the triplet state density sub-matrix ρ_{mn} , which are most

naturally expressed in terms of the irreducible components \mathcal{P}_{jm} using Eq. (8.19). The spontaneous emission term simplifies to

$$(\dot{f}_{\alpha\beta})_{jm}(\omega)|_{\text{sp.em}} = n_{\text{H}}x_{1\text{s}}\frac{\sigma(\omega)c}{3}\sqrt{3(2j+1)}\alpha\beta\begin{pmatrix} 1 & 1 & j \\ \alpha & -\beta & \beta-\alpha \end{pmatrix}\mathcal{P}_{jm}, \quad (10.21)$$

and the stimulated emission term simplifies to

$$\begin{aligned} (\dot{f}_{\alpha\beta})_{jm}|_{\text{st.em}} &= \frac{2j+1}{2}n_{\text{H}}x_{1\text{s}}\frac{\sigma(\omega)c}{3}(-1)^m\sum_{j_1m_1j_2m_2\gamma}\sqrt{3(2j_2+1)}\left[\alpha\gamma\begin{pmatrix} j_1 & j_2 & j \\ -m_1 & -m_2 & m \end{pmatrix}\right. \\ &\quad \times\begin{pmatrix} 1 & 1 & j_2 \\ \alpha & -\gamma & \gamma-\alpha \end{pmatrix}\begin{pmatrix} j_1 & j_2 & j \\ \gamma-\beta & \alpha-\gamma & \beta-\alpha \end{pmatrix}(f_{\gamma\beta})_{j_1m_1}\mathcal{P}_{j_2m_2}] \\ &\quad \left. +(-1)^{-m}[\alpha\leftrightarrow\beta, m\rightarrow-m]^*. \right. \end{aligned} \quad (10.22)$$

We can further rewrite the source terms of (10.20), (10.21), and (10.22) in terms of the parity invariants of Eq. (8.34).

As noted earlier in Section 10.1.1, the only relevant moments are the intensity monopole $f_{\text{I},00}$ and quadrupole $f_{\text{I},2m}$, and the polarization quadrupole $f_{\text{E},2m}$. Summing up all the contributions yields the following source terms for these moments:

$$\dot{f}_{\text{I},00}(\omega)|_{\text{s}} = n_{\text{H}}x_{1\text{s}}\frac{\sigma(\omega)c}{3}[-(3-4\mathcal{P}_{00})f_{\text{I},00} + \mathcal{P}_{00}], \quad (10.23\text{a})$$

$$\dot{f}_{\text{I},2m}(\omega)|_{\text{s}} = n_{\text{H}}x_{1\text{s}}\frac{\sigma(\omega)c}{3}[-(3-4\mathcal{P}_{00})f_{\text{I},2m} + \frac{1}{\sqrt{2}}(1+f_{\text{I},00})\mathcal{P}_{2m}], \text{ and} \quad (10.23\text{b})$$

$$\dot{f}_{\text{E},2m}(\omega)|_{\text{s}} = n_{\text{H}}x_{1\text{s}}\frac{\sigma(\omega)c}{3}[-(3-4\mathcal{P}_{00})f_{\text{E},2m} + \sqrt{3}(1+f_{\text{I},00})\mathcal{P}_{2m}]. \quad (10.23\text{c})$$

10.2 Solution for the brightness temperature

In this section, we collect the results of the previous sections, and derive their effect on observables, i.e., the 21-cm brightness temperature fluctuations.

Let us first consider the Boltzmann equation [Eq. (10.1)]. It is useful to define a few quantities to facilitate its solution and interpretation.

First, the optical depth τ of the neutral hydrogen gas is proportional to the absorption cross section integrated over the line. For a given Hubble rate H , and a peculiar velocity along the line of sight v_{\parallel} ,

$$\tau = \frac{\pi^2c^3n_{\text{H}}x_{1\text{s}}A(3-4\mathcal{P}_{00})}{H\omega_{\text{hf}}^3[1+(1/H)(dv_{\parallel}/dr_{\parallel})]}$$

Table 10.1: Sizes of terms. They are classified as follows: A) terms included in the usual, lowest-order calculation, B) terms relevant to the effect under consideration, and C) other terms of the same order.

Quantity	Sizes of relevant constituents		
	A	B	C
$f_{1,00}(\mathcal{X})$	$T_\gamma/T_* + () \tau$		$() \tau^2$
$f_{1,2m}(\mathcal{X})$	$() \delta \tau$	$() \delta \tau^2$	
$f_{E,2m}(\mathcal{X})$			$() \delta \tau^2$
\mathcal{P}_{2m}		$() \delta \tau$	

$$= 9.7 \times 10^{-3} \times x_{1s} \left(\frac{T_\gamma}{T_s} \right) \left[1 + \frac{4}{3} \delta \right] \left(\frac{\Omega_b h^2}{0.022} \right) \times \left(\frac{\Omega_m h^2}{0.143} \right)^{-1/2} \left(\frac{1 - Y_{\text{He}}}{0.75} \right) \left(\frac{1+z}{10} \right)^{1/2}. \quad (10.24)$$

This expression is correct to first order in the fluctuation δ , and assumes that the slow variation of factors of ω in front of the absorption profile in Eq. (10.17) can be neglected. Expression (10.24) is the optical depth for the monopole, since it is derived by averaging out the dependence of the velocity-gradient on direction.

Next is the cumulative function $\mathcal{X}(\omega)$ for the absorption profile $\phi(\omega)$, which is defined as

$$\mathcal{X}(\omega) = \int_{-\infty}^{\omega} d\omega' \phi(\omega'). \quad (10.25)$$

It is convenient to express the frequency dependence of quantities in terms of \mathcal{X} , which varies between 0 and 1 from the red- to the blue-side of the line. The boundary conditions for the moments are fixed on the blue side of the line i.e. at $\mathcal{X} = 1$:

$$f_{1,00} = f_\gamma \approx \frac{T_\gamma}{T_*} \quad \text{and} \quad f_{1,2m} = f_{E,2m} = 0 \quad \text{at} \quad \mathcal{X} = 1. \quad (10.26)$$

Finally, the 21-cm brightness temperature fluctuation relative to the CMB, δT_b , is defined via the phase-space density on the red side of the line:

$$\delta T_b(\hat{\mathbf{n}}) = \frac{T_*}{1+z} (f_1(\mathcal{X} = 0, \hat{\mathbf{n}}) - f_\gamma) \approx \frac{T_*}{1+z} \left(f_1(\mathcal{X} = 0, \hat{\mathbf{n}}) - \frac{T_\gamma}{T_*} \right). \quad (10.27)$$

Before we write down the form of the Boltzmann equation, it is worthwhile to note the sizes of various relevant terms. Table 10.1 shows the sizes of the relevant pieces, and summarizes the estimates made in Section 8.3.

We solve for the phase-space density in the steady state approximation. This holds if the time taken for the photon to redshift through the line is much smaller than a Hubble time, which is the case for a narrow line. Thus we safely neglect the time-derivatives in the free-streaming term [Eq. (10.11)], and take the source terms from Eq. (10.23). With the above definitions and assumptions, the

Boltzmann equations for the various moments simplify to

$$\frac{\partial f_{1,00}}{\partial \mathcal{X}} = \tau \left[f_{1,00} - \frac{T_s}{T_*} \right], \quad (10.28a)$$

$$\frac{\partial f_{1,2m}}{\partial \mathcal{X}} = \tau \left[f_{1,2m} - \frac{2\sqrt{2} T_\gamma T_s}{3 T_*^2} \mathcal{P}_{2m} \right] + \frac{2}{3} \delta \frac{\partial f_{1,00}}{\partial \mathcal{X}} \sqrt{\frac{4\pi}{5}} Y_{2m}(\hat{\mathbf{k}}), \text{ and} \quad (10.28b)$$

$$\frac{\partial f_{E,2m}}{\partial \mathcal{X}} = \tau \left[f_{E,2m} - \frac{4\sqrt{3}}{3} \frac{T_\gamma T_s}{T_*^2} \mathcal{P}_{2m} \right]. \quad (10.28c)$$

The velocity-gradient contribution to the optical depths of the quadrupoles is different, but these moments vanish in the absence of fluctuations. Hence Eq. (10.28) is correct to first order in the overdensity δ . The simplifications here use the sizes of various terms from Table 10.1, the relation of Eq. (8.23) between the excited state occupancy \mathcal{P}_{00} and the spin temperature T_s , and neglect spontaneous emission contributions.

The Boltzmann equation must be solved along with the evolution equations for the hydrogen atom-density matrix. We obtain these from the Sections 9.1 and 9.2, and include the effects of interaction with radio photons, [Section 9.1], optical pumping by Lyman- α photons [Section 9.2.3], collisions with other hydrogen atoms [Section 9.2.2] and precession within an external magnetic field [Section 9.2.1]. Similar to the phase-space density, we solve for the various parts of the density matrix under the steady state approximation.

Firstly, we obtain the evolution of the excited state occupancy \mathcal{P}_{00} (or alternatively, the spin temperature T_s) by summing Eqs. (9.15a), (9.32a), and (9.61) and equating the result to zero:

$$\begin{aligned} \dot{\mathcal{P}}_{00} = A \left[-\mathcal{P}_{00} + (3 - 4\mathcal{P}_{00}) \overline{f_{1,00}} \right] - \frac{32\pi \lambda_{\text{Ly}\alpha}^2 \gamma_{2p}}{9} \tilde{S}_\alpha J_\alpha \left(\mathcal{P}_{00} - \frac{3}{4} + \frac{3}{16} \frac{T_*}{T_{c,\text{eff}}} \right) \\ - 4\kappa(1-0)n_{\text{H}} \left(\mathcal{P}_{00} - \frac{3}{4} + \frac{3}{16} \frac{T_*}{T_{\text{k}}} \right) = 0. \end{aligned} \quad (10.29)$$

In a similar manner, we obtain the equation for the evolution of the alignment tensor \mathcal{P}_{2m} by summing Eqs. (9.15b), (9.32b), (9.62), and (9.18). It is most convenient to continue in the coordinate system used in Section 9.2.1, with the z -axis along the direction of the magnetic field; in this system, the angular indices jm are not mixed:

$$\begin{aligned} \dot{\mathcal{P}}_{2m} = A \left[-\frac{T_\gamma}{T_*} \mathcal{P}_{2m} + \frac{3}{20\sqrt{2}} \frac{T_*}{T_s} \overline{f_{1,2m}} \right] - 3.607\pi \lambda_{\text{Ly}\alpha}^2 \gamma_{2p} \tilde{S}_{\alpha,(2)} J_\alpha \mathcal{P}_{2m} - n_{\text{H}} \kappa^{(2)}(1-0) \mathcal{P}_{2m} \\ + i \frac{m}{2} \frac{g_e \mu_{\text{B}}}{\hbar} B \mathcal{P}_{2m} \approx 0. \end{aligned} \quad (10.30)$$

As earlier, the above equation neglects spontaneous emission and is correct up to the sizes of terms

from Table 10.1. We carry out the averages over the line-profile in Eqs. (10.29) and (10.30) using

$$\bar{f} = \int_{-\infty}^{\infty} d\omega f(\omega) = \int_0^1 d\mathcal{X} f(\mathcal{X}). \quad (10.31)$$

Equations (10.29) and (10.28a) together determine the spin temperature T_s and the intensity monopole $f_{1,00}$, which is given in terms of the former by

$$f_{1,00}(\mathcal{X}) = \frac{1}{T_*} \left[T_s + (T_\gamma - T_s) e^{-\tau(1-\mathcal{X})} \right]. \quad (10.32)$$

Likewise, we use Eqs. (10.30) and (10.28b) to solve for the alignment tensor \mathcal{P}_{2m} , and the intensity quadrupole $f_{1,2m}(\mathcal{X})$ in a simultaneous manner. They are given by the following solutions, which are correct to the orders in Table 10.1:

$$\mathcal{P}_{2m} = \frac{1}{20\sqrt{2}} \frac{T_*}{T_\gamma} \left(1 - \frac{T_\gamma}{T_s} \right) \frac{\tau}{1 + x_{\alpha,(2)} + x_{c,(2)} - imx_B} \delta \sqrt{\frac{4\pi}{5}} Y_{2m}(\hat{\mathbf{k}}) \quad (10.33)$$

and

$$f_{1,2m}(\mathcal{X}) = \frac{T_s}{T_*} \left(1 - \frac{T_\gamma}{T_s} \right) \left[\frac{1}{30} \frac{\tau}{1 + x_{\alpha,(2)} + x_{c,(2)} - imx_B} + \frac{2}{3} (1 - \tau(1 - \mathcal{X})) \right] \delta \tau (1 - \mathcal{X}) \sqrt{\frac{4\pi}{5}} Y_{2m}(\hat{\mathbf{k}}), \quad (10.34)$$

where the quantities $x_{\alpha,(2)}$, $x_{c,(2)}$, and x_B parametrize the rates of depolarization by optical pumping and collisions, and precession relative to radiative depolarization. They are given by

$$x_{\alpha,(2)} = \frac{3.607\pi\lambda_{Ly\alpha}^2\gamma_{2p}T_*}{AT_\gamma} \tilde{S}_{\alpha,(2)} J_\alpha = 0.073 \tilde{S}_{\alpha,(2)} \left(\frac{1+z}{10} \right)^{-1} \left(\frac{J_\alpha}{10^{-12} \text{cm}^{-2} \text{sr}^{-1} \text{s}^{-1} \text{Hz}^{-1}} \right), \quad (10.35)$$

$$x_{c,(2)} = \kappa^{(2)}(1-0) \frac{n_H T_*}{AT_\gamma} = 2 \times 10^{-3} \left(\frac{1+z}{10} \right)^2 \left(\frac{\kappa^{(2)}(1-0)}{1.3 \times 10^{-11} \text{cm}^3 \text{s}^{-1}} \right), \text{ and} \quad (10.36)$$

$$x_B = \frac{g_e \mu_B T_*}{2\hbar AT_\gamma} B = 0.698 \left(\frac{1+z}{10} \right)^{-1} \left(\frac{B}{10^{-19} \text{G}} \right). \quad (10.37)$$

We compute the brightness temperature fluctuation, δT_b , from Eq. (10.27), wherein the phase-space density is given by the sum of the monopole and quadrupole from Eqs. (10.32) and (10.34), respectively. We get the following expression, which is one of the main results of this work:

$$\begin{aligned} \delta T_b(\hat{\mathbf{n}}) &= \left(1 - \frac{T_\gamma}{T_s} \right) x_{1s} \left(\frac{1+z}{10} \right)^{1/2} \left[26.4 \text{ mK} \left\{ 1 + \left(1 + (\hat{\mathbf{k}} \cdot \hat{\mathbf{n}})^2 \right) \delta \right\} - 0.128 \text{ mK} \left(\frac{T_\gamma}{T_s} \right) x_{1s} \left(\frac{1+z}{10} \right)^{1/2} \right. \\ &\quad \left. \times \left\{ 1 + 2 \left(1 + (\hat{\mathbf{k}} \cdot \hat{\mathbf{n}})^2 \right) \delta - \frac{\delta}{15} \sum_m \frac{4\pi}{5} \frac{Y_{2m}(\hat{\mathbf{k}}) [Y_{2m}(\hat{\mathbf{n}})]^*}{1 + x_{\alpha,(2)} + x_{c,(2)} - imx_B} \right\} \right]. \end{aligned} \quad (10.38)$$

Equation (10.37) offers a rough guide to estimate the strengths of magnetic fields to which the

method outlined in this work is most sensitive. We must keep in mind that the coefficient x_B only measures the strength of the precession relative to radiative de-polarization, and a full analysis of the discriminating power of this method must estimate the sizes of Ly α and collisional de-polarization, or the coefficients $x_{\alpha,(2)}$ and $x_{c,(2)}$ in Eqs. (10.35) and (10.36). Subsequent work in this series will study this in more detail. For now, we note that field strengths of $\mathcal{O}(10^{-19}$ G) at redshifts of $z \sim 10$ are associated with $x_B \sim 1$.

Given this scale of field strengths, we identify two physical regimes – one with weaker fields, and one with much stronger ones. We use the weak-field limit of Eq. (10.38) to make contact with the intuitive picture laid out in Section 8.3. Taking the limit of $x_B \rightarrow 0$ in Eq. (10.38) and writing the result in a coordinate independent fashion, we get the following response to a weak magnetic field:

$$\frac{d\delta T_b}{dB}(\hat{\mathbf{n}}) = 1.786 \times 10^{17} \frac{\text{mK}}{\text{G}} [\hat{\mathbf{B}} \cdot (\hat{\mathbf{k}} \times \hat{\mathbf{n}})] (\hat{\mathbf{n}} \cdot \hat{\mathbf{k}}) \times \left(1 - \frac{T_\gamma}{T_s}\right) x_{1s}^2 \left(\frac{T_\gamma}{T_s}\right) \frac{\delta}{(1 + x_{\alpha,(2)} + x_{c,(2)})^2}. \quad (10.39)$$

In the geometry of Fig. 8.2, the direction to the observer is $\hat{\mathbf{n}} = -\hat{\mathbf{y}}$. If we substitute this in the above equation, we recover the angular structure of the correction to the brightness temperature in Section 8.3, in particular, the form of Eq. (8.10). The latter only accounted for the radiative decay of the magnetic moment, while Eq. (10.39) includes the additional effect of collisions and optical pumping through the dimensionless factors of $x_{\alpha,(2)}$ and $x_{c,(2)}$.

We realize the complementary strong field limit by taking the limit $x_B \rightarrow \infty$ in Eq. (10.38). The change in brightness temperature over the case with no external magnetic field is

$$\delta T_b(\hat{\mathbf{n}})|_{x_B \rightarrow \infty} - \delta T_b(\hat{\mathbf{n}})|_{x_B=0} = 8.53 \mu\text{K} \times \left[P_2(\hat{\mathbf{k}} \cdot \hat{\mathbf{B}}) P_2(\hat{\mathbf{n}} \cdot \hat{\mathbf{B}}) - P_2(\hat{\mathbf{k}} \cdot \hat{\mathbf{n}}) \right] \times \left(1 - \frac{T_\gamma}{T_s}\right) x_{1s}^2 \left(\frac{1+z}{10}\right) \left(\frac{T_\gamma}{T_s}\right) \frac{\delta}{1 + x_{\alpha,(2)} + x_{c,(2)}}. \quad (10.40)$$

From the above expression, we see that the effect saturates at large values of the magnetic field strength. However, we observe that it is still possible to reconstruct the direction of the magnetic field in the plane of the sky using the form of the isotropy breaking in $\hat{\mathbf{k}}$ space. The correction is roughly three orders of magnitude fainter than the raw 21-cm brightness even for the optimal range of $\hat{\mathbf{k}}$, $\hat{\mathbf{B}}$, and J_α . However, it should be noted that it is exactly in phase with the conventional brightness temperature fluctuations – that is, it traces the same underlying density field δ and is changing the coefficient in front of this. Thus its effect on the power spectrum is of order 10^{-3} , not 10^{-6} (as would be the case if the magnetic field correction were a new random field, independent of the density but with an amplitude three orders of magnitude smaller).

10.3 Summary and Conclusions

In this study, we propose a new method to probe magnetic fields present in the universe prior to and during the early stages of cosmic reionization. The method relies on the spin-polarization of the triplet state of the hyperfine sublevels of neutral hydrogen by an anisotropic radiation field near the energy of the 21-cm transition. These anisotropies naturally arise in the early universe due to density fluctuations in the high redshift gas. In the presence of an external magnetic field, the precession of these spin-polarized atoms changes the angular distribution of the emitted 21-cm radiation at second order in optical depth. This produces a characteristic signature in the power spectrum, or two-point correlation function, of the fluctuations in brightness temperature. In particular, large-scale magnetic fields break the isotropy of the power spectrum in a way that can be identified in data from future low-frequency radio surveys.

Due to the long lifetimes of the excited states of the hyperfine transition, this method is naturally optimal for measuring very weak magnetic fields ($\lesssim 10^{-19}$ G at the epoch of reionization, or $\lesssim 10^{-21}$ G scaled to the present day). It thus raises the exciting possibility of probing seed fields that possibly gave rise to the magnetic fields observed in the present-day universe. As the background magnetic field increases, the effect saturates; however, even in the saturated case, it is possible to recover some information about the direction of the magnetic fields.

In order to estimate the size of the effect, we present a detailed calculation of the coupled evolution of atomic and photon density matrices. We account for all the processes which affect the atomic magnetic moments, such as the Wouthuysen-Field effect, atomic collisions, and radiative decay. The main results are Eq. (10.38), which includes the corrections to the brightness temperature due to all these effects, and Eqs. (10.39) and (10.40), which show the weak- and strong-field limits, respectively. This calculation provides a complete theoretical basis for the microphysics of the hyperfine transition, which can be used to compute the detectability of any particular model for primordial magnetic fields with future surveys after folding in the astrophysics which determines background parameters such as the Lyman- α flux. We will carry out this program in subsequent investigations.

The method we proposed here adds to the already exciting opportunities for the use of the 21-cm line as a probe of the early universe, and is in principle sensitive to extremely weak magnetic fields which are far beyond the reach of any other methods (including other techniques based on the 21-cm radiation). Paper II of this series [Gluscevic et al., in prep] presents the formalism to evaluate detectability of primordial magnetic fields with 21-cm surveys using this new method, and discusses the sensitivity of different radio-array designs for probing a range of magnetic-field models.

10.A Conventions for spherical tensors

In this section, we lay out the conventions for spherical tensors, and our reasons for adopting the same.

Consider a passive rotation around the z -axis by an angle α , which connects two coordinate systems S and S' as follows:

$$(\theta, \phi)|_S = (\theta, \phi - \alpha)|_{S'}, \quad (10.41)$$

where both sides refer to the same point on the unit sphere. Within quantum mechanics, the coefficients of a state and expectation values of spherical tensors transform with opposite signs:

$$c_m|_{S'} = e^{im\alpha} c_m|_S \quad \text{with} \quad |\psi\rangle = \sum_m c_m |m\rangle \quad (10.42)$$

for states and

$$\langle T_m^{(k)} \rangle|_{S'} = e^{-im\alpha} \langle T_m^{(k)} \rangle|_S \quad (10.43)$$

for spherical tensors. The spherical tensors of interest are the irreducible components of the matter density matrix (\mathcal{P}_{jm}), and the moments of the phase-space density matrix of the radiation $[(f_{\alpha\beta})_{jm}]$. They are defined in Eqs. (8.17) and (8.33); these definitions transform in the manner of Eq. (10.43).

Note that the definition of the multipoles of the radiation in Eq. (8.33) differs from the usual convention adopted in cosmology literature, which omits the complex conjugate on its RHS. The latter considers these moments as state-coefficients rather than expectation values of spherical tensors. Considering that the majority of the calculations in this work have an atomic physics flavor, our definition is convenient, though unconventional.

10.B Spherical Wave Basis for the Radiation's Phase-space Density Matrix

The standard choice of basis for the EM field's expansion is one consisting of plane waves, whose defining characteristic is that they are eigenfunctions of the linear momentum and helicity of the EM field. This is the basis used in Section 8.4.2. However, it is also possible to use eigenstates of the total angular momentum, parity and energy of the EM field as basis elements. This section expands on this, and details how to transform between these two bases.

Eigenstates of total angular momentum have the usual indices j and m . They are classified as electric and magnetic type states depending on how they behave under a parity transformation –

electric type states pick up a factor of $(-1)^j$, while those of the magnetic type pick up $(-1)^{j+1}$. The explicit form of these eigenstates is [396]

$$\mathbf{A}_{\omega,jm}^{(\lambda)}(\mathbf{r}) = \int \frac{d^3\mathbf{k}_\gamma}{(2\pi)^3} \mathbf{A}_{\omega,jm}^{(\lambda)}(\mathbf{k}_\gamma) e^{i\mathbf{k}_\gamma \cdot \mathbf{r}}, \quad \lambda = \text{E, M} \quad (10.44)$$

$$\mathbf{A}_{\omega,jm}^{(\lambda)}(\mathbf{k}_\gamma) = 4\pi^2 \left(\frac{\hbar c^3}{\omega^3} \right)^{1/2} \delta(k_\gamma - \omega/c) \mathbf{Y}_{jm}^{(\lambda)}(\hat{\mathbf{n}}), \text{ and} \quad (10.45)$$

$$\mathbf{Y}_{jm}^{(\lambda)}(\hat{\mathbf{n}}) = \begin{cases} \frac{1}{\sqrt{j(j+1)}} \nabla_{\hat{\mathbf{n}}} Y_{jm} & \lambda = \text{E} \\ \frac{1}{\sqrt{j(j+1)}} \hat{\mathbf{n}} \times \nabla_{\hat{\mathbf{n}}} Y_{jm} & \lambda = \text{M} \end{cases}, \quad (10.46)$$

where $\hat{\mathbf{n}} = \hat{\mathbf{k}}_\gamma$ is the direction of propagation and the index j runs over integers greater than zero, while m runs over integers from $-j$ to j .

We expand the vector potential \mathbf{A} in the same manner as in Eq. (8.25).

$$\mathbf{A}(\mathbf{r}) = \sum_{j,m} \int [\{a_{jm}^{(\text{E})}(\omega) \mathbf{A}_{\omega,jm}^{(\text{E})}(\mathbf{r}) + a_{jm}^{(\text{M})}(\omega) \mathbf{A}_{\omega,jm}^{(\text{M})}(\mathbf{r})\} + \text{h.c.}] d\omega, \quad (10.47)$$

where the operators $a_{\omega,jm}^{(e/m)}$ and $a_{\omega,jm}^{(e/m)\dagger}$ are annihilation and creation operators for photons of the electric and magnetic type. Operators for photons of the same type have the following commutation relations:

$$\begin{aligned} [a_{jm}(\omega), a_{j'm'}^\dagger(\omega')] &= \delta(\omega - \omega') \delta_{j,j'} \delta_{m,m'} \text{ and} \\ [a_{jm}(\omega), a_{j'm'}(\omega')] &= [a_{jm}^\dagger(\omega), a_{j'm'}^\dagger(\omega')] = 0, \end{aligned} \quad (10.48)$$

while those of different types commute with each other.

The phase-space density matrix in this basis can be defined in the same manner as in Eq. (8.30) for the plane wave basis:

$$\langle a_{jm}^{(\lambda)\dagger}(\omega) a_{j'm'}^{(\lambda')}(\omega') \rangle = f_{m',m}^{(\lambda'j')(\lambda j)}(\omega) \delta(\omega - \omega') \quad (10.49)$$

for $\lambda, \lambda' = \text{E, M}$.

At this stage, it is worthwhile to examine the general considerations leading to the forms of the density matrices in the two bases. Phase coherence between frequencies separated by $\Delta\omega$ leads to oscillatory features on time-scales of $\Delta t \sim 1/\Delta\omega$. If the time-interval Δt over which the statistical properties of the radiation field are stationary is sufficiently long, the width of the two-point function in frequency space is $\sim 1/\Delta t \rightarrow 0$. Thus the δ -function in the definition in the spherical wave basis [Eq. (10.49)] is a consequence of time-translation invariance.

The δ -function in the definition in the plane wave basis [Eq. (8.30)] is a consequence of invariance

under spatial translations, the argument paralleling the one for time-translation invariance above. It is relatively simple to express a state given in the plane wave basis in the spherical one, but the inverse transformation involves averaging over the positions of the interacting atoms to recover translational invariance. This is dealt with in greater detail in Section 10.1.2.

In the rest of this section, we describe the transformation from the plane wave basis (the $f_{X,jm}$ s) to the spherical wave one (the $f_{m,m'}^{(\lambda j)(\lambda' j')}$ s) centered at the position of a hydrogen atom interacting with the radiation. The transformation is

$$f_{m,m'}^{(\lambda j)(\lambda' j')}(\omega) = \sum_{\alpha,\beta} \int d^2\mathbf{n} f_{\alpha\beta}(\omega, \hat{\mathbf{n}}) [\mathbf{e}_{(\alpha)} \cdot \mathbf{Y}_{jm}^{(\lambda)*}](\hat{\mathbf{n}}) [\mathbf{e}_{(\beta)}^* \cdot \mathbf{Y}_{j'm'}^{(\lambda')}](\hat{\mathbf{n}}). \quad (10.50)$$

The normalization is such that if the radiation is unpolarized and isotropic (e.g. a thermal state), the elements of the phase-space density matrix are

$$f_{m,m'}^{(\lambda j)(\lambda' j')}(\omega) = \begin{cases} f_{1,00}(\omega) \delta_{j,j'} \delta_{m,m'} & \text{if } \lambda = \lambda' \\ 0 & \text{if } \lambda \neq \lambda' \end{cases}. \quad (10.51)$$

We further simplify the angular integral in the transformation of Eq. (10.50) using the moments of the phase-space density matrix in the plane wave basis [Eq. (8.33)], and the Clebsch-Gordan rule for evaluating the angular integral of the product of three spherical harmonics [401].

The M1–M1 block of the phase-space density matrix contributes to the evolution of the atom density matrix [see Section 9.1]. We derive its explicit form for arbitrarily polarized radiation by simplifying Eq. (10.50):

$$f_{m,m'}^{(\text{M1})(\text{M1})}(\omega) = \frac{3}{2} \sum_{j,m_2} \sum_{\alpha,\beta} \alpha\beta(-1)^{\alpha-m'} (f_{\alpha\beta})_{jm_2}(\omega) \begin{pmatrix} 1 & 1 & j \\ -\alpha & \beta & \alpha - \beta \end{pmatrix} \begin{pmatrix} 1 & 1 & j \\ -m & m' & -m_2 \end{pmatrix}. \quad (10.52)$$

This 3×3 block is equivalently described in terms of its irreducible components $\mathcal{F}_{jm}(\omega)$ of ranks $j = \{0, 1, 2\}$, in exactly the same manner as the matter density matrix $\rho_{m_1 m_2}$ in Eqs. (8.17) and (8.19):

$$\mathcal{F}_{jm}(\omega) = \sqrt{(2j+1)3} \sum_{m_1, m_2} (-1)^{1-m_2} \begin{pmatrix} 1 & j & 1 \\ -m_2 & \mu & m_1 \end{pmatrix} f_{m_1, m_2}^{(\text{M1})(\text{M1})}(\omega), \quad (10.53)$$

with the inverse relation

$$f_{m_1 m_2}^{(\text{M1})(\text{M1})}(\omega) = \sum_{jm} \sqrt{\frac{2j+1}{3}} (-1)^{1-m_2} \begin{pmatrix} 1 & j & 1 \\ -m_2 & m & m_1 \end{pmatrix}$$

$$\times \mathcal{F}_{jm}(\omega). \quad (10.54)$$

Substitution in Eq. (10.52) gives the explicit forms of these irreducible components

$$\mathcal{F}_{00}(\omega) = 3f_{1,00}(\omega), \quad (10.55a)$$

$$\mathcal{F}_{1m}(\omega) = \sqrt{\frac{3}{2}}f_{V,1m}(\omega), \text{ and} \quad (10.55b)$$

$$\mathcal{F}_{2m}(\omega) = \frac{3}{5\sqrt{2}} \left[f_{1,2m}(\omega) + \sqrt{6} f_{E,2m}(\omega) \right]. \quad (10.55c)$$

10.C Three-point functions of the atoms and the radiation field

Three-point functions of the atom and the radiation field affect the evolution of the atoms' density matrix ρ and the radiation's phase-space density matrix f . In this section, we derive expressions for their contribution.

The Hamiltonians for the hydrogen atoms and radiation are

$$H_{\text{hf}} = E_0|00\rangle\langle 00| + E_1 \sum_m |1m\rangle\langle 1m|, \quad (10.56)$$

$$H_\gamma = \sum_{j,m,\lambda} \int d\omega \hbar\omega a_{jm}^{(\lambda)\dagger}(\omega) a_{jm}^{(\lambda)}(\omega), \quad (10.57)$$

where E_0 and E_1 are the energies of the singlet and triplet levels. The zero-point energy has been left out of Eq. (10.57).

A three-point function is the expectation value of an operator consisting of the product of creation and annihilation operators for the hydrogen atoms and for the radiation. This function's evolution is governed by the operator's commutator with the total Hamiltonian:

$$\begin{aligned} \frac{d}{dt} \langle |1m_1\rangle\langle 00| a_{jm}^{(\lambda)}(\omega) \rangle &= \frac{i}{\hbar} \langle [H_{\text{hf}} + H_\gamma + H_{\text{hf},\gamma}, |1m_1\rangle\langle 00| a_{jm}^{(\lambda)}(\omega)] \rangle \\ &= i(\omega_{\text{hf}} - \omega) \langle |1m_1\rangle\langle 00| a_{jm}^{(\lambda)}(\omega) \rangle + \frac{i}{\hbar} \langle [H_{\text{hf},\gamma}, |1m_1\rangle\langle 00| a_{jm}^{(\lambda)}(\omega)] \rangle. \end{aligned} \quad (10.58)$$

Assuming that the interaction is turned on at $t = 0$, the formal solution to Eq. (10.58) is

$$\langle |1m_1\rangle\langle 00| a_{jm}^{(\lambda)}(\omega) \rangle = \mathcal{C} e^{i(\omega_{\text{hf}} - \omega)t} + \frac{i}{\hbar} \int_0^t dt' e^{-i(\omega_{\text{hf}} - \omega)(t' - t)} \langle [H_{\text{hf},\gamma}, |1m_1\rangle\langle 00| a_{jm}^{(\lambda)}(\omega)] \rangle. \quad (10.59)$$

If the expectation value in the integrand of the second term varies slowly with time, the exponential dominates the integral and results in a δ -function which picks out the frequency resonant with the level gap. This behaves like a rate term when the three-point function is input to an evolution

equation (the Fermi golden rule). The first term does not lead to such a secular rate contribution. We have the identity

$$\langle |1m_1\rangle\langle 00|a_{jm}^{(\lambda)}(\omega)\rangle = \frac{i}{\hbar}\pi\delta(\omega - \omega_{\text{hf}})\langle [H_{\text{hf},\gamma}, |1m_1\rangle\langle 00|a_{jm}^{(\lambda)}(\omega)]\rangle. \quad (10.60)$$

We use the form of the interaction Hamiltonian from Eq. (9.4) to evaluate the expectation value on the RHS,

$$\begin{aligned} \langle [H_{\text{hf},\gamma}, |1m_1\rangle\langle 00|a_{jm}^{(\lambda)}(\omega)]\rangle &= \sum_{m_2, m'} \int d\omega' V_{m_2 a, m'}^*(\omega') \left[\delta_{m_1 m_2} \langle |00\rangle\langle 00|a_{1m'}^{(M)\dagger}(\omega') a_{jm}^{(\lambda)}(\omega)\rangle \right. \\ &\quad \left. - \langle |1m_1\rangle\langle 1m_2| a_{jm}^{(\lambda)}(\omega) a_{1m'}^{(M)\dagger}(\omega')\rangle \right]. \end{aligned} \quad (10.61)$$

The dominant contribution to the four-point function is from the classical, disconnected part. We evaluate this using the commutation relations Eq. (10.48) and the definitions of the photon and atom density matrices. The final result is

$$\begin{aligned} \langle [H_{\text{hf},\gamma}, |1m_1\rangle\langle 00|a_{jm}^{(\lambda)}(\omega)]\rangle &= \sum_{m_2, m'} V_{m_2 a, m'}^*(\omega) \left[\delta_{m_1 m_2} \rho_{aa} f_{m, m'}^{(\lambda j), (M1)}(\omega) \right. \\ &\quad \left. - \rho_{m_2 m_1} \left\{ \delta_{(\lambda)(M)} \delta_{j1} \delta_{mm'} + f_{m, m'}^{(\lambda j), (M1)}(\omega) \right\} \right]. \end{aligned} \quad (10.62)$$

Part IV

The stability of tidally deformed neutron stars to three- and four-mode coupling

Chapter 11

Preliminaries¹

11.1 Introduction

Compact binary systems are thought to host some of the most energetic phenomena in the universe. In particular, neutron star binaries can be exceptionally bright sources of both gravitational and electromagnetic radiation during their inspiral and eventual merger. Such systems provide a unique window into a variety of fundamental physical processes. For example, merging binaries which host at least one neutron star are thought to be sources of short gamma ray bursts. These binary inspirals are also the most promising sources for the upcoming generation of gravitational wave detectors, such as Advanced LIGO [210], Advanced VIRGO [211], and KAGRA [212]. Observations of compact binaries through their gravitational wave emission should provide precise measurements of the binary parameters [e.g. 214–216], including possibly the indirect measurement of the neutron star equation of state through the effects of tidal deformation of the binary companions on the gravitational waveform [e.g. 217–220] or the final cutoff frequency of the gravitational waveform [e.g. 221–223]. Since the phase of the waveform depends sensitively on the binary parameters, it is imperative that we have accurate theoretical templates in order to extract useful information from observed inspirals.

The evolution of a compact binary through radiation reaction is understood up to high order general relativistic effects in the post-Newtonian expansion, which accounts fully for the inspiral of pairs of black holes. When the binary hosts at least one neutron star, tidal interactions in principle also play a role. Tidal dissipation allows for the transfer of orbital energy into oscillations and the internal heating of the stars, which corrects the predicted rate of inspiral due to purely gravitational effects. Studies of the effect of tidal interactions and the excitation of linear perturbations have shown that tidal effects have a negligible impact on the last stages of binary inspiral [226, 227, 408–410]. In particular, they can be ignored for the purpose of gravitational wave detection and parameter extraction.

¹The material in Chapters 11–13 was adapted from the paper *The stability of tidally deformed neutron stars to three- and four-mode coupling*, Venumadhav, T., Zimmerman, A., & Hirata, C. M. 2014, *Astrophys. J.*, 781, 23. Reproduced here with permission, copyright (2013) by the American Astronomical Society.

Recently, attention has been drawn to nonlinear tidal effects in close binary systems. Weinberg et al. [411] investigated a variety of scenarios in which nonlinear instabilities can produce strong tidal effects and corresponding dissipation, through both the familiar parametric resonance mechanism and the less-familiar, nonlinear driving of modes due to strong mode-mode coupling. Even more recently, Weinberg et al. [228] (hereafter abbreviated WAB) considered nonlinear coupling between modes in a tidally perturbed neutron star and found a potential non-resonant instability. The essential idea is that the tidal perturbation can set up a strong coupling between a high-order p -mode and a high-order g -mode, through a three-mode interaction term. Since these two daughter modes have widely spaced frequencies, with $\omega_p \gg \omega_g$, they cannot suffer from a resonant instability. But, when they have nearly identical wave numbers, $k_p \simeq k_g$, WAB found that the three-mode coupling was so strong that it destabilized the daughter modes. In this case, the tidal forces on the star rapidly drive the g -mode to large amplitudes, and nonlinear dissipation of these modes in turn converts the orbital energy of the binary into tidal heating of the star. Depending on the saturation amplitude, such behavior can lead to a large correction to the orbital phase of binary inspiral, at around the time that the inspiral enters into the sensitive frequency band of gravitational wave detectors. This would represent a potential difficulty for gravitational wave detection via matched filtering with a template that accumulates signal-to-noise ratio over many orbits.

In fact, the nature of the instability discussed in WAB implies that a neutron star immersed in a static tidal field is also unstable, even when the tidal perturbation is weak compared to the star's self-gravity. In this case, the star is unstable to a sort of buckling effect: the static p -mode would cause the star to separate radially into alternating layers of increased and decreased compression, while the static g -mode gives these layers an alternating horizontal shear relative to their initial positions. We may thus consider WAB's instability to be "quasi-static" in the sense that it exists even as the tidal forcing frequency is taken to zero (see WAB Section 2 and Appendix A). However, the work of WAB focused in detail only on the three-mode coupling terms, neglecting other potentially important effects such as four-mode coupling terms.

In this work, we present an investigation of a static, tidally perturbed star, including all of the necessary three- and four-mode terms to determine whether the star is stable to the first nonlinear corrections to perturbation theory. In order to complete the analysis, we present a novel technique for computing the four-mode coupling terms between two daughter modes and the tidal perturbation. We find that the four-mode coupling terms cancel the three-mode coupling terms when the latter become large, protecting the star from non-resonant instabilities. We consider a non-rotating neutron star and a static tidal field in order to simplify the analysis. It is important to note that for the case of possible non-resonant instabilities, having a fixed rather than a slowly-varying tidal field (as compared to the neutron star's dynamical time scale) does not change the essential problem. This is because a quasi-static instability (such as WAB) occurs when perturbations of the deformed star can

possess negative potential energy, as opposed to a parametric resonance instability where a time-varying tidal field excites oscillatory modes of positive energy (a phenomenon that is impossible if the forcing frequency vanishes). WAB also investigated parametric resonances in neutron star binaries, and found that these did not contribute significantly to the orbital evolution of the binary. Other possible effects of the time-varying tidal field are considered in Appendix 13.E, and in the discussion.

For simplicity, we only consider inviscid, normal fluid neutron stars in Newtonian gravity: this physics is sufficient to capture the instability in WAB. Including the solid neutron star crust would produce additional modes at the crust-core interface (*i*) and due to shear waves (*s*) in the crust [412]; linear resonant excitation of the *i*-mode has been studied in the context of an energy source for gamma-ray burst precursors [413]. However the quasi-static instability in WAB occurs due to mode overlap in the core, and we would not expect crustal modes to play a role. General relativistic effects are also not considered: they make modest (order GM/R_*c^2) perturbations to the mode frequencies, but their only qualitative effect is a small damping due to gravitational wave emission not present in the Newtonian theory [see e.g. 414–417]. We also make use of the Cowling approximation, where the background gravitational field is held fixed while the fluid elements are perturbed about their original configuration [e.g. 418], and this approximation does have a potentially important impact, since it is necessary in the technique we use to compute the four-mode coupling. In fact, the Cowling approximation is at its worst when treating the tidal deformation. However, the high-order daughter modes whose stability we are ultimately interested in should be very well described by the Cowling approximation.

Before entering into a detailed discussion of our results, it is worthwhile to first examine a simple toy problem in order to gain an intuition regarding what order in perturbation theory we need to go to. This directly illustrates why four-mode terms are significant in the stability analysis.

11.1.1 A toy model: Two dimensional oscillator

Consider a two-dimensional harmonic oscillator with characteristic frequencies ω_1 and ω_2 , such that $\omega_1 \gg \omega_2$. The potential energy of this system for a general displacement η from equilibrium, written in coordinates with a unit-mass normalized kinetic energy term $\mathcal{T} = \frac{1}{2}\dot{\eta}^\top \dot{\eta}$, is given by

$$\mathcal{V}(\eta) = \frac{1}{2}\eta^\top \mathcal{M}\eta, \quad \text{where } \mathcal{M} = \begin{pmatrix} \omega_1^2 & 0 \\ 0 & \omega_2^2 \end{pmatrix}. \quad (11.1)$$

Consider some effect (like interaction with a third degree of freedom, for example) which rotates the coordinate basis, so that displacement vectors become $\eta' = U(\theta)\eta$, where $U(\theta)$ is in the $SO(2)$

representation of the rotation. In the new basis, the potential energy is given by

$$\mathcal{V}(\eta') = \frac{1}{2}(\eta')^\top \mathcal{M}' \eta', \quad \text{where } \mathcal{M}' = U \mathcal{M} U^\top. \quad (11.2)$$

Putting in the form of $U(\theta)$, we see that

$$\mathcal{M}'(\theta) = \begin{pmatrix} \omega_1^2 \cos^2 \theta + \omega_2^2 \sin^2 \theta & (\omega_1^2 - \omega_2^2) \cos \theta \sin \theta \\ (\omega_1^2 - \omega_2^2) \cos \theta \sin \theta & \omega_1^2 \sin^2 \theta + \omega_2^2 \cos^2 \theta \end{pmatrix} = \mathcal{M} + \delta \mathcal{M}, \quad \text{where} \quad (11.3)$$

$$\delta \mathcal{M} = \begin{pmatrix} (\omega_2^2 - \omega_1^2) \theta^2 & (\omega_1^2 - \omega_2^2) \theta \\ (\omega_1^2 - \omega_2^2) \theta & (\omega_1^2 - \omega_2^2) \theta^2 \end{pmatrix} + \mathcal{O}(\theta^3). \quad (11.4)$$

The change in the smaller eigenvalue of \mathcal{M} due to this change can be formally calculated using second-order perturbation theory as

$$\omega_-^2 = \omega_2^2 + \delta \mathcal{M}_{22} + \frac{\delta \mathcal{M}_{12}^2}{\omega_2^2 - \omega_1^2} + \dots = \omega_2^2 + \theta^2 (\omega_1^2 - \omega_2^2) + \frac{[(\omega_1^2 - \omega_2^2) \theta]^2}{\omega_2^2 - \omega_1^2} + \dots = \omega_2^2. \quad (11.5)$$

We could have predicted this from the fact that the interactions act as a pure rotation, but this avenue of analysis highlights a fact which is useful when we do not have such global, non-perturbative information. When calculating perturbations to the eigenvalues, perturbations to the matrix elements along the diagonal (\mathcal{M}_{22}) enter into the analysis at the same order as perturbations to those off the diagonal (\mathcal{M}_{12}) squared. Hence, if the angle θ is a small angle such that $\omega_2^2/(\omega_1^2 - \omega_2^2) \simeq \omega_2^2/\omega_1^2 < \theta^2 \ll 1$, the diagonal perturbation $\delta \mathcal{M}_{22}$ is much smaller than the off-diagonal perturbation $\delta \mathcal{M}_{12}$, but the latter cannot be ignored in the calculation of ω_- . Ignoring it would lead us to the conclusion that the deformed potential has an unstable direction, i.e. $\omega_-^2 = \omega_2^2 + \theta^2 (\omega_2^2 - \omega_1^2) + \dots < 0$. Figure 11.1 illustrates this point by plotting contours of constant potential \mathcal{V} using both the full rotation, and using only the leading order term in small angle θ . In the former case, it is clear that the origin remains a stable equilibrium, but in the latter case, neglecting the higher order terms leads the origin to become a saddle point.

This example captures much of the physics describing the system we are interested in, i.e., a tidally-deformed neutron star. In Section 12.1.4, we show that in the sub-matrix of a pair of high order modes, the off-diagonal perturbation to the potential is given by the three-mode coupling between the modes and the tidal deformation, and the diagonal perturbations are given by appropriate four-mode couplings. Lessons learned from the toy model tell us that we need to evaluate both the three- and the four-mode couplings in order to determine the lowest order or ϵ^2 (in dimensionless tidal strength ϵ) perturbation to the eigenfrequencies.

The example also captures one other aspect of our analysis: what happens if the shallow direction of the potential changes with time. In the limit of $\omega_1 \rightarrow \infty$, this example corresponds to that of

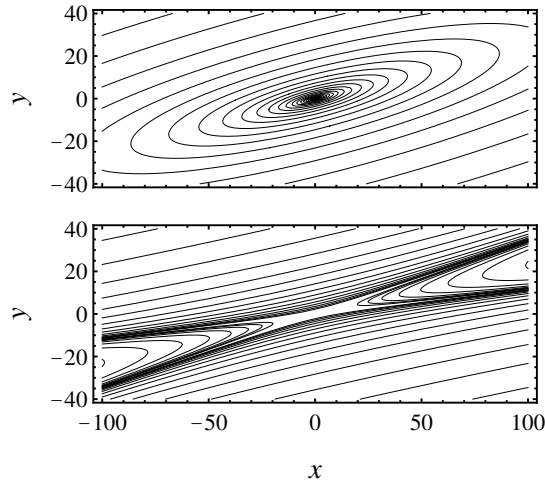


Figure 11.1: Potential surfaces for a perturbed two-dimensional oscillator, with the perturbation taking the form of a rotation. This plot is for characteristic frequencies $\omega_1/\omega_2 = 5$ and the angle of rotation $\theta = 0.25$. The top panel shows the contours of constant potential after adding perturbations of all orders in θ , while the bottom panel shows the contours after adding only terms that are first order in θ .

a bead in a restoring force ($-\omega_2^2 x$) sliding on a wire at position angle θ . If θ varies, then the bead experiences a centrifugal or anti-restoring force ($\dot{\theta}^2 x$). In Appendix 13.E we consider the consequences of this effect when the tidal field is varying with time due to the motion of the binary.

The presentation is structured as follows: we review the formalism of nonlinear perturbations of a star in Chapter 12. We introduce variational techniques in Section 12.1. We first discuss the Lagrangian formulation of the dynamics in Section 12.1.1, review the expansion of the problem in the basis of the linear modes of the star in Section 12.1.2, and discuss the equilibrium tidal deformation in Section 12.1.3. We arrive at the full expression of the perturbations to the mode frequencies due to three- and four-mode coupling in Section 12.1.4. We compute four-mode couplings in Chapter 13. In Section 13.1 we compute the four-mode coupling terms using a novel technique. We describe this technique in Sections 13.1.1–13.1.2, apply it to recast the problem of perturbations of the mode frequencies in Sections 13.1.3–13.1.4, and show that largest potentially unstable terms cancel in Section 13.1.6. In Section 13.2 we estimate the size of the remaining perturbations, and show that they are small in the case of high-order daughter modes in the presence of the tidal deformation. Finally, we conclude with an overview and discussion of our results in Section 13.3. Some technical details that arise along the way are collected into the Appendices.

Chapter 12

Formalism of mode couplings

12.1 Perturbations in tidally deformed stars

We now discuss the equations which govern stellar perturbations, focusing on three- and four-mode interactions between tidal deformations and additional perturbations of the star. First we review the Lagrangian formulation of general perturbations of a background star, and then we expand these perturbations in the basis of the linear modes of the star. This allows us to examine how nonlinear interactions perturb the eigenfrequencies of the linear perturbations. We show how coupling between modes can generate an instability, and we also show that in order to determine if an instability exists, we must account for both three- and four-mode interactions.

12.1.1 Lagrangian formulation of perturbations

Consider a non-rotating, inviscid, fluid neutron star with total mass M , radius R_* , and a characteristic dynamical frequency $\omega_0^2 = GM/R_*^3$, which is perturbed by a weak tidal field. The tidal potential has the form $\epsilon U(\mathbf{x})$, where ϵ is the dimensionless tidal strength. Our particular expression for U is the leading-order tidal potential due to a distant companion star of mass m , held at a fixed separation a , so that $\epsilon = Gm/(\omega_0^2 a^3)$. We consider the leading multipole of the corresponding tidal potential, which is

$$U = -\omega_0^2 r^2 P_2(\cos \theta), \quad (12.1)$$

where P_l is a Legendre polynomial with unit normalization, and θ measures the angle from the line joining the star to its companion. The perturbing potential is axisymmetric in this coordinate system. This work can be generalized to include the higher, weaker multipoles of the potential in a straightforward manner.

Let ξ denote a general displacement field on the star. Each fluid element of the star is labeled by its initial coordinates, \mathbf{x} (the Lagrangian coordinates of the element), so that elements initially at \mathbf{x}

are displaced to their actual (Eulerian) positions \mathbf{x}' as $\mathbf{x} \rightarrow \mathbf{x}' = \mathbf{x} + \xi$. Whatever coordinate system we choose to use, whether it be \mathbf{x} , \mathbf{x}' , or some other coordinate system \mathbf{X} , note that the masses of the elements are invariant, so that $d^3x\rho(\mathbf{x}) = d^3x'\rho'(\mathbf{x}') = d^3X\rho_{\mathbf{X}}(\mathbf{X})$. From now on, quantities such as ρ are taken to be defined in the coordinate system being used at that stage.

The displacement field has a Lagrangian \mathcal{L} given by

$$\mathcal{L}(\xi, \dot{\xi}) = \int d^3x \rho(\mathbf{x}) \frac{1}{2} \dot{\xi}(\mathbf{x}) \cdot \dot{\xi}(\mathbf{x}) - \mathcal{V}(\xi), \quad (12.2)$$

where the potential $\mathcal{V}(\xi)$ incorporates both the internal energy of the perturbed star and the gravitational energy. For a star with an external perturbing field, the potential energy with an arbitrary displacement field takes the form

$$\begin{aligned} \mathcal{V}(\xi) &= \int d^3x' \rho(\mathbf{x}') [\mathcal{E}_{\text{int}}(\mathbf{x}') + \Phi_0(\mathbf{x}') + \epsilon U(\mathbf{x}')] + \mathcal{C} \\ &= \int d^3x \rho(\mathbf{x}) [\mathcal{E}_{\text{int}}(\mathbf{x} + \xi) + \Phi_0(\mathbf{x} + \xi) + \epsilon U(\mathbf{x} + \xi)] + \mathcal{C} \\ &= \int d^3x \rho(\mathbf{x}) \left[\mathcal{E}_{\text{int}}(\mathbf{x}) + \Phi_0(\mathbf{x}) + \frac{1}{2} \xi \cdot \mathbf{C} \cdot \xi + \frac{1}{3!} f_3(\xi, \xi, \xi) + \frac{1}{4!} f_4(\xi, \xi, \xi, \xi) + \dots \right. \\ &\quad \left. + \epsilon \xi \cdot \nabla U + \frac{1}{2} \epsilon \xi \cdot (\xi \cdot \nabla) \nabla U + \dots \right] + \mathcal{C}. \end{aligned} \quad (12.3)$$

In the case of linear perturbations, only the symmetric bilinear \mathbf{C} and the gradient of U contribute to the dynamics of the displacement field. Physically, $\mathbf{C} \cdot \xi$ is the linear restoring force opposing an infinitesimal displacement ξ . Lynden-Bell and Ostriker [419] [see also, e.g. 420] derive a functional form for \mathbf{C} . The functionals f_n , meanwhile, encode the nonlinear corrections to the restoring forces due to the internal and self-gravitational energy of the star. These functionals are symmetric and linear under addition and scalar multiplication of displacements, but not under multiplication of the displacements by scalar functions. Later, when we expand the displacement in terms of the linear modes, they give us the n -mode couplings.

The term \mathcal{C} in this case contains the contributions to the energy from the gravitational field itself, which are fixed by the Cowling approximation and do not contribute to the dynamics of ξ . The issue of the appropriate division of gravitational potential energy between the field degrees of freedom and the interaction between the fluid elements and those fields is discussed in Appendix 13.A. We also remark that for the tidal field given in Eq. (12.1), $\int d^3x \rho U = 0$ due to the fact that the background ρ is spherically symmetric and U is dipolar, and so has not been written in Eq. (12.3). In addition, since U is a quadratic function of \mathbf{x} , all third and higher derivatives of U vanish, and as such have not been written.

12.1.2 Mode expansion of the Lagrangian

The most convenient language in which to discuss nonlinear perturbations is in terms of an expansion in the orthonormal basis of linear modes of the star. We write the mode functions themselves are as ξ_a , and a general displacement can be expanded as

$$\xi(\mathbf{x}) = \sum_a c_a \xi_a(\mathbf{x}) \quad (12.4)$$

using this basis. In spherical coordinates, the mode functions have the form¹

$$\xi_a = \xi_r Y_a \hat{\mathbf{r}} + \xi_h \left(\partial_\theta Y_a \hat{\theta} + \frac{1}{\sin\theta} \partial_\phi Y_a \hat{\phi} \right), \quad (12.5)$$

where ξ_r and ξ_h are functions of r and $Y_a = Y_{l_a, m_a}(\theta, \phi)$. The basis obeys the orthonormality condition

$$\int d^3x \rho \xi_a^* \cdot \xi_b = \frac{E_0}{\omega_a^2} \delta_{ab}, \quad (12.6)$$

where $E_0 = GM^2/R_*$. This normalization, which is the same as the one used by WAB but differs from that of Schenk et al. [420], means that when a basis mode is excited to unit amplitude, it has energy E_0 . By expanding in these basis functions, we can re-express our Lagrangian and potential as sums over mode amplitudes.

The square of the mode frequencies ω_a^2 are the eigenvalues of the bilinear \mathbf{C} in the mode basis,

$$\mathbf{C} \cdot \xi_a = \omega_a^2 \xi_a. \quad (12.7)$$

By defining the mode expansions of the remaining terms in the Lagrangian, we can write it entirely in terms of the mode amplitudes. The definitions we need are

$$U_a = -\frac{1}{E_0} \int d^3x \rho \xi_a^* \cdot \nabla U, \quad (12.8)$$

$$U_{ab} = -\frac{1}{E_0} \int d^3x \rho \xi_a \cdot (\xi_b \cdot \nabla) \nabla U, \quad (12.9)$$

$$\kappa_{abc} = -\frac{1}{2E_0} \int d^3x \rho f_3(\xi_a, \xi_b, \xi_c), \quad \text{and} \quad (12.10)$$

$$\kappa_{abcd} = -\frac{1}{3!E_0} \int d^3x \rho f_4(\xi_a, \xi_b, \xi_c, \xi_d). \quad (12.11)$$

Due to the symmetry of the functionals f_n , the coupling terms κ_{abc} and κ_{abcd} are symmetric in all their indices. When we expand the Lagrangian in this mode basis, we use the fact that the displacement ξ is real, and can be replaced by ξ^* as and when needed. Using these definitions and

¹We do not consider toroidal displacements, $\xi \propto \mathbf{r} \times \nabla Y_a$, since they do not couple to the tidal field [e.g. 418].

the potential (12.3), we rewrite the Lagrangian (12.2) in the form

$$\mathcal{L} = E_0 \sum \left[\frac{\dot{c}_a \dot{c}_a^*}{2\omega_a^2} - \frac{1}{2} c_a c_a^* + \frac{1}{3} \kappa_{\bar{a}b\bar{c}} c_a^* c_b^* c_c^* + \frac{1}{4} \kappa_{\bar{a}\bar{b}\bar{c}\bar{d}} c_a^* c_b^* c_c^* c_d^* + \epsilon U_a c_a^* + \frac{1}{2} \epsilon U_{\bar{a}\bar{b}} c_a^* c_b^* + \dots \right] - \mathcal{V}(0). \quad (12.12)$$

Here, our convention is that the sum runs over all the repeated indices in each term (including the index a in the first two terms). Bars indicate the use of complex conjugate wave-functions in the respective terms. Note that in the first and second terms, the amplitude of a mode with a given m comes up twice – in the terms corresponding to m and in those corresponding to $-m$, since the reality of ξ implies that they are related by $c_{a-m} = (-1)^m c_{a_m}^*$. We recall that the potential term \mathcal{V} with the displacement set to zero has the form

$$\mathcal{V}(0) = \int d^3x \rho [\mathcal{E}_{\text{int}}(\mathbf{x}) + \Phi_0(\mathbf{x})] + \mathcal{C}. \quad (12.13)$$

We use the rule that sums run over repeated indices throughout this work, except where noted. Though we do not do so here, the equations of motion, as presented in e.g. Schenk et al. [420], can be derived by varying this Lagrangian with respect to the amplitude c_a^* .

With the formalism of the mode expansion established, we now investigate the perturbations excited by a static tidal field.

12.1.3 The static response to the tide

The star responds to the external tidal field ϵU by deforming to a new equilibrium configuration. We denote this equilibrium tidal deformation χ and set ξ equal to χ in the preceding equations. The tidal displacement χ is such the internal restoring forces balance the external perturbing force,

$$\left. \frac{\delta \mathcal{V}}{\delta \xi} \right|_{\xi \rightarrow \chi} = 0. \quad (12.14)$$

Physically, χ takes the spherically symmetric star to a static configuration where elements along contours of constant gravitational potential $\Phi_0 + \epsilon U$ have the same density and pressure. The displacement χ has a part linear in the tidal strength ϵ , which is the so-called linear tide. There are also higher terms, which arise from the nonlinear restoring forces and the nonlinear tide. In order to consistently account for the changes in the eigenfrequencies ω_a of additional perturbations due to coupling with the tide, we need to keep terms up to $O(\epsilon^2)$. As such, we write the expansion of χ in the mode basis as

$$\chi = \sum \chi_a \xi_a = \sum (\epsilon \chi_a^{(1)} + \epsilon^2 \chi_a^{(2)}) \xi_a. \quad (12.15)$$

Varying just the potential terms of the Lagrangian (12.12) with respect to a given mode amplitude c_a^* , and then substituting the amplitudes χ_a into the result gives an equation for χ_a ,

$$\chi_a - \epsilon U_a - \sum [\kappa_{\bar{a}\bar{b}\bar{c}} \chi_b^* \chi_c^* + \kappa_{\bar{a}\bar{b}\bar{c}\bar{d}} \chi_b^* \chi_c^* \chi_d^* + \epsilon U_{\bar{a}\bar{b}} \chi_b^* + \dots] = 0. \quad (12.16)$$

Solving order by order for χ_a , we find that

$$\chi_a^{(1)} = U_a \quad \text{and} \quad (12.17)$$

$$\chi_a^{(2)} = \sum [\kappa_{\bar{a}\bar{b}\bar{c}} U_b^* U_c^* + U_{\bar{a}\bar{b}} U_b^*]. \quad (12.18)$$

Given the tidal field ϵU , the fluid elements respond by the nonlinear displacement χ . Note that since U is axisymmetric, χ is also axisymmetric and χ_a contains only terms where $m = 0$. This means that all of the terms in Eqs (12.17) and (12.18) are actually real. The question we must answer is whether or not this deformed star is stable.

12.1.4 Stability of the deformed star

Now we allow the star to undergo further perturbations, so that

$$\xi = \chi + \eta, \quad (12.19)$$

where η is an additional displacement field on the star away from the equilibrium configuration. We are interested in the interaction of pairs of daughter modes with the tidal perturbation, and so we expand our Lagrangian only to second order in the additional small perturbations, $O(\eta^2)$. We do not deal with the coupling of three or more non-tidal modes either to each other or to the tide, and so $O(\eta^3)$ and higher terms are dropped in what follows.

By expanding η as $\sum \eta_a \xi_a$, and substituting the corresponding expansion of the displacement $c_a = \chi_a + \eta_a$ into the Lagrangian (12.12), we arrive at the following form of the Lagrangian, up to the order we are interested in,

$$\begin{aligned} \mathcal{L} &= E_0 \sum \left[\frac{\dot{\eta}_a \dot{\eta}_a^*}{2\omega_a^2} - \frac{1}{2} (\chi_a \chi_a^* + \eta_a \eta_a^*) + \kappa_{\bar{a}\bar{b}\bar{c}} \eta_a^* \eta_b^* \chi_c^* + \frac{3}{2} \kappa_{\bar{a}\bar{b}\bar{c}\bar{d}} \eta_a^* \eta_b^* \chi_c^* \chi_d^* + \epsilon U_a \chi_a^* + \frac{1}{2} \epsilon U_{\bar{a}\bar{b}} \eta_a^* \eta_b^* \right] - \mathcal{V}(0) \\ &= E_0 \sum \left[\frac{\dot{\eta}_a \dot{\eta}_a^*}{2\omega_a^2} - \frac{1}{2} \eta_a \eta_a^* + \left(\epsilon [\kappa_{\bar{a}\bar{b}\bar{c}} \chi_c^{(1)*} + \frac{1}{2} U_{\bar{a}\bar{b}}] + \epsilon^2 [\kappa_{\bar{a}\bar{b}\bar{c}} \chi_c^{(2)*} + \frac{3}{2} \kappa_{\bar{a}\bar{b}\bar{c}\bar{d}} \chi_c^{(1)*} \chi_d^{(1)*}] \right) \eta_a^* \eta_b^* \right] \\ &\quad + \frac{E_0}{2} \sum \epsilon^2 |U_a|^2 - \mathcal{V}(0). \end{aligned} \quad (12.20)$$

In the first line we have written only those terms which are of the correct order, and we have also neglected terms which have only a single factor of η_a , since these vanish upon substitution of our solution for χ_a . The terms linear in η vanish because the displacement χ takes the star to an

equilibrium state. In the next line, we have substituted the decomposition (12.15), collected terms in orders of ϵ , and used Eq. (12.17) to isolate the $|U_a|^2$ term. For now, we ignore the overall constant terms $\mathcal{V}(0)$ and $E_0 \sum \epsilon^2 |U_a|^2/2$, which follow along for the ride but do not affect the dynamics.

The $O(\epsilon)$ term in Eq. (12.20) is the three-mode interaction $\kappa_{\bar{a}\bar{b}\bar{c}} \eta_a^* \eta_b^* \chi_c^{(1)*}$. If the coupling $\kappa_{\bar{p}\bar{g}\bar{c}} \chi_c^{(1)*}$ happens to be large and positive for a particular pair of modes (p, g) then it can overcome the smallness of the tidal coupling strength ϵ . As first noted by WAB, $\kappa_{\bar{p}\bar{g}\bar{c}} \chi_c^{(1)*}$ is in fact large for certain high order p -mode and g -mode pairs, due to a spatial resonance of the mode functions ξ_p and ξ_g . However, as we show below, this three-mode term perturbs the characteristic frequencies at $O(\epsilon^2)$, as do all of the terms in Eq. (12.20) multiplied by ϵ^2 . It is not immediately clear what role these terms play.

By varying the Lagrangian (12.20) with respect to the amplitudes η_a we can derive the equations of motion, and from there the characteristic frequencies. We instead adopt an equivalent, but hopefully more transparent strategy to obtain the characteristic frequencies. Defining rescaled amplitudes $\eta'_a = \eta_a/\omega_a$ leads us to the analogy to a system of coupled oscillators, for which we can rewrite the Lagrangian in matrix notation as

$$\mathcal{L} = \frac{E_0}{2} (\eta')^\dagger \dot{\eta}' - \frac{E_0}{2} (\eta')^\dagger \mathcal{M} \eta', \quad (12.21)$$

where η' is a vector of mode amplitudes and the matrix \mathcal{M} contains the leading restoring terms, the effect of the tidal potential, and the mode-mode interactions. The rescaling introduces factors of ω_a at each instance of an η_a , and it is equivalent to normalizing the mode functions to all have the same moment of inertia MR_*^2 at unit amplitude rather than the same energy E_0 , which is the choice of normalization used in [420].

The eigenvalues of \mathcal{M} are the characteristic frequencies of this set of oscillators, and consideration of \mathcal{M} is equivalent to writing out the equations of motion and solving the corresponding characteristic equation. Because the tidal potential is axisymmetric, there is an ordering of the basis modes where the matrix \mathcal{M} is made up of 2×2 and 1×1 blocks along the diagonal, where each block consists of those modes which are allowed to interact given conservation of angular momentum. The blocks are all independent of each other, and analysis of one essentially applies to the rest.

We now focus on a particular pair of modes with $m = 0$, which we give indices p and g , and write the sub-block of \mathcal{M} for this pair. We discuss the structure of \mathcal{M} and the case of modes where $m \neq 0$ further in Appendix 13.B. The modes have unperturbed frequencies ω_p and ω_g , and we set $\omega_p > \omega_g$. The sub-block of \mathcal{M} is composed of

$$\mathcal{M}_{pp} = \omega_p^2 - \epsilon \omega_p^2 \left(U_{pp} + \sum 2\kappa_{app} \chi_a^{(1)} \right) - \epsilon^2 \omega_p^2 \sum \left[2\kappa_{app} \chi_a^{(2)} + 3\kappa_{abpp} \chi_a^{(1)} \chi_b^{(1)} \right], \quad (12.22)$$

$$\mathcal{M}_{pg} = \mathcal{M}_{gp} = -\epsilon \omega_p \omega_g \left(U_{pg} + \sum 2\kappa_{apg} \chi_a^{(1)} \right), \quad \text{and} \quad (12.23)$$

$$\mathcal{M}_{gg} = \omega_g^2 - \epsilon \omega_g^2 \left(U_{gg} + \sum 2\kappa_{agg} \chi_a^{(1)} \right) - \epsilon^2 \omega_g^2 \sum \left[2\kappa_{agg} \chi_a^{(2)} + 3\kappa_{abgg} \chi_a^{(1)} \chi_b^{(1)} \right], \quad (12.24)$$

and note that since p and g denote particular modes, they are not summed over in the expressions for \mathcal{M} . Formally expanding in powers of ϵ , we can compute the perturbed eigenvalues of this matrix as

$$\begin{aligned} \omega_+^2 &= \omega_p^2 - \epsilon \omega_p^2 \left(U_{pp} + \sum 2\kappa_{app} \chi_a^{(1)} \right) - \epsilon^2 \omega_p^2 \sum \left[2\kappa_{app} \chi_a^{(2)} + 3\kappa_{abpp} \chi_a^{(1)} \chi_b^{(1)} \right] \\ &\quad + \epsilon^2 \frac{\omega_p^2 \omega_g^2}{\omega_p^2 - \omega_g^2} \left(U_{pg} + \sum 2\kappa_{apg} \chi_a^{(1)} \right)^2, \end{aligned} \quad (12.25)$$

and

$$\begin{aligned} \omega_-^2 &= \omega_g^2 - \epsilon \omega_g^2 \left(U_{gg} + \sum 2\kappa_{agg} \chi_a^{(1)} \right) - \epsilon^2 \omega_g^2 \sum \left[2\kappa_{agg} \chi_a^{(2)} + 3\kappa_{abgg} \chi_a^{(1)} \chi_b^{(1)} \right] \\ &\quad - \epsilon^2 \frac{\omega_p^2 \omega_g^2}{\omega_p^2 - \omega_g^2} \left(U_{pg} + \sum 2\kappa_{apg} \chi_a^{(1)} \right)^2. \end{aligned} \quad (12.26)$$

Since ω_g is the smaller frequency to begin with, the negative-definite term involving κ_{apg} in Eq. (12.26) is in danger of pushing ω_g to a negative value, especially if the mode is a high order g -mode with $\omega_g^2 \ll \omega_0^2 = GM/R_*^3 \ll \omega_p^2$. This is the potential nonlinear instability described by WAB.

In order to make definite statements, we need to know how the other terms behave, in particular the four-mode interaction term $\kappa_{abgg} \chi_a^{(1)} \chi_b^{(1)}$. If they are large when the three-mode coupling is large, they can in principle prevent the instability. We now discuss a method for computing the interaction between two daughter modes and the tidal deformation at the level of the four-mode coupling. Along the way we also find a way to simply derive the three-mode terms. We find that the four-mode term serves to precisely cancel the κ_{apg} term.

Chapter 13

Four-mode coupling and the stability of the tidal deformation

13.1 Computing the four-mode coupling terms

In this section we derive the four-mode terms discussed in Section 12.1.4. The method we use is straightforward in practice, but it is not obvious from the outset that such a method will be useful. Briefly, we utilize a coordinate transform that removes the lowest order perturbation, thereby restructuring the orders of ϵ in the potential of the star. By matching the mode expansions of the potential of the transformed star with those derived in the original coordinates, we can write higher-order mode coupling terms as functions of the lower terms and the coordinate transform itself.

Figure 13.1 shows the two stars – the star in the original coordinates and in the transformed coordinates – and the various perturbations that are applied to the stars. The first, which we call star A, has already been given a full treatment in Section 12.1. There we considered the interactions between the tidal displacement χ and further perturbations η . In star B, we use a volume-preserving coordinate transform to map the tidally deformed star back into a spherically symmetric configuration. This transform is generated by an infinitesimal, volume-preserving displacement field ζ . We then consider further perturbations on star B. It is important to note that A and B are the same stars, just in different coordinate systems. Table 13.1 provides a key for the various vector quantities which are used in the discussion of the two stars.

In order to gain any new insights from star B, we expand the potentials of both stars in the same mode basis, which is the basis of linearized modes of the original, unperturbed star. The mode functions in star B are linear combinations of the original mode functions, and so are related by the Jacobian matrix of the coordinate transform, expanded in the mode basis. We find that we can write the three- and four-mode couplings in star A as functions of this Jacobian and a modified tidal perturbation field.

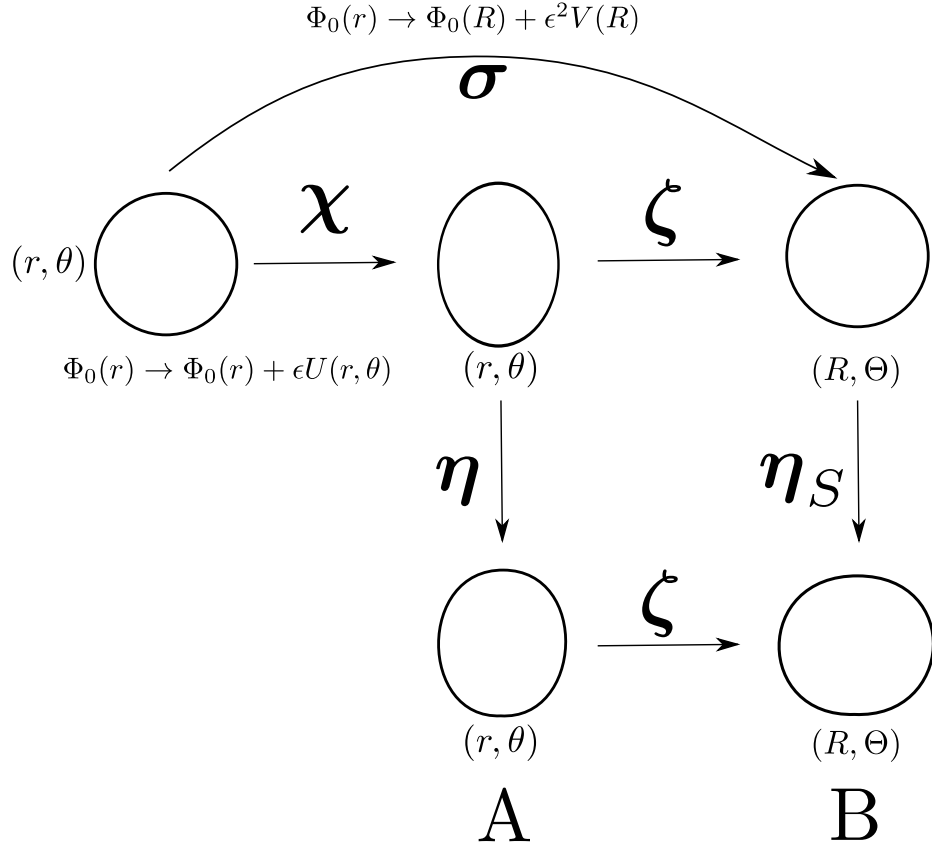


Figure 13.1: Schematic of the two stellar models. The external tidal field produces a deformation χ . In star A, we consider further perturbations η . Star B is obtained by mapping the tidally deformed star back to a spherically symmetric configuration by a coordinate transform. Further perturbations are now expressed in this new coordinate system; the field η_S is that perturbation in model B which corresponds to the perturbation η in model A.

13.1.1 The volume-preserving transform

To begin with, we apply the tidal perturbation ϵU to a spherical star, so that the total gravitational potential becomes $\Phi_0 + \epsilon U$. In response the fluid elements of the star are displaced by the field χ as discussed in Section 12.1.3. Next, we consider a coordinate transform $\psi : \mathbf{x} = (r, \theta, \phi) \rightarrow \mathbf{X} = (R, \Theta, \phi)$. We require this transform to have the special properties that it is volume-preserving, and that it returns the star to spherical symmetry. These properties completely determine our mapping in terms of a power series expansion in ϵ . The resulting spherically symmetric star is not the original star, because χ itself is not volume-preserving; but as we will see the coordinate transform reverses χ at leading order in ϵ . Since our problem is axisymmetric, the ϕ coordinate is unchanged, and from here on we can safely ignore the coordinate ϕ .

We require an expansion of the coordinate transform in orders in ϵ , and so we represent ψ by a coordinate flow under an infinitesimal generator $\zeta(\mathbf{x})$. Explicitly, the finite transformation ψ generated by the infinitesimal transformation ζ is defined via a parameterized transform $\varphi(s, \mathbf{x})$

Table 13.1: Key for the vector quantities involved in the two stellar models

Vector Quantity	Definition
χ	Equilibrium tidal deformation
ζ	Infinitesimal generator of the volume-preserving coordinate transform ψ
σ	Combined application of the equilibrium tide and the coordinate transform ψ
η	Further, general perturbation of Star A
η_S	Further, general perturbation of Star B
1, 2, 3	Virtual displacement vectors that sum to χ
\mathbf{J}_ψ	The Jacobian transformation matrix for the coordinate transform ψ

by the ordinary differential equation $d\varphi(s, \mathbf{x})/ds = \zeta(\varphi(s, \mathbf{x}))$, initial condition $\varphi(0, \mathbf{x}) = \mathbf{x}$, and assignment $\mathbf{X} = \psi(\mathbf{x}) \equiv \varphi(1, \mathbf{x})$. The flow forward, ψ , gives us our new coordinates in the form of a Taylor expansion

$$\mathbf{X} = \mathbf{x} + \zeta(\mathbf{x}) + \frac{1}{2}(\zeta \cdot \nabla)\zeta \Big|_{\mathbf{x}}, \quad (13.1)$$

up to order ζ^2 . The volume-preserving requirement is equivalent to requiring the generator to be divergenceless, $\nabla \cdot \zeta = 0$.¹ It is actually more convenient to first get an explicit representation of ψ^{-1} : this is actually the transformation generated by the negative of the generator. (This can be seen from the integral curve definition of a generator if we reverse the sign of d/ds ; for an explicit proof see Appendix 13.C.) Thus the mapping from \mathbf{X} to \mathbf{x} via $-\zeta$ is

$$\mathbf{x} = \mathbf{X} + (-\zeta)(\mathbf{X}) + \frac{1}{2}[(-\zeta) \cdot \nabla](-\zeta) \Big|_{\mathbf{X}}. \quad (13.2)$$

Because of this, once we find an expression for the generator of the inverse flow $-\zeta$ in (R, Θ) coordinates, we have the desired generator $\zeta(\mathbf{x})$.²

The vector $-\zeta(\mathbf{X})$ has an expansion in powers of ϵ , which is

$$\zeta = \epsilon\zeta^{(1)} + \epsilon^2\zeta^{(2)} + O(\epsilon^3). \quad (13.3)$$

From Eq. (13.2), the magnitude r of the coordinate vector \mathbf{x} is

$$r = R - \epsilon \hat{\mathbf{R}} \cdot \zeta^{(1)} + \epsilon^2 \left[\frac{\zeta^{(1)} \cdot \zeta^{(1)}}{2R} - \frac{(\hat{\mathbf{R}} \cdot \zeta^{(1)})^2}{2R} + \frac{\hat{\mathbf{R}} \cdot (\zeta^{(1)} \cdot \nabla)\zeta^{(1)}}{2} - \hat{\mathbf{R}} \cdot \zeta^{(2)} \right], \quad (13.4)$$

¹The Jacobian $J^i_j(s, \mathbf{x}) = \partial\varphi^i(s, \mathbf{x})/\partial x^j$ satisfies the differential equation or chain rule $\partial J^i_j/\partial s = \partial^2\varphi^i(s, \mathbf{x})/\partial x^j\partial s = \partial\zeta^i(\varphi(s, \mathbf{x}))/\partial x^j = \zeta^i_{,k}(\varphi(t, \mathbf{x}))J^k_j$, from which we see that its determinant $|\mathbf{J}|$ satisfies $\partial \ln |\mathbf{J}|/\partial s = \zeta^i_{,i}(\varphi(s, \mathbf{x}))$ – thus a divergenceless ζ leads to a volume-preserving transformation.

²A similar construction is used in the Lie transformation theory of small but finite canonical transformations of Hamiltonian systems [e.g. 421]. There a transformation is generated by the infinitesimal flow in phase space $\zeta(\mathbf{x}, \mathbf{p})$; the requirement for the transformation to be canonical corresponds to the requirement that ζ be derivable from a Hamiltonian. The rule that a transformation can be inverted by reversing the sign of the generator is the same.

which can be further simplified using the vector identity $(\mathbf{A} \cdot \nabla)\mathbf{A} = \nabla A^2/2 - \mathbf{A} \times (\nabla \times \mathbf{A})$, to yield

$$r = R - \epsilon \zeta_R^{(1)} + \epsilon^2 \left[\frac{\zeta_R^{(1)} \partial_R \zeta_R^{(1)}}{2} + \frac{\zeta_\Theta^{(1)} \partial_\Theta \zeta_R^{(1)}}{2R} - \zeta_R^{(2)} \right], \quad (13.5)$$

with the definitions $\zeta^{(i)} \cdot \hat{\mathbf{R}} = \zeta_R^{(i)}$ and $\zeta^{(i)} \cdot \hat{\Theta} = \zeta_\Theta^{(i)}$. Also useful is the expansion

$$P_2(\cos \theta) = (1 - \epsilon \zeta \cdot \nabla) P_2(\cos \Theta) = P_2(\cos \Theta) - \epsilon \frac{\zeta_\Theta^{(1)} \partial_\Theta P_2(\cos \Theta)}{R} \quad (13.6)$$

to the order needed. Now we are in place to solve for ζ , and at the same time to determine the form of the total gravitational potential $\Phi(R)$ out to order ϵ^2 . The tidally perturbed potential is

$$\begin{aligned} \Phi_0(r) - \epsilon \omega_0^2 r^2 P_2(\cos \theta) = & \Phi_0(R) - \epsilon \left[\zeta_R^{(1)} \mathbf{g} + \omega_0^2 R^2 P_2(\cos \Theta) \right] + \epsilon^2 \left[\left(\frac{\zeta_R^{(1)} \partial_R \zeta_R^{(1)}}{2} + \frac{\zeta_\Theta^{(1)} \partial_\Theta \zeta_R^{(1)}}{2R} - \zeta_R^{(2)} \right) \mathbf{g} \right. \\ & \left. + \frac{1}{2} (\zeta_R^{(1)})^2 \frac{d\mathbf{g}}{dr} + 2\omega_0^2 R \zeta_R^{(1)} P_2(\cos \Theta) + \omega_0^2 R \zeta_\Theta^{(1)} \partial_\Theta P_2(\cos \Theta) \right]. \end{aligned} \quad (13.7)$$

For convenience here and later, we have denoted the local gravitational acceleration as $\mathbf{g} = d\Phi_0/dR$.

By insisting that all Θ dependence in Φ vanishes, we find at first order

$$\zeta_R^{(1)} = -\omega_0^2 \frac{R^2}{\mathbf{g}} P_2(\cos \Theta), \quad (13.8)$$

and at second order

$$\zeta_R^{(2)} = \frac{\zeta_R^{(1)} \partial_R \zeta_R^{(1)}}{2} + \frac{\zeta_\Theta^{(1)} \partial_\Theta \zeta_R^{(1)}}{2R} + \frac{(\zeta_R^{(1)})^2}{2R} \frac{d \ln \mathbf{g}}{d \ln R} + \frac{\omega_0^2}{\mathbf{g}} \left[2R \zeta_R^{(1)} P_2(\cos \Theta) + R \zeta_\Theta^{(1)} \partial_\Theta P_2(\cos \Theta) \right]. \quad (13.9)$$

In order to write this last equation entirely in terms of the gravitational potentials, we need an expression for $\zeta_\Theta^{(1)}$. For this, we use the requirement that ψ be volume-preserving. The volume-preserving infinitesimal displacements are spanned by the vectors

$$\mathbf{f}_{lm}^1 = l(l+1) \frac{u_{lm}}{R} \hat{\mathbf{R}} + \left(\frac{u_{lm}}{R} + \partial_R u_{lm} \right) R \nabla Y_{lm} \quad \text{and} \quad (13.10)$$

$$\mathbf{f}_{lm}^2 = w_{lm} \mathbf{R} \times \nabla Y_{lm}. \quad (13.11)$$

This can be seen by considering the usual decomposition of vectors into vector spherical harmonics, and finding those combinations which satisfy $\nabla \cdot \mathbf{f}_{lm} = 0$. These naturally decompose into the spheroidal displacements \mathbf{f}_{lm}^1 and the toroidal displacements \mathbf{f}_{lm}^2 [see also 422, Ch. 12]. We are interested in axially symmetric perturbations, so we only need to use the basis vectors \mathbf{f}_{lm}^1 . We further absorb the normalization of the spherical harmonics into the definition of the u_{lm} and write

(with $m = 0$ implicit)

$$\zeta = \sum_l l(l+1) \frac{u_l}{R} P_l(\cos \Theta) \hat{\mathbf{R}} + \left(\frac{u_l}{R} + \partial_R u_l \right) [\partial_\Theta P_l(\cos \Theta)] \hat{\Theta}, \quad \text{where} \quad (13.12)$$

$$u_l = \epsilon u_l^{(1)} + \epsilon^2 u_l^{(2)} + O(\epsilon^3). \quad (13.13)$$

We see that the ζ_Θ is simply related to ζ_R through the requirement that ζ be volume-preserving. Comparing Eq. (13.8) to Eq. (13.12), we immediately find that

$$u_l^{(1)} = -\omega_0^2 \frac{R^3}{6\mathbf{g}} \delta_{l2}. \quad (13.14)$$

Substituting this into Eqs. (13.9) and (13.12) allows us to solve for the functions $u_l^{(2)}$. The angular terms are of the form $(P_2)^2$ and $(\partial_\Theta P_2)^2$, which when re-expanded in terms of Legendre polynomials couple only to $l = 2, 4$. We can pick off each of these terms by integrating Eq. (13.9) with the appropriate Legendre polynomial and weight $d\mu = d[\cos \Theta]$. Orthogonality then gives

$$u_2^{(2)} = -\frac{\omega_0^4 R^4 (8-n)}{84 \mathbf{g}^2} \quad \text{and} \quad u_4^{(2)} = \frac{3\omega_0^4 R^4 (1-n)}{350 \mathbf{g}^2}; \quad (13.15)$$

all the other $u_l^{(2)}$ vanish. We have defined $n = d \ln \mathbf{g} / d \ln R$, which proves to be a convenient short hand in the estimates in Section 13.2. When \mathbf{g} has a simple power-law dependence on R , n is just its constant power law index. Note that the $l = 0$ contribution, which is Θ independent, represents the correction to the spherically symmetric potential $\Phi_0(R)$. Because of this we also have from the matching that

$$\Phi(R) = \Phi_0(R) + \epsilon^2 V(R) + O(\epsilon^3), \quad \text{where} \quad (13.16)$$

$$V(R) = -\frac{\omega_0^4 R^3 (6-n)}{10 \mathbf{g}}. \quad (13.17)$$

In order to have the generator of the transform ψ we simply need to replace the coordinates (R, Θ) with (r, θ) , since we have already accounted for the sign change in reversing the flow. As such, we have completed the construction of ψ up to $O(\epsilon^2)$.

13.1.2 Understanding the transform

We have an expression for the volume-preserving transform which takes the tidally perturbed star A into the spherically symmetric star B. We have seen that star B is more weakly perturbed than star A, and this allows us to match orders in perturbation in a way that gives useful relations. First though, it is useful to step back and consider the physical intuition underlying the transformation. Figure 13.2 illustrates the principles behind the transformation. Consider an element displaced from

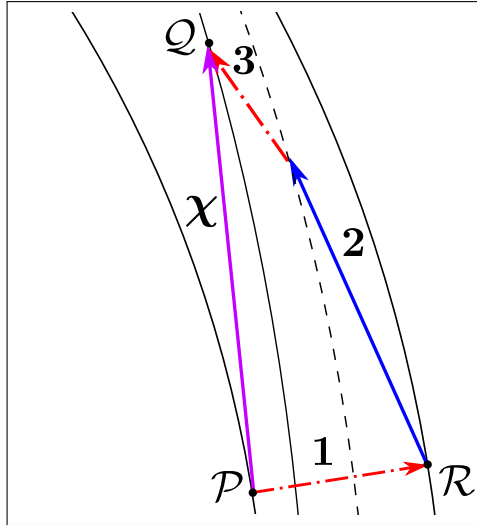


Figure 13.2: Depiction of the nonlinear tidal response χ as a sum of virtual displacements. The purely radial displacement **1** changes the density and pressure of the fluid elements. The virtual displacements **2** and **3** are volume-preserving, and correspond to the linear $l = 2$ tide and the volume-preserving component of the nonlinear tide, respectively.

point \mathcal{P} to point \mathcal{Q} by the tidal displacement χ . As we noted before, this tidal displacement takes the star to a configuration where elements along contours of equal potential have the same density and pressure. Point \mathcal{Q} lies on one such contour. The displacement field χ can be decomposed as the sum of certain virtual displacement fields, appropriate members of which are marked as **1**, **2**, and **3** in the figure. These virtual displacements are chosen to have some nice properties.

First, each virtual displacement is chosen to be adiabatic. This is possible since their sum, χ , is adiabatic. Second, we choose **2** and **3** such that they both preserve the volume of fluid elements. The pressure and density of an element at \mathcal{P} is not necessarily equal to the pressure and density of the element once it is displaced to \mathcal{Q} , as the tidal deformation χ is not volume-preserving beyond linear order. With this choice for **2** and **3**, the entire volume change of an element, and the related pressure and density change, occurs during displacement **1**. Third, the displacement **2** is chosen to be the linear part of χ (the so-called linear tide). This is possible because the linear tide is a volume-preserving deformation. Given this choice, the displacements **1** and **3** make up the nonlinear part of χ . Fourth, **3** is chosen to be that part of the nonlinear tide which preserves volumes, such that the remaining displacement, **1**, takes the initial spherical potential contour that \mathcal{P} lies on to another spherical contour. Hence, the displacement **1** is a radial displacement, which takes \mathcal{P} to a point \mathcal{R} .

We are now faced with the question of what sort of perturbing fields we would need to apply to make the elements follow these virtual displacements. We have seen that **2** and **3** correspond to a pure coordinate transformation (they make up ψ^{-1}), so that the potential \mathcal{V} of the element is frozen in during these displacements. The overall stellar structure naturally flows forward along

with the transformation. Hence the potential at \mathcal{R} is same as the potential at \mathcal{Q} . This differs from the background star's potential at \mathcal{P} , and the difference can be seen as a spherically symmetric perturbing potential causing the elements of the star to deform along **1**.

We could judge this decomposition scheme solely on its power to illuminate the underlying components of the equilibrium tide χ , but its real value manifests in the study of small displacements on top of this, away from equilibrium. This is because these weak displacements, say η , which are originally on a star deformed to $O(\epsilon)$, when pulled back along **3** and **2** pick up additional corrections of $O(\epsilon)$ and higher while the transformed star is more weakly deformed [perturbed at $O(\epsilon^2)$]. We can explicitly compute these corrections to the displacements from the pullback. In order to get the $\epsilon^2\eta^2$ part of the energy, we have to look at both of the functionals f_3 and f_4 in the original picture. Here we find that we only need f_3 .

13.1.3 Potential of star B

Now that we have an explicit form for the transformation between star A and star B, and a better understanding of the motivation behind this transform, we can consider the potential \mathcal{V} of star B. Star B sits in a spherically symmetric gravitational potential, and its fluid elements have been adjusted by the combination of the displacement field χ and the coordinate transform. In total, the star has undergone a radial deformation σ (before called **1**), sourced by the external potential ϵ^2V , so that $\mathbf{x} \rightarrow \mathbf{X} = \mathbf{x} + \sigma$. As before, we have for the new configuration

$$\begin{aligned}
\mathcal{V}(\sigma) &= \int d^3X \rho(\mathbf{X}) [\mathcal{E}_{\text{int}}(\mathbf{X}) + \Phi_0(\mathbf{X}) + \epsilon^2V(\mathbf{X})] \\
&= \int d^3x \rho(\mathbf{x}) [\mathcal{E}_{\text{int}}(\mathbf{x} + \sigma) + \Phi_0(\mathbf{x} + \sigma) + \epsilon^2V(\mathbf{x} + \sigma)] \\
&= \mathcal{V}(0) + \int d^3x \rho(\mathbf{x}) \left[\frac{1}{2} \sigma \cdot \mathbf{C} \cdot \sigma + \frac{1}{3!} f_3(\sigma, \sigma, \sigma) + \dots + \epsilon^2V(\mathbf{x}) + \epsilon^2 \sigma \cdot \nabla V + \epsilon^2 \frac{1}{2} \sigma \cdot (\sigma \cdot \nabla) \nabla V + \dots \right].
\end{aligned} \tag{13.18}$$

Expanding σ in the mode basis of the unperturbed star, $\sigma = \sum \sigma_a \xi_a$, we can write the potential as

$$\mathcal{V} = \mathcal{V}(0) + \int d^3x \rho \epsilon^2V + E_0 \sum \left[\frac{1}{2} \sigma_a^2 - \frac{1}{3} \kappa_{abc} \sigma_a \sigma_b \sigma_c - \epsilon^2 V_a \sigma_a - \epsilon^2 \frac{1}{2} V_{ab} \sigma_a \sigma_b + \dots \right], \tag{13.19}$$

with

$$V_a = -\frac{1}{E_0} \int d^3x \rho \xi_a^* \cdot \nabla V \quad \text{and} \quad V_{ab} = -\frac{1}{E_0} \int d^3x \rho \xi_a \cdot (\xi_b \cdot \nabla) \nabla V. \tag{13.20}$$

Defining an expansion in ϵ for σ_a which must begin at $O(\epsilon^2)$ because the perturbing tidal field enters only at this order,

$$\sigma_a = \epsilon^2 \sigma_a^{(2)} + O(\epsilon^3), \quad (13.21)$$

we can again solve for σ_a for this static configuration by minimizing the variation in \mathcal{V} with respect to the amplitude σ_a . At leading order, we simply have

$$\sigma_a^{(2)} = V_a. \quad (13.22)$$

It is worth noting here that since $\sigma^{(1)} = 0$, we immediately have that

$$\chi^{(1)} = -\zeta^{(1)}. \quad (13.23)$$

To see this, we note that by definition the displacement of a point \mathbf{x} in the unperturbed star by σ is the same as the composition of a displacement by χ and then the application of the coordinate transform ψ . Keeping only the leading order terms in ϵ this gives

$$\mathbf{x} + \sigma(\mathbf{x}) = \mathbf{x} + O(\epsilon^2) = \mathbf{x} + \epsilon \chi^{(1)}(\mathbf{x}) + \epsilon \zeta^{(1)}(\mathbf{x}) + O(\epsilon^2), \quad (13.24)$$

from which Eq. (13.23) follows.

As before, we now consider further perturbations to star B, which we denote η_S . From the original unperturbed star we have a displacement

$$\mathbf{x} \rightarrow \mathbf{x} + \xi = \mathbf{x} + \sigma + \eta_S \quad \text{where} \quad (13.25)$$

$$\eta_S = \mathbf{J}_\psi \cdot \eta. \quad (13.26)$$

Here, η is the form of the corresponding oscillations of star A, which must be transformed into the coordinates \mathbf{X} of the spherical star B if we are to consider further displacements beyond σ . This is the origin of the Jacobian transformation matrix \mathbf{J}_ψ in Eq. (13.26). In principle, Eq. (13.26) should include terms of order η^2 ; however, since star B is an equilibrium solution, the potential energy contains no terms of first order in η_S and the leading dependence is η_S^2 . Therefore to compute the potential energy to order η^2 , we need only obtain η_S to linear order in η .

Now we consider the potential \mathcal{V} of star B when the additional perturbations $\mathbf{J}_\psi \cdot \eta$ are present. We define the expansion of the Jacobian in orders of ϵ ,

$$\mathbf{J}_\psi = \mathbf{1} + \epsilon \mathbf{J}_\psi^{(1)} + \epsilon^2 \mathbf{J}_\psi^{(2)} + O(\epsilon^3), \quad (13.27)$$

and its expansion in the mode basis ξ_a of the original star,

$$J_{ab} = \frac{\omega_a^2}{E_0} \int d^3x \rho \xi_a^* \cdot \mathbf{J}_\psi \cdot \xi_b, \quad (13.28)$$

so that the basis coefficients are naturally transformed as

$$\eta_S = \sum \eta_{S,a} \xi_a = \sum J_{ab} \eta_b \xi_a = \sum (\delta_{ab} + \epsilon J_{ab}^{(1)} + \epsilon^2 J_{ab}^{(2)}) \eta_b \xi_a. \quad (13.29)$$

Taking all of this into account, we have for star B the mode expansion of the potential

$$\begin{aligned} \mathcal{V}(\sigma + \eta_S) &= \mathcal{V}(0) + \int d^3x \rho \epsilon^2 V + \frac{E_0}{2} \sum \left[\eta_a^2 + \epsilon \left(J_{ab}^{(1)} + J_{ba}^{(1)} \right) \eta_a \eta_b + \epsilon^2 \left(J_{ca}^{(1)} J_{cb}^{(1)} + J_{ab}^{(2)} + J_{ba}^{(2)} \right) \eta_a \eta_b \right. \\ &\quad \left. - 2\kappa_{abc} \eta_a \eta_b \sigma_c - \epsilon^2 V_{ab} \eta_a \eta_b + \dots \right] \\ &= \mathcal{V}(0) + \int d^3x \rho \epsilon^2 V + \frac{E_0}{2} \sum \left[\eta_a^2 + \epsilon \left(J_{ab}^{(1)} + J_{ba}^{(1)} \right) \eta_a \eta_b \right. \\ &\quad \left. + \epsilon^2 \left(J_{ca}^{(1)} J_{cb}^{(1)} + J_{ab}^{(2)} + J_{ba}^{(2)} - 2\kappa_{abc} V_c - V_{ab} \right) \eta_a \eta_b \right], \end{aligned} \quad (13.30)$$

where again in the first equality we have already eliminated the terms which vanish when the solution for σ_a is inserted and terms higher order in ϵ or η than we are considering. In the second equality we have substituted the solution (13.22) for σ_a and collected terms according to their order in ϵ .

13.1.4 Matching stars A and B in the mode basis

We have computed an expression for \mathcal{V} in the mode basis using two different methods, and we can now equate these expressions. For star A, \mathcal{V} is given by the Lagrangian of Eq. (12.12), through $\mathcal{V} = \sum \dot{\eta}_a^2 / \omega_a^2 - \mathcal{L}$. Matching this to Eq. (13.30) order by order in ϵ and η , we get the following conditions on the three- and four-mode coupling terms.

At order ϵ , matching terms gives

$$U_{ab} + \sum 2\kappa_{abc} \chi_c^{(1)} = - \left(J_{ab}^{(1)} + J_{ba}^{(1)} \right), \quad (13.31)$$

which results in an expression for $\kappa_{abc} \chi_c^{(1)}$ in terms of the Jacobian transform and the tidal potential. Meanwhile, matching the ϵ^2 terms gives

$$\sum \left(2\kappa_{abc} \chi_c^{(2)} + 3\kappa_{abcd} \chi_c^{(1)} \chi_d^{(1)} \right) = - \sum \left(J_{ca}^{(1)} J_{cb}^{(1)} + J_{ab}^{(2)} + J_{ba}^{(2)} - 2\kappa_{abc} V_c - V_{ab} \right). \quad (13.32)$$

In both of Eqs. (13.31) and (13.32), the indices (a, b) refer to particular modes and are not summed over.

13.1.5 Expressions for the Jacobian in the mode basis

Before using the matching conditions in Eqs. (13.31) and (13.32), we derive the explicit equations for the Jacobian that transforms the perturbations η on star A to the perturbations η_S . This is achieved by considering the difference between two series of active transformations as depicted in Fig. 13.1, using a fixed background coordinate system. We begin by considering a fluid element at a point \mathbf{x} in the unperturbed star. We then consider the application of the tidal perturbation, which takes $\mathbf{x} \rightarrow \mathbf{x} + \chi(\mathbf{x})$, followed by the coordinate transform ψ acting on this element, which acts on the element at its displaced position $\mathbf{x} + \chi(\mathbf{x})$. This takes us across the top row of Fig. 13.1, and acts to transform the initial point as

$$\mathbf{x} \rightarrow \mathbf{x} + \chi(\mathbf{x}) + \zeta|_{\mathbf{x}+\chi(\mathbf{x})} + \frac{1}{2} (\zeta \cdot \nabla) \zeta|_{\mathbf{x}+\chi(\mathbf{x})}. \quad (13.33)$$

Next, consider the series of transforms which first takes \mathbf{x} to the corresponding point in star A, $\mathbf{x} \rightarrow \mathbf{x} + \chi(\mathbf{x}) + \eta(\mathbf{x})$. Since we wish to express all perturbations in Lagrangian coordinates, the η is written as a function of the position of the original, unperturbed element. We follow this pair of displacements by the coordinate transform ψ , which acts on the actual position of the element. This gives us the position of the element in star B,

$$\mathbf{x} \rightarrow \mathbf{x} + \chi(\mathbf{x}) + \eta(\mathbf{x}) + \zeta|_{\mathbf{x}+\chi(\mathbf{x})+\eta(\mathbf{x})} + \frac{1}{2} (\zeta \cdot \nabla) \zeta|_{\mathbf{x}+\chi(\mathbf{x})+\eta(\mathbf{x})}. \quad (13.34)$$

The difference between Eqs. (13.34) and (13.33) is simply $\eta_S(\mathbf{x}) = \mathbf{J}_\psi \eta(\mathbf{x})$. Taking this difference, and expanding our expressions in terms of small η , we have

$$\mathbf{J}_\psi \eta = \eta(\mathbf{x}) + \eta(\mathbf{x}) \cdot (\nabla \zeta)|_{\mathbf{x}+\chi(\mathbf{x})} + \frac{1}{2} \eta(\mathbf{x}) \cdot [\nabla (\zeta \cdot \nabla) \zeta]|_{\mathbf{x}+\chi(\mathbf{x})} + O(\eta^2). \quad (13.35)$$

Further expanding out χ and ζ in terms of ϵ , this expression becomes

$$\mathbf{J}_\psi \eta = \eta + \epsilon (\eta \cdot \nabla) \zeta^{(1)} + \epsilon^2 \left((\eta \cdot \nabla) \zeta^{(2)} + \eta \cdot [(\chi^{(1)} \cdot \nabla) \nabla \zeta^{(1)}] + \frac{1}{2} (\eta \cdot \nabla) (\zeta^{(1)} \cdot \nabla) \zeta^{(1)} \right) + O(\eta^3). \quad (13.36)$$

Here, all terms are evaluated at the base point \mathbf{x} . This allows us to simply read off the Jacobian of Eq (13.27). It is useful to recall that $\chi^{(1)} = -\zeta^{(1)}$, which allows us to simplify the Jacobian somewhat:

$$\mathbf{J}_\psi^{(1)} \eta = (\eta \cdot \nabla) \zeta^{(1)} \quad \text{and} \quad \mathbf{J}_\psi^{(2)} \eta = (\eta \cdot \nabla) \zeta^{(2)} + [(\eta \cdot \nabla) \zeta^{(1)}] \cdot \nabla \zeta^{(1)} - \frac{1}{2} (\eta \cdot \nabla) (\zeta^{(1)} \cdot \nabla) \zeta^{(1)}. \quad (13.37)$$

To simplify Eq. (13.36) we have temporarily resorted to a Cartesian basis in order to commute the

covariant derivatives.

Now that we have an explicit expression for the Jacobian, we can express it in the mode basis using the expansion for η . The result, for the first and second order terms, is

$$J_{ab}^{(1)} = \frac{\omega_a^2}{E_0} \int d^3x \rho \xi_a \cdot (\xi_b \cdot \nabla) \zeta^{(1)} \quad \text{and} \quad (13.38)$$

$$J_{ab}^{(2)} = \frac{\omega_a^2}{E_0} \int d^3x \rho \xi_a \cdot (\xi_b \cdot \nabla) \left[\zeta^{(2)} - \frac{1}{2} (\zeta^{(1)} \cdot \nabla) \zeta^{(1)} \right] + \xi_a \cdot \left(\left[(\xi_b \cdot \nabla) \zeta^{(1)} \right] \cdot \nabla \zeta^{(1)} \right). \quad (13.39)$$

For our initial check of the mode stability in Section 12.1.4, we note here that for a particular high-order mode, $\xi_a \sim \omega_a^{-1}$, and so we have the useful fact that for a particular pair of modes (a, b) ,

$$J_{ab}^{(i)} \sim \frac{\omega_a}{\omega_b} \quad (13.40)$$

so long as the angular integrations satisfy selection rules and the contraction of indices in Eqs. (13.38,13.39) do not lead to a much smaller value. This fact is made more explicit in Section 13.2.

13.1.6 Lagrangian perturbations of star A revisited

With our matching results from Section 13.1.4, we can return to the expressions for the perturbed eigenvalues from Section 12.1.4. We focus on the case of interest for the instability proposed by WAB, that of a high-order (p, g) mode pair with comparable wave numbers and widely spaced frequencies, $\omega_p \gg \omega_g$. Working in the rescaled mode amplitudes $\eta'_a = \eta_a/\omega_a$, consider the eigenvalues of the matrix \mathcal{M} in the Lagrangian (12.21). Substituting the matching conditions (13.31) and (13.32) into \mathcal{M} as given by Eqs. (12.22)–(12.24), we have now that

$$\mathcal{M}_{pp} = \omega_p^2 + 2\epsilon\omega_p^2 J_{pp}^{(1)} + \epsilon^2\omega_p^2 \left[\sum \left(J_{ap}^{(1)} J_{ap}^{(1)} - 2\kappa_{ppa} V_a \right) + 2J_{pp}^{(2)} - V_{pp} \right], \quad (13.41)$$

$$\mathcal{M}_{pg} = \mathcal{M}_{gp} = \epsilon\omega_p\omega_g \left(J_{pg}^{(1)} + J_{gp}^{(1)} \right), \quad \text{and} \quad (13.42)$$

$$\mathcal{M}_{gg} = \omega_g^2 + 2\epsilon\omega_g^2 J_{gg}^{(1)} + \epsilon^2\omega_g^2 \left[\sum \left(J_{ag}^{(1)} J_{ag}^{(1)} - 2\kappa_{gga} V_a \right) + 2J_{gg}^{(2)} - V_{gg} \right]. \quad (13.43)$$

The resulting perturbed eigenvalues are similarly re-expressed in terms of the Jacobian and the potential V . Let us focus on the smaller frequency, which is perturbed to a lower (and possibly negative value):

$$\frac{\omega_-^2}{\omega_g^2} = 1 + 2\epsilon J_{gg}^{(1)} + \epsilon^2 \left[\left(J_{pg}^{(1)} \right)^2 + \left(J_{gp}^{(1)} \right)^2 + 2J_{gg}^{(2)} - V_{gg} - \sum 2\kappa_{gga} V_a \right] - \epsilon^2 \frac{\omega_p^2}{\omega_p^2 - \omega_g^2} \left(J_{pg}^{(1)} + J_{gp}^{(1)} \right)^2. \quad (13.44)$$

Keeping in mind the origin of each of the terms, and our estimate that $J_{ab}^{(i)} \sim \omega_a/\omega_b$, we can see how Eq. (13.44) encodes a potential instability, and the particular manner in which it is actually canceled. The final $O(\epsilon^2)$ term in Eq. (13.44) is just the three-mode term $\kappa_{pga}\chi_a^{(1)}$ in Eq. (12.26), expressed in the language of Jacobians. When the frequency of the p -mode is much larger than that of the g -mode, the size of this term is $\sim (J_{pg}^{(1)})^2 \sim (\omega_p^2/\omega_g^2) \gg 1$. In principle, this can overcome the ϵ^2 suppression when the tidal field is relatively strong (but with $\epsilon \ll 1$), and overwhelm the order-unity contribution from the restoring force. However, when we express the perturbation to the diagonal terms [entering from the four-mode and $\kappa_{abc}\chi_c^{(2)}$ terms in Eq. (12.26)] in terms of Jacobians, we observe that it contains an identical contribution with the opposite sign.

Before we explicitly write down the remaining terms, it is worthwhile to pause and consider the impact of our coordinate transformation. The three- and four- mode terms in Eq. (12.26) both affect the eigenvalues equally. Independently calculating their individual contributions would have involved careful book-keeping in order to accurately track the cancellation of large terms. Instead, our approach has confirmed the intuition developed from the toy model of Sec. 11.1.1, and illuminated the fact that large coupling terms can arise from rotations of modes into each other.

We now write down the terms that remain after the large cancellations. Expanding the prefactor of the final term in Eq. (13.44),

$$\frac{\omega_p^2}{\omega_p^2 - \omega_g^2} = \left(1 + \frac{\omega_g^2}{\omega_p^2}\right) + \mathcal{O}\left(\frac{\omega_g^4}{\omega_p^4}\right), \quad (13.45)$$

we can simplify Eq. (13.44) to

$$\frac{\omega_-^2}{\omega_g^2} = 1 + 2\epsilon J_{gg}^{(1)} + \epsilon^2 \left[\frac{\omega_g^2}{\omega_p^2} \left(J_{pg}^{(1)}\right)^2 + \left(J_{gg}^{(1)}\right)^2 + 2J_{gg}^{(2)} - V_{gg} - 2J_{pg}^{(1)}J_{gp}^{(1)} - \sum 2\kappa_{gga}V_a \right]. \quad (13.46)$$

Our estimate for the size of the Jacobian terms shows us that all the terms are $\mathcal{O}(1)$ in terms of frequency, except perhaps the V_{gg} and $\kappa_{gga}V_a$ terms. We need to check that these terms are not large for the case of the high-order (p, g) -mode coupling. We show this formally and estimate the size of these terms in Section 13.2.

In both this section and in Section 12.1.4, we have considered the coupling of a single pair of modes (p, g) , but in general \mathcal{M} contains entries for all modes and their mode-mode coupling terms. Equations (13.41)–(13.46) extend naturally to this case. For example, if we consider a single g -mode, there is an off-diagonal matrix entry \mathcal{M}_{ag} for every other mode η_a , and this entry couples the g -mode to η_a . In addition, the sum $\sum J_{ag}^{(1)}J_{ag}^{(1)}$ in \mathcal{M}_{gg} contains a contribution from each of these other modes. When computing the perturbation to the g -mode frequency, the off-diagonal terms all enter as a sum of squared terms analogous to the last term in Eq. (13.44). In those cases where a mode strongly couples to the g -mode, the same leading-order cancellation of large terms occurs

mode-by-mode. This means that even in the case where many p -modes strongly couple to a single g -mode, cancellation between the large parts of the three-mode couplings (squared) and four-mode couplings prevents the g -mode from developing an instability.

It is remarkable that up until now, our investigation of the generation of the daughter modes from the tidal perturbation has been formal and general in nature, with no reference made to a particular stellar model. In our estimates we have only needed to note that $\xi_a \sim \omega_a^{-1}$ given our normalization of the mode functions.

13.2 Estimating the remaining terms

So far, we have shown that the major potential contributions to the instability discussed in WAB cancel out in the limit $\omega_p \gg \omega_g$ for the (p, g) pair of daughter modes. This result alone does not guarantee the stability of the star to the production of the (p, g) mode pair, since there are other terms whose sizes need to be estimated for the modes of interest. We carry out these estimates in this section, relying on the WKB approximation for the mode functions when we need to explicitly compute the size of the various terms in Eq. (13.44). The WKB approximation is appropriate in this case, since the proposed instability occurs when high order p - and g -modes have resonant spatial eigenfunctions, a condition which requires large wave numbers k_p and k_g for the modes.

First, though, we develop some confidence in the matching results of Section 13.1.4 by showing that the three-mode coupling term $\kappa_{pgc}\chi_c^{(1)}$ as derived in WAB can be recovered from our matching equations. We then turn to estimating the size of the remaining terms.

13.2.1 The three-mode coupling

We begin by considering the amplitude $U_a = \chi_a^{(1)} = -\zeta_a^{(1)}$. It is conveniently obtained by considering the leading order part of ζ ,

$$\zeta^{(1)} = -\chi^{(1)} = -\omega_0^2 \frac{r^2}{\mathfrak{g}} \left[P_2(\cos \theta) \hat{\mathbf{r}} + \frac{4-n}{6} \partial_\theta P_2(\cos \theta) \hat{\theta} \right]. \quad (13.47)$$

When we recall the definition that $\epsilon = Gm/(a^3\omega_0^2)$ this recovers the linear tidal response,

$$\epsilon\chi^{(1)} = \frac{Gm}{a^3} \frac{r^2}{\mathfrak{g}} \left[P_2(\cos \theta) \hat{\mathbf{r}} + \frac{4-n}{6} \partial_\theta P_2(\cos \theta) \hat{\theta} \right], \quad (13.48)$$

which can be compared to Eqs (A12) and (A13) of Weinberg et al. [411]. Recall that our eigenmodes ξ_a have the form in Eq. (12.5), and that here we have specialized to the $m = 0$ case. We see that $\chi^{(1)}$ has the correct form for an $l = 2$ displacement.

Before continuing, it is useful to note that we have frequent need of integrals of the form

$$I_{abc} = \int d^3x \rho \xi_a \cdot (\xi_b \cdot \nabla) \xi_c. \quad (13.49)$$

With our convention that ξ_a take the form in Eq. (12.5), the integral (13.49) resolves to

$$I_{abc} = \int dr r^2 \rho(r) \left[T_{abc} a_r b_r \frac{dc_r}{dr} + F_{a,bc} \frac{a_r b_h}{r} (c_r - c_h) + F_{b,ac} a_h b_r \frac{dc_h}{dr} + \frac{a_h b_h}{r} (G_{c,ab} c_h + F_{c,ab} c_r) \right]. \quad (13.50)$$

The angular integrals T_{abc} , $F_{a,bc}$, and $G_{a,bc}$ are those originally defined in Wu and Goldreich [423] and match those listed in Eqs. (A20–A22) of Weinberg et al. [411]. We give them in Appendix 13.D, and they are determined by the angular indices (l_a, l_b, l_c) of the mode vectors in the integral. These integrals vanish unless the angular momentum indices obey the triangle inequality $|l_b - l_c| \leq l_a \leq l_b + l_c$, and in addition the sum $l_a + l_b + l_c$ must be even.

Now we are ready to consider the three-mode coupling term for the case of a pair of (p, g) modes excited by the tide. From Eq. (13.31), we have

$$\sum \kappa_{pgc} \chi_c^{(1)} = -\frac{1}{2} U_{pg} - \frac{1}{2} (J_{pg}^{(1)} + J_{gp}^{(1)}). \quad (13.51)$$

The coupling κ_{pgc} can be large in the case $\omega_p \gg \omega_g$, and when the spatial resonance condition $k_p \simeq k_g$ is met [228]. This means that the (p, g) modes must be high order modes with large wave numbers, and as such we use the WKB approximation [411, 424] to get analytic forms for the eigenfunctions ξ_p and ξ_g . In this case, the radial functions (p_r, p_h) and (g_r, g_h) are

$$(p_r, p_h) \simeq \frac{A_p}{\omega_p} \left(\cos k_p r, \frac{c_s \sin k_p r}{\omega_p r} \right) \quad \text{and} \quad (13.52)$$

$$(g_r, g_h) \simeq \frac{A_g}{\omega_g} \left(\frac{\omega_g \sin k_g r}{N}, \frac{\cos k_g r}{\Lambda_g} \right), \quad (13.53)$$

where c_s is the adiabatic sound speed, N is the Brünt-Väisälä frequency,

$$N^2 = - \left(\frac{1}{\rho} \frac{d\rho}{dr} - \frac{1}{\Gamma_1 P} \frac{dP}{dr} \right) \mathbf{g}, \quad (13.54)$$

Γ_1 is the adiabatic index, $\Lambda_a^2 = l_a(l_a + 1)$, and we set

$$(k_p, k_g) \simeq \left(\frac{\omega_p}{c_s}, \frac{\Lambda_g N}{r \omega_g} \right), \quad A_{p,g} = \sqrt{\frac{E_0 \alpha_{p,g}}{\rho r^2}}, \quad \alpha_p = \left(c_s \int c_s^{-1} dr \right)^{-1}, \quad \text{and} \quad \alpha_g = \frac{N}{r} \left(\int N d \ln r \right)^{-1}. \quad (13.55)$$

In the WKB approximation, $k_p \simeq k_g$ implies that $\omega_p \omega_g \simeq \Lambda_g N c_s / r$. The key consideration for

estimating the largest terms is that for the p -mode, p_r is the dominant component of the mode (the acoustic modes are mostly radial) and for the g -mode, g_h is the dominant component (the gravity wave modes are mostly horizontal).

When we have need for a specific stellar model, we use rough approximations to the neutron star model [425] used by WAB, generated with the Skyrme-Lyon equation of state [SLy4; 426]. In this model the density is approximately constant throughout the core of the neutron star, where the coupling κ_{pgc} is large. When this is true the gravitational acceleration grows linearly with the radius, $\mathfrak{g} \simeq 4\pi G\rho r/3$. In addition, c_s is roughly constant throughout the core of the star and so $c_s \simeq \omega_0 R_*$. We also use the expression for N from Reisenegger and Goldreich [427], derived to leading order in small electron fraction Y_e ,

$$N \simeq \frac{\mathfrak{g}}{c_s} \sqrt{\frac{Y_e}{2}}. \quad (13.56)$$

This leads us to see that Nc_s/r is constant, and moreover that $N \sim \omega_0 r/R_*$, since $\omega_0^2 \simeq G\rho$ for a nearly constant density. Taken together with the condition that the wave numbers for the (p, g) modes are nearly equal, we have that $\omega_p \omega_g \sim \omega_0^2$. In this model, Eq. (13.47) shows that $\chi_r^{(1)} \sim \chi_h^{(1)} \sim r$. These approximations are expected to hold for a variety of neutron star models (see WAB Section 3.3).

We begin our computation of the three-mode coupling constant by evaluating U_{pg} ,

$$\begin{aligned} U_{pg} &= -\frac{\omega_0^2}{E_0} \int d^3x \rho \xi_p \cdot (\xi_g \cdot \nabla) \nabla [r^2 P_2(\cos \theta)] \\ &= -\frac{\omega_0^2}{E_0} \sqrt{\frac{4\pi}{5}} \int dr r^2 \rho [2p_r g_r T_{pg2} + p_r g_h F_{p,g2} + p_h g_r F_{g,p2} + p_h g_h (2F_{2,pg} + G_{2,pg})] \\ &\simeq -\frac{\omega_0^2}{E_0} \sqrt{\frac{4\pi}{5}} \int dr r^2 \rho p_r g_h F_{p,g2} \sim \frac{\omega_0^2}{\omega_p \omega_g} \sim \mathcal{O}(1), \end{aligned} \quad (13.57)$$

where in the third line terms have been dropped since they are higher order in ω_g/ω_0 or ω_0/ω_p . We see that U_{pg} contains no large terms.

Similarly, we can consider the leading order Jacobian terms, using Eqs. (13.38) and (13.50) to write them as,

$$J_{ab}^{(1)} = \frac{\omega_a^2}{E_0} I_{ab\zeta} = -\frac{\omega_a^2}{E_0} I_{ab\chi^{(1)}}, \quad (13.58)$$

where the subscripts ζ and $\chi^{(1)}$ indicate the substitution of the corresponding displacement for the mode function ξ_c in the integral I_{abc} . The radial functions χ_r and χ_h are defined as in Eq. (12.5),

with $l = 2$ and $m = 0$, so that the largest contributions to the Jacobian terms are

$$J_{pg}^{(1)} = -\frac{\omega_p^2}{E_0} \int dr r^2 \rho F_{p,g2} \frac{p_r g_h}{r} (\chi_r^{(1)} - \chi_h^{(1)}) \sim \frac{\omega_p}{\omega_g} \quad \text{and} \quad (13.59)$$

$$J_{gp}^{(1)} = -\frac{\omega_g^2}{E_0} \int dr r^2 \rho F_{g,p2} g_h p_r \frac{d\chi_h^{(1)}}{dr} \sim \frac{\omega_g}{\omega_p}. \quad (13.60)$$

At leading order, then,

$$\sum \kappa_{pgc} \chi_c^{(1)} \sim \frac{\omega_p^2}{2E_0} \int dr r^2 \rho F_{p,g2} \frac{p_r g_h}{r} (\chi_r^{(1)} - \chi_h^{(1)}) \sim \frac{\omega_p}{\omega_g}. \quad (13.61)$$

This matches the leading order terms in WAB, and arises solely from our consideration of the volume-preserving transform. As we have shown, a correction involving the four-mode coupling term cancels its influence on the eigenfrequencies. We now show that none of the remaining terms are large enough to produce a potential instability.

13.2.2 Size of the remaining terms

We have calculated the correction to the frequency of the almost-neutrally stable g -modes in the presence of the tidal deformation, in Eq. (13.46). We can write the relative corrections as

$$\frac{\omega_-^2 - \omega_g^2}{\omega_g^2} = 2\epsilon J_{gg}^{(1)} + \epsilon^2 \left[\left\{ \frac{\omega_g^2}{\omega_p^2} \left(J_{pg}^{(1)} \right)^2 + \left(J_{gg}^{(1)} \right)^2 - 2J_{pg}^{(1)} J_{gp}^{(1)} + 2J_{gg}^{(2)} \right\} - \left\{ V_{gg} + \sum 2\kappa_{gga} V_a \right\} \right]. \quad (13.62)$$

The corrections can be divided into two classes - a set of Jacobian terms, and a set of potential terms.

We have previously encountered Jacobian terms while estimating the three-mode coupling. For high-order modes a and b , the leading order dependence of the first-order Jacobian $J_{ab}^{(1)}$ on the frequencies is $J_{ab}^{(1)} \sim \mathcal{O}(\omega_a/\omega_b)$. From this observation, we see that all the terms involving a first-order Jacobian in Eq. (13.62) are $\mathcal{O}(1)$ in the large frequency ratio ω_p/ω_g .

The second-order Jacobian term $J_{ab}^{(2)}$ is given by Eq. (13.39). We observe that it has the same frequency dependence as the first-order Jacobian, with a prefactor of ω_a^2/E_0 and the two eigenfunctions ξ_a and ξ_b present in the integrand. As we did for the first order Jacobian, we recall that for high-order modes the WKB eigenfunctions have a size $\xi_a \sim \sqrt{E_0}/\omega_a$, as seen in Eqs. (13.52) and (13.53). Hence, the second-order Jacobian term is $\mathcal{O}(1)$ in the frequency ratio ω_p/ω_g .

Having established that all the Jacobian terms in Eq. (13.46) are of the form ϵ or ϵ^2 times terms of $\mathcal{O}(1)$ in the frequency ratio, we turn to the potential terms in Eq. (13.62). Using Eq. (13.22), we

can write

$$-\epsilon^2 \left(V_{gg} + \sum 2\kappa_{gga} V_a \right) = -\epsilon^2 \left(V_{gg} + \sum 2\kappa_{gga} \sigma_a^{(2)} \right) = -\epsilon^2 (V_{gg} + 2\kappa_{gg\sigma}), \quad (13.63)$$

where in the last equality we have used the notation introduced in Eq. (13.58), and further dropped the superscript on σ with the understanding that we are using the leading ϵ^2 term in the expansion of the displacement. The key point is that $\epsilon^2 \kappa_{gg\sigma}$ can be computed by substituting the displacement σ in place of the eigenfunction ξ_c in the definition (12.10) of the three-mode coupling, as κ_{abc} is linear in its arguments.

The nonlinear tidal term V_{gg} is given by Eq. (13.20):

$$\begin{aligned} V_{gg} &= -\frac{1}{E_0} \int d^3x \rho \xi_g \cdot (\xi_g \cdot \nabla) \nabla V \\ &= -\sqrt{4\pi} \frac{1}{E_0} \int dr r^2 \rho(r) \left(g_r g_r \frac{d^2 V}{dr^2} T_{\sigma gg} + \frac{g_h g_h}{r} \frac{dV}{dr} F_{\sigma, gg} \right) \\ &= -\frac{1}{E_0} \int dr r^2 \rho(r) \left(g_r g_r \frac{d^2 V}{dr^2} + \Lambda_g^2 \frac{g_h g_h}{r} \frac{dV}{dr} \right). \end{aligned} \quad (13.64)$$

In this expression, we have used expressions for the angular integrals from Wu and Goldreich [423], together with the fact that the radial displacement σ has the angular quantum numbers $l = 0$, $m = 0$. The integrals are elaborated upon in Appendix 13.D. Note that in this expression for V_{gg} , we have a potentially large part $\sim g_h g_h$ due to the large size of the horizontal displacement g_h of the g -mode. We see that this term cancels exactly with a part of the three-mode term.³

The three-mode term $\kappa_{gg\sigma}$ has a covariant form [e.g. 420, Eq. 4.20]. It can be evaluated in terms of the radial and angular parts of the mode eigenfunctions [411, 423]. Before continuing, we should note a complication which arises in the case we are dealing with, namely that of a radial displacement coupled to non-radial displacements.

The process of expanding and simplifying the expression for the three-mode coupling involves using the equations of motion for the constituent displacements. The equation for the divergence of a displacement of the form of Eq. (12.5) is

$$(\nabla \cdot \xi_a)_r = \frac{da_r}{dr} + \frac{2}{r} a_r - \frac{\Lambda_a^2}{r} a_h, \quad (13.65)$$

where we have written the divergence as $(\nabla \cdot \xi_a)_r$ because we have omitted its spherical harmonic angular dependence, which is absorbed in the angular integrals. The equations of motion for a mode

³The expression V_{gg} as defined by Eq. (13.20) is the spherical ($l = 0$) counterpart of the nonlinear driving terms J_{ablm} of Weinberg et al. [411], as given by their Eq. (A23). We can anticipate that there are large cancellations with the inhomogeneous part of the three-mode coupling terms, just as it happens for the functions J_{ablm} in Weinberg et al. [411].

with angular index $l > 0$ are

$$\Gamma_1 P(\nabla \cdot \xi_a)_r = -(\delta P)_r = \rho \mathbf{g} a_r - \omega_a^2 \rho r a_h + \rho \Phi' \quad \text{and} \quad (13.66)$$

$$\frac{d}{dr} [\Gamma_1 P(\nabla \cdot \xi_a)_r] = \frac{\Lambda_a^2}{r} \rho \mathbf{g} a_h - \left(\omega_a^2 + \frac{2\mathbf{g}}{r} - \frac{d\mathbf{g}}{dr} \right) \rho a_r + \rho \frac{d\Phi'}{dr}. \quad (13.67)$$

The Eulerian perturbation of the potential is denoted by Φ' . Within the Cowling approximation, it has a contribution only from the external driving potential V . Spherical symmetry demands that it only has a contribution from the part of the driving potential with the same spherical harmonic dependence as the displacement. For the g -mode, the external driving potential V_g vanishes, because the mode's eigenfunction is nonradial, and the potential is spherically symmetric.

We cannot use Eqs. (13.65–13.67) for the radial displacement σ just by setting the angular displacement σ_h to zero. Deriving Eq. (13.66) involves using the angular parts of the equations of motion, which do not exist for a radial displacement. We could still have used Eq. (13.66) for the radial displacement had we been operating within the hydrostatic approximation, with the Eulerian pressure perturbation $P' = \rho g \sigma_r = -\rho \Phi'$ and the Lagrangian pressure perturbation $\delta P = 0$. We cannot use the approximation, as it is not consistent with our construction of the radial displacement as that part of the tidal displacement χ which changes the volume of the elements. The root of the difference is that radial and angular modes have different analytic structures. For instance, the Lagrangian and Eulerian pressure perturbations δP and P' do not necessarily vanish at the center of the star for a radial displacement. This fact is noted in Cox [418, Section 17.6]. Another point of view is that for just a single degree of freedom, Eqs. (13.65)–(13.67) are overdetermined, and would need to satisfy a consistency condition.

We *can* still use Eq. (13.65) (the definition of divergence) and Eq. (13.67) (the radial equation of motion) for the radial displacement σ , with the Eulerian perturbation to the potential Φ' given by the external potential V on star B . Equation (13.67) still holds even though σ does not represent a normal mode of the star because it represents a force balance: star B is in hydrostatic equilibrium in the modified potential and hence we may use Eq. (13.67) with $\omega_\sigma = 0$.

Keeping this in mind, the starting point for simplifying the three-mode term $\kappa_{gg\sigma}$ is Eqs. (A27)–(A30) of Weinberg et al. [411]. Our paths diverge from the point where the equations of motion are used. The end goal of our simplification is to get an expression which consists of terms which have dominant contributions of the form $g_r g_r$ and $g_h g_h$, since given the WKB forms of the mode function, these are the forms which pick up a growing contribution as we integrate through the star. In order to do so, we repeatedly use the equations of motion for the nonradial mode \mathbf{g} and the radial displacement σ , and integrate by parts wherever needed.

The final expression for the combination of coupling terms needed is

$$\begin{aligned}
& \epsilon^2 (V_{gg} + 2\kappa_{\sigma gg}) \\
&= \frac{1}{E_0} \int dr \left[r^2 P \left\{ \Gamma_1 (\Gamma_1 + 1) + \left(\frac{\partial \Gamma_1}{\partial \ln \rho} \right)_s \right\} (\nabla \cdot \sigma) (\nabla \cdot \mathbf{g})_r (\nabla \cdot \mathbf{g})_r - 4r \sigma_r \Gamma_1 P (\nabla \cdot \mathbf{g})_r (\nabla \cdot \mathbf{g})_r \right. \\
&\quad - 2r^2 (\Lambda_g^2 \omega_g^2 \rho r g_h g_h + 2g_r \Gamma_1 P (\nabla \cdot \mathbf{g})_r) \frac{d}{dr} \left(\frac{\sigma_r}{r} \right) - \rho \mathfrak{g} r^3 g_r g_r \frac{d^2}{dr^2} \left(\frac{\sigma_r}{r} \right) \\
&\quad \left. + \left(-\rho \mathfrak{g}^2 r \frac{d}{dr} \left(\frac{\sigma_r}{\mathfrak{g}} \right) + \rho r \epsilon^2 \frac{dV}{dr} \right) \left(2r g_r (\nabla \cdot \mathbf{g})_r + g_r g_r \frac{d \ln \rho}{d \ln r} \right) \right]. \tag{13.68}
\end{aligned}$$

The process of simplifying the terms from their canonical forms, and the cancellation of the large term in the inhomogeneous driving V_{gg} with the three-mode coupling are demonstrated in more detail in Appendix 13.D.

In estimating the size of the remaining terms in the above expression, we find it useful to approximate the divergence of the g -mode by using Eq. (13.66) in the following way. First we note that $\omega_g^2 g_h$ is small, and that

$$(\nabla \cdot \mathbf{g})_r \simeq \frac{\rho}{\Gamma_1 P} \mathfrak{g} g_r = \frac{\mathfrak{g}}{c_s^2} g_r. \tag{13.69}$$

The radial eigenfunction for the g -mode is given by Eq. (13.53) within the WKB approximation, which involves the Brünt-Väisälä frequency N . Recall that for typical equations of state N and the acceleration due to gravity \mathbf{g} grow nearly linearly with radius till well outside the core, $N \sim \omega_0 r / R_*$ and $\mathfrak{g} \sim r \omega_0^2$, and the sound speed c_s is nearly constant, with $c_s \sim \omega_0 R_*$. The radial displacement σ is regular near the center; in fact σ_r / r is an analytic function everywhere including around the center $r \rightarrow 0$. From these observations, we can check that none of the potential terms given by Eq. (13.68) pick up large contributions as we integrate through the star, and that their contribution is of the order $\sim \mathcal{O}(1)$ in the large frequency ratio ω_p / ω_g .

To sum up, we have shown that all the corrections to the frequency of the almost-neutrally stable g -mode due to inhomogeneous driving and the lowest nonlinear interactions are small. Specifically, they are the form ϵ or ϵ^2 times terms of $\mathcal{O}(1)$ in the frequency ratio ω_p / ω_g . Since ϵ is a small parameter [$\epsilon = \Omega^2 / \omega_0^2 = (m/M)(R_*/a)^3$, where Ω is the orbital frequency of the binary] during the early part of the in-spiral phase, the interaction of internal modes with the equilibrium tide does not cause them to go unstable in this region of parameter space.

13.3 Discussion

The volume-preserving coordinate transformation enables us to calculate the four-mode coupling terms which arise when we look at the interaction of the equilibrium tide with two high-order p - and

g -modes, as long as we stay within the Cowling approximation. This coupling is important since we are interested in the effect of nonlinear interactions on the frequencies of the almost-neutrally stable g -modes, and for consistency we should consider all corrections which affect it at a given order in the tidal strength ϵ . Using this estimation of the four-mode terms, we have found that there are no large corrections to ω_g up to the second order in ϵ . This is true because of cancellations between large terms, some arising in the three-mode coupling and others in the four-mode coupling terms.

The cancellation occurs transparently using our method, but it is a useful check to see if the four-mode coupling computed using more traditional methods contains terms of the appropriate size for this cancellation. Using Eq. (49) from Van Hoolst [428], where repeated coordinate indices are summed over, we see that there are terms of the form

$$\kappa_{gg\chi^{(1)}\chi^{(1)}} = -\frac{1}{3E_0} \int d^3x \Gamma_1 P \left[(\nabla_j \chi^{(1)k}) (\nabla_k \xi_g^j) \right]^2 + \dots \sim \frac{1}{E_0} \int dr r^2 \Gamma_1 P \left(\frac{dg_h}{dr} \right)^2 \sim \frac{\omega_0^2 R_*^2 k_g^2}{\omega_g^2} \sim \frac{\omega_p^2}{\omega_g^2}. \quad (13.70)$$

For the first approximation, we have neglected factors of order unity, as well as lower order terms in the expression for $\kappa_{gg\chi\chi}$. For the second, we have used the simple stellar model and WKB eigenfunctions from Section 13.2. The final relation uses the fact that $k_g \simeq k_p \simeq \omega_p/c_s \sim \omega_p/(\omega_0 R_*)$. We can see that this term has the right size to cancel with the square of the large three-mode term in equation for the perturbed frequency, Eq. (12.26).

Although the analysis of this work has introduced the four-mode corrections to the stability of the star, a number of assumptions and approximations have been invoked along the way. We now briefly summarize them, discuss their validity, and comment on topics for future investigation.

Higher-order couplings: Given that four-mode interactions have an important role in keeping the modes stable, one might wonder whether the five- and higher-mode couplings are important. The immediate answer to these concerns is that these couplings do not correct ω_g at $\mathcal{O}(\epsilon^2)$ – the terms we have considered are the only terms which enter at this order. Of course, we have not shown that the star is stable against these sorts of non-resonant instabilities at even higher orders in ϵ . However, our results and the intuition we derive from both our toy model and our coordinate transformation method indicate the reason that many large, cross-canceling terms enter into the analysis is that the mode expansion of the Lagrangian displacement c_a is not the most natural choice of coordinates in the full nonlinear problem. We suspect that there exists some other coordinate system, in analogy to the simply rotated basis of the harmonic oscillator, which is better suited for analyzing the stability of the star, and in particular where the “valleys” of the potential energy surface (which would be exactly flat for a neutrally buoyant star with uniform specific entropy and composition) are straightened out. A more natural coordinate system could be related to our transformation, but we have not investigated this issue further. The search for a more natural coordinate system can

serve as the subject of future work.

Dynamical tide: We have not considered the stability of the dynamical tide in this work; it is not amenable to study using the volume-preserving transform here, which made use of the equilibrium nature of the background in an essential way. However, the dynamical tide is transiently excited during $\ell = 2$ g -mode resonance crossings – thus the energy input and gravitational wave template phase error do not depend on the details of the damping mechanism (see discussion in WAB Section 5.3), and in any case the phase error is tiny [410, Eq. 7.5].

Cowling approximation: The Cowling approximation, while a very good description of high-order p - and g -modes, is a poor model for the tidal bulge. The volume-preserving transformation makes use of the Cowling approximation in an essential way since we need to know the gravitational potential in order to construct it. This is however not a critical omission: since we are examining dynamics of only the daughter modes and not the excitation of the tidal bulge, we could have used as our background potential U the perturbed potential including both the tidal bulge and the external field instead of just the latter. (This would have required including higher derivatives of the potential, e.g. U_{abc} , since then $U(\mathbf{x})$ is not a quadratic function of \mathbf{x} , but these terms do not affect the arguments about the volume-preserving transform.)

Time dependence of the external tidal field: Throughout this study, we considered stability to a static perturbation of the star, since the instability in WAB exists even for a static perturbation (constant amplitude of the parent). If we instead consider the physically relevant scenario, where the tidal field is sourced by a distant companion in a circular orbit, the matrix of potential energies \mathcal{M} for the daughter modes is positive-definite at any given time, but it varies at the orbital frequency, and one may wonder whether this leads to an instability. We investigate this in Appendix 13.E, and show that at second order in the tidal field, the *only* mathematically possible instabilities in this problem are the parametric resonance instability, the quasi-static instability considered by WAB and revisited here, and a centrifugal correction to the latter due to the rotation of \mathcal{M} (as discussed in Section 11.1.1). The parametric resonance instability was considered in WAB and found not to occur for the equilibrium tide. The centrifugal instability would occur with a growth timescale of order

$$t_{\text{cen}} \sim \frac{1}{\epsilon\Omega} = \frac{\omega_0^2}{\Omega^3} \approx 4 \left(\frac{f_{\text{gw}}}{100 \text{ Hz}} \right)^{-3} \text{ s} \quad (13.71)$$

for parameters in WAB and $f_{\text{gw}} \equiv 2\Omega$, and only for modes with $\omega_g \lesssim t_{\text{cen}}^{-1}$. This is very slow compared to the original growth rate estimated in WAB, of order $\sim (\epsilon\omega_p)^{-1}$. Indeed, one may think of the centrifugal modification to the quasi-static instability as resulting from a failure at order Ω^2/ω_p^2 of the near-exact cancellation of three-mode and four-mode contributions to ω_{\pm}^2 . In principle a more detailed analysis would be required to determine whether the high-order g -modes can grow

due to the centrifugal instability. However, the centrifugal instability timescale is comparable to the gravitational wave inspiral timescale (see WAB Eq. 20),

$$\frac{t_{\text{cen}}}{t_{\text{gw}}} \sim 0.6 \left(\frac{M_{\text{chirp}}}{1.2 M_{\odot}} \right)^{5/3} \left(\frac{f_{\text{gw}}}{100 \text{ Hz}} \right)^{-1/3}, \quad (13.72)$$

where $M_{\text{chirp}} = \mu^{3/5} M_{\text{tot}}^{2/5}$ is the chirp mass of the binary, μ here is the reduced mass of the binary, and M_{tot} is the total mass of the binary. Thus the instability has time only to grow by of order one e -fold during the inspiral phase, and even this is neglecting any viscous damping of the g -modes. Detailed investigation of the factors of order unity and the possibility of modest growth due to centrifugal effects at the very latest stages of the inspiral is left to future work.

To summarize, we have shown that four-mode couplings play a critical role in the stability of equilibrium tides, and almost exactly cancel the three-mode coupling terms responsible for the p -mode- g -mode instability identified by WAB. This near-cancellation is generic and not dependent on the details of the equation of state. We conclude that in the quasi-static approximation the p -mode- g -mode instability and its deleterious effects on template-based searches for binary neutron stars go away. The principal caveat is that, when the time variability of the tidal field is taken into account, this near-cancellation is not exact, and it remains possible that an instability would develop over a much longer timespan – but likely longer than the lifetime of the binary system.

The tools we have developed in this work are quite general, and can be applied to a variety of interacting binary systems, including white dwarf binaries, stellar binaries, and possibly close planetary systems. A detailed treatment of the first nonlinear effects in stellar binaries may be needed to understand such systems, or very long-term secular effects in compact binaries.

White dwarf binaries are particularly well suited to studying tidal effects on inspirals. The physics describing tidal dissipation in these systems is much richer than in the case of neutron stars, primarily because these binaries inspiral for a much longer time in units of the dynamical timescale (ω_0^{-1}). The dimensionless tidal strength ϵ evolves with time as

$$\frac{1}{\omega_0} \frac{d \ln \epsilon}{dt} \sim \epsilon^{4/3} (\omega_0 M_{\text{chirp}})^{5/3}. \quad (13.73)$$

The dynamical frequency goes as the square root of the density, and the density of a typical neutron star is around 10^8 times that of a typical white dwarf. Hence, a white dwarf binary spends more time (in units of the dynamical timescale) at a given value of tidal strength than a neutron star binary, by a factor of $\sim 10^6$. For these slowly-evolving systems, subtler secular effects can become important, as well as both linear and nonlinear wave damping and the effect of entropy injection from tidal dissipation on the background state of the star [429–432]. Similarly, the cumulative effect of tidal lag can result in the spin-up of the white dwarfs, which both “Doppler shifts” the tidal field

to lower frequencies in the frame rotating with the white dwarf, and modifies the mode spectrum due to Coriolis forces [e.g. 433]. For the same reasons that they appeared here, four-mode couplings are likely to be necessary for a consistent treatment of nonlinear effects, and the results and techniques of this study may be of use for future lines of inquiry in these systems.

13.A Gravitational Potential Energy and the Cowling Approximation

In this appendix, we briefly go into greater detail regarding the division of gravitational potential energy between the fields and the fluid elements, and the manner in which it relates to the Cowling approximation. The essential idea is that when writing the gravitational potential energy of a system of particles, there is an ambiguity in how to divide the energy between that stored in the gravitational field itself and that stored by the particles because of their position in the field. Here we follow the discussion presented in Chapter 13 of [422]. One can choose a constant β and write the gravitational potential energy of a mass distribution ρ as

$$\mathcal{V}_{\text{grav}} = \int d^3x \left[(1 - \beta)\rho\Phi + (1 - 2\beta)\frac{\nabla\Phi \cdot \nabla\Phi}{8\pi G} \right]. \quad (13.74)$$

The Poisson equation then guarantees that any choice of β gives the same total gravitational potential energy as any other. However, when we use the Cowling approximation, the Poisson equation is no longer valid; instead, the gravitational potential Φ is frozen to its value on the background matter distribution. As such, we need to take some care in our division of potential energy.

The usual choice for the constant β when the self gravity of a system of particles is important is $\beta = 1/2$, since it places the gravitational potential energy into the pairwise interactions of the particles. The most natural choice when using the Cowling approximation is to choose $\beta = 0$, as this gives the usual expression for the gravitational potential energy of matter in an externally prescribed potential Φ . The integral over the energy density of the field becomes our constant \mathcal{C} in Eq. (12.3), and this accounts for the lack of a factor of $1/2$ in front of the term $\Phi_0 + \epsilon U$ in these equations.

13.B Non-Axisymmetric Modes

In this appendix, we extend our analysis to the full set of non-axisymmetric modes with all possible values of m . As before, we consider a particular pair of p - and g -modes with angular momentum quantum numbers l_p and l_g . Since these are coupled to the $l = 2$ tidal potential U , the triad $(l_p, l_g, 2)$ satisfies the triangle inequality, and their sum is even. There are $2l_p + 1$ p -modes with azimuthal quantum numbers m_p ranging from $-l_p$ to l_p , and likewise a number of g -modes, whose unperturbed

frequencies ω_p and ω_g are independent of m by the symmetry of the background star. As before, we set $\omega_p > \omega_g$. The sub-block of \mathcal{M} for this pair of modes is

$$\mathcal{M} = \begin{pmatrix} \mathcal{M}_{pp} & \mathcal{M}_{pg} \\ \mathcal{M}_{gp} & \mathcal{M}_{gg} \end{pmatrix}, \quad (13.75)$$

$\underbrace{\hspace{10em}}_{2l_p+1} \quad \underbrace{\hspace{10em}}_{2l_g+1}$

where

$$\begin{aligned} [\mathcal{M}_{pp}]_{m_1, m_2} &= \omega_p^2 \left[\delta_{m_1, m_2} - \epsilon \left(U_{\bar{p}m_1 p m_2} + \sum 2\kappa_{a\bar{p}m_1 p m_2} \chi_a^{(1)} \right) \right. \\ &\quad \left. - \epsilon^2 \sum \left(2\kappa_{a\bar{p}m_1 p m_2} \chi_a^{(2)} + 3\kappa_{ab\bar{p}m_1 p m_2} \chi_a^{(1)} \chi_b^{(1)} \right) \right] + \mathcal{O}(\epsilon^3), \\ [\mathcal{M}_{pg}]_{m_1, m_2} &= [\mathcal{M}_{gp}]_{m_2, m_1}^* = \omega_p \omega_g \left[-\epsilon \left(U_{\bar{p}m_1 g m_2} + \sum 2\kappa_{a\bar{p}m_1 g m_2} \chi_a^{(1)} \right) \right] + \mathcal{O}(\epsilon^2), \quad \text{and} \\ [\mathcal{M}_{gg}]_{m_1, m_2} &= \omega_g^2 \left[\delta_{m_1, m_2} - \epsilon \left(U_{\bar{g}m_1 g m_2} + \sum 2\kappa_{a\bar{g}m_1 g m_2} \chi_a^{(1)} \right) \right. \\ &\quad \left. - \epsilon^2 \sum \left(2\kappa_{a\bar{g}m_1 g m_2} \chi_a^{(2)} + 3\kappa_{ab\bar{g}m_1 g m_2} \chi_a^{(1)} \chi_b^{(1)} \right) \right] + \mathcal{O}(\epsilon^3). \end{aligned} \quad (13.76)$$

In the above expressions, the convention is that \mathcal{M}_{ab} is the coefficient of $\eta'_a{}^* \eta'_b$ in the expansion of the Lagrangian given by Eq. (12.20), after the rescaling $\eta'_a = \eta_a / \omega_a$. In writing this expression, we have used the symmetry of the coupling coefficients and the reality of χ .

Until now, we have not used the fact that U and χ are axisymmetric, i.e. they only have $m = 0$ components. By angular momentum conservation, such a U and χ can only couple modes of the same azimuthal quantum number m . In addition to this, the strengths of the couplings between modes with m are the same as those between modes with $-m$ by parity. This implies that the matrix \mathcal{M} has a sparse structure as shown in the left hand side of Fig. 13.3. In order to study the perturbations to a particular mode at the lowest order, we need to consider a 2×2 sub-matrix corresponding to the members of the p and g subspaces with the same quantum number m , when possible. Otherwise, the subspace is a 1×1 block.

The resulting perturbations to the mode frequencies are, to second order in ϵ ,

$$\begin{aligned} \omega_{p_m}^2 &= \omega_p^2 \left[1 - \epsilon \left(U_{\bar{p}m p m} + \sum 2\kappa_{a\bar{p}m p m} \chi_a^{(1)} \right) - \epsilon^2 \sum \left(2\kappa_{a\bar{p}m p m} \chi_a^{(2)} + 3\kappa_{ab\bar{p}m p m} \chi_a^{(1)} \chi_b^{(1)} \right) \right] \\ &\quad + \epsilon^2 \frac{\omega_p^2 \omega_g^2}{\omega_p^2 - \omega_g^2} \left| U_{\bar{p}m g m} + \sum 2\kappa_{a\bar{p}m g m} \chi_a^{(1)} \right|^2 \quad \text{and} \\ \omega_{g_m}^2 &= \omega_g^2 \left[1 - \epsilon \left(U_{\bar{g}m g m} + \sum 2\kappa_{a\bar{g}m g m} \chi_a^{(1)} \right) - \epsilon^2 \sum \left(2\kappa_{a\bar{g}m g m} \chi_a^{(2)} + 3\kappa_{ab\bar{g}m g m} \chi_a^{(1)} \chi_b^{(1)} \right) \right] \\ &\quad - \epsilon^2 \frac{\omega_p^2 \omega_g^2}{\omega_p^2 - \omega_g^2} \left| U_{\bar{p}m g m} + \sum 2\kappa_{a\bar{p}m g m} \chi_a^{(1)} \right|^2. \end{aligned} \quad (13.77)$$

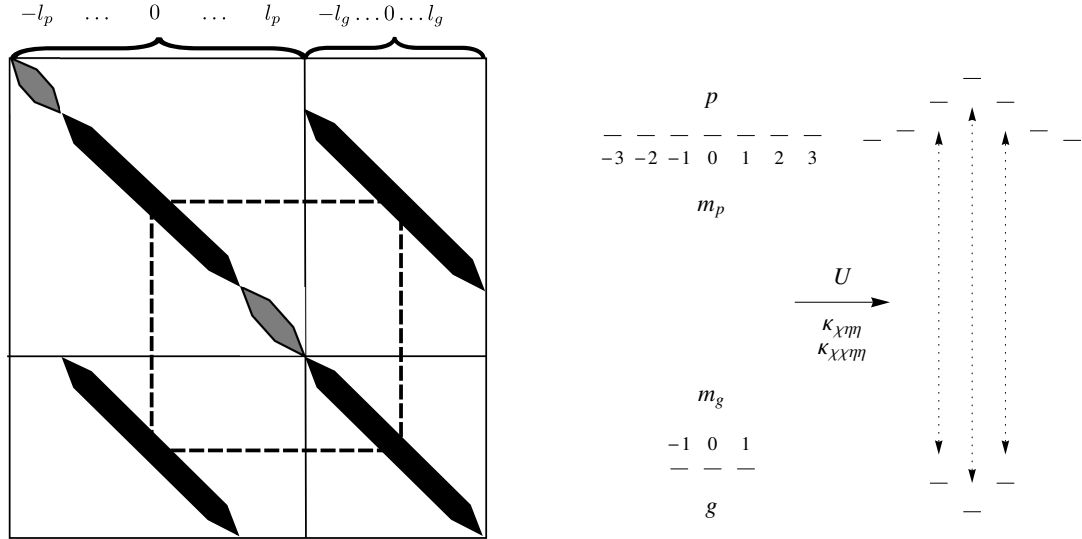


Figure 13.3: Left panel: Illustration of the form of the sub-block of \mathcal{M} , for the interaction of two modes p and g . We take $l_p > l_g$. Only the diagonals and those entries which couple terms with $m_p = m_g$ are nonzero. The entries marked with the black, thick line can be rearranged into independent 2×2 blocks, and an example block is marked out by the dashed square. Those entries of the sub-block which do not interact are marked with the gray thick line, and they form independent 1×1 blocks. Right panel: The tidal field and mode couplings correct the frequencies of the various modes as illustrated for a pair (p, g) with $l_p = 3$ and $l_g = 1$. These corrections are due to both off-diagonal and diagonal perturbations in the sub-block of \mathcal{M} .

We can recognize Eqs. (12.25) and (12.26) as special cases of this for $m = 0$. This level splitting is schematically shown in the right hand side of Fig. 13.3. For any m , the analysis of the cancellations between the four-mode terms and the three-mode terms proceeds exactly as for the axisymmetric case.

13.C Reversing the Flow of an Infinitesimal Coordinate Transform

In this appendix, we briefly derive the identity for reversing the direction of the flow discussed in Section 13.1.1. Consider a point \mathcal{P} on a manifold, and define an origin so that this point has the coordinate vector $\mathbf{x}_{\mathcal{P}}$. Next, consider the diffeomorphism generated by a flow in the direction of an infinitesimal vector field $\zeta(\mathbf{x})$. Viewed from the perspective of an active transformation, this diffeomorphism sends the points on the manifold a small distance along the integral curves of ζ , and the point \mathcal{P} is mapped to a point \mathcal{Q} whose coordinate vector is given by (keeping track of terms to second order in the small motion)

$$\mathbf{x}_{\mathcal{Q}} = \mathbf{x}_{\mathcal{P}} + \zeta(\mathbf{x}_{\mathcal{P}}) + \frac{1}{2}(\zeta \cdot \nabla)\zeta \Big|_{\mathbf{x}_{\mathcal{P}}} + \dots \quad (13.78)$$

We can then express $\mathbf{x}_{\mathcal{P}}$ as

$$\begin{aligned}\mathbf{x}_{\mathcal{P}} &= \mathbf{x}_{\mathcal{Q}} - \zeta(\mathbf{x}_{\mathcal{P}}) - \frac{1}{2}(\zeta \cdot \nabla)\zeta \Big|_{\mathbf{x}_{\mathcal{P}}} + \dots = \mathbf{x}_{\mathcal{Q}} - \zeta(\mathbf{x}_{\mathcal{Q}}) + (\zeta \cdot \nabla)\zeta \Big|_{\mathbf{x}_{\mathcal{Q}}} - \frac{1}{2}(\zeta \cdot \nabla)\zeta \Big|_{\mathbf{x}_{\mathcal{Q}}} + \dots \\ &= \mathbf{x}_{\mathcal{Q}} - \zeta(\mathbf{x}_{\mathcal{Q}}) + \frac{1}{2}(\zeta \cdot \nabla)\zeta \Big|_{\mathbf{x}_{\mathcal{Q}}} + \dots,\end{aligned}\quad (13.79)$$

where we have used Eq. (13.78) to eliminate $\mathbf{x}_{\mathcal{P}}$ from the right side of the equation. On the other hand, we could have considered the inverse flow, carrying $\mathbf{x}_{\mathcal{Q}}$ to $\mathbf{x}_{\mathcal{P}}$. It is clear that this flow is accomplished by simply reversing the sign of the generator field ζ and evaluating it at the new base point $\mathbf{x}_{\mathcal{Q}}$. Generalizing to the coordinates of points on the entire manifold, if we call the coordinates we begin with \mathbf{x} and transform to coordinates \mathbf{X} by the infinitesimal transform ζ , the transformation is

$$\mathbf{X} = \mathbf{x} + \zeta(\mathbf{x}) + \frac{1}{2}(\zeta \cdot \nabla)\zeta \Big|_{\mathbf{x}} + \dots,\quad (13.80)$$

while the inverse transform is

$$\mathbf{x} = \mathbf{X} - \zeta(\mathbf{X}) + \frac{1}{2}(\zeta \cdot \nabla)\zeta \Big|_{\mathbf{X}} + \dots.\quad (13.81)$$

These relations allow us to invert our coordinate transform derived in Section 13.1.1.

13.D Additional Details in Estimating the Perturbations to the Eigenfrequencies

Here, we collect the details of the various computations needed to estimate the various terms in Eq. (13.46). As before we define $\Lambda_a^2 = l_a(l_a + 1)$. The angular integrals are

$$T_{abc} = \int d\Omega Y_a Y_b Y_c = \sqrt{\frac{(2l_a + 1)(2l_b + 1)(2l_c + 1)}{4\pi}} \begin{pmatrix} l_a & l_b & l_c \\ m_a & m_b & m_c \end{pmatrix} \begin{pmatrix} l_a & l_b & l_c \\ 0 & 0 & 0 \end{pmatrix},\quad (13.82)$$

$$F_{a,bc} = \int d\Omega Y_a (\nabla Y_b) \cdot (\nabla Y_c) = \frac{T_{abc}}{2} (\Lambda_b^2 + \Lambda_c^2 - \Lambda_a^2),\quad (13.83)$$

$$G_{a,bc} = \int d\Omega (\nabla_j \nabla_k Y_a) (\nabla^j Y_b) (\nabla^k Y_c) = \frac{T_{abc}}{4} [\Lambda_a^4 - (\Lambda_b^2 - \Lambda_c^2)^2],\quad (13.84)$$

$$S_{abc} = \frac{1}{2} (\Lambda_a^2 F_{a,bc} + \Lambda_b^2 F_{b,ca} + \Lambda_c^2 F_{c,ab}), \quad \text{and}\quad (13.85)$$

$$V_{a,bc} = \Lambda_b^2 \Lambda_c^2 T_{abc} - F_{a,bc} - S_{abc},\quad (13.86)$$

where for $G_{a,bc}$ we have used Einstein summation convention and we use the standard metric on a unit sphere to raise indices.

In the remainder of this section, we expand on our derivation of the three-mode coupling $\kappa_{\sigma gg}$, with two of the modes being high-order g -modes and the third being the radial displacement σ . As mentioned in subsection 13.2.2, we build upon the results of Weinberg et al. [411]. We take as our starting point their Eqs. (A27)–(A30),

$$\begin{aligned} \kappa_{abc} &= \frac{1}{2E_0} \int dr \left[r^2 P \left\{ \Gamma_1(\Gamma_1 - 2) + \frac{\partial \Gamma_1}{\partial \ln \rho} \right\}_s \right] (\nabla \cdot \mathbf{a})_r (\nabla \cdot \mathbf{b})_r (\nabla \cdot \mathbf{c})_r T_{abc} \end{aligned} \quad (13.87)$$

$$\begin{aligned} &+ 2T_{abc} \rho \mathbf{g} a_r b_r c_r + (F_{a,bc} + S_{abc}) \rho \mathbf{g} a_r b_h c_h + (F_{b,ca} + S_{abc}) \rho \mathbf{g} b_r c_h a_h + (F_{c,ab} + S_{abc}) \rho \mathbf{g} c_r a_h b_h \\ &- T_{abc} \Lambda_a^2 \rho \mathbf{g} a_h b_r c_r - T_{abc} \Lambda_b^2 \rho \mathbf{g} b_h c_r a_r - T_{abc} \Lambda_c^2 \rho \mathbf{g} c_h a_r b_r - 2S_{abc} \rho \mathbf{g} a_h b_h c_h \end{aligned} \quad (13.88)$$

$$\begin{aligned} &+ \left(\frac{da_r}{dr} \frac{db_r}{dr} + \frac{2}{r^2} a_r b_r \right) r^2 \Gamma_1 P(\nabla \cdot \mathbf{c})_r T_{abc} + \left(a_r \frac{db_h}{dr} + b_r \frac{da_h}{dr} - \frac{d}{dr} (a_h b_h) \right) r \Gamma_1 P(\nabla \cdot \mathbf{c})_r F_{c,ab} \\ &- (\Lambda_b^2 a_r b_h + \Lambda_a^2 a_h b_r) \Gamma_1 P(\nabla \cdot \mathbf{c})_r T_{abc} + a_h b_h \Gamma_1 P(\nabla \cdot \mathbf{c})_r V_{c,ab} \\ &+ \left(\frac{db_r}{dr} \frac{dc_r}{dr} + \frac{2}{r^2} b_r c_r \right) r^2 \Gamma_1 P(\nabla \cdot \mathbf{a})_r T_{abc} + \left(b_r \frac{dc_h}{dr} + c_r \frac{db_h}{dr} - \frac{d}{dr} (b_h c_h) \right) r \Gamma_1 P(\nabla \cdot \mathbf{a})_r F_{a,bc} \\ &- (\Lambda_c^2 b_r c_h + \Lambda_b^2 b_h c_r) \Gamma_1 P(\nabla \cdot \mathbf{a})_r T_{abc} + b_h c_h \Gamma_1 P(\nabla \cdot \mathbf{a})_r V_{a,bc} \\ &+ \left(\frac{dc_r}{dr} \frac{da_r}{dr} + \frac{2}{r^2} c_r a_r \right) r^2 \Gamma_1 P(\nabla \cdot \mathbf{b})_r T_{abc} + \left(c_r \frac{da_h}{dr} + a_r \frac{dc_h}{dr} - \frac{d}{dr} (c_h a_h) \right) r \Gamma_1 P(\nabla \cdot \mathbf{b})_r F_{b,ca} \\ &- (\Lambda_a^2 c_r a_h + \Lambda_c^2 c_h a_r) \Gamma_1 P(\nabla \cdot \mathbf{b})_r T_{abc} + c_h a_h \Gamma_1 P(\nabla \cdot \mathbf{b})_r V_{b,ca} \end{aligned} \quad (13.89)$$

$$- r^2 \rho a_r b_r c_r \frac{d^2 \mathbf{g}}{dr^2} T_{abc} - r^2 \rho \frac{d}{dr} \left(\frac{\mathbf{g}}{r} \right) (F_{a,bc} a_r b_h c_h + F_{b,ca} a_h b_r c_h + F_{c,ab} a_h b_h c_r) \Big]. \quad (13.90)$$

In writing this, we are including only those terms which arise within the Cowling approximation. The above expression assumes that the radial mode, taken to be the \mathbf{a} mode, is defined in the manner of Eq. (12.5), i.e. its radial component a_r is such that $\mathbf{a} = a_r Y_{00}(\theta, \phi) \hat{r}$. As such, when we later plug in the radial displacement σ , we need to account for our different normalization by inserting stray factors of $\sqrt{4\pi}$. We consider the case where the other two modes are azimuthally symmetric g -modes ($m = 0$). Relaxing this assumption leads to extra phase factors of $(-1)^{-m}$, which do not affect our conclusions.

In order to simplify these terms, we initially proceed as in Weinberg et al. [411]. We integrate by parts the $d(a_h b_h)/dr$ terms in line (13.89) and cancel against the $S_{abc} \rho \mathbf{g} a_h b_h c_h$ term in line (13.88) after using the radial equation of motion (13.67) for the displacements. We then deal with the $a_r db_h/dr$ terms in the same manner. Next, we use the definition of divergence (13.65) for the modes to eliminate factors of da_r/dr in line (13.88), and residual terms which are leftover from the previous steps. However, we cannot subsequently use the angular equations of motion to simplify terms with one factor of $(\nabla \cdot \mathbf{a})_r$, as one of the modes is radial.

When we use the radial equation of motion (13.67) for the modes, we collect the restoring force terms into a homogeneous part $\kappa_{abc,H}$ and the driving terms into an inhomogeneous part $\kappa_{abc,I}$. The homogeneous part is given by

$$\kappa_{abc,H} = \frac{1}{2E_0} \int dr \left[r^2 P \left\{ \Gamma_1(\Gamma_1 + 1) + \frac{\partial \Gamma_1}{\partial \ln \rho} \Big|_s \right\} (\nabla \cdot \mathbf{a})_r (\nabla \cdot \mathbf{b})_r (\nabla \cdot \mathbf{c})_r T_{abc} \right. \quad (13.91)$$

$$\begin{aligned} & + \Gamma_1 P r (\nabla \cdot \mathbf{a})_r (\nabla \cdot \mathbf{c})_r \{ -4b_r + \Lambda_b^2 b_h \} T_{abc} + \Gamma_1 P r (\nabla \cdot \mathbf{b})_r (\nabla \cdot \mathbf{a})_r \{ -4c_r + \Lambda_c^2 c_h \} T_{abc} \\ & + \Gamma_1 P r (\nabla \cdot \mathbf{c})_r (\nabla \cdot \mathbf{b})_r \{ -4a_r + \Lambda_a^2 a_h \} T_{abc} \end{aligned} \quad (13.92)$$

$$\begin{aligned} & + \Gamma_1 P (\nabla \cdot \mathbf{c})_r (G_{c,ab} a_h b_h + 6T_{abc} a_r b_r + \{ F_{c,ab} - 3\Lambda_b^2 T_{abc} \} a_r b_h + \{ F_{c,ab} - 3\Lambda_a^2 T_{abc} \} b_r a_h) \\ & + \Gamma_1 P (\nabla \cdot \mathbf{a})_r (G_{a,bc} b_h c_h + 6T_{abc} b_r c_r + \{ F_{a,bc} - 3\Lambda_c^2 T_{abc} \} b_r c_h + \{ F_{a,bc} - 3\Lambda_b^2 T_{abc} \} c_r b_h) \\ & + \Gamma_1 P (\nabla \cdot \mathbf{b})_r (G_{b,ca} a_h c_h + 6T_{abc} c_r a_r + \{ F_{b,ca} - 3\Lambda_a^2 T_{abc} \} c_r a_h + \{ F_{b,ca} - 3\Lambda_c^2 T_{abc} \} a_r c_h) \end{aligned} \quad (13.93)$$

$$\begin{aligned} & + T_{abc} \left(2\mathbf{g} - r^2 \frac{d^2 \mathbf{g}}{dr^2} \right) \rho a_r b_r c_r + S_{abc} \rho \mathbf{g} (a_r b_h c_h + b_r c_h a_h + c_r a_h b_h) \\ & + \rho \left(\mathbf{g} - r \frac{d\mathbf{g}}{dr} \right) \{ \Lambda_a^2 a_h b_r c_r + \Lambda_b^2 b_h c_r a_r + \Lambda_c^2 c_h a_r b_r \} T_{abc} \\ & - \rho r (F_{c,ab} \omega_c^2 a_h b_h c_r + F_{a,bc} \omega_a^2 a_r b_h c_h + F_{b,ca} \omega_b^2 a_h b_r c_h) - (a_r b_h + a_h b_r) F_{c,ab} (\Lambda_c^2 \rho \mathbf{g} c_h - \omega_c^2 \rho r c_r) \\ & - (b_r c_h + b_h c_r) F_{a,bc} (\Lambda_a^2 \rho \mathbf{g} a_h - \omega_a^2 \rho r a_r) - (c_r a_h + c_h a_r) F_{b,ca} (\Lambda_b^2 \rho \mathbf{g} b_h - \omega_b^2 \rho r b_r) \}. \end{aligned} \quad (13.94)$$

For a triplet of modes (σ, g, g) with angular quantum numbers $(\{0, 0\}, \{l_g, 0\}, \{l_g, 0\})$, the angular integrals in the above expression are

$$T_{\sigma gg} = \sqrt{\frac{1}{4\pi}}, \quad (F_{\sigma,gg}, F_{g,g\sigma}) = T_{\sigma gg} (\Lambda_g^2, 0), \quad (G_{\sigma,gg}, G_{g,\sigma g}) = (0, 0), \quad \text{and} \quad S_{\sigma gg} = 0. \quad (13.95)$$

Plugging in the forms of the displacements, the angular integrals, and the fact that $\omega_\sigma = 0$, we arrive at the expression

$$\begin{aligned} \epsilon^2 \kappa_{\sigma gg,H} = \frac{1}{2E_0} \int dr \left[r^2 P \left\{ \Gamma_1(\Gamma_1 + 1) + \frac{\partial \Gamma_1}{\partial \ln \rho} \Big|_s \right\} (\nabla \cdot \sigma) (\nabla \cdot \mathbf{g})_r (\nabla \cdot \mathbf{g})_r \right. \\ & + 2\Gamma_1 P r (\nabla \cdot \sigma) (\nabla \cdot \mathbf{g})_r \{ -4g_r + \Lambda_g^2 g_h \} - 4\Gamma_1 P r (\nabla \cdot \mathbf{g})_r (\nabla \cdot \mathbf{g})_r \sigma_r \\ & + 6\Gamma_1 P (\nabla \cdot \mathbf{g})_r \sigma_r (2g_r - \Lambda_g^2 g_h) + 2\Gamma_1 P (\nabla \cdot \sigma) g_r (3g_r - 2\Lambda_g^2 g_h) \\ & \left. + \rho \left(2\mathbf{g} - r^2 \frac{d^2 \mathbf{g}}{dr^2} \right) \sigma_r g_r g_r + \rho \left(2\mathbf{g} - 2r \frac{d\mathbf{g}}{dr} \right) \Lambda_g^2 \sigma_r g_r g_h \right]. \end{aligned} \quad (13.96)$$

As we have noted in Section 13.2.2, the potential $V(\mathbf{r})$ only couples to the radial displacement σ due to its spherical symmetry. Hence only the radial displacement has an inhomogeneous term in its equation of motion. Keeping track of when we have used the radial equation of motion

(force-balance) for this displacement, this residual inhomogeneous term is

$$\epsilon^2 \kappa_{\sigma gg, I} = \frac{1}{2E_0} \int dr \Lambda_g^2 \rho r (g_h g_h - 2g_r g_h) \epsilon^2 \frac{dV}{dr}. \quad (13.97)$$

These homogeneous and inhomogeneous contributions to the three-mode coupling, when combined with the nonlinear driving term from the potential as $\epsilon^2(V_{gg} + 2\kappa_{\sigma gg, H} + 2\kappa_{\sigma gg, I})$, give the perturbation to the restoring force. Note that the largest contribution to this sum, due to the horizontal displacement of the g -mode in the two inhomogeneous terms given by Eq. (13.64) and Eq. (13.97), cancels exactly.

The remaining terms can be simplified further using the divergence equation, the radial equations of motion for the modes and the angular equation of motion for the g -mode. We have chosen to reduce them to the form given in Eq. (13.68) in order to emphasize terms whose dominant dependence on the frequency ratio ω_p/ω_g can be easily estimated from the WKB form of the g -mode eigenfunction. In particular, the only remaining term involving the horizontal displacement in Eq. (13.68) contains the combination of factors $\omega_g^2 g_h g_h$, so that the small factor ω_g^2 suppresses the large contribution from $g_h g_h$.

13.E Rotating tidal fields

We have thus far considered the stability of small daughter perturbations η for a static tidal field. This section considers a rotating tidal field, as occurs for a binary on a circular orbit, and shows that – as we would expect – the quasi-static instability (considered by WAB) and the parametric resonance instability are the only two possible instability mechanisms at second order in the tidal perturbation and while considering the behavior of two roots of the secular equation at a time. (The “collective instability” in Weinberg et al. 411 is of higher order in the sense that it requires multiple resonance criteria to be satisfied.) The only difference is that the quasi-static instability criterion is modified by the time dependence of the tidal field: the natural frequency of the g -mode oscillation ω_g^2 picks up not just the static three- and four-mode coupling corrections, but a “centrifugal” correction due to the time variation of the shallow direction in configuration space (i.e. the small eigenvalue of \mathcal{M}).

We suppose that the daughter perturbation modes have an evolution matrix \mathcal{M} in the instantaneous frame with the tidal field aligned on the z -axis, so that in the case of a static tidal field we have as before $\ddot{\eta} = -\mathcal{M}\eta$. (In the case where the tidal field is rotating, the frame where the tidal field is aligned with the z -axis is not an inertial frame, and the equations of motion have additional centrifugal and Coriolis corrections.) The eigenvalues of \mathcal{M} are the squares of the mode frequencies in the static approximation. Here \mathcal{M} is an $N \times N$ matrix, where $N = (2\ell_p + 1) + (2\ell_g + 1)$ is

the number of normal modes under consideration. In terms of the basis of Appendix 13.B, \mathcal{M} is symmetric, real, has nonzero entries only when the azimuthal quantum numbers are equal, and has equivalent components for m and $-m$. (In the main text, we treated \mathcal{M} as a 2×2 matrix, since it is trivially block-diagonal by rotational symmetry and hence there is no need to consider more than 2 modes at the same time. For a rotating tidal field, we must generalize this.)

We would like to express \mathcal{M} in an inertial frame where the binary orbit is in the xy -plane; this is achieved via the rotation by Ωt around the z -axis, followed by rotation by $\pi/2$ around the y -axis:

$$\mathbf{R}(t) = \exp\left(-i\frac{\pi}{2}\mathbf{L}_y\right) \exp(-i\Omega t\mathbf{L}_z) = \mathbf{R}(0) \exp(-i\Omega t\mathbf{L}_z), \quad (13.98)$$

where \mathbf{L}_x , \mathbf{L}_y , and \mathbf{L}_z are the angular momentum operators, each of which is an $N \times N$ Hermitian matrix. This is a unitary rotation matrix in the sense that if $\eta^{(\text{inert})}$ is the daughter perturbation in the inertial frame, then $\eta = \mathbf{R}(t)\eta^{(\text{inert})}$ is the daughter in the frame aligned with the instantaneous tidal field, where \mathcal{M} is defined. The evolution equation in the rotated frame is

$$\ddot{\eta}^{(\text{inert})} = -\mathbf{R}^\dagger \mathcal{M} \mathbf{R} \eta^{(\text{inert})}. \quad (13.99)$$

We now define a partially rotated daughter perturbation $\mu \equiv \exp(-i\Omega t\mathbf{L}_z)\eta^{(\text{inert})}$, in a basis where the z axis is normal to the orbital plane, but the x axis always points in the direction of the companion. We then left-multiply Eq. (13.99) by $\exp(-i\Omega t\mathbf{L}_z)$ to get

$$\exp(-i\Omega t\mathbf{L}_z) \frac{d^2}{dt^2} [\exp(i\Omega t\mathbf{L}_z)\mu] = -\mathbf{R}^\dagger(0) \mathcal{M} \mathbf{R}(0)\mu, \quad (13.100)$$

which expands to

$$\ddot{\mu} + 2i\Omega\mathbf{L}_z\dot{\mu} - \Omega^2\mathbf{L}_z^2\mu = -\mathbf{R}^\dagger(0)\mathcal{M}\mathbf{R}(0)\mu. \quad (13.101)$$

It is convenient to Taylor-expand \mathcal{M} in the tidal deformation,

$$\mathcal{M} = \mathcal{M}^{(0)} + \delta\mathcal{M}, \quad \text{where} \quad \delta\mathcal{M} = \epsilon\mathcal{M}^{(1)} + \epsilon^2\mathcal{M}^{(2)} + \dots; \quad (13.102)$$

then since $\mathcal{M}^{(0)}$ is spherically symmetric, we have $\mathbf{R}^\dagger(0)\mathcal{M}^{(0)}\mathbf{R}(0) = \mathcal{M}^{(0)}$. If we substitute into Eq. (13.101) and take a solution of the form $\mu \propto e^{-i\omega t}$, then

$$\mathbf{A}(\omega)\mu \equiv [-\omega^2\mathbf{I} + 2\omega\Omega\mathbf{L}_z - \Omega^2\mathbf{L}_z^2 + \mathcal{M}^{(0)} + \mathbf{R}^\dagger(0)\delta\mathcal{M}\mathbf{R}(0)]\mu = 0, \quad (13.103)$$

where \mathbf{I} is the identity matrix. An unstable daughter can then exist if Eq. (13.103) has a nontrivial solution (i.e. $\mu \neq 0$) in the upper-half complex plane. Since $\det \mathbf{A}(\omega)$ is a $2N^{\text{th}}$ order polynomial in

ω , there are $2N$ solutions. Also \mathbf{L}_z and $\delta\mathcal{M}$ are real and symmetric, and $\mathbf{R}(0)$ is real (this is because in the standard basis, the generator \mathbf{L}_y is purely imaginary; hence the finite rotation matrices around the y -axis have all real entries). Therefore $\det \mathbf{A}(\omega)$ is symmetric and has real coefficients, and so non-real solutions for ω occur in conjugate pairs.

It is also important to note that if we define the reflection matrix Σ through the xz -plane, so that in the spherical harmonic basis $\Sigma_{m,m'} = (-1)^m \delta_{m,-m'}$, we have that Σ anti-commutes with \mathbf{L}_z , i.e. $\{\Sigma, \mathbf{L}_z\} = 0$, but Σ commutes with \mathcal{M} and $\mathbf{R}(0)$. It follows that $\Sigma \mathbf{A}(\omega) = \mathbf{A}(-\omega) \Sigma$ and, since Σ is nonsingular, $\det \mathbf{A}(\omega) = \det \mathbf{A}(-\omega)$. Thus if ω is a solution, then so is $-\omega$.

In the *unperturbed* case where $\delta\mathcal{M} = 0$, we can immediately see that $\mathbf{A}(\omega) = \mathbf{A}^{(0)}(\omega)$ is diagonal in the usual basis for spheroidal modes: the diagonal entries are

$$-\omega^2 + 2m\omega\Omega - m^2\Omega^2 + \omega_p^2 = (\omega_p + m\Omega - \omega)(\omega_p - m\Omega + \omega) \quad (13.104)$$

for the $2\ell_p + 1$ p -modes with $m = -\ell_p \dots + \ell_p$, and similarly for the g -modes. Therefore the unperturbed solutions are $\pm\omega_{p,g} + m\Omega$, as one would expect. For the perturbations, we note that the correction $\delta\mathbf{A}(\omega) = \mathbf{R}^\dagger(0)\delta\mathcal{M}\mathbf{R}(0)$ does not depend on ω ; our task is “simply” to add this correction, re-compute the determinant $\mathbf{A}(\omega)$, and find the new zeroes.

We are now in a position to determine what the tidal perturbation does to the eigenfrequencies in the co-rotating frame. In order for the roots to leave the real axis, the perturbation due to the motion must first cause a pair of roots to collide and then split into a complex conjugate pair. For a general problem of the form of Eq. (13.103), we can understand this phenomenon by taking two nearby roots of the unperturbed problem, say ω_e and ω_d , which correspond to zeroes in the diagonal elements $A_{ee}^{(0)}(\omega)$ and $A_{dd}^{(0)}(\omega)$, respectively. Two cases present themselves – that e and d correspond to different modes (i.e. are zeroes of distinct diagonal elements), or the same mode (i.e. are zeroes of the same diagonal element, which has very nearly a repeated root). Our approach is to compute $\det \mathbf{A}(\omega)$ to second order in the detuning $\omega_e - \omega_d$, the separation of ω from the natural frequencies $\omega - \omega_{e,d}$, and the perturbation $\delta\mathcal{M}$. We then ask whether the resulting polynomial possesses roots in the upper half complex plane.

13.E.1 Case of distinct modes, $e \neq d$

In this case, we further suppose that ω'_e and ω'_d are the alternative roots associated with the same diagonal entries $A_{ee}^{(0)}$ and $A_{dd}^{(0)}$. To do this, we take $\omega - \omega_e$, $\omega - \omega_d$, and $\delta\mathbf{A}$ as perturbations and expand to second order. The determinant is given by the usual formula,

$$\det \mathbf{A}(\omega) = \sum_{\pi} (-1)^{\pi} A_{1\pi(1)}(\omega) A_{2\pi(2)}(\omega) \dots A_{N\pi(N)}(\omega), \quad (13.105)$$

where the sum is over the $N!$ permutations π of $\{1\dots N\}$ and $(-1)^\pi$ denotes whether the permutation is odd or even. Inspection shows that if at zeroth order (in $\omega - \omega_e$, $\omega - \omega_d$, and $\delta\mathbf{A}$) $\mathbf{A}(\omega)$ is diagonal and has zero entries in the ee and dd slots, then $\det \mathbf{A}(\omega)$ is second-order and the only terms at second order have $\pi(h) = h$ for $h \notin \{e, d\}$. Then $\det \mathbf{A}(\omega)$ is the product of the diagonal entries with $h \notin \{e, d\}$, times the determinant of the 2×2 sub-block,

$$\mathbf{A}(\omega) \ni \begin{pmatrix} (\omega - \omega_e)(\omega'_e - \omega) + \delta A_{ee} & \delta A_{ed} \\ \delta A_{de} & (\omega - \omega_d)(\omega'_d - \omega) + \delta A_{dd} \end{pmatrix}. \quad (13.106)$$

Moreover, at second order $\omega'_e - \omega$ in the above determinant may be replaced with $\omega'_e - \omega_e$. The latter gives a quadratic equation for ω :

$$0 = (\omega'_e - \omega_e)(\omega'_d - \omega_d)(\omega - \omega_e)(\omega - \omega_d) + (\omega'_d - \omega_d)\delta A_{ee}(\omega - \omega_d) \\ + (\omega'_e - \omega_e)\delta A_{dd}(\omega - \omega_e) + \delta A_{ee}\delta A_{dd} - \delta A_{ed}^2, \quad (13.107)$$

and from the discriminant (treating the above equation as a quadratic in $\omega - \omega_e$) we get the criterion for an instability:

$$(4\varpi_e\varpi_d\Delta - 2\varpi_d\delta A_{ee} - 2\varpi_e\delta A_{dd})^2 - 16\varpi_e\varpi_d(\delta A_{ee}\delta A_{dd} - 2\varpi_d\delta A_{ee}\Delta - \delta A_{ed}^2) < 0, \quad (13.108)$$

where we have defined $\Delta = \omega_e - \omega_d$ and $2\varpi_e = \omega_e - \omega'_e$ (so that $\varpi_e = \pm\omega_p$ for p -modes and $\pm\omega_g$ for g -modes; in general ϖ denotes an inertial-frame unperturbed frequency). Algebraic simplification leads to

$$\left(\Delta + \frac{\delta A_{ee}}{2\varpi_e} - \frac{\delta A_{dd}}{2\varpi_d}\right)^2 + \frac{\delta A_{ed}^2}{\varpi_e\varpi_d} < 0. \quad (13.109)$$

This is in fact the familiar criterion for parametric resonance. It requires first that ϖ_e and ϖ_d have opposite signs; if we take ϖ_e to be positive, then $\omega_e = \varpi_e + m_e\Omega$, $\omega_d = \varpi_d + m_d\Omega$, and hence the resonance criterion is $|\varpi_e| + |\varpi_d| \approx (m_d - m_e)\Omega$, and thus it occurs only when the unperturbed frequencies sum to a harmonic of the orbital frequency. The coupling strength must be at least $|\delta A_{ed}| > |\varpi_e\varpi_d|^{1/2}|\Delta|$, with a correction to the detuning if the applied perturbation leads to first-order corrections to the mode frequencies (δA_{ee} and δA_{dd}).

13.E.2 Case of the same mode, $e = d$

This time we are interested in the case where two frequencies associated with the same mode are “near” each other and may merge – say ω_e and ω'_e . Here the frequency difference is $2\varpi_e = \omega_e - \omega'_e$ and is treated as small; we have $\omega_e = m_e\Omega + \varpi_e$ and $\omega'_e = m_e\Omega - \varpi_e$. We suppose that ω is near

these frequencies, i.e. $\omega \approx m_e \Omega$, and we work to second order in ϖ_e , $\omega - m_e \Omega$, and $\delta \mathcal{M}$.

Evaluation of $\det \mathbf{A}(\omega)$ is more subtle than the case of $e \neq d$ because many more terms in the determinant are important. In Eq. (13.105), we have two types of terms: those with $\pi(e) = e$ and those with $\pi(e) \neq e$. Since $A_{ee}(\omega)$ is at least first order, as are all off-diagonal entries, the only surviving term with $\pi(e) = e$ is where π is the identity permutation (i.e. corresponding to the product of all diagonal entries in \mathbf{A}). If $\pi(e) = h \neq e$, then A_{eh} is first order, and so such a term can only survive if there is at most one other off-diagonal entry in the product, i.e. if $\pi(h) = e$ and $\pi(i) = i$ for all $i \notin \{e, h\}$. These terms lead to the approximation

$$\det \mathbf{A}(\omega) \approx A_{ee}(\omega) \prod_{i \neq e} A_{ii}(\omega) - \sum_{h \neq e} \delta A_{eh}^2 \prod_{i \notin \{e, h\}} A_{ii}(\omega). \quad (13.110)$$

We now set this to zero and divide by $\prod_{i \neq e} A_{ii}(\omega)$ to get

$$0 \approx A_{ee}(\omega) - \sum_{h \neq e} \frac{\delta A_{eh}^2}{A_{hh}(\omega)}. \quad (13.111)$$

Finally we see that $A_{hh}(\omega)$ can be approximated by its zeroth-order value (since it already appears multiplying a second-order perturbation), which is $(\omega - \omega_h)(\omega'_h - \omega) \approx (m_e \Omega - \omega_h)(\omega'_h - m_e \Omega)$. Also we substitute for $A_{ee}(\omega)$:

$$0 \approx \varpi_e^2 - (\omega - m_e \Omega)^2 + \delta A_{ee} - \sum_{h \neq e} \frac{\delta A_{eh}^2}{(m_e \Omega - \omega_h)(\omega'_h - m_e \Omega)}. \quad (13.112)$$

Finally, replacing ω_h and ω'_h by $\pm \varpi_h + m_h \Omega$, we see that the roots of this equation become complex, i.e., unstable, when

$$\varpi_e^2 + \delta A_{ee} - \sum_{h \neq e} \frac{\delta A_{eh}^2}{\varpi_h^2 - (m_e - m_h)^2 \Omega^2} = (\omega - m_e \Omega)^2 < 0. \quad (13.113)$$

This resembles the quasi-static instability criterion including both A_{ee} (which through second order includes both three-mode and four-mode couplings of mode e to the tidal field) and the square of A_{eh} (three-mode coupling of e and h to the tidal field), modified by the rotating reference frame term, $(m_e - m_h)^2 \Omega^2$. In the case of interest, where e is a g -mode and there is a perturbation coupling to p -modes h , the instability criterion becomes

$$\omega_g^2 + \delta A_{gg} - \frac{1}{\omega_p^2} \sum_{h \text{ is } p\text{-mode}} \delta A_{gh}^2 \left[1 - \frac{(m_g - m_h)^2 \Omega^2}{\omega_p^2} \right]^{-1} = (\omega - m_g \Omega)^2 < 0. \quad (13.114)$$

The last term can be expanded to leading order in Ω^2/ω_p^2 to give

$$\omega_g^2 + \delta A_{gg} - \frac{1}{\omega_p^2} \sum_{h \text{ is } p\text{-mode}} \delta A_{gh}^2 - \frac{\Omega^2}{\omega_p^4} \sum_{h \text{ is } p\text{-mode}} (m_g - m_h)^2 \delta A_{gh}^2 = (\omega - m_g \Omega)^2 < 0. \quad (13.115)$$

We see that the instability criterion – that the left-hand side be negative – differs from the quasi-static case only in the introduction of a “centrifugal correction” of order

$$\frac{\Omega^2 \delta A_{gp}^2}{\omega_p^4} \sim \left(\frac{\Omega \mathcal{M}_{gp}}{\omega_p^2} \right)^2 \sim \left(\frac{\Omega \epsilon \omega_p \omega_g J_{pg}^{(1)}}{\omega_p^2} \right)^2 \sim \left[\frac{\Omega \epsilon \omega_p \omega_g (\omega_p/\omega_g)}{\omega_p^2} \right]^2 \sim \epsilon^2 \Omega^2, \quad (13.116)$$

where we have used that $\delta A_{gp} \sim \mathcal{M}_{gp}$, used Eq. (13.42) for \mathcal{M}_{pg} , and the value of the Jacobian. This correction goes in the direction of de-stabilizing the star. It has a simple interpretation in the language of the 2-dimensional oscillator of Section 11.1.1: if the eigenvectors of \mathcal{M} rotate at some rate $\dot{\theta}$, then a particle moving in the shallow direction in the potential well experiences a “centrifugal force” correction $-\dot{\theta}^2$ to ω_-^2 . In our case where the external tidal field is rotating, the shallow direction varies by an angle $\mathcal{O}(\epsilon)$ over a timescale Ω^{-1} , hence its rotation rate squared is $\sim \epsilon^2 \Omega^2$. The interpretation as such a term is clear since in Eq. (13.115), the “rotation angle” of mode e into mode h is $\delta A_{eh}/\omega_p^2$, and it oscillates at a rate $(m_e - m_h)\Omega$. The second summation then represents the sum of squared angular rates.

For the highest-order g -modes with frequencies $\omega_g \lesssim \epsilon\Omega$, it is possible that the centrifugal term may dominate and lead to an instability whose growth timescale would be $t_{\text{cen}} \sim (\epsilon\Omega)^{-1}$.

Bibliography

- [1] M. Tegmark, *Max tegmark's sdss page* (2006), [Online; accessed 29-July-2015], URL <http://space.mit.edu/home/tegmark/sdss.html>.
- [2] A. A. Penzias and R. W. Wilson, *Astrophys. J.* **142**, 419 (1965).
- [3] J. C. Mather, E. S. Cheng, D. A. Cottingham, R. E. Eplee, Jr., D. J. Fixsen, T. Hewagama, R. B. Isaacman, K. A. Jensen, S. S. Meyer, P. D. Noerdlinger, et al., *Astrophys. J.* **420**, 439 (1994).
- [4] G. F. Smoot, C. L. Bennett, A. Kogut, E. L. Wright, J. Aymon, N. W. Boggess, E. S. Cheng, G. de Amici, S. Gulkis, M. G. Hauser, et al., *Astrophys. J. Lett.* **396**, L1 (1992).
- [5] P. de Bernardis, P. A. R. Ade, J. J. Bock, J. R. Bond, J. Borrill, A. Boscaleri, K. Coble, B. P. Crill, G. De Gasperis, P. C. Farese, et al., *Nature* **404**, 955 (2000), [astro-ph/0004404](#).
- [6] S. Padin, J. K. Cartwright, B. S. Mason, T. J. Pearson, A. C. S. Readhead, M. C. Shepherd, J. Sievers, P. S. Udomprasert, W. L. Holzapfel, S. T. Myers, et al., *Astrophys. J. Lett.* **549**, L1 (2001), [astro-ph/0012211](#).
- [7] J. M. Kovac, E. M. Leitch, C. Pryke, J. E. Carlstrom, N. W. Halverson, and W. L. Holzapfel, *Nature* **420**, 772 (2002), [astro-ph/0209478](#).
- [8] C. L. Bennett, M. Halpern, G. Hinshaw, N. Jarosik, A. Kogut, M. Limon, S. S. Meyer, L. Page, D. N. Spergel, G. S. Tucker, et al., *Astrophys. J. Suppl.* **148**, 1 (2003), [astro-ph/0302207](#).
- [9] L. Page, G. Hinshaw, E. Komatsu, M. R. Nolta, D. N. Spergel, C. L. Bennett, C. Barnes, R. Bean, O. Doré, J. Dunkley, et al., *Astrophys. J. Suppl.* **170**, 335 (2007), [astro-ph/0603450](#).
- [10] J. W. Fowler, V. Acquaviva, P. A. R. Ade, P. Aguirre, M. Amiri, J. W. Appel, L. F. Barrientos, E. S. Battistelli, J. R. Bond, B. Brown, et al., *Astrophys. J.* **722**, 1148 (2010), [1001.2934](#).
- [11] K. T. Story, C. L. Reichardt, Z. Hou, R. Keisler, K. A. Aird, B. A. Benson, L. E. Bleem, J. E. Carlstrom, C. L. Chang, H.-M. Cho, et al., *Astrophys. J.* **779**, 86 (2013), [1210.7231](#).

- [12] Planck Collaboration, P. A. R. Ade, N. Aghanim, C. Armitage-Caplan, M. Arnaud, M. Ashdown, F. Atrio-Barandela, J. Aumont, C. Baccigalupi, A. J. Banday, et al., *Astron. Astrophys.* **571**, A15 (2014), 1303.5075.
- [13] M. S. Vogeley, C. Park, M. J. Geller, and J. P. Huchra, *Astrophys. J. Lett.* **391**, L5 (1992).
- [14] K. B. Fisher, M. Davis, M. A. Strauss, A. Yahil, and J. P. Huchra, *Astrophys. J.* **402**, 42 (1993).
- [15] H. A. Feldman, N. Kaiser, and J. A. Peacock, *Astrophys. J.* **426**, 23 (1994), [astro-ph/9304022](#).
- [16] H. Lin, R. P. Kirshner, S. A. Shectman, S. D. Landy, A. Oemler, D. L. Tucker, and P. L. Schechter, *Astrophys. J.* **471**, 617 (1996), [astro-ph/9606055](#).
- [17] W. J. Percival, C. M. Baugh, J. Bland-Hawthorn, T. Bridges, R. Cannon, S. Cole, M. Colless, C. Collins, W. Couch, G. Dalton, et al., *Mon. Not. R. Astron. Soc.* **327**, 1297 (2001), [astro-ph/0105252](#).
- [18] M. Tegmark, M. R. Blanton, M. A. Strauss, F. Hoyle, D. Schlegel, R. Scoccimarro, M. S. Vogeley, D. H. Weinberg, I. Zehavi, A. Berlind, et al., *Astrophys. J.* **606**, 702 (2004), [astro-ph/0310725](#).
- [19] D. J. Eisenstein, I. Zehavi, D. W. Hogg, R. Scoccimarro, M. R. Blanton, R. C. Nichol, R. Scranton, H.-J. Seo, M. Tegmark, Z. Zheng, et al., *Astrophys. J.* **633**, 560 (2005), [astro-ph/0501171](#).
- [20] B. A. Reid, L. Samushia, M. White, W. J. Percival, M. Manera, N. Padmanabhan, A. J. Ross, A. G. Sánchez, S. Bailey, D. Bizyaev, et al., *Mon. Not. R. Astron. Soc.* **426**, 2719 (2012), 1203.6641.
- [21] K. M. Smith, O. Zahn, and O. Doré, *Phys. Rev. D* **76**, 043510 (2007), 0705.3980.
- [22] C. M. Hirata, S. Ho, N. Padmanabhan, U. Seljak, and N. A. Bahcall, *Phys. Rev. D* **78**, 043520 (2008), 0801.0644.
- [23] S. Das, B. D. Sherwin, P. Aguirre, J. W. Appel, J. R. Bond, C. S. Carvalho, M. J. Devlin, J. Dunkley, R. Dünner, T. Essinger-Hileman, et al., *Physical Review Letters* **107**, 021301 (2011), 1103.2124.
- [24] Planck Collaboration, P. A. R. Ade, N. Aghanim, C. Armitage-Caplan, M. Arnaud, M. Ashdown, F. Atrio-Barandela, J. Aumont, C. Baccigalupi, A. J. Banday, et al., *Astron. Astrophys.* **571**, A17 (2014), 1303.5077.

- [25] R. A. C. Croft, D. H. Weinberg, M. Pettini, L. Hernquist, and N. Katz, *Astrophys. J.* **520**, 1 (1999), [astro-ph/9809401](#).
- [26] P. McDonald, J. Miralda-Escudé, M. Rauch, W. L. W. Sargent, T. A. Barlow, R. Cen, and J. P. Ostriker, *Astrophys. J.* **543**, 1 (2000), [astro-ph/9911196](#).
- [27] P. McDonald, U. Seljak, R. Cen, D. Shih, D. H. Weinberg, S. Burles, D. P. Schneider, D. J. Schlegel, N. A. Bahcall, J. W. Briggs, et al., *Astrophys. J.* **635**, 761 (2005), [astro-ph/0407377](#).
- [28] A. Slosar, A. Font-Ribera, M. M. Pieri, J. Rich, J.-M. Le Goff, É. Aubourg, J. Brinkmann, N. Busca, B. Carithers, R. Charlassier, et al., *Journal of Cosmology and Astroparticle Physics* **9**, 001 (2011), [1104.5244](#).
- [29] N. G. Busca, T. Delubac, J. Rich, S. Bailey, A. Font-Ribera, D. Kirkby, J.-M. Le Goff, M. M. Pieri, A. Slosar, É. Aubourg, et al., *Astron. Astrophys.* **552**, A96 (2013), [1211.2616](#).
- [30] A. Songaila, L. L. Cowie, C. J. Hogan, and M. Rugers, *Nature* **368**, 599 (1994).
- [31] D. Tytler, X.-M. Fan, and S. Burles, *Nature* **381**, 207 (1996), [astro-ph/9603069](#).
- [32] Y. I. Izotov and T. X. Thuan, *Astrophys. J.* **500**, 188 (1998).
- [33] M. Peimbert, V. Luridiana, and A. Peimbert, *Astrophys. J.* **666**, 636 (2007), [astro-ph/0701580](#).
- [34] M. Fumagalli, J. M. O'Meara, and J. X. Prochaska, *Science* **334**, 1245 (2011), [1111.2334](#).
- [35] M. Pettini and R. Cooke, *Mon. Not. R. Astron. Soc.* **425**, 2477 (2012), [1205.3785](#).
- [36] E. Aver, K. A. Olive, R. L. Porter, and E. D. Skillman, *Journal of Cosmology and Astroparticle Physics* **11**, 017 (2013), [1309.0047](#).
- [37] R. J. Cooke, M. Pettini, R. A. Jorgenson, M. T. Murphy, and C. C. Steidel, *Astrophys. J.* **781**, 31 (2014), [1308.3240](#).
- [38] A. G. Riess, A. V. Filippenko, P. Challis, A. Clocchiatti, A. Diercks, P. M. Garnavich, R. L. Gilliland, C. J. Hogan, S. Jha, R. P. Kirshner, et al., *Astron. J.* **116**, 1009 (1998), [astro-ph/9805201](#).
- [39] A. M. Koekemoer, S. M. Faber, H. C. Ferguson, N. A. Grogin, D. D. Kocevski, D. C. Koo, K. Lai, J. M. Lotz, R. A. Lucas, E. J. McGrath, et al., *Astrophys. J. Suppl.* **197**, 36 (2011), [1105.3754](#).
- [40] N. Suzuki, D. Rubin, C. Lidman, G. Aldering, R. Amanullah, K. Barbary, L. F. Barrientos, J. Botyanszki, M. Brodwin, N. Connolly, et al., *Astrophys. J.* **746**, 85 (2012), [1105.3470](#).

- [41] G. Hinshaw, D. Larson, E. Komatsu, D. N. Spergel, C. L. Bennett, J. Dunkley, M. R.olta, M. Halpern, R. S. Hill, N. Odegard, et al., *Astrophys. J. Suppl.* **208**, 19 (2013), 1212.5226.
- [42] Planck Collaboration, P. A. R. Ade, N. Aghanim, C. Armitage-Caplan, M. Arnaud, M. Ashdown, F. Atrio-Barandela, J. Aumont, C. Baccigalupi, A. J. Banday, et al., *ArXiv e-prints* (2013), 1303.5076.
- [43] Planck Collaboration, P. A. R. Ade, N. Aghanim, M. Arnaud, M. Ashdown, J. Aumont, C. Baccigalupi, A. J. Banday, R. B. Barreiro, J. G. Bartlett, et al., *ArXiv e-prints* (2015), 1502.01589.
- [44] D. J. Fixsen, *Astrophys. J.* **707**, 916 (2009), 0911.1955.
- [45] G. Mangano, G. Miele, S. Pastor, and M. Peloso, *Physics Letters B* **534**, 8 (2002), astro-ph/0111408.
- [46] E. W. Kolb and M. S. Turner, *The Early Universe* (Addison-Wesley, 1990).
- [47] A. A. Starobinsky, *Physics Letters B* **91**, 99 (1980).
- [48] A. H. Guth, *Phys. Rev. D* **23**, 347 (1981).
- [49] J. R. Gott, III, *Nature* **295**, 304 (1982).
- [50] A. D. Linde, *Physics Letters B* **108**, 389 (1982).
- [51] A. Albrecht and P. J. Steinhardt, *Physical Review Letters* **48**, 1220 (1982).
- [52] V. F. Mukhanov and G. V. Chibisov, *Soviet Journal of Experimental and Theoretical Physics Letters* **33**, 532 (1981).
- [53] S. W. Hawking, *Physics Letters B* **115**, 295 (1982).
- [54] A. H. Guth and S.-Y. Pi, *Physical Review Letters* **49**, 1110 (1982).
- [55] A. D. Linde, *Physics Letters B* **116**, 335 (1982).
- [56] A. A. Starobinsky, *Physics Letters B* **117**, 175 (1982).
- [57] J. M. Bardeen, P. J. Steinhardt, and M. S. Turner, *Phys. Rev. D* **28**, 679 (1983).
- [58] L. P. Grishchuk, *Soviet Journal of Experimental and Theoretical Physics* **40**, 409 (1975).
- [59] A. A. Starobinskiĭ, *Soviet Journal of Experimental and Theoretical Physics Letters* **30**, 682 (1979).
- [60] V. A. Rubakov, M. V. Sazhin, and A. V. Veryaskin, *Physics Letters B* **115**, 189 (1982).

- [61] R. Fabbri and M. D. Pollock, *Physics Letters B* **125**, 445 (1983).
- [62] L. F. Abbott and M. B. Wise, *Nuclear Physics B* **244**, 541 (1984).
- [63] A. G. Polnarev, *Soviet Astronomy* **29**, 607 (1985).
- [64] R. Crittenden, J. R. Bond, R. L. Davis, G. Efstathiou, and P. J. Steinhardt, *Physical Review Letters* **71**, 324 (1993), [astro-ph/9303014](#).
- [65] M. Zaldarriaga and U. Seljak, *Phys. Rev. D* **55**, 1830 (1997), [astro-ph/9609170](#).
- [66] U. Seljak and M. Zaldarriaga, *Physical Review Letters* **78**, 2054 (1997), [astro-ph/9609169](#).
- [67] M. Kamionkowski, A. Kosowsky, and A. Stebbins, *Physical Review Letters* **78**, 2058 (1997), [astro-ph/9609132](#).
- [68] P. A. R. Ade, R. W. Aikin, D. Barkats, S. J. Benton, C. A. Bischoff, J. J. Bock, J. A. Brevik, I. Buder, E. Bullock, C. D. Dowell, et al., *Physical Review Letters* **112**, 241101 (2014), [1403.3985](#).
- [69] BICEP2/Keck and Planck Collaborations, P. A. R. Ade, N. Aghanim, Z. Ahmed, R. W. Aikin, K. D. Alexander, M. Arnaud, J. Aumont, C. Baccigalupi, A. J. Banday, et al., *Physical Review Letters* **114**, 101301 (2015), [1502.00612](#).
- [70] R. Keisler, S. Hoover, N. Harrington, J. W. Henning, P. A. R. Ade, K. A. Aird, J. E. Austermann, J. A. Beall, A. N. Bender, B. A. Benson, et al., *Astrophys. J.* **807**, 151 (2015), [1503.02315](#).
- [71] J. P. Filippini, P. A. R. Ade, M. Amiri, S. J. Benton, R. Bihary, J. J. Bock, J. R. Bond, J. A. Bonetti, S. A. Bryan, B. Burger, et al., in *Society of Photo-Optical Instrumentation Engineers (SPIE) Conference Series* (2010), vol. 7741 of *Society of Photo-Optical Instrumentation Engineers (SPIE) Conference Series*, p. 1, [1106.2158](#).
- [72] G. Gamow, *Physical Review* **70**, 572 (1946).
- [73] R. A. Alpher, H. Bethe, and G. Gamow, *Physical Review* **73**, 803 (1948).
- [74] R. A. Alpher, J. W. Follin, and R. C. Herman, *Physical Review* **92**, 1347 (1953).
- [75] P. J. Peebles, *Physical Review Letters* **16**, 410 (1966).
- [76] P. J. E. Peebles, *Astrophys. J.* **146**, 542 (1966).
- [77] R. V. Wagoner, W. A. Fowler, and F. Hoyle, *Astrophys. J.* **148**, 3 (1967).
- [78] C. Hayashi, *Progress of Theoretical Physics* **5**, 224 (1950).

- [79] J. Yang, M. S. Turner, D. N. Schramm, G. Steigman, and K. A. Olive, *Astrophys. J.* **281**, 493 (1984).
- [80] R. H. Cyburt, B. D. Fields, K. A. Olive, and T.-H. Yeh, *ArXiv e-prints* (2015), 1505.01076.
- [81] R. H. Dicke, P. J. E. Peebles, P. G. Roll, and D. T. Wilkinson, *Astrophys. J.* **142**, 414 (1965).
- [82] I. D. Novikov and Y. B. Zel'dovich, *Annual Rev. Astron. Astrophys.* **5**, 627 (1967).
- [83] P. Peebles, *Astrophys. J.* **153**, 1 (1968).
- [84] Y. B. Zel'dovich, V. G. Kurt, and R. A. Syunyaev, *Soviet Journal of Experimental and Theoretical Physics* **28**, 146 (1969).
- [85] P. J. E. Peebles, *Astrophys. J.* **142**, 1317 (1965).
- [86] R. Weymann, *Astrophys. J.* **145**, 560 (1966).
- [87] A. Sakharov, *Zh. E. T. F.* **59**, 345 (1965).
- [88] R. K. Sachs and A. M. Wolfe, *Astrophys. J.* **147**, 73 (1967).
- [89] J. Silk, *Astrophys. J.* **151**, 459 (1968).
- [90] M. S. Longair and R. A. Sunyaev, *Nature* **223**, 719 (1969).
- [91] R. A. Sunyaev and Y. B. Zeldovich, *Astrophysics and Space Science* **7**, 3 (1970).
- [92] P. J. E. Peebles and J. T. Yu, *Astrophys. J.* **162**, 815 (1970).
- [93] A. G. Doroshkevich, Y. B. Zel'dovich, and R. A. Sunyaev, *Soviet Astronomy* **22**, 523 (1978).
- [94] U. Seljak, *Astrophys. J. Lett.* **435**, L87 (1994), [astro-ph/9406050](#).
- [95] W. Hu and N. Sugiyama, *Astrophys. J.* **444**, 489 (1995), [astro-ph/9407093](#).
- [96] J. Silk, *Nature* **215**, 1155 (1967).
- [97] S. Weinberg, *Astrophys. J.* **168**, 175 (1971).
- [98] J. H. Jeans, *Royal Society of London Philosophical Transactions Series A* **199**, 1 (1902).
- [99] E. Lifshitz, *J. Phys. U.S.S.R* **10**, 116 (1946).
- [100] W. B. Bonnor, *Mon. Not. R. Astron. Soc.* **117**, 104 (1957).
- [101] E. M. Lifshitz and I. M. Khalatnikov, *Advances in Physics* **12**, 185 (1963).
- [102] M. Guyot and Y. B. Zeldovic, *Astron. Astrophys.* **9**, 227 (1970).

- [103] P. Meszaros, *Astron. Astrophys.* **37**, 225 (1974).
- [104] P. J. E. Peebles, *Astrophys. J.* **258**, 415 (1982).
- [105] P. J. E. Peebles, *Astrophys. J. Lett.* **263**, L1 (1982).
- [106] G. R. Blumenthal, S. M. Faber, J. R. Primack, and M. J. Rees, *Nature* **311**, 517 (1984).
- [107] J. R. Bond and A. S. Szalay, *Astrophys. J.* **274**, 443 (1983).
- [108] D. J. Heath, *Mon. Not. R. Astron. Soc.* **179**, 351 (1977).
- [109] J. M. Bardeen, J. R. Bond, N. Kaiser, and A. S. Szalay, *Astrophys. J.* **304**, 15 (1986).
- [110] N. Sugiyama, *Astrophys. J. Suppl.* **100**, 281 (1995), [astro-ph/9412025](#).
- [111] W. Hu and N. Sugiyama, *Astrophys. J.* **471**, 542 (1996), [astro-ph/9510117](#).
- [112] D. J. Eisenstein and W. Hu, *Astrophys. J.* **496**, 605 (1998), [astro-ph/9709112](#).
- [113] D. J. Eisenstein and W. Hu, *Astrophys. J.* **511**, 5 (1999), [astro-ph/9710252](#).
- [114] R. J. Scherrer and M. S. Turner, *Phys. Rev. D* **33**, 1585 (1986).
- [115] G. Jungman, M. Kamionkowski, and K. Griest, *Phys. Rep.* **267**, 195 (1996), [hep-ph/9506380](#).
- [116] W. H. Press and P. Schechter, *Astrophys. J.* **187**, 425 (1974).
- [117] M. Davis and P. J. E. Peebles, *Astrophys. J. Suppl.* **34**, 425 (1977).
- [118] M. Davis, G. Efstathiou, C. S. Frenk, and S. D. M. White, *Astrophys. J.* **292**, 371 (1985).
- [119] J. Dubinski and R. G. Carlberg, *Astrophys. J.* **378**, 496 (1991).
- [120] J. F. Navarro, C. S. Frenk, and S. D. M. White, *Astrophys. J.* **490**, 493 (1997), [astro-ph/9611107](#).
- [121] R. K. Sheth and G. Tormen, *Mon. Not. R. Astron. Soc.* **308**, 119 (1999), [astro-ph/9901122](#).
- [122] B. Moore, *Nature* **370**, 629 (1994).
- [123] R. A. Flores and J. R. Primack, *Astrophys. J. Lett.* **427**, L1 (1994), [astro-ph/9402004](#).
- [124] J. F. Navarro, C. S. Frenk, and S. D. M. White, *Astrophys. J.* **462**, 563 (1996), [astro-ph/9508025](#).
- [125] S. S. McGaugh and W. J. G. de Blok, *Astrophys. J.* **499**, 41 (1998), [astro-ph/9801123](#).
- [126] W. J. G. de Blok and A. Bosma, *Astron. Astrophys.* **385**, 816 (2002), [astro-ph/0201276](#).

- [127] G. Kauffmann, S. D. M. White, and B. Guiderdoni, *Mon. Not. R. Astron. Soc.* **264**, 201 (1993).
- [128] A. Klypin, A. V. Kravtsov, O. Valenzuela, and F. Prada, *Astrophys. J.* **522**, 82 (1999), [astro-ph/9901240](#).
- [129] B. Moore, S. Ghigna, F. Governato, G. Lake, T. Quinn, J. Stadel, and P. Tozzi, *Astrophys. J. Lett.* **524**, L19 (1999), [astro-ph/9907411](#).
- [130] M. Boylan-Kolchin, J. S. Bullock, and M. Kaplinghat, *Mon. Not. R. Astron. Soc.* **415**, L40 (2011), [1103.0007](#).
- [131] S. Gelato and J. Sommer-Larsen, *Mon. Not. R. Astron. Soc.* **303**, 321 (1999), [astro-ph/9806289](#).
- [132] A. Pontzen and F. Governato, *Mon. Not. R. Astron. Soc.* **421**, 3464 (2012), [1106.0499](#).
- [133] A. Burkert, *Astrophys. J. Lett.* **447**, L25 (1995), [astro-ph/9504041](#).
- [134] D. N. Spergel and P. J. Steinhardt, *Physical Review Letters* **84**, 3760 (2000), [astro-ph/9909386](#).
- [135] S. Dodelson and L. M. Widrow, *Physical Review Letters* **72**, 17 (1994), [hep-ph/9303287](#).
- [136] X. Shi and G. M. Fuller, *Physical Review Letters* **82**, 2832 (1999), [astro-ph/9810076](#).
- [137] K. Abazajian, G. M. Fuller, and M. Patel, *Phys. Rev. D* **64**, 023501 (2001), [astro-ph/0101524](#).
- [138] M. Laine and M. Shaposhnikov, *Journal of Cosmology and Astroparticle Physics* **2008**, 031 (2008), URL <http://stacks.iop.org/1475-7516/2008/i=06/a=031>.
- [139] C. T. Kishimoto and G. M. Fuller, *Phys. Rev. D* **78**, 023524 (2008), [0802.3377](#).
- [140] R. Shrock, *Phys. Rev.* **D9**, 743 (1974).
- [141] P. B. Pal and L. Wolfenstein, *Phys. Rev. D* **25**, 766 (1982), URL <http://link.aps.org/doi/10.1103/PhysRevD.25.766>.
- [142] K. Abazajian, G. M. Fuller, and W. H. Tucker, *Astrophys. J.* **562**, 593 (2001), [astro-ph/0106002](#).
- [143] E. Bulbul, M. Markevitch, A. Foster, R. K. Smith, M. Loewenstein, et al., *Astrophys. J.* **789**, 13 (2014), [1402.2301](#).
- [144] A. Boyarsky, O. Ruchayskiy, D. Iakubovskiy, and J. Franse, *Phys.Rev.Lett.* **113**, 251301 (2014), [1402.4119](#).

- [145] A. Boyarsky, J. Franse, D. Iakubovskiy, and O. Ruchayskiy (2014), 1408.2503.
- [146] A. Boyarsky, J. Lesgourgues, O. Ruchayskiy, and M. Viel, Phys. Rev. Lett. **102**, 201304 (2009), 0812.3256.
- [147] A. Boyarsky, O. Ruchayskiy, and M. Shaposhnikov, Ann. Rev. Nucl. Part. Sci. **59**, 191 (2009), 0901.0011.
- [148] A. V. Maccio, O. Ruchayskiy, A. Boyarsky, and J. C. Munoz-Cuartas, Mon. Not. Roy. Astron. Soc. **428**, 882 (2013), 1202.2858.
- [149] D. Anderhalden, A. Schneider, A. V. Maccio, J. Diemand, and G. Bertone, Journal of Cosmology and Astroparticle Physics **1303**, 014 (2013), 1212.2967.
- [150] A. Schneider, D. Anderhalden, A. Maccio, and J. Diemand, Mon. Not. Roy. Astron. Soc. **441**, 6 (2014), 1309.5960.
- [151] R. Kennedy, C. Frenk, S. Cole, and A. Benson, Mon. Not. Roy. Astron. Soc. **442**, 2487 (2014), 1310.7739.
- [152] K. N. Abazajian, Phys. Rev. Lett. **112**, 161303 (2014), 1403.0954.
- [153] U. Maio and M. Viel, Mon. Not. R. Astron. Soc. **446**, 2760 (2015), 1409.6718.
- [154] S. Bose, W. A. Hellwing, C. S. Frenk, A. Jenkins, M. R. Lovell, et al. (2015), 1507.01998.
- [155] I. H. Gilbert, Astrophys. J. **144**, 233 (1966).
- [156] G. S. Bisnovatyi-Kogan and Y. B. Zel'dovich, Soviet Astronomy **14**, 758 (1971).
- [157] J. R. Bond, G. Efstathiou, and J. Silk, Physical Review Letters **45**, 1980 (1980).
- [158] P. Bode, J. P. Ostriker, and N. Turok, Astrophys. J. **556**, 93 (2001), astro-ph/0010389.
- [159] M. Viel, J. Lesgourgues, M. G. Haehnelt, S. Matarrese, and A. Riotto, Phys. Rev. D **71**, 063534 (2005), astro-ph/0501562.
- [160] C.-P. Ma and E. Bertschinger, Astrophys. J. **455**, 7 (1995), astro-ph/9506072.
- [161] D. Tseliakhovich and C. Hirata, Phys. Rev. D **82**, 083520 (2010), 1005.2416.
- [162] N. J. Shaviv, Mon. Not. R. Astron. Soc. **297**, 1245 (1998), astro-ph/9804292.
- [163] G.-C. Liu, K. Yamamoto, N. Sugiyama, and H. Nishioka, Astrophys. J. **547**, 1 (2001), astro-ph/0006223.
- [164] S. Singh and C.-P. Ma, Astrophys. J. **569**, 1 (2002), astro-ph/0111450.

- [165] G. B. Rybicki and I. P. dell'Antonio, *Astrophys. J.* **427**, 603 (1994), [astro-ph/9312006](#).
- [166] W. Hu, D. Scott, N. Sugiyama, and M. White, *Phys. Rev. D* **52**, 5498 (1995), [astro-ph/9505043](#).
- [167] V. K. Dubrovich and V. A. Stolyarov, *Astron. Astrophys.* **302**, 635 (1995).
- [168] Y. Ali-Haïmoud and C. M. Hirata, *Phys. Rev. D* **82**, 063521 (2010), [1006.1355](#).
- [169] Y. Ali-Haïmoud and C. M. Hirata, *Phys. Rev. D* **83**, 043513 (2011), [1011.3758](#).
- [170] J. Chluba and R. M. Thomas, *Mon. Not. R. Astron. Soc.* **412**, 748 (2011), [1010.3631](#).
- [171] R. A. Sunyaev and Y. B. Zeldovich, *Astrophysics and Space Science* **7**, 20 (1970).
- [172] Y. B. Zeldovich, A. F. Illarionov, and R. A. Syunyaev, *Zhurnal Eksperimentalnoi i Teoreticheskoi Fiziki* **62**, 1217 (1972).
- [173] J. Chluba, A. L. Erickcek, and I. Ben-Dayan, *Astrophys. J.* **758**, 76 (2012), [1203.2681](#).
- [174] G. B. Field, *Astrophys. J.* **129**, 525 (1959).
- [175] J. E. Gunn and B. A. Peterson, *Astrophys. J.* **142**, 1633 (1965).
- [176] P. R. Shapiro, in *The Physics of the Interstellar Medium and Intergalactic Medium*, edited by A. Ferrara, C. F. McKee, C. Heiles, and P. R. Shapiro (1995), vol. 80 of *Astronomical Society of the Pacific Conference Series*, p. 55.
- [177] R. Barkana and A. Loeb, *Phys. Rep.* **349**, 125 (2001), [astro-ph/0010468](#).
- [178] R. H. Becker, X. Fan, R. L. White, M. A. Strauss, V. K. Narayanan, R. H. Lupton, J. E. Gunn, J. Annis, N. A. Bahcall, J. Brinkmann, et al., *Astron. J.* **122**, 2850 (2001), [astro-ph/0108097](#).
- [179] D. N. Spergel, R. Bean, O. Doré, M. R. Nolta, C. L. Bennett, J. Dunkley, G. Hinshaw, N. Jarosik, E. Komatsu, L. Page, et al., *Astrophys. J. Suppl.* **170**, 377 (2007), [astro-ph/0603449](#).
- [180] B. E. Robertson, R. S. Ellis, S. R. Furlanetto, and J. S. Dunlop, *Astrophys. J. Lett.* **802**, L19 (2015), [1502.02024](#).
- [181] S. R. Furlanetto, S. P. Oh, and F. H. Briggs, *Phys. Rep.* **433**, 181 (2006), [astro-ph/0608032](#).
- [182] J. R. Pritchard and A. Loeb, *Reports on Progress in Physics* **75**, 086901 (2012), [1109.6012](#).
- [183] J. D. Bowman, M. F. Morales, J. N. Hewitt, and MWA Collaboration, in *American Astronomical Society Meeting Abstracts #218* (2011), p. 132.06.

- [184] O. Martinez-Rubi, V. K. Veligatla, A. G. de Bruyn, P. Lampropoulos, A. R. Offringa, V. Jelic, S. Yatawatta, L. V. E. Koopmans, and S. Zaroubi, in *Astronomical Data Analysis Software and Systems XXII*, edited by D. N. Friedel (2013), vol. 475 of *Astronomical Society of the Pacific Conference Series*, p. 377, 1302.4462.
- [185] A. R. Parsons, A. Liu, J. E. Aguirre, Z. S. Ali, R. F. Bradley, C. L. Carilli, D. R. DeBoer, M. R. Dexter, N. E. Gugliucci, D. C. Jacobs, et al., *Astrophys. J.* **788**, 106 (2014), 1304.4991.
- [186] L. J. Greenhill and G. Bernardi, ArXiv e-prints (2012), 1201.1700.
- [187] C. L. Carilli, ArXiv e-prints (2008), 0802.1727.
- [188] D. G. Yamazaki, K. Ichiki, T. Kajino, and G. J. Mathews, *Advances in Astronomy* **2010** (2010), 1112.4922.
- [189] P. Blasi, S. Burles, and A. V. Olinto, *Astrophysical Journal, Letters* **514**, L79 (1999), astro-ph/9812487.
- [190] T. Kahniashvili, Y. Maravin, A. Natarajan, N. Battaglia, and A. G. Tevzadze, *Astrophys. J.* **770**, 47 (2013), 1211.2769.
- [191] D. Paoletti and F. Finelli, *Physics Letters B* **726**, 45 (2013), 1208.2625.
- [192] K. E. Kunze and E. Komatsu, *Journal of Cosmology and Astroparticle Physics* **1**, 009 (2014), 1309.7994.
- [193] A. Neronov and I. Vovk, *Science* **328**, 73 (2010), 1006.3504.
- [194] F. Tavecchio, G. Ghisellini, L. Foschini, G. Bonnoli, G. Ghirlanda, and P. Coppi, *MNRAS* **406**, L70 (2010), 1004.1329.
- [195] K. Dolag, M. Kachelriess, S. Ostapchenko, and R. Tomàs, *Astrophysical Journal, Letters* **727**, L4 (2011), 1009.1782.
- [196] A. E. Broderick, P. Chang, and C. Pfrommer, *Astrophysical Journal* **752**, 22 (2012), 1106.5494.
- [197] F. Miniati and A. Elyiv, *Astrophys. J.* **770**, 54 (2013), 1208.1761.
- [198] L. Sironi and D. Giannios, *Astrophys. J.* **787**, 49 (2014), 1312.4538.
- [199] P. Chang, A. E. Broderick, C. Pfrommer, E. Puchwein, A. Lamberts, and M. Shalaby, ArXiv e-prints (2014), 1410.3797.
- [200] C. D. Dermer, M. Cavadini, S. Razzaque, J. D. Finke, J. Chiang, and B. Lott, *Astrophys. J. Lett.* **733**, L21 (2011), 1011.6660.

- [201] A. M. Taylor, I. Vovk, and A. Neronov, *Astron. Astrophys.* **529**, A144 (2011), 1101.0932.
- [202] C. D. Murray and S. F. Dermott, *Solar system dynamics* (Princeton University Press, 1999).
- [203] A. Einstein, *Sitzungsberichte der Königlich Preußischen Akademie der Wissenschaften* (Berlin) pp. 154–167 (1918).
- [204] P. C. Peters and J. Mathews, *Physical Review* **131**, 435 (1963).
- [205] C. W. Misner, K. S. Thorne, and J. A. Wheeler, *Gravitation* (W.H. Freeman and Co., 1973).
- [206] J. H. Taylor and J. M. Weisberg, *Astrophys. J.* **253**, 908 (1982).
- [207] B. Paczynski, *Astrophys. J. Lett.* **308**, L43 (1986).
- [208] L.-X. Li and B. Paczyński, *Astrophys. J. Lett.* **507**, L59 (1998), astro-ph/9807272.
- [209] E. Nakar, *Phys. Rep.* **442**, 166 (2007), astro-ph/0701748.
- [210] G. Harry and the LIGO Scientific Collaboration, *Classical and Quantum Gravity* **27**, 084006 (2010).
- [211] T. Accadia, F. Acernese, M. Alshourbagy, P. Amico, F. Antonucci, S. Aoudia, N. Arnaud, C. Arnault, K. G. Arun, P. Astone, et al., *Journal of Instrumentation* **7**, 3012 (2012).
- [212] K. Somiya, *Classical and Quantum Gravity* **29**, 124007 (2012), URL <http://stacks.iop.org/0264-9381/29/i=12/a=124007>.
- [213] J. Abadie, B. P. Abbott, R. Abbott, M. Abernathy, T. Accadia, F. Acernese, C. Adams, R. Adhikari, P. Ajith, B. Allen, et al., *Classical and Quantum Gravity* **27**, 173001 (2010), 1003.2480.
- [214] C. Cutler and É. E. Flanagan, *Phys. Rev. D* **49**, 2658 (1994), arXiv:gr-qc/9402014.
- [215] K. G. Arun, B. R. Iyer, B. S. Sathyaprakash, and P. A. Sundararajan, *Phys. Rev. D* **71**, 084008 (2005), URL <http://link.aps.org/doi/10.1103/PhysRevD.71.084008>.
- [216] J. Aasi, J. Abadie, B. P. Abbott, R. Abbott, T. D. Abbott, M. Abernathy, T. Accadia, F. Acernese, C. Adams, T. Adams, et al., *Phys. Rev. D* **88**, 062001 (2013), 1304.1775.
- [217] E. E. Flanagan and T. Hinderer, *Phys. Rev. D* **77**, 021502 (2008), URL <http://link.aps.org/doi/10.1103/PhysRevD.77.021502>.
- [218] T. Hinderer, B. D. Lackey, R. N. Lang, and J. S. Read, *Phys. Rev. D* **81**, 123016 (2010), URL <http://link.aps.org/doi/10.1103/PhysRevD.81.123016>.

- [219] K. Hotokezaka, K. Kyutoku, and M. Shibata, *Phys. Rev. D* **87**, 044001 (2013), URL <http://link.aps.org/doi/10.1103/PhysRevD.87.044001>.
- [220] J. S. Read, L. Baiotti, J. D. E. Creighton, J. L. Friedman, B. Giacomazzo, K. Kyutoku, C. Markakis, L. Rezzolla, M. Shibata, and K. Taniguchi, *Phys. Rev. D* **88**, 044042 (2013), 1306.4065.
- [221] C. Cutler, T. A. Apostolatos, L. Bildsten, L. S. Finn, E. E. Flanagan, D. Kennefick, D. M. Markovic, A. Ori, E. Poisson, and G. J. Sussman, *Physical Review Letters* **70**, 2984 (1993), [arXiv:astro-ph/9208005](https://arxiv.org/abs/astro-ph/9208005).
- [222] R. Oechslin and H.-T. Janka, *Phys. Rev. Lett.* **99**, 121102 (2007), URL <http://link.aps.org/doi/10.1103/PhysRevLett.99.121102>.
- [223] K. Kiuchi, Y. Sekiguchi, M. Shibata, and K. Taniguchi, *Phys. Rev. Lett.* **104**, 141101 (2010), URL <http://link.aps.org/doi/10.1103/PhysRevLett.104.141101>.
- [224] J. R. Oppenheimer and G. M. Volkoff, *Physical Review* **55**, 374 (1939).
- [225] J.-P. Zahn, *Astron. Astrophys.* **57**, 383 (1977).
- [226] C. S. Kochanek, *Astrophys. J.* **398**, 234 (1992).
- [227] L. Bildsten and C. Cutler, *Astrophys. J.* **400**, 175 (1992).
- [228] N. N. Weinberg, P. Arras, and J. Burkart, *Astrophys. J.* **769**, 121 (2013).
- [229] K. Olive et al. (Particle Data Group), *Chin. Phys.* **C38**, 090001 (2014).
- [230] B. H. J. McKellar and M. J. Thomson, *Phys. Rev. D* **49**, 2710 (1994).
- [231] A. Kusenko, *Phys. Rept.* **481**, 1 (2009), 0906.2968.
- [232] B. Pontecorvo, *Sov. Phys. JETP* **26**, 984 (1968).
- [233] A. C. Vincent, E. Fernández Martínez, P. Hernández, O. Mena, and M. Lattanzi, *Journal of Cosmology and Astroparticle Physics* **4**, 006 (2015), 1408.1956.
- [234] E. Aver, K. A. Olive, and E. D. Skillman, *ArXiv e-prints* (2015), 1503.08146.
- [235] S. Hannestad, I. Tamborra, and T. Tram, *Journal of Cosmology and Astroparticle Physics* **7**, 025 (2012), 1204.5861.
- [236] S. Hannestad, R. S. Hansen, and T. Tram, *Phys. Rev. Lett.* **112**, 031802 (2014), 1310.5926.
- [237] B. Dasgupta and J. Kopp, *Phys. Rev. Lett.* **112**, 031803 (2014), 1310.6337.

- [238] T. Bringmann, J. Hasenkamp, and J. Kersten, *Journal of Cosmology and Astroparticle Physics* **1407**, 042 (2014), 1312.4947.
- [239] P. Ko and Y. Tang, *Phys. Lett.* **B739**, 62 (2014), 1404.0236.
- [240] A. Boyarsky, O. Ruchayskiy, and M. Shaposhnikov, *Annual Review of Nuclear and Particle Science* **59**, 191 (2009), URL <http://dx.doi.org/10.1146/annurev.nucl.010909.083654>.
- [241] K. A. Olive and M. S. Turner, *Phys. Rev. D* **25**, 213 (1982), URL <http://link.aps.org/doi/10.1103/PhysRevD.25.213>.
- [242] A. Dolgov and S. Hansen, *Astroparticle Physics* **16**, 339 (2002), ISSN 0927-6505, URL <http://www.sciencedirect.com/science/article/pii/S0927650501001153>.
- [243] T. Asaka, M. Shaposhnikov, and M. Laine, *Journal of High Energy Physics* **1**, 091 (2007), hep-ph/0612182.
- [244] M. Davis, M. Lecar, C. Pryor, and E. Witten, *Astrophys. J.* **250**, 423 (1981).
- [245] G. R. Blumenthal, H. Pagels, and J. R. Primack, *Nature* **299**, 37 (1982).
- [246] J. J. Dalcanton and C. J. Hogan, *Astrophys. J.* **561**, 35 (2001), astro-ph/0004381.
- [247] K. Abazajian, *Phys. Rev. D* **73**, 063513 (2006), URL <http://link.aps.org/doi/10.1103/PhysRevD.73.063513>.
- [248] U. Seljak, A. Makarov, P. McDonald, and H. Trac, *Phys. Rev. Lett.* **97**, 191303 (2006), URL <http://link.aps.org/doi/10.1103/PhysRevLett.97.191303>.
- [249] M. Viel, J. Lesgourgues, M. G. Haehnelt, S. Matarrese, and A. Riotto, *Phys. Rev. Lett.* **97**, 071301 (2006), URL <http://link.aps.org/doi/10.1103/PhysRevLett.97.071301>.
- [250] A. Boyarsky, J. Lesgourgues, O. Ruchayskiy, and M. Viel, *Journal of Cosmology and Astroparticle Physics* **2009**, 012 (2009), URL <http://stacks.iop.org/1475-7516/2009/i=05/a=012>.
- [251] E. Polisensky and M. Ricotti, *Phys. Rev. D* **83**, 043506 (2011), URL <http://link.aps.org/doi/10.1103/PhysRevD.83.043506>.
- [252] R. S. de Souza, A. Mesinger, A. Ferrara, Z. Haiman, R. Perna, and N. Yoshida, *Monthly Notices of the Royal Astronomical Society* **432**, 3218 (2013), <http://mnras.oxfordjournals.org/content/432/4/3218.full.pdf+html>, URL <http://mnras.oxfordjournals.org/content/432/4/3218.abstract>.
- [253] M. Viel, G. D. Becker, J. S. Bolton, and M. G. Haehnelt, *Phys. Rev. D* **88**, 043502 (2013), URL <http://link.aps.org/doi/10.1103/PhysRevD.88.043502>.

- [254] S. Horiuchi, P. J. Humphrey, J. Oñorbe, K. N. Abazajian, M. Kaplinghat, and S. Garrison-Kimmel, *Phys. Rev. D* **89**, 025017 (2014), URL <http://link.aps.org/doi/10.1103/PhysRevD.89.025017>.
- [255] C. R. Watson, J. F. Beacom, H. Yüksel, and T. P. Walker, *Phys. Rev. D* **74**, 033009 (2006), URL <http://link.aps.org/doi/10.1103/PhysRevD.74.033009>.
- [256] A. Boyarsky, D. Iakubovskiy, O. Ruchayskiy, and V. Savchenko, *Monthly Notices of the Royal Astronomical Society* **387**, 1361 (2008), <http://mnras.oxfordjournals.org/content/387/4/1361.full.pdf+html>, URL <http://mnras.oxfordjournals.org/content/387/4/1361.abstract>.
- [257] C. R. Watson, Z. Li, and N. K. Polley, *Journal of Cosmology and Astroparticle Physics* **2012**, 018 (2012), URL <http://stacks.iop.org/1475-7516/2012/i=03/a=018>.
- [258] K. C. Y. Ng, S. Horiuchi, J. M. Gaskins, M. Smith, and R. Preece, *ArXiv e-prints* (2015), 1504.04027.
- [259] T. Asaka and M. Shaposhnikov, *Physics Letters B* **620**, 17 (2005), ISSN 0370-2693, URL <http://www.sciencedirect.com/science/article/pii/S0370269305008087>.
- [260] M. Shaposhnikov and I. Tkachev, *Physics Letters B* **639**, 414 (2006), ISSN 0370-2693, URL <http://www.sciencedirect.com/science/article/pii/S0370269306008124>.
- [261] A. Kusenko, *Phys. Rev. Lett.* **97**, 241301 (2006), URL <http://link.aps.org/doi/10.1103/PhysRevLett.97.241301>.
- [262] K. Petraki and A. Kusenko, *Phys. Rev. D* **77**, 065014 (2008), URL <http://link.aps.org/doi/10.1103/PhysRevD.77.065014>.
- [263] S. Khalil and O. Seto, *Journal of Cosmology and Astroparticle Physics* **2008**, 024 (2008), URL <http://stacks.iop.org/1475-7516/2008/i=10/a=024>.
- [264] A. Merle, V. Niro, and D. Schmidt, *Journal of Cosmology and Astroparticle Physics* **2014**, 028 (2014), URL <http://stacks.iop.org/1475-7516/2014/i=03/a=028>.
- [265] T. Asaka, M. Shaposhnikov, and A. Kusenko, *Physics Letters B* **638**, 401 (2006), ISSN 0370-2693, URL <http://www.sciencedirect.com/science/article/pii/S0370269306006733>.
- [266] F. Bezrukov, H. Hettmansperger, and M. Lindner, *Phys. Rev. D* **81**, 085032 (2010), URL <http://link.aps.org/doi/10.1103/PhysRevD.81.085032>.
- [267] M. Nemevek, G. Senjanovi, and Y. Zhang, *Journal of Cosmology and Astroparticle Physics* **2012**, 006 (2012), URL <http://stacks.iop.org/1475-7516/2012/i=07/a=006>.

- [268] D. J. Robinson and Y. Tsai, *Phys. Rev. D* **90**, 045030 (2014), 1404.7118.
- [269] A. Adulpravitchai and M. A. Schmidt, *Journal of High Energy Physics* **1**, 6 (2015), 1409.4330.
- [270] A. Merle and A. Schneider, *ArXiv e-prints* (2014), 1409.6311.
- [271] B. Shuve and I. Yavin, *Phys. Rev. D* **89**, 113004 (2014), URL <http://link.aps.org/doi/10.1103/PhysRevD.89.113004>.
- [272] L. Lello and D. Boyanovsky, *Phys. Rev. D* **91**, 063502 (2015), 1411.2690.
- [273] A. Merle and M. Totzauer, *Journal of Cosmology and Astroparticle Physics* **6**, 011 (2015), 1502.01011.
- [274] A. V. Patwardhan, G. M. Fuller, C. T. Kishimoto, and A. Kusenko (2015), 1507.01977.
- [275] J. P. Kneller, R. J. Scherrer, G. Steigman, and T. P. Walker, *Phys. Rev. D* **64**, 123506 (2001), [astro-ph/0101386](https://arxiv.org/abs/astro-ph/0101386).
- [276] M. Lattanzi, R. Ruffini, and G. V. Vereshchagin, *Phys. Rev. D* **72**, 063003 (2005), [astro-ph/0509079](https://arxiv.org/abs/astro-ph/0509079).
- [277] K. Abazajian, N. F. Bell, G. M. Fuller, and Y. Y. Y. Wong, *Phys. Rev. D* **72**, 063004 (2005), [astro-ph/0410175](https://arxiv.org/abs/astro-ph/0410175).
- [278] C. J. Smith, G. M. Fuller, C. T. Kishimoto, and K. N. Abazajian, *Phys. Rev. D* **74**, 085008 (2006), [astro-ph/0608377](https://arxiv.org/abs/astro-ph/0608377).
- [279] M. Shimon, N. J. Miller, C. T. Kishimoto, C. J. Smith, G. M. Fuller, and B. G. Keating, *Journal of Cosmology and Astroparticle Physics* **5**, 037 (2010), 1001.5088.
- [280] M. E. Anderson, E. Churazov, and J. N. Bregman, *ArXiv e-prints* (2014), 1408.4115.
- [281] S. Riemer-Sorensen, *ArXiv e-prints* (2014), 1405.7943.
- [282] T. Jeltema and S. Profumo, *Mon. Not. R. Astron. Soc.* **450**, 2143 (2015), 1408.1699.
- [283] A. Boyarsky, J. Franse, D. Iakubovskiy, and O. Ruchayskiy, *ArXiv e-prints* (2014), 1408.4388.
- [284] E. Bulbul, M. Markevitch, A. R. Foster, R. K. Smith, M. Loewenstein, and S. W. Randall, *ArXiv e-prints* (2014), 1409.4143.
- [285] T. Jeltema and S. Profumo, *ArXiv e-prints* (2014), 1411.1759.
- [286] D. Malyshev, A. Neronov, and D. Eckert, *Phys. Rev. D* **90**, 103506 (2014), URL <http://link.aps.org/doi/10.1103/PhysRevD.90.103506>.

- [287] O. Urban, N. Werner, S. W. Allen, A. Simionescu, J. S. Kaastra, and L. E. Strigari, *Mon. Not. R. Astron. Soc.* **451**, 2447 (2015), 1411.0050.
- [288] D. Nötzold and G. Raffelt, *Nuclear Physics B* **307**, 924 (1988).
- [289] T. Asaka, M. Laine, and M. Shaposhnikov, *Journal of High Energy Physics* **6**, 053 (2006), hep-ph/0605209.
- [290] D. Blas, J. Lesgourgues, and T. Tram, *Journal of Cosmology and Astroparticle Physics* **7**, 034 (2011), 1104.2933.
- [291] S. Horiuchi, P. J. Humphrey, J. Onorbe, K. N. Abazajian, M. Kaplinghat, et al., *Phys.Rev.* **D89**, 025017 (2014), 1311.0282.
- [292] D. Malyshev, A. Neronov, and D. Eckert, *Phys.Rev.* **D90**, 103506 (2014), 1408.3531.
- [293] T. Tamura, R. Iizuka, Y. Maeda, K. Mitsuda, and N. Y. Yamasaki, *Publ.Astron.Soc.Jap.* **67**, 23 (2015), 1412.1869.
- [294] K. N. Abazajian, J. F. Beacom, and N. F. Bell, *Phys. Rev. D* **66**, 013008 (2002), astro-ph/0203442.
- [295] R. A. Harris and L. Stodolsky, *Physics Letters B* **116**, 464 (1982).
- [296] L. Stodolsky, *Phys. Rev. D* **36**, 2273 (1987).
- [297] G. Raffelt, G. Sigl, and L. Stodolsky, *Phys. Rev. D* **45**, 1782 (1992), URL <http://journals.aps.org/prd/abstract/10.1103/PhysRevD.45.1782>.
- [298] G. Raffelt, G. Sigl, and L. Stodolsky, *Phys. Rev. Lett.* **70**, 2363 (1993), URL <http://journals.aps.org/prl/abstract/10.1103/PhysRevLett.70.2363>.
- [299] N. F. Bell, R. R. Volkas, and Y. Y. Y. Wong, *Phys. Rev. D* **59**, 113001 (1999), hep-ph/9809363.
- [300] R. R. Volkas and Y. Y. Y. Wong, *Phys. Rev. D* **62**, 093024 (2000), hep-ph/0007185.
- [301] K. S. M. Lee, R. R. Volkas, and Y. Y. Y. Wong, *Phys. Rev. D* **62**, 093025 (2000), hep-ph/0007186.
- [302] D. Boyanovsky and C. Ho, *JHEP* **0707**, 030 (2007), hep-ph/0612092.
- [303] J. Ghiglieri and M. Laine, *ArXiv e-prints* (2015), 1506.06752.
- [304] T. Venumadhav, F.-Y. Cyr-Racine, K. N. Abazajian, and C. M. Hirata, *ArXiv e-prints* (2015), 1507.06655.

- [305] R. Hagedorn, Lect. Notes Phys. **221**, 53 (1985).
- [306] E. Megías, E. Ruiz Arriola, and L. L. Salcedo, Nuclear Physics B Proceedings Supplements **234**, 313 (2013), 1207.7287.
- [307] J. I. Kapusta and C. Gale, *Finite-Temperature Field Theory: Principles and Applications* (Cambridge University Press, 2006).
- [308] M. Laine and Y. Schröder, Phys. Rev. D **73**, 085009 (2006), hep-ph/0603048.
- [309] S. Borsányi, Z. Fodor, S. D. Katz, S. Krieg, C. Ratti, and K. Szabó, Journal of High Energy Physics **1**, 138 (2012), 1112.4416.
- [310] A. Bazavov, T. Bhattacharya, C. E. DeTar, H.-T. Ding, S. Gottlieb, R. Gupta, P. Hegde, U. M. Heller, F. Karsch, E. Laermann, et al., Phys. Rev. D **86**, 034509 (2012), 1203.0784.
- [311] S. Gottlieb, W. Liu, D. Toussaint, R. L. Renken, and R. L. Sugar, Physical Review Letters **59**, 2247 (1987).
- [312] C. Ratti, S. Borsanyi, G. Endrodi, Z. Fodor, S. D. Katz, et al., Nucl. Phys. **A904-905**, 869c (2013).
- [313] S. Hannestad and J. Madsen, Phys. Rev. D **52**, 1764 (1995), astro-ph/9506015.
- [314] W. R. Yueh and J. R. Buchler, Astrophysics and Space Science **39**, 429 (1976).
- [315] M. Srednicki, *Quantum Field Theory* (Cambridge University Press, 2007).
- [316] R. Unterdorfer and G. Ecker, Journal of High Energy Physics **10**, 017 (2005), hep-ph/0507173.
- [317] C. T. Kishimoto, G. M. Fuller, and C. J. Smith, Phys. Rev. Lett. **97**, 141301 (2006), astro-ph/0607403.
- [318] M. Viel, G. D. Becker, J. S. Bolton, and M. G. Haehnelt, Phys. Rev. D **88**, 043502 (2013), 1306.2314.
- [319] S. Horiuchi, P. J. Humphrey, J. Oñorbe, K. N. Abazajian, M. Kaplinghat, and S. Garrison-Kimmel, Phys. Rev. D **89**, 025017 (2014), 1311.0282.
- [320] E. Polisensky and M. Ricotti, Mon. Not. R. Astron. Soc. **437**, 2922 (2014), 1310.0430.
- [321] A. Lewis, A. Challinor, and A. Lasenby, Astrophys. J. **538**, 473 (2000), astro-ph/9911177.
- [322] J. Lesgourgues and T. Tram, Journal of Cosmology and Astroparticle Physics **9**, 032 (2011), 1104.2935.

- [323] S. Hannestad, R. S. Hansen, T. Tram, and Y. Y. Y. Wong (2015), 1506.05266.
- [324] G. Boyd, J. Engels, F. Karsch, E. Laermann, C. Legeland, M. Lütgemeier, and B. Petersson, Nuclear Physics B **469**, 419 (1996), hep-lat/9602007.
- [325] T. Bhattacharya et al., Phys. Rev. Lett. **113**, 082001 (2014), 1402.5175.
- [326] T. Takahashi, K. Mitsuda, R. Kelley, F. Aharonian, H. Akamatsu, F. Akimoto, S. Allen, N. Anabuki, L. Angelini, K. Arnaud, et al., in *Society of Photo-Optical Instrumentation Engineers (SPIE) Conference Series* (2014), vol. 9144 of *Society of Photo-Optical Instrumentation Engineers (SPIE) Conference Series*, p. 25, 1412.1356.
- [327] E. Figueroa-Feliciano, A. J. Anderson, D. Castro, D. C. Goldfinger, J. Rutherford, M. E. Eckart, R. L. Kelley, C. A. Kilbourne, D. McCammon, K. Morgan, et al., ArXiv e-prints (2015), 1506.05519.
- [328] Planck Collaboration, P. A. R. Ade, N. Aghanim, C. Armitage-Caplan, M. Arnaud, M. Ashdown, F. Atrio-Barandela, J. Aumont, C. Baccigalupi, A. J. Banday, et al., ArXiv e-prints (2013), 1303.5082.
- [329] D. Larson, J. Dunkley, G. Hinshaw, E. Komatsu, M. R. Nolta, C. L. Bennett, B. Gold, M. Halpern, R. S. Hill, N. Jarosik, et al., Astrophys. J. Suppl. **192**, 16 (2011), 1001.4635.
- [330] Planck Collaboration, P. A. R. Ade, N. Aghanim, C. Armitage-Caplan, M. Arnaud, M. Ashdown, F. Atrio-Barandela, J. Aumont, C. Baccigalupi, A. J. Banday, et al., ArXiv e-prints (2013), 1303.5077.
- [331] K. S. Dawson et al., Astron. J. **145**, 10 (2013), 1208.0022.
- [332] P. André et al., Journal of Cosmology and Astroparticle Physics **2**, 006 (2014), 1310.1554.
- [333] D. J. Eisenstein and W. Hu, Astrophys. J. **496**, 605 (1998), astro-ph/9709112.
- [334] J. Silk, Astrophys. J. **151**, 459 (1968).
- [335] W. H. Press and E. T. Vishniac, Nature **279**, 137 (1979).
- [336] S. Seager, D. D. Sasselov, and D. Scott, Astrophys. J. Suppl. **128**, 407 (2000), astro-ph/9912182.
- [337] R. Weymann, Physics of Fluids (1958-1988) **8**, 2112 (1965), URL <http://scitation.aip.org/content/aip/journal/pof1/8/11/10.1063/1.1761165>.
- [338] J. Chluba and R. A. Sunyaev, Astron. Astrophys. **475**, 109 (2007), astro-ph/0702531.

- [339] S. P. Goldman, *Phys. Rev. A* **40**, 1185 (1989).
- [340] D. Blas, J. Lesgourgues, and T. Tram, *Journal of Cosmology and Astroparticle Physics* **7**, 034 (2011), 1104.2933.
- [341] E. Kolb and M. Turner, *The Early Universe.*, vol. 69 of *Front. Phys.* (Addison-Wesley, Reading, MA, 1990).
- [342] B. Novosyadlyj, *Mon. Not. R. Astron. Soc.* **370**, 1771 (2006), astro-ph/0603674, URL <http://mnras.oxfordjournals.org/content/370/4/1771.abstract>.
- [343] R. Khatri and B. D. Wandelt, *Phys. Rev. D* **79**, 023501 (2009), 0810.4370.
- [344] L. Senatore, S. Tassev, and M. Zaldarriaga, *Journal of Cosmology and Astroparticle Physics* **8**, 031 (2009), 0812.3652.
- [345] C. Pitrou, J.-P. Uzan, and F. Bernardeau, *Journal of Cosmology and Astroparticle Physics* **7**, 003 (2010), 1003.0481.
- [346] C. Dvorkin, K. Blum, and M. Zaldarriaga, *Phys. Rev. D* **87**, 103522 (2013), 1302.4753.
- [347] U. Seljak and M. Zaldarriaga, *Astrophys. J.* **469**, 437 (1996), astro-ph/9603033.
- [348] A. Lewis, A. Challinor, and A. Lasenby, *Astrophys. J.* **538**, 473 (2000), astro-ph/9911177.
- [349] J. Lesgourgues, ArXiv e-prints (2011), 1104.2932.
- [350] R. Barkana and A. Loeb, *Astrophys. J.* **626**, 1 (2005), astro-ph/0410129.
- [351] J. R. Pritchard and S. R. Furlanetto, *Mon. Not. R. Astron. Soc.* **376**, 1680 (2007), astro-ph/0607234.
- [352] K. Ahn, P. R. Shapiro, I. T. Iliev, G. Mellema, and U.-L. Pen, *Astrophys. J.* **695**, 1430 (2009), 0807.2254.
- [353] L. N. Holzbauer and S. R. Furlanetto, *Mon. Not. R. Astron. Soc.* **419**, 718 (2012), 1105.5648.
- [354] V. B. Berestetskii, E. M. Lifshitz, and V. B. Pitaevskii, *Relativistic quantum theory. Pt.1* (Pergamon Press, Oxford, 1971).
- [355] D. G. Hummer, *Mon. Not. R. Astron. Soc.* **125**, 21 (1962).
- [356] C. M. Hirata, *Phys. Rev. D* **78**, 023001 (2008), 0803.0808.
- [357] Y. Ali-Haïmoud, D. Grin, and C. M. Hirata, *Phys. Rev. D* **82**, 123502 (2010), 1009.4697.
- [358] W. Unno, *Publications of the Astronomical Society of Japan* **7**, 81 (1955).

- [359] J. A. Gubner, *Journal of Physics A Mathematical General* **27**, L745 (1994).
- [360] W. Hu and M. White, *Phys. Rev. D* **56**, 596 (1997), [astro-ph/9702170](#).
- [361] D. Pequignot, P. Petitjean, and C. Boisson, *Astron. Astrophys.* **251**, 680 (1991).
- [362] A. Lewis, *Phys. Rev. D* **76**, 063001 (2007), [0707.2727](#).
- [363] A. Lewis and A. Challinor, *Phys. Rev. D* **76**, 083005 (2007), [astro-ph/0702600](#).
- [364] B. D. Hughes, *Random walks and random environments* (Clarendon Press, Oxford, 1995), ISBN 0198537891 0198537883 0198537883 0198537891.
- [365] R. Wielebinski, in *Cosmic Magnetic Fields*, edited by R. Wielebinski and R. Beck (2005), vol. 664 of *Lecture Notes in Physics*, Berlin Springer Verlag, p. 89.
- [366] R. Beck, *Space Science Reviews* **166**, 215 (2012).
- [367] M. L. Bernet, F. Miniati, S. J. Lilly, P. P. Kronberg, and M. Dessauges-Zavadsky, *Nature* **454**, 302 (2008), [0807.3347](#).
- [368] J. P. Vallee, *New Astronomy Reviews* **48**, 763 (2004), ISSN 1387-6473, URL <http://www.sciencedirect.com/science/article/pii/S138764730400065X>.
- [369] R. Durrer and A. Neronov, *Astron. and Astrophys. Review* **21**, 62 (2013), [1303.7121](#).
- [370] L. M. Widrow, D. Ryu, D. R. G. Schleicher, K. Subramanian, C. G. Tsagas, and R. A. Treumann, *Space Science Reviews* **166**, 37 (2012), [1109.4052](#).
- [371] S. Naoz and R. Narayan, *Physical Review Letters* **111**, 051303 (2013), [1304.5792](#).
- [372] F. Miniati and A. R. Bell, *Astrophys. J.* **729**, 73 (2011), [1001.2011](#).
- [373] T. Kobayashi, *Journal of Cosmology and Astroparticle Physics* **5**, 040 (2014), [1403.5168](#).
- [374] D. A. Varshalovich, *Astrophysics* **4**, 215 (1968).
- [375] D. A. Varshalovich, *Soviet Physics Uspekhi* **13**, 429 (1971).
- [376] H. Yan and A. Lazarian, *Astrophys. J.* **653**, 1292 (2006), [astro-ph/0611281](#).
- [377] H. Yan and A. Lazarian, *Astrophys. J.* **657**, 618 (2007), [astro-ph/0611282](#).
- [378] H. Yan and A. Lazarian, *Astrophys. J.* **677**, 1401 (2008), [0711.0926](#).
- [379] H. Tashiro and N. Sugiyama, *Mon. Not. R. Astron. Soc.* **372**, 1060 (2006), [astro-ph/0607169](#).
- [380] D. R. G. Schleicher, R. Banerjee, and R. S. Klessen, *Astrophys. J.* **692**, 236 (2009), [0808.1461](#).

- [381] M. Shiraishi, H. Tashiro, and K. Ichiki, *Phys. Rev. D* **89**, 103522 (2014), 1403.2608.
- [382] A. Loeb and M. Zaldarriaga, *Physical Review Letters* **92**, 211301 (2004), astro-ph/0312134.
- [383] P. Madau, A. Meiksin, and M. J. Rees, *Astrophys. J.* **475**, 429 (1997), astro-ph/9608010.
- [384] D. Babich and A. Loeb, *Astrophys. J.* **635**, 1 (2005), astro-ph/0505358.
- [385] S. De and H. Tashiro, *Phys. Rev. D* **89**, 123002 (2014), 1307.3584.
- [386] W. Hanle, *Naturwissenschaften* **11**, 690 (1923).
- [387] J. O. Stenflo, *Solar Physics* **80**, 209 (1982).
- [388] J. L. Leroy, in *Measurements of Solar Vector Magnetic Fields*, edited by M. J. Hagyard (1985), pp. 121–140.
- [389] E. Landi Degl’Innocenti, in *IAU Colloq. 117: Dynamics of Quiescent Prominences*, edited by V. Ruzdjak and E. Tandberg-Hanssen (1990), vol. 363 of *Lecture Notes in Physics, Berlin Springer Verlag*, pp. 206–230.
- [390] V. Bommier, E. Landi Degl’Innocenti, J.-L. Leroy, and S. Sahal-Brechot, *Solar Physics* **154**, 231 (1994).
- [391] P. Goldreich, D. A. Keeley, and J. Y. Kwan, *Astrophys. J.* **179**, 111 (1973).
- [392] P. Goldreich, D. A. Keeley, and J. Y. Kwan, *Astrophys. J.* **182**, 55 (1973).
- [393] P. Goldreich and N. D. Kylafis, *Astrophys. J. Lett.* **243**, L75 (1981).
- [394] H. Yan and A. Lazarian, *J. Quant. Spec. Rad. Trans.* **113**, 1409 (2012), 1203.5571.
- [395] K. Blum, *Density Matrix Theory and Applications* (Springer Berlin Heidelberg, 2012).
- [396] V. B. Berestetskii, E. M. Lifshitz, and V. B. Pitaevskii, *Relativistic quantum theory. Pt.1* (Pergamon Press, 1971).
- [397] W. Hu and M. White, *Phys. Rev. D* **56**, 596 (1997), astro-ph/9702170.
- [398] V. Bommier and S. Sahal-Brechot, *Astron. Astrophys.* **69**, 57 (1978).
- [399] L. Mandel and E. Wolf, *Optical Coherence and Quantum Optics* (Cambridge University Press, 1995).
- [400] C. M. Hirata and K. Sigurdson, *MNRAS* **375**, 1241 (2007), astro-ph/0605071.
- [401] D. A. Varshalovich, A. N. Moskalev, and V. K. Khersonskii, *Quantum Theory of Angular Momentum* (World Scientific, Singapore, 1988).

- [402] C. M. Hirata, Mon. Not. R. Astron. Soc. **367**, 259 (2006), [astro-ph/0507102](#).
- [403] B. Zygelman, Astrophysical Journal **622**, 1356 (2005).
- [404] B. Zygelman, Phys. Rev. A **81**, 032506 (2010).
- [405] L. C. Balling, R. J. Hanson, and F. M. Pipkin, Phys. Rev. **133**, A607 (1964), URL <http://link.aps.org/doi/10.1103/PhysRev.133.A607>.
- [406] W. Happer, Reviews of Modern Physics **44**, 169 (1972).
- [407] Barrat, J.P. and Cohen-Tannoudji, C., J. Phys. Radium **22**, 329 (1961), URL <http://dx.doi.org/10.1051/jphysrad:01961002206032900>.
- [408] D. Lai, F. A. Rasio, and S. L. Shapiro, Astrophys. J. **420**, 811 (1994), [arXiv:astro-ph/9304027](#).
- [409] D. Lai, F. A. Rasio, and S. L. Shapiro, Astrophys. J. **423**, 344 (1994), [arXiv:astro-ph/9307032](#).
- [410] D. Lai, Mon. Not. R. Astron. Soc. **270**, 611 (1994), [arXiv:astro-ph/9404062](#).
- [411] N. N. Weinberg, P. Arras, E. Quataert, and J. Burkart, Astrophys.J. **751**, 136 (2012), 1107.0946.
- [412] P. N. McDermott, H. M. van Horn, and C. J. Hansen, Astrophys. J. **325**, 725 (1988).
- [413] D. Tsang, J. S. Read, T. Hinderer, A. L. Piro, and R. Bondarescu, Physical Review Letters **108**, 011102 (2012), 1110.0467.
- [414] K. S. Thorne and A. Campolattaro, Astrophys. J. **149**, 591 (1967).
- [415] K. S. Thorne, Astrophys. J. **158**, 1 (1969).
- [416] K. S. Thorne, Astrophys. J. **158**, 997 (1969).
- [417] P. N. McDermott, H. M. van Horn, and J. F. Scholl, Astrophys. J. **268**, 837 (1983).
- [418] J. P. Cox, *Theory of Stellar Pulsation* (Princeton University Press, Princeton, NJ, 1980).
- [419] D. Lynden-Bell and J. P. Ostriker, Mon. Not. R. Astron. Soc. **136**, 293 (1967).
- [420] A. K. Schenk, P. Arras, E. E. Flanagan, S. A. Teukolsky, and I. Wasserman, Phys.Rev. **D65**, 024001 (2002), [gr-qc/0101092](#).
- [421] A. Deprit, Celestial Mechanics **1**, 12 (1969).

- [422] R. D. Blandford and K. S. Thorne, *Applications of Classical Physics* (California Institute of Technology, 2011), URL <http://www.pma.caltech.edu/Courses/ph136/yr2011/>.
- [423] Y. Wu and P. Goldreich, *Astrophys.J.* **546**, 469 (2001), [astro-ph/0003163](#).
- [424] W. Unno, Y. Osaki, H. Ando, H. Saio, and H. Shibahashi, *Nonradial Oscillations of Stars* (University of Tokyo Press, Tokyo, 1989).
- [425] A. W. Steiner and A. L. Watts, *Physical Review Letters* **103**, 181101 (2009), [0902.1683](#).
- [426] E. Chabanat, P. Bonche, P. Haensel, J. Meyer, and R. Schaeffer, *Nuclear Physics A* **635**, 231 (1998).
- [427] A. Reisenegger and P. Goldreich, *Astrophys. J.* **395**, 240 (1992).
- [428] T. Van Hoolst, *Astron. Astrophys.* **286**, 879 (1994).
- [429] J. Fuller and D. Lai, *Mon. Not. R. Astron. Soc.* **412**, 1331 (2011), [1009.3316](#).
- [430] J. Fuller and D. Lai, *Mon. Not. R. Astron. Soc.* **421**, 426 (2012), [1108.4910](#).
- [431] J. Fuller and D. Lai, *Mon. Not. R. Astron. Soc.* **430**, 274 (2013), [1211.0624](#).
- [432] J. Burkart, E. Quataert, P. Arras, and N. N. Weinberg, *Mon. Not. R. Astron. Soc.* **433**, 332 (2013), [1211.1393](#).
- [433] L. Bildsten, G. Ushomirsky, and C. Cutler, *Astrophys. J.* **460**, 827 (1996).